Structural systematics of drug-like molecules: from benzamides to tennimides

by

Pavle Močilac, M. Pharm.

A thesis presented for the degree of Doctor of Philosophy

at

Dublin City University

Ollscoil Chathair Bhaile Atha Cliath

School of Chemical Sciences

May 2012

to my lovely wife Lei who was supporting me through rain and shine,
and my parents Ivan and Barbara whose love, strength and wisdom
sent me to the way I follow

DECLARATION

I hereby certify that this material, which I now submit for the assessment on the programme of study leading to the award of Ph.D. is entirely my own fork and has not been taken from the work of others save and to the extent that such work has been cited and acknowledged within the text of my work

Signed:________________________ ID No:_____________________

Pavle Mocilac

Date: ______________________________

ACKNOWLEDGEMENTS

First and foremost I would like to thank to my supervisor, Dr. John F. Gallagher for his outstanding support, encouragement and patience during this work.

I would also like to express my gratitude to:

Dr. Alan J. Lough at the Department of Chemistry, University of Toronto, Canada, for obtaining X-ray crystallographic data in period from January 2009 to January 2010.

Dr. Christine Loscher in the School of Biotechnology, Dublin City University, for excellently organised T3 programme.

Dr. Neal Lemon and Sharon Whyte for managing T3 programme.

Prof. Kieran Nolan in the School of Chemical Sciences, Dublin City University for useful advice and help.

Dr. Turlough Downes, in the School of Mathematical Sciences in Dublin City University on useful help on calculations.

All students that worked with me, Niall Hehir, Islam Ali Osman, Chloe Violin, Mark Farrell, Marie Bélières, Marion Lefevre and Fabian Pohl for their work and friendship, as well as to former students Mark Talon and Katie Donnelly for their contributions.

All technicians and staff of the School of Chemical Sciences especially to John McLoughlin for his excellent help and advice on NMR, as well as to Damien McGuirk, Veronica Dobbyn, Ambrose May, Vincent Hooper and Brendan Twamley for their high professionalism and excellent service.

Staff and professionals at Irish Centre for High-End Computing, Dr. Alin M. Elena, Eoin Brazil, Rosemarie Lalor and Dr. Jean-Christophe Desplat for their cooperation and help.

All my colleagues from organic lab, Sarrah Kebbell, Ian G. Beadham, Declan Daly, Andy Garry, Sharon Murphy, Brian Murphy, Oksana Shvydkiv, Kieran Joyce, William Butler, Monika Grubisz, Thomas Hayes, Marcello Iacono, Shelly Long, Rohitkumar Gore, Fadi Hatoum and Mukund Ghavre for their help, support and friendship.

ABSTRACT

A structural systematic study was undertaken on benzamides, carbamates and substituted benzamide derivatives as 3×3 isomer grids comprising *N*-(pyridyl)benzamide (**Fxx** and **Mxx**) (**x** = *para-/meta-/ortho-*) and *N*-(phenyl)pyridinecarboxamide (**NxxF** and **NxxM**) grids. These were synthesised and characterised, with their crystal structures determined by single crystal X-ray diffraction. Five series of **CxxR** (**R** = CH_3, OCH_3, F, Cl, Br) carbamate isomer grids have been synthesised and characterised, with some pertinent structures determined by X-ray diffraction. *Ab initio* modelling, conformational analysis and comparisons of experimental solid state with optimised molecular geometries have facilitated an examination of the relationships between conformations and inter/intramolecular interactions, rationalisation of differences between the solid state and calculated structures, as well as the presence of molecular disorder and polymorphism.

New classes of macrocycles have been developed including tetramers and trimers, based on our earlier research on benzamides and carbamates. These systems include various *para*-substituted derivatives (**F**, **Cl**, **Br**, $\mathbf{CH_3}$ $\mathbf{CO_2CH_3}$) and have been fully characterized by ^{1}H, ^{13}C, ^{19}F NMR and IR spectroscopy, while their crystal and molecular structures have been determined by single crystal X-ray diffraction.

The development of tennimides and trezimides as new macrocycles based on an imide backbone, presents an important entry point into a potentially fruitful area. Furthermore, discovery of trezimides is especially important since no analogous macrocycle has been reported. Synthesis of tennimides and trezimides has been accomplished using a one-step synthetic strategy over a range of derivatives and presents a basis for synthesis of analogous macrocycles. Tennimides and trezimides proved to be rigid and stable compounds. The determining factors in the cyclisation are (*i*) the presence of the imide *ortho*-pyridine/pyrimidine rings and (*ii*) the inherent ability of the imide group to twist by 80-120°, as measured by the '**CO**···**CO**' torsion angle, providing a 'hinge' for ring closure or helical assembly. The trezimides can adopt two distinct conformations in the solid state, (though one is preferred), whereas the tennimides adopt discrete conformational states as *oc*, *cc* and *oo* that highlight subtle macrocyclic geometric changes on cavity opening (*o*) and closing (*c*) (though these interconvert in solution).

ABBREVIATIONS

ATR-IR	Attenuated Total Reflectance Infrared spectroscopy
B3LYP	Becke, Three-parameter, Lee-Yang-Parr
CBS-QB3	Complete Basis Set-Quadratic Becke3
CCD	Charge-Coupled Device
COSY	Correlation Spectroscopy
CSD	Cambridge Structural Database
DEPT	Distortionless Enhancement by Polarization Transfer
DEPTQ	Distortionless Enhancement by Polarization Transfer - Quaternery atoms
DFT	Density Functional Theory
ESI	Electronic Supplementary Information file
HMBC	Heteronuclear multiple-bond correlation spectroscopy
HQSC	Heteronuclear single-quantum correlation spectroscopy
IR	Infrared spectroscopy
K_v channels	Voltage Gated Potassium Channels
m.p.	Melting Point
MALDI-TOF	Matrix-Assisted Laser Desorption/Ionization - Time-Of-Flight
MS	Mass spectroscopy
NMR	Nuclear Magnetic Resonance
NOESY	Nuclear Overhauser effect Spectroscopy
PCM	Polarizable Continuum Model
PES	Potential Energy Surface
RT	Room Temperature
SAR	Structure Activity Relationship
SMD	Solvation Model Density
SXRD	Single Crystal X-Ray Diffraction
TLC	Thin layer chromatography
XRD	X-Ray Diffraction

Reagents and solvents:

2-AP	2-aminopyridine
26-APM	2-aminopyrimidine
3,4-DAP	3,4-diaminopyridine
3-AP	3-aminopyridine
4-AP	4-aminopyridine
AP	Aminopyridine
$CDCl_3$	Deuterated chloroform
CH_2Cl_2	Dichloromethane
CH_3CN	Acetonitrile
CH_3COCH_3	Acetone
$CHCl_3$	Chloroform
Cl_3FC	Trichlorofluoromethane
DBU	1,8-Diazabicycloundec-7-ene
DMAP	Dimethylaminopyridine
DMSO	Dimethyl sulfoxide
DMSO-d_6	Deuterated dimethyl sulfoxide
DPPA	Diphenylphosphoryl azide
Et_2O	Diethyl ether
Et_3N	Triethylamine
EtOH	Ethanol
HCl	Hydrochloric acid
H_2SO_4	Sulphuric acid
IPA	*Iso*-propyl alcohol
$KHCO_3$`	Potassium Hydrogen Carbonate
MeOH	Methanol
$MgSO_4$	Magnesium Sulphate
N_2	Nitrogen gas
Na_2CO_3	Sodium Carbonate
NaCl	Sodium Chloride
NaOH	Sodium Hydroxide
NH_4Cl	Ammonium Chloride
$SOCl_2$	Thionyl chloride
THF	Tetrahydrofuran
TTP	Triphenyl phosphite

TABLE OF CONTENTS

CHAPTER III: TENNIMIDES AND TREZIMIDES 187

Electronic supplementary information files (**ESI**) are provided comprising spectral, crystallographic and modelling information:

ESI I.pdf – benzamides and pyridinecarboxamides
ESI II.pdf – carbamates
ESI III.pdf – tennimides and trezimides

INTRODUCTION

1. Basic concepts

1.1. Structural systematics, crystallography and computational modelling

Structural systematics[1,2] presents a systematic approach in structural science by the comprehensive multidisciplinary survey of structurally related compounds. This term is usually related to methods in solid-state chemistry with the central role of crystallography, however, investigations of structurally related compounds are important in other fields of chemistry where the solid state is not central, such as medicinal chemistry and drug design. The main concept of structural systematics is comparison of chemical structure data, usually derived from single crystal or powder X-ray diffraction, with physical properties of structurally similar compounds (salts, complexes and small organic molecules).

The concept of structural systematics originates in inorganic, coordination and organometallic chemistry[1] and later was extended to areas where more flexible molecules were in focus, such as *drug-like* small organic molecules. X-ray diffraction (XRD) has a key role in structural systematics, as the most powerful experimental structural method that enables scientists to "see" atoms and molecules, from simple arrays of ions to large, complex biomolecules. Advancement of crystallographic methods, computational power (including software for structure solving)[3] makes XRD a routine analytical method of choice. Very often XRD analyses are done just for the sake of unambiguous identification. XRD is an experimental method that provides real, averaged information on the structure of crystallised compounds and/or co-crystals.

Structural systematics is a step beyond simple XRD analyses. It implies usage of structural data derived from many different but similar structures to compare amongst themselves or with known physical properties, in order to test hypotheses and eventually expand knowledge in different areas of chemical sciences.

Advances in quantum and computational chemistry,[4] modelling methods (*ab initio*[5], semi-empirical[6] and molecular mechanics methods)[7] together with increasing available computational power has brought in new, virtual methods of structural science, where a molecule is commonly viewed as an isolated entity in *gas phase* (vacuum) or as solvated if one of the solvation methods is introduced. A common name for this area is molecular modelling and is seen as part of theoretical and computational chemistry. Molecular modelling is usually a corner stone for physico-organic chemistry, atmospheric chemistry as well as for chemistry of the *liquid phase*. However, the most important application of molecular modelling is in medicinal chemistry, drug design and drug development, as *'big pharma'* heavily invests in molecular modelling in order to develop cheaper and structure based ways of drug design.

Structural systematics relies on merging several areas of structural research (including both crystallography and molecular modelling) and the ability to collate, integrate and correlate physico-chemical data to provide an insight into physical or chemical properties within, or between, molecular organic groups.[8-11] Such studies and the comprehensive analyses of large groups of small organic molecules have undergone enormous advances in the past decade with the advent of information technologies and instrumentation.[8,9,12] Studies combining high throughput syntheses, structural chemistry and *ab initio* calculations provide chemical and structural information together with affording an insight into many physico-chemical properties and trends within molecular organic series.[8,13-16] Advances in synthetic chemistry has allowed for the systematic synthesis of chemical analogues using reactions amenable to combinatorial chemistry and high through-put synthesis.[17] In tandem, developments in crystallographic and computational (modelling) fields have facilitated a surge in data generation and structural analyses for publication and/or archiving[8] and based on many classes of organic molecules.[13-16] Structural systematic approaches have utilised polymorphs,[9,12] solvates, salts,[18] isomers[13,16] and homologous series,[19,20] with combinations thereof, to identify patterns of similarities or differences that can aid in the understanding of chemical and structural properties.[8,9,12-16]

Comprehensive chemical and computational analyses of small '*drug-like*' molecules together with structural systematic approaches allow us to utilise an increasing data stream from both crystallography and computational resources.[8,9,13,21] Integration can yield essential information for analysing trends and provide an insight into similar/different physical or chemical properties within or between molecular organic series.[8,9,13,14,16]

1.2. Conformational analysis

One of the important tools in structural systematics is conformational analysis.[22] It is an assessment of the relative energies (or thermodynamic stabilities), reactivities, and physical properties of alternative conformations of a molecular entity, usually by the application of different modelling methods. Conformation can be defined as a spatial arrangement of the atoms affording distinction between stereoisomers which can be interconverted by rotations about formally single bonds.[23]

Conformational isomers or conformers (specifically as rotamers) differ by rotation about only one single bond. Hence, interconversion of conformers does not involve breaking or reforming of chemical bonds. The rotational barrier, or barrier to rotation, is the activation energy required to interconvert rotamers. Rotation of a single bond in a molecular entity changes the total energy of a molecular system; one or more particular positions are stable (minimum). The most stable position is called the global minimum (GM), while others are local minima (LM) or *meta*-stable positions. An unstable position where a first derivation equals zero is called a transition state (TS).

Rotation of a single bond that links an individual atom (*e.g.* H, Cl, F, *etc.*) or a linear moiety (*e.g.* CN group) to a molecular entity will not change the geometry or energy of a molecular system and therefore, will be neglected in conformational analyses. Only rotable single bonds whose rotation changes the energy of a system can be considered. Those are usually bonds linking bulky and/or asymmetric groups and moieties, as well as rings. Each single bond whose rotation brings a change of energy presents one *degree* of conformational freedom (conformational coordinate). A molecular entity can have one or more degrees of conformational freedom (conformational coordinates).

In a crystalline solid state, molecular entities are constrained in the crystal structure by intermolecular interactions, typically in one particular conformation. A solid state conformation usually presents the most stable one (global minimum, GM_0)[22] however, in many cases *meta*-stable or unstable conformations can be adopted due to the energy compensation by strong and favourable intermolecular interactions.[24] Sometimes different conformations can be found in different polymorphs of the same molecular entity.

In the liquid (solution, melt) phase or in the *gas phase*, free rotation is enabled, and therefore, different conformations are possible. A solution or melt is, in fact, a complex equilibrium of different conformers of the same molecular entity with the major prevalence of one, the most stable conformer. Prevalence of a particular conformation depends on the conformational energy difference between conformers as well as temperature and is driven by the Boltzmann distribution:

$$\frac{N_i}{N_{total}} = \frac{e^{-E_{rel}/RT}}{\sum_{k=1}^{N_{total}} e^{-E_k/RT}} \qquad \text{(Eq. 1)}$$

The left hand side is the equilibrium ratio of conformer i to the total number of conformers. E_{rel} is the relative energy of the i-th conformer from the minimum energy conformer. R is the molar ideal gas constant equal to 8.31 J/mol.K) and T is the temperature in Kelvin (K). The denominator of the right side is the partition function. For a molecular system that can adopt two conformations equation 1 can be rearranged into:

$$P = \frac{100}{1 + e^{-E_{rel}/RT}} \qquad \text{(Eq. 2)}$$

P represents the percentage of the lower energy conformer (Fig. **1**). Energy differences between the conformational states are related thermodynamically to their populations, with a ratio of 1:10 for a free energy difference of ≈ 5.7 kJ.mol^{-1} at room temperature. Consequently, conformations with relative free energies larger then 8.4 kJ.mol^{-1} are populated to a very minor extent (Fig. **1**). Conformational analysis can be accomplished by experimental or theoretical methods. Experimental methods imply spectroscopic techniques such as dynamic NMR (D-NMR) or IR.

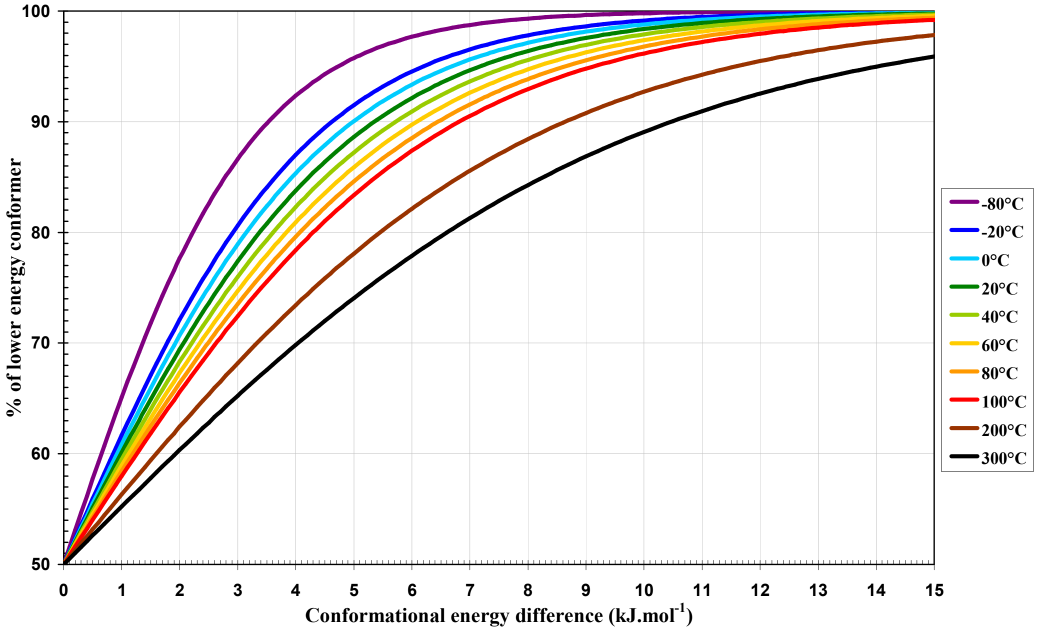

Fig. 1: Boltzmann distribution as the percentage of the lower energy conformation in a two conformation equilibrating system as a function of conformational energy difference (x-axis, kJ.mol^{-1}) at various temperatures (°C, colour).

Theoretical methods that are routinely used, however, differ by the approach and level of theory (Monte Carlo methods, molecular dynamics, molecular mechanics, semi-empirical methods, *ab initio* methods).[4-7] Monte Carlo methods and molecular mechanics are less accurate but they take into account the molecule as a whole. Alternatively, computationally costly *ab initio* methods are robust and more accurate. Since computation of all possible conformational space can be very demanding, a specific, simplified approach can be applied in order to investigate each separate (isolated) but critical conformational coordinate that is not constrained due to delocalisation and is likely to be rotated under normal circumstances.[4-7]

In a particular molecular entity some conformational coordinates may be considered as generally constrained. One example is the amide bond (NH-C=O). Due to the delocalisation of electrons (partial double bond) the amide group is relatively planar, while rotation of the C-N bond at ambient temperature is less likely. Therefore, constrained conformational coordinates, such as amide C-N bonds, are excluded from conformational analyses.

Selected critical conformational coordinates are subjected to a method known as the "conformational scan" in which the conformational coordinate (dihedral angle) is rotated by a certain increment, and at each step the total energy is calculated. When the calculated energy is plotted against the corresponding angle the result is a potential energy surface (PES) diagram. The described method is approximate since it takes into account only the separated coordinates, and will not give total conformational space. On the other hand if the method used for energy calculation is accurate enough (*ab initio*, DFT) and includes partial optimisation (coordinate relaxation) that allows the entire molecule to adopt a new conformation, the resulting PES diagram can be considered as a very accurate model of conformational behaviour in one dimension. Theoretical conformational analyses are usually accomplished using available quantum chemistry software packages as Gaussian.[25]

Crystallisation is a complex process involving thermodynamic as well as kinetic and many other factors. Such studies with conformational analysis can provide valuable information on relative energies of different molecular conformations to aid in an indepth understanding of factors that promote the aggregation and isolation of distinct and favoured conformations in the solid state.

1.3. Isomer grids

The concept originates from combinatorial chemistry methods where isomers and moieties are combined into more complex compound libraries in order to yield numerous compounds that share similar structural motifs, as well as pharmacological activities.[26] In medicinal chemistry and drug design the purpose is to cover structural space in order to increase the probability of a positive outcome ("hit"). In structural systematics exploring isomer grids is a useful concept to examine the influence of position variation on structure, aggregation or physico-chemical properties such as morphology, melting point, reactivity, solubility, stability, crystallinity, optical and mechanical.

Isomer grids are specific sets of isomers where two or more identical (or different) substituents (or heteroatoms) exchange their places in a systematic and combinatorial manner. Isomer grids are based on a fixed scaffold, usually a simple ring system (6-, 5- or 4-membered aromatic or cycloalkane/ene ring), or complex systems like tropane, steroid, morphinan, porphyrin and calixarene. A good example of a simple scaffold is a six-membered aromatic ring. Systematic exchange of the place of the substituent(s) or heteroatom(s) will give an isomer grid. Two homo- or hetero-substituents or heteroatoms, (X-A, Y-B; X, Y = any moiety different from H; A, B = N, O, S) can be arranged to give three different isomers (*para*, *meta*, *ortho*, Scheme **1**). Addition of one more Y-B substituent can yield six possible isomers (Scheme **2**). If there are three different substituents the number of possible isomers increases to ten (Scheme **3**).

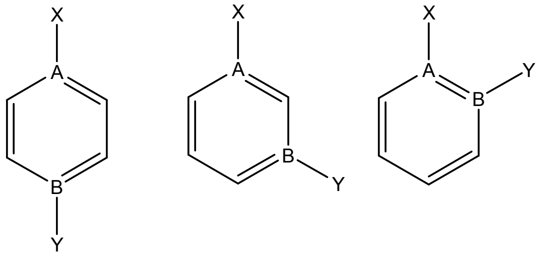

Scheme 1: Possible combinations with two different substituents (***p****ara*, ***m****eta*, ***o****rtho*)

The examples represent simple, one-dimensional isomers grids. If a molecular scaffold contains two rings connected by a linker it can be used to build a two dimensional isomer grid. A linker can be symmetric (*e.g.* simple bond, hydrocarbon chain, methylene, amino, ether, thio, diazo, ureido, guanido, keto, sulpho, *etc.*) or asymmetric (amide, carbamate, ester, sulfonamide, *etc.*).

Two rings can be labelled **X** and **Y** according to the substituent/heteroatom (Scheme **4**). For this particular example the number of possible isomers is 9, since the combination of two rings with one substituent changing positions gives a 3×3 matrix *i.e.* isomer grid (Table **1**). Similarly, a two ring scaffold with two identical substituents at each ring gives a 6×6 isomer grid with 36 possible isomers (Table **2**), while if substituents were dissimilar the number of isomers is 100 (10×10 isomer grid).

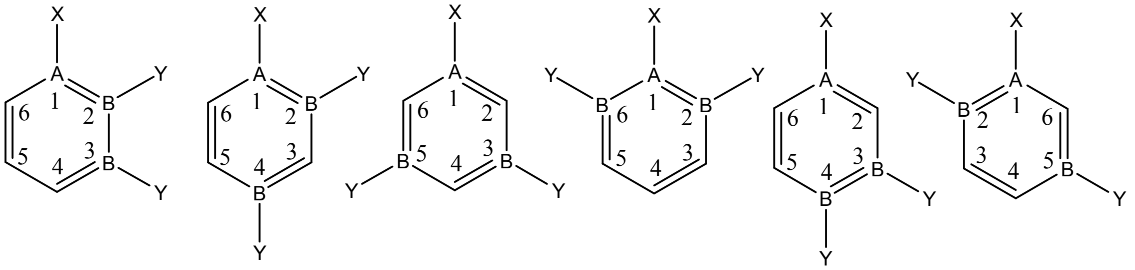

Scheme 2: Possible combinations (6) with three substituents (two being identical): "23", "24", "35", "26", "34", "25"

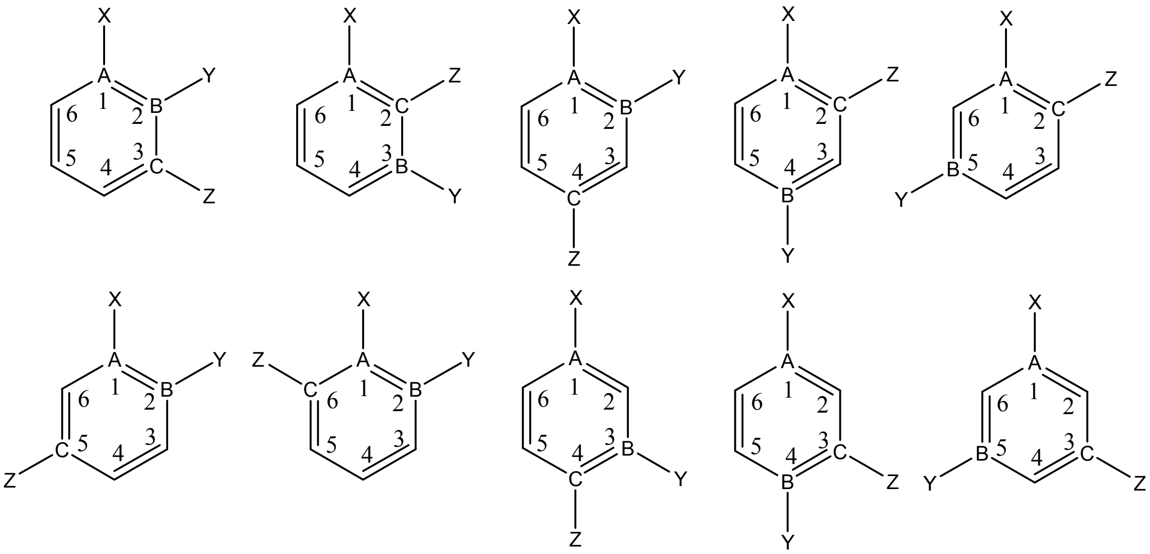

Scheme 3: Possible combinations (10) with three substituents (all different): 2Y3Z, 2Z3Y, 2Y4Z, 2Z4Y, 2Z5Y, 2Y5Z, 2Z6Y, 3Y4Z, 3Z4Y, 3Z5Y

Table 1: A two dimensional (3×3) isomer grid with each ring (**X** or **Y**) having one substituent/heteroatom (X/A or Y/B). A designated letter ***p***, ***m*** or ***o*** indicates positions of the substituent on each isomer.

Y **X**	*para*	*meta*	*ortho*
para	**XppY**	**XpmY**	**XpoY**
meta	**XmpY**	**XmmY**	**XmoY**
ortho	**XopY**	**XomY**	**XooY**

If three rings are connected with a trivalent linker then it is a tridimensional isomer grids with 27 (3×3×3), 216 (6×6×6) or 1000 (10×10×10) possible isomers. Certainly, a complex system can be conceived with *n* rings, giving a *n*-dimensional isomer grid. Therefore, an isomer grid is a matrix of all possible combinations of one dimensional isomers based on an *n*-dimensional molecular scaffold. Synthesis of isomer grids has been useful in medicinal and combinatorial chemistry, however, their role in structural systematics and solid-state chemistry is yet to be established.

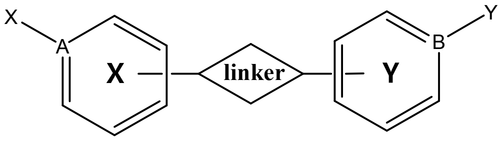

Scheme 4: A scaffold with two rings and a linker is the basis for a two dimensional isomer grid

Table 2: A two dimensional (6×6) isomer grid with each ring (**X** or **Y**) having two identical substituent/heteroatoms (X/A or Y/B). A designated number indicates the positions of the substituent on each isomer.

Y **X**	2,3-	2,4-	2,5-	2,6-	3,4-	3,5-
2,3-	X23-23Y	X23-24Y	X23-25Y	X23-26Y	X23-34Y	X23-35Y
2,4-	X24-23Y	X24-24Y	X24-25Y	X24-26Y	X24-34Y	X24-35Y
2,5-	X25-23Y	X25-24Y	X25-25Y	X25-26Y	X25-34Y	X25-35Y
2,6-	X26-23Y	X26-24Y	X26-25Y	X26-26Y	X26-34Y	X26-35Y
3,4-	X34-23Y	X34-24Y	X34-25Y	X34-26Y	X34-34Y	X34-35Y
3,5-	X35-23Y	X35-24Y	X35-25Y	X35-26Y	X35-34Y	X35-35Y

2. Objectives

Our research is directed towards structural systematics of isomer grids integrating crystal structure analyses with computational (*ab initio*) modelling methods to explore the influence of positions of different functional groups *e.g.* **F**/**Cl**/**Br**/**I**/**Me**/**OMe** and/or heteroatoms (**N**) in two dimensional isomer grids based on semi-rigid *drug-like* scaffold on inter- and intramolecular interactions, conformations, physicochemical properties and solid-state packing. Comparisons involve analysis of the (*a*) spectroscopic data (*b*) crystal structures, (*c*) computational calculations (geometry optimisation in the *gas phase* and solvated forms CH_2Cl_2 and H_2O), molecular energies and ΔG_{solv} and (*d*) conformational analyses of the optimised structures.

The questions to be addressed involve correlations between the various permutations of the group site with molecular conformation, solid-state aggregation and physicochemical properties. The formation of inter/intramolecular hydrogen bonds in the solid state and their influences on molecular conformations are analysed and collated with conformational and structural differences between theory and experiment.

2.1. Benzamides

Benzamides are a simple molecular scaffold with two aromatic rings (not just a phenyl ring) connected by an amide moiety. Compounds selected for the structural survey are *N*-(pyridyl)benzamides (Table **3**) having fluorine or methyl substituents *i.e.* methyl-*N*-(pyridyl)benzamides (generally named as the **Mxx** isomer grid) and fluoro-*N*-(pyridyl)benzamides (**Fxx** isomer grid). Two isomer grids (3×3) were built by varying the position of the pyridine N atom and the F/CH_3 substituent at the aromatic rings.

Similar benzamide derivatives[27,28] have importance as potential drugs *e.g.* anti-ulcer agents, modulators of human vanilloid receptor 1 (TRPV1) and as K_v channel blockers and activators.[29-32] The reasons for using *N*-(pyridyl)benzamides are multiple. The existence of both pyridine nitrogen and carbonyl oxygen as strong hydrogen bond acceptors and amide hydrogen as a hydrogen bond donor, as well as fluorine and methyl groups in the scaffold can promote different and unusual aggregation and physicochemical properties depending on the particular isomer combination.

Table 3: Structures and nomenclature of the **Mxx and Fxx** isomer grids

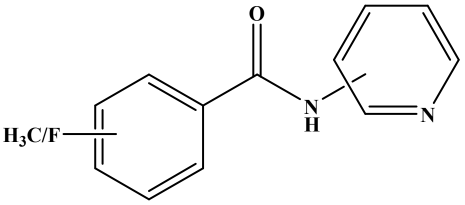

	Mxx			**Fxx**		
	p-methyl benzoyl	*m*-methyl benzoyl	*o*-methyl benzoyl	*p*-fluoro benzoyl	*m*-fluoro benzoyl	*o*-fluoro benzoyl
para (4-aminopyridinyl)	**Mpp**	**Mmp**	**Mop**	**Fpp**	**Fmp**	**Fop**
meta (3-aminopyridinyl)	**Mpm**	**Mmm**	**Mom**	**Fpm**	**Fmm**	**Fom**
ortho (2-aminopyridinyl)	**Mpo**	**Mmo**	**Moo**	**Fpo**	**Fmo**	**Foo**

Given the isosteric relationship that fluorine has with the hydrogen atom and the ability of fluorine to participate in weak interactions,[33] there is ample evidence that a wealth of interesting structural motifs involving 'organic fluorine' will be revealed in systematic studies. *N*-(pyridyl)benzamides are derivatives of aminopyridine, a well known potassium channel blocker,[34] and some of them have been identified[32] to have pharmacological properties. Building isomer grids as a compound library would be useful for both structural and medicinal studies.

2.2. Pyridinecarboxamides

Pyridinecarboxamides are almost identical and isomeric to *N*-(pyridyl)benzamides, however, with the amide linkage being swopped between the rings (Scheme **5**) As in the previous group the fluoro and methyl groups were used as substituents, giving *N*-(fluorophenyl)pyridinecarboxamides (**NxxF** isomer grid) and *N*-(tolyl)pyridinecarboxamides (**NxxM** isomer grid). All four isomer grids are in relationships regarding the substitent/amide linker variation (Scheme **5**).

In contrast to benzamides, pyridinecarboxamides are not direct derivatives of 4-AP, but rather the reverse or indirect *pseudo*-derivatives. A literature review reveals **NppF** has been used as an intermediate in the synthesis of 4-pyridinium cationic-dimer antimalarials.[35] The **NmxF** triad has been studied in an unusual synthesis of nicotinamides[36] and recently **NmoF** has been cited as a promising candidate for lead design as a selective inhibitor of LmSir2, a sirtuin protein from *Leishmania*, and therefore, a potential new drug and/or scaffold for leishmaniasis drug design.[37]

Table 4: Structures and nomenclature of the **NxxF** and **NxxM** isomer grids

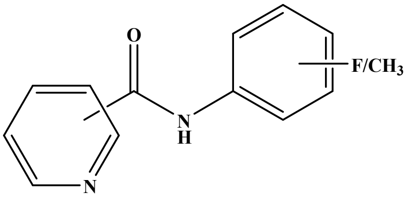

	NxxF			**NxxM**		
	p-fluoro phenyl	*m*-fluoro phenyl	*o*-fluoro phenyl	*p*-tolyl	*m*-tolyl	*o*-tolyl
para (4-pyridinoyl)	**NppF**	**NpmF**	**NpoF**	**NppM**	**NpmM**	**NpoM**
meta (3-pyridinoyl)	**NmpF**	**NmmF**	**NmoF**	**NmpM**	**NmmM**	**NmoM**
ortho (2-pyridinoyl)	**NopF**	**NomF**	**NooF**	**NopM**	**NomM**	**NooM**

In the **NoxF** series, **NopF** has been used as a deprotonated ligand in a $\mathrm{Co^{III}}$ complex[38] (its crystal structures has been published previously)[39] and **NomF** as an intermediate in the synthesis of thioamide analogues; **NooF** has been employed as a ligand in a ruthenium complex developed as a potential cytotoxic agent.[40] The **NppM** isomer has been examined as a ligand in metal complexes and complex based polymers with Cu,[41,42] whereas **NoxM** ligands have been widely studied in metal complexes *e.g*. Fe,[43] Ni,[43] Co,[43,44] Ru,[45,46] Ir,[47] Au,[48] Mn[49,50] and Pt[51] with potential and defined catalytic or electrochemical properties.

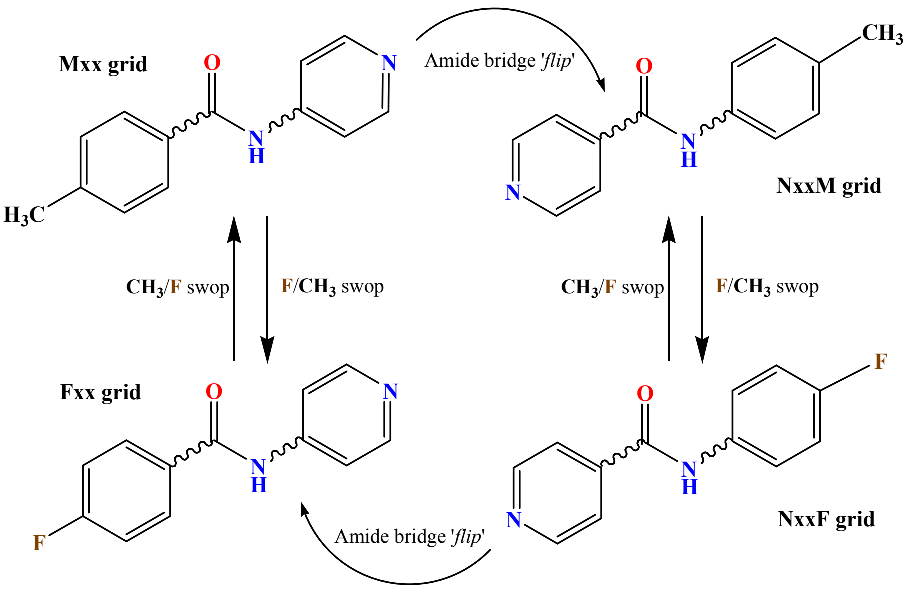

Scheme 5: Structural relationships between the four selected isomer grids

2.3. Carbamates

Generally, carbamates are derivatives of carbamic acid (NH_2COOH), sometimes called urethanes. They are widely known as versatile protecting groups[52] (BOC, FMOC, Cbz) or as linkage functional group in polyurethane polymers. Furthermore, carbamates can be found among some insecticides (1-naphthyl methylcarbamate, Carbaryl) and drugs (neostigmin, meprobamate).

Table 5: Structures and nomenclature of the **CxxR** isomer grids

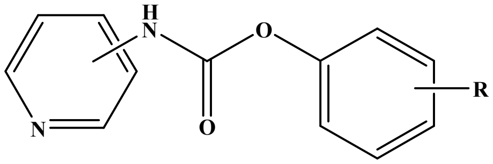

CxxR, R = F, Cl, Br, OMe (OCH_3), M (CH_3)

	p-R-phenyl	*m*-R-phenyl	*o*-R-phenyl
para (4-aminopyridinyl)	**CppR**	**CpmR**	**CpoR**
meta (3-aminopyridinyl)	**CmpR**	**CmmR**	**CmoR**
ortho (2-aminopyridinyl)	**CopR**	**ComR**	**CooR**

From our interest are the phenyl-*N*-pyridinyl-carbamates (**CxxR**), where two aromatic rings (Table **5**) with variable substituent/heteroatom positions make two dimensional isomer grids. These compounds are analogous to benzamides and pyridinecarboxamides with an additional oxygen atom between the carbonyl and phenyl moiety. Therefore, they are direct derivatives of 4-AP. The rationale for exploring phenyl-*N*-pyridinyl-carbamates (**CxxR**) comes from the fact that similar carbamates were found to be blockers of potassium channels.[30,53,54] Our intention is to create a small compound library suitable for screening of potassium channel modulators. More importantly, phenyl-*N*-pyridinyl-carbamates are relatively unknown and unexplored in structural science. There are no *N*-(pyridyl)phenyl carbamates found in CSD and just 29 basic phenylcarbamates structures are known.[8]

Some of the reasons might be difficulties in synthesis, the commercial unavailability of synthons, difficulties in their crystal growth, and instability[55] (slow decomposition) over weeks. Despite the possible difficulties, two dimensional isomer grids of **CxxR** with halogen, methoxy or methyl as functional groups would be a challenging system for structural systematics studies. Some *N*-pyridinyl-carbamates have been found to have antifungal,[56] herbicidal[57] and plant anticytokinin activity.[58-62]

3. Pharmacological role of the selected compounds

An important rationale behind the selected isomer grids is that similar compounds have been found to have potential pharmacological activity as potassium channel modulators (blockers and/or openers). New studies[32,63] show that two aromatic moieties, linked *via* an amide bridge, play critical pharmacological roles in the activation of K_v channels. The main synthon in selected benzamide/carbamate grids is 4-aminopyridine (4-AP), a well know potassium channel blocker and recently approved by the FDA for the treatment of multiple sclerosis.[34] Several derivatives of 4-AP are shown to have specific pharmacological activity. Nevertheless, the aim of our research is not the pharmacological evaluation of aminopyridine derivatives but their synthesis, characterisation and structural investigation.

3.1. Potassium channels

Voltage gated potassium channels (K_v channels) are a ubiquitous group of pore-forming transmembrane proteins (Fig. **2**) and play critical roles in a wide variety of physiological processes. K_v channels participate in establishing and control of the voltage gradient across the cell membrane by allowing the flow of potassium ions across cell membrane. K_v channels can be found in virtually any type of cell in the human organism. As a result, K_v channels are involved in wide range of physiological processes[64-69] like neuronal excitability, muscle contraction, heart rate, neurotransmitter release, epithelial electrolyte transport, immunology and many other physiological processes. Also, K_v channels are involved in huge number of pathophysiological processes responsible for various diseases, like epilepsy,[70] arrhythmia[71] and demyelinating diseases.[72,73]

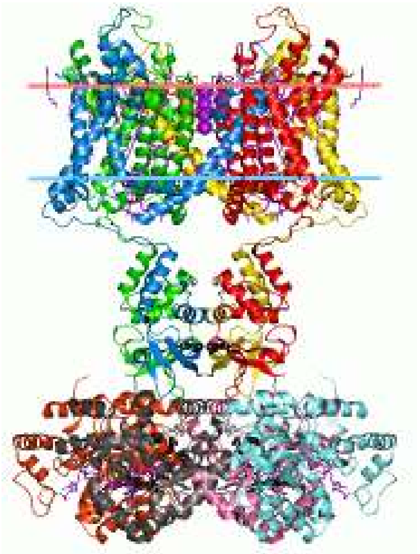

Fig. 2: Potassium channel K_vAP, structure in a membrane-like environment

K_v channels have been recognized as potential drug targets for many years. However, knowledge about the K_v channels function and structure has been notably improved this decade, due to the recent advances in technology. Now it is known that the list of diseases that could be alleviated by targeting a particular K_v channel is significant, encompassing not only proven K_v channelopathies, but also a range of other diseases. Therefore, development of selective K_v channel modulators is attractive.

3.1.1. Structure and assembly of K_v channels

The K_v channel is a tetramer, consisting of four glycosylated transmembrane pore-forming α-subunits that surround a water-filled, K^+ selective pore[74] and, in some types of K_v channels, β-subunits that interact with the intracellular surfaces of α-subunits modifying their function. The transmembrane tetramer, consisting of α-subunits, can be composed in the form of a homotetramer or heterotetramer. Homotetramers form a four fold symmetric (C_4) complex arranged around a central ion conducting pore. Alternatively four related but not identical protein subunits may associate to form heterotetrameric complexes with pseudo C_4 symmetry.

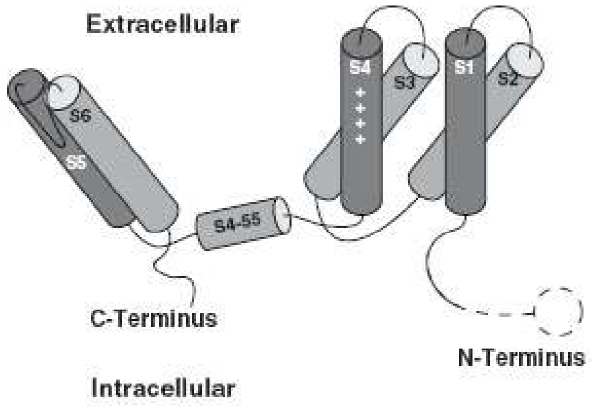

Fig. 3: Spatial orientation of the helixes of a single K_v α subunit

Various β-subunits have been found in association with different K_v channels. They also form a tetramer of with C_4 symmetry, and appear to be docked at the cytoplasmic moiety of the α-subunits. A single α-subunit (Fig. **3**) is a glycosylated[75] protein, comprising 6 transmembrane spanning α-helical regions (S1–S6) and a loop (P segment) between the fifth and sixth α-helical regions that, when 4 α-subunits associate, forms the selectivity filter of the pore. The selectivity filter passes through Rb^+ and Cs^+ ions and this possibility is used in K_v channel research methods.[76,77] Segments S5 and S6 together with the P loop are called a pore region, and transmembrane segments S1-S4 encompass a voltage-sensing region. The fourth helical region (S4) is the actual voltage sensor because it has a positively charged amino acid at every third residue so that it is polarized. The S6 helix participates in gate forming, and the N-terminal part is a so-called "ball and chain" region since the bulky N-terminus is involved in N-type inactivation of the K_v channel. It was shown that the ion translocation pore is occluded by the binding of a hydrophobic N-terminal "ball" to the cytoplasmic vestibule of the pore.

Although the fully assembled K_v1 channel has been visualised by electron microscopy (Fig. **4**),[75] the described model of K_v channel is mainly based on the well investigated bacterial KcsA potassium channel, shown by protein crystallography.[78,79]

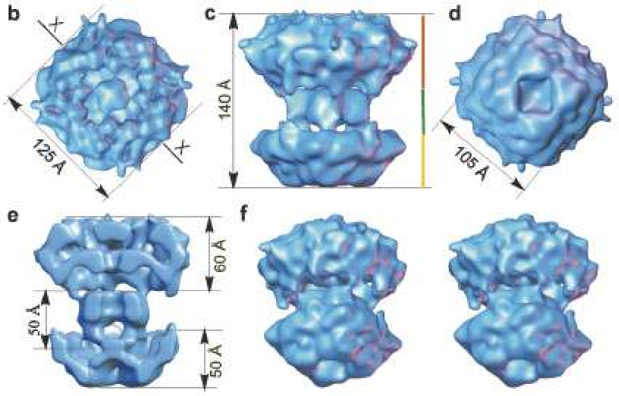

Fig. 4: 3-D distribution of densities of the brain K^+ channel and views of the reconstruction

Also, K_v channel structures from several other prokaryotic species such as KirBac1.1 channel,[80] bacterial K_vAP channel[81] from *Aeropyrum pernix* have been elucidated and a very important breakthrough was the crystallographic structure of mammalian (rat) $K_v1.2$ channel.[82] These structures enabled the emergence of a large number of simulation studies,[76,83] where the structure of known K_v channels were used as templates, combining computational methods of molecular modelling and primary structure of the various human K_v channels to calculate/predict molecular structure of these human proteins without X-ray crystallography. Many of the simulation studies examined the relationship between the K_v channel structure and their function.[64-69]

Recently, simulation studies based on 3-D homology models made further progress encompassing docking methods and SAR investigations of known and possible new K_v channel modulators.[84-86]

3.1.2. Physiology of K_v channels

There are three possible functional states of K_v channels; closed, open and inactivated. The K_v channel opens at the intracellular gate in response to membrane depolarization which raises the membrane potential from -70 mV to +40 mV. At that point K^+ ions pass through the ion translocation pore of the K_v channel, causing the repolarisation down to the hyperpolarisation level. This triggers the next step, an inactivation of the K_v channel.

There are two types of inactivation. The first type is called the rapid or N-type inactivation during which the ion translocation pore is occluded by the binding of a hydrophobic N-terminal "ball" to the cytoplasmic vestibule of the pore.[87] A second type of inactivation, termed "C-type inactivation", emerges with prolonged depolarization leading to decrease of current flow due to structural changes that constrict the extracellular end of the ion translocation pore.[88-92]

Several models have been brought up for debate regarding the voltage-sensing mechanism. The best known of these are the "helical screw",[93-95] the "gating pore",[96] the "transporter",[97] and the "paddle".[81,98] The gating mechanism is also vague; however, the K_V1.2 crystal structure[82] indicates that the S4–S5 linker interacts with the S6 gate suggesting strongly that it couples movement of the S4 voltage sensor to opening of the S6 gate. The opening of the pore involves bending of the S6 helices in a region occupied by a highly conserved glycine near the centre of the S4 segment (Gly-bend). This bending allows the S6 to swing away from the pore. The K_V1.2 crystal structure[82] and computational simulations[84] revealed a second hinge region (PVP-bend) and outward rotation of the outer S5 segments.

3.2. Potassium channel modulators

3.2.1. The K_v blockers

There are three categories of known K_v channel blocking agents, organic compounds, venom-derived peptide toxins and metallic ions. While some metallic ions appeared to be just non-selective blockers, venom derived peptide toxins, originating from snakes, spiders, scorpions and anemones proved to be highly selective for particular types of K_v channel, however, with low therapeutic potential. Therefore, venom derived peptide toxins have become long-standing primary tools in experiments for determination of K_v channel function and differential localization. Also, some of them are good templates for the peptidomimetic drug design of new, specific small molecule K_v channel therapeutics.

Organic compounds have potential to reach the clinical level; moreover, some of them are known drugs. There is a general lack of highly specific, small molecule K_v channel blockers, with good drug-like characteristics and an acceptable safety profile. It is expected that new progress in K_v channel knowledge when combined with advancements in drug design, protein modelling methods and high throughput screening technologies will ultimately result in new K_v channel therapeutics.

Here, several representative examples of representative K_v channel blocker classes are described. One of the best known groups of K_v channel blockers is the tetraethylammonium (TEA) derivative group; however, due to the lack of potency and selectivity this group became obsolete.

3.2.1.1. **Aminopyridines (APs)**

Among all K_v channel blockers, aminopyridines are the most investigated K_v channel blockers. The lead compounds of this class are 4-aminopyridine (4-AP, dalfampridine) and 3,4-diaminopyrinine (3,4-DAP) (Scheme **6**).

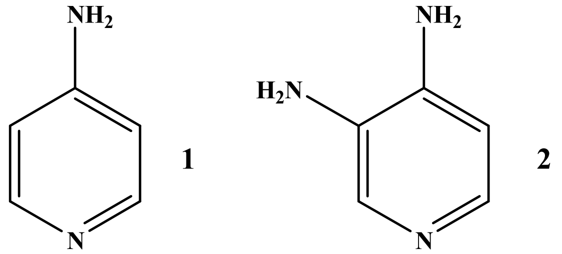

Scheme 6: Chemical structures of 4-aminopyridine (**1**) and 3,4-diaminopyridine (**2**)

The ability of aminopyridines to block K_v channels has been seen more than 30 years ago (in 1975 for 4-AP[99] and in 1978 for 3,4-DAP[100]). Since then, 4-AP has been studied extensively, and, in fact, became a standard for synthetic K_v blockers. Apart for the venom derived peptide toxins, 4-AP, as a small organic molecule, exhibits a very broad range of affinities; 4-AP binds to various K_v channels, from K_v1 to K_v4, having different intensities and mechanisms depending on the type of K_v channel.

Preliminary preclinical data[101-104] have triggered series of clinical trials in patients with chronic spinal cord injury (SCI) and multiple sclerosis (MS), many of which have shown that 4-AP can produce just modest or little improvements.[105-116] Despite the relatively poor benefit and considerable toxicity (particularly epileptogenesis) clinical trials ended positively. After extensive clinical studies 4-AP (with a generic name "dalfampridine") has been recently approved by the FDA for treatment of SCI and MS.[34] Despite modest improvements in patients, toxicological concerns regarding 4-AP remain. One obvious reason is that the maximum tolerable blood level of 4-AP in both animals and humans is only 0.5–1 μM, while the most effective concentration determined *in vitro* is 100 μM.[117] Concentrations above 1 μM produce side effects such as respiratory distress, anxiety and epileptiform seizures.[118-120]

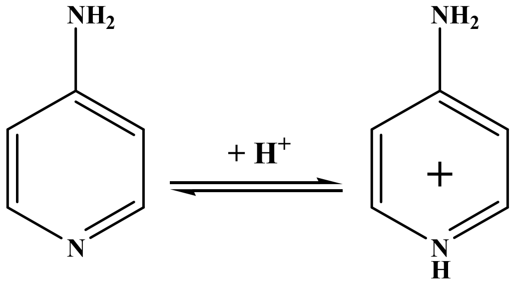

Scheme 7: The equilibrium of 4-AP in aqueous solution.

Possible reasons for the negative side effects associated with higher doses of 4-AP are increased synaptic transmission or additional blockade of potassium channel currents associated with the resting membrane potential.[117] Between the years 1990 and 2001, there have been a large number of studies on electrophysiologal aspects and kinetics of the 4-AP binding effect on native or mutated K_v channels. These experiments partially revealed the mechanisms of 4-AP blockage of K_v channels. For instance, it was noted that 4-AP blocks the K_v channel only in its protonated, cationic form[121] (Scheme **7**), from the intracellular face of the K_v channel. Also, some of the conclusions were about the probable binding site, and how 4-AP promotes the blockage.[122]

The real advance came only after the structure of the K_v channel was revealed. The information about the structure of K_v channels in conjunction with molecular modelling and theoretical (DFT) methods gave important conclusions regarding aminopyridine binding.[123-125] The previous findings that aminopyridines bind to the K_v channels in a protonated, cationic form is theoretically supported and explained.

Further, it was suggested that the pyridine ring plays an active role in the interaction with the receptor site. This interaction with the protonated pyridine nitrogen can involve a cation–π interaction or a donor hydrogen bond. In fact, the pyridine ring was recognized as a pharmacophor, while a second amine group, at different relative positions of the pyridine nitrogen, can form one or more hydrogen bonds due to the C_4 symmetry of the inner part of the pore in the K_v channel. One of the important conclusions was that the pK_a of 4-aminopyridine (9.4) is important for binding affinity. Future derivatives with decreased pK_a, but intact pyridine nitrogen might have a better potency than 4-AP.

3.2.1.2. **Carbamates**

Recently, new carbamate derivatives of 4-AP were identified to be evaluated in an electrophysiological test.[53] The modifications were made by preserving the pyridine ring, but the amine nitrogen was alkylated and acylated to give amides, carbamates and urea derivatives of 4-AP. This way, the pK_a fell from 9.4 to *ca.* 6.4. Biological evaluations pinpointed methyl, ethyl and *tert*-butyl carbamate of 4-AP (Scheme **8**) as promising new candidates; all produced positive biological responses at or below the 4-AP optimal concentration, with *tert*-butyl carbamate exhibiting a similar level of effect at 1% of the concentration required for 4-AP. Further experiments confirmed these results.[30,54] Therefore, these derivatives, especially *N*-(4-pyridyl)-*tert*-butyl carbamate may represent an alternative to 4-AP.

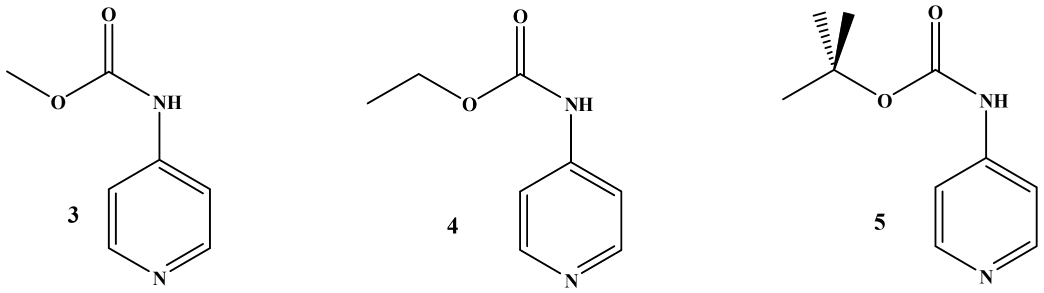

Scheme 8: Chemical structures of *N*-(4-pyridyl)-methyl carbamate (**3**), *N*-(4-pyridyl)-ethyl carbamate (**4**) and *N*-(**4**-pyridyl)-*tert*-butyl carbamate (**5**); Each of the derivatives is similar in structure to 4-AP however, the side groups are modified.

The newest theoretical studies of 4-AP as applied to modern docking methods solved the binding site mystery - aminopyridines block the K_v channel by forming several N-H···O hydrogen bonds with the tetrameric structure formed by the four carbonyl oxygens at the Thr107 or Ala111 residues of the K_v channel α-subunits.[126] These findings could promote advances in the further design of new aminopyridine derivatives, that are more selective and potent blockers of K_v channels.

3.2.1.3. **Disubstituted cyclohexyl benzamides**

An important group of small molecule $K_V1.3$ blockers are the disubstituted cyclohexyl benzamides, *i.e.* 4,4-disubstituted cyclohexyl analogues. The lead compound was 4-phenyl-4-[3-(2-methoxyphenyl)-3-oxo-2-azaprop-1-yl] cyclohexanone (PAC) (**6**, Scheme **9**), identified[127] in a screening system that monitors $^{86}Rb^+$ efflux from CHO cells stably transfected with $K_V1.3$ channel; PAC blocked the efflux reaction with an IC_{50} value of 273 nM. Additional tests confirmed its good $K_V1.3$ blockage activity. PAC has undergone electrophysiological tests by whole human T-lymphocytes recording, kinetics and specificity surveys and also proliferation assays.

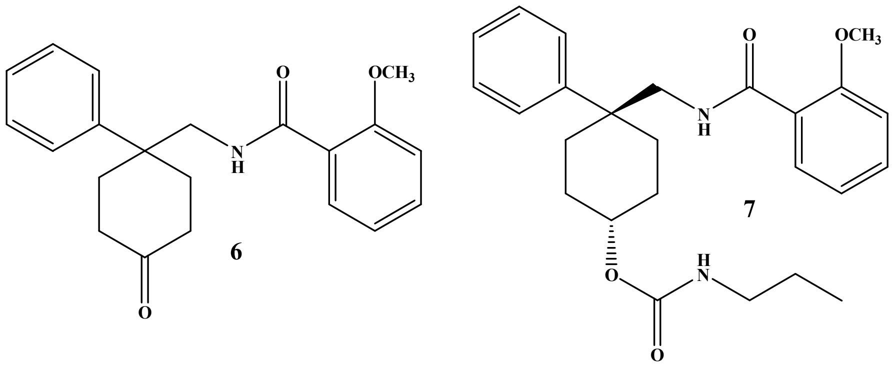

Scheme 9: Molecules **6** (4-phenyl-4-[3-(2-methoxyphenyl)-3-oxo-2-azaprop-1-yl] cyclohexanone (PAC)) and **7** (*trans-N*-propylcarbamoyloxy PAC))

The results showed that PAC reversibly blocks currents through $K_V1.3$ channels in human T-lymphocytes. PAC inhibited $K_V1.1$, $K_V1.2$, $K_V1.5$, and $K_V1.6$ with very similar potencies as had been found for $K_V1.3$ (IC_{50} of 200-400 nM). Thus, no selectivity is observed for blocking K_V1 family channels by this compound. The following step is a chemical modification of PAC. Reduction of the C-1 ketone in the A ring was used to generate *trans* (down) and *cis* (up) isomer pairs. A number of *trans*- and *cis*-N-carbamoyloxy-substituted analogues have been prepared at this position. The most potent compound in this series was the *trans*-N-propylcarbamoyloxy derivative (compound **7** in Scheme **9**), which displayed an IC_{50} of 50 nM in the $K_V1.3$ $^{86}Rb^+$ efflux assay, approximately 5-6-fold more potent than the PAC parent compound.

Another publication[29] with benzamides also brought a new range of derivatives with similar activities, but without meaningful advances regarding potency and selectivity.

3.2.1.4. **Porphyrins and calixarenes**

The 4-AP acts on the inner portion of the potassium channel. Unfortunately this portion is evolutionally conserved which implies the absence of acceptable selectivity throughout different classes of K_v channels, and therefore, the absence of therapeutic specificity towards certain maladies. On the other hand animal venoms like δ-dendrotoxin are efficient blockers with selectivity towards certain subclasses. Since K_v channels bear C_4 symmetry a concept using a macromolecule with the same C_4 symmetry appeared. It was postulated that a similar molecule would block the potassium channel from the extracellular side, have increased and easy controlled selectivity, therefore, capable of controlling major symptoms of MS and SCI. The two well known classes of compounds that bear C_4 symmetry are porphyrins and calixarenes. Therefore, Gradl and co-workers[128] have synthesised various water-soluble tetraphenylporphyrin derivatives substituted with various amino acids, peptides, or diamines. The interaction of the porphyrin ligands with potassium channels was investigated in competitive binding assays with ^{125}I-hongotoxin$_1$-A19Y/Y37F and in electrophysiological assays using the *Xenopus* oocyte system. A cationic porphyrin (Scheme **10**), was found to bind with the highest affinity (K_i = 13 nM) and significantly inhibited the *Shaker* current, in a reversible fashion. Although porphyrins fulfil the symmetry requirements, they are flat macrocycles that do not ideally complement the conical pore entrance of the K_v channels.

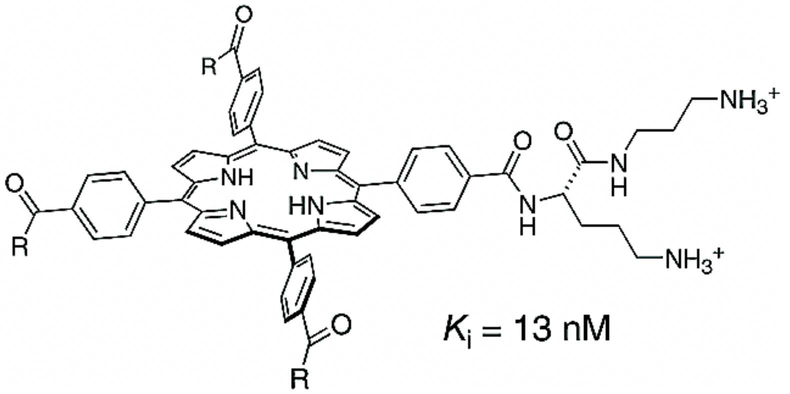

Scheme 10: Cationic porphyrin with its binding affinity[128]

In fact, solid-state NMR and molecular dynamics have shown that the porphyrins do not sit like a lid on top of the channel, which was the original model, but are oriented in parallel to the channel axis, with only one positively charged side arm actually interacting with the selectivity filter.[129]

Unlike porphyrins, calixarenes display conical shapes that would likely complement the shape of the outer vestibule of a K_v channel. Thus, calixarenes ligands[130] (Fig. **5**) were synthesized containing cationic substituents (guanidines) attached to the upper rim of the calixarenes to ideally complement the mainly negatively charged extracellular surface groups of the channel at the ''turret loop'', specifically residue Asp-379 in K_v1.2, thus improving binding affinities and selectivities by both electrostatic interactions and hydrogen bonding. The interaction of calixarene compounds with potassium channels was investigated by using electrophysiological methods on *Xenopus laevis* oocytes expressing the Shaker potassium channel, a prototypical member of the K_v1.x subfamily.

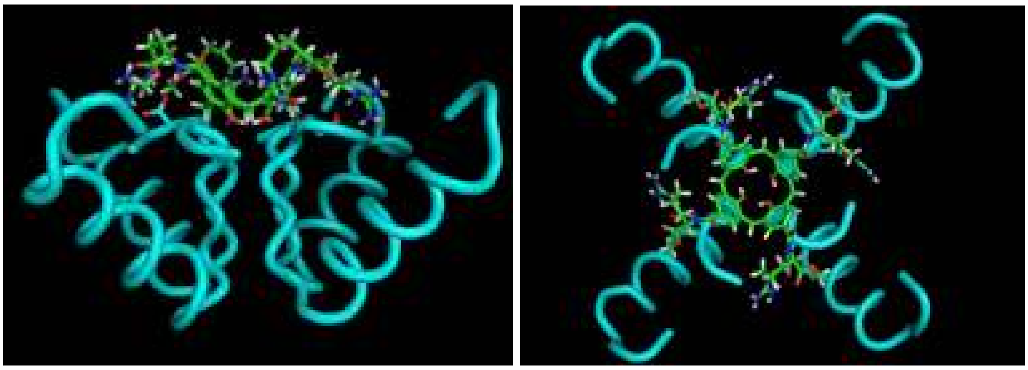

Fig. 5: Top and side wire frame views of calixarene ligand **4** docked into the X-ray structure of the human voltage dependent K_v1.2 potassium channel.[130]

The ligand 4 (Fig. **5**)[130] bearing charged CO-Arg-OMe substituents, was found to be the most promising lead compounds with 35% of inhibition at 50 µM. Further functionalization of ligand 4 with suitable peptide chains attached to the upper rim is expected to increase the affinity of the channel-calixarene.

3.2.1.5. **Other small molecule blockers of potassium channels.**

Khellinones

Khellinone (Scheme **11**) is a naturally occurring benzofuran derivative isolated from *Ammi visnaga*. Just recently, khellinone and khellinone derivatives were found to be blockers of K_v1.3 channels with considerable potential as future immunosuppresive agents. While khellinone itself only weakly blocks $K_V1.3$ it also serves as a versatile starting material for at least two different classes of new $K_V1.3$ blockers[131] that block $K_V1.3$ channels and inhibit *anti*-CD3 activated T-cell proliferation at submicromolar concentrations. The khellinones are indisputably a very promising group of potent $K_V1.3$ blockers that possibly contain future potent immunomodulating drugs. Since there has been a significant rise of individual khellinone derivatives with good $K_V1.3$ blocking activity, the next step in the search of an ultimate drug candidate should be modelling, QSAR and docking studies with the assistance of structural information (experimental or modelled) on $K_V1.3$ channels.

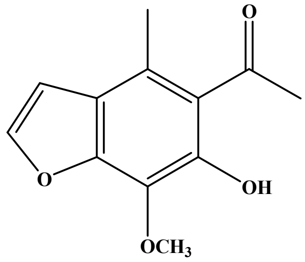

Scheme 11: Structure of khellinone

Anthranilic amides

Discovery of anthranilic amides as potent blockers of $K_V1.5$ is an interesting example of the so-called "pharmacophore based search" for new lead compounds.[132,133] The result was several promising compounds having good potency (0.5-0.7 μM), acceptable selectivity over $K_V11.1$ (HERG), whereas compound **8** (Scheme **12**) had oral bioavailability in animal model of 43%: therefore being a promising drug substance for a new and safe treatment of atrial fibrillation.[132,133]

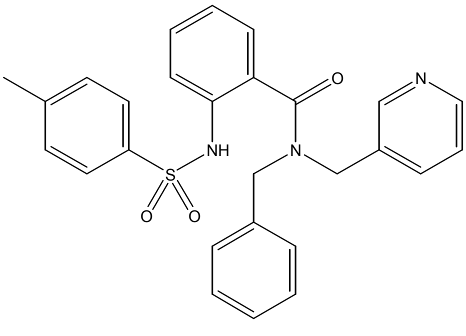

Scheme 12: Molecule **8**

Correolide derivatives

Correolide (Scheme **13**) is a nortriterpene isolated from the roots and bark of the Costarican tree *Spachea correa*.[134] The compound has a large, complex pentacyclic triterpenoid, heavily oxygenated structure, displaying five acetoxy moieties and an epoxide group. It was proven[135] to be a highly potent, reversible blocker of $K_V1.3$ channel, the first small molecule inhibitor of K_V1 series potassium channels to be isolated from a natural, plant source. Preliminary $^{86}Rb^+$ efflux assay from CHO/$K_V1.3$ cells showed high potency IC_{50} value of 80 nM. One of the most important features of correolide is an excellent selectivity over other members of the K_V1 family. That characteristic made correolide a likely candidate as a new immunosuppressant. However, the most serious obstacle for advancement of correolide towards drug candidate status was the fact that correolide and its analogues also appear to inhibit $K_V1.1$ channels present in some peripheral nerve terminals,[136] thereby causing acetylcholine release, which explains some of the limited toxicity observed *in vivo* with this structural series. Another problem is the structure of correolide; its molecular complexity makes organic synthesis of new analogues both challenging and expensive.

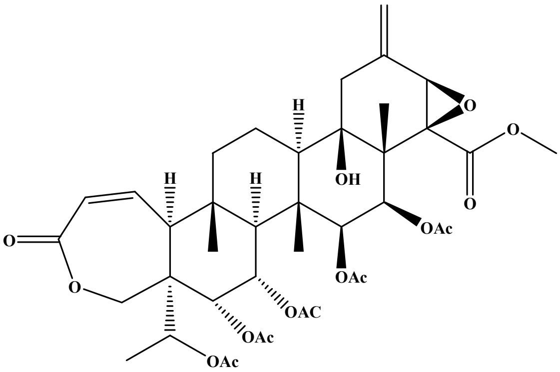

Scheme 13: Chemical structure of correolide

3.2.2. The K_V activators

In comparison with K_V channel blockers, the K_V channel activators can be regarded as an emerging group, since just recently there was no known K_V activator, and efforts in this field have become intensive. Modern drug discovery methods accompanied with structural information on K_V channels made the pursuit of new K_V activators easier. Several groups are known, comprising benzamides, acrylamides, difenylurea derivatives and fenamates. There is only one K_V channel activator in clinical usage, retigabine, as a new anti-convulsive. It is expected that the K_V activators of future will take place in the therapy of epilepsy, neuropathic pain, arrhythmia, deafness (DFNA) and episodic ataxia 1. Several representative examples of K_V activators and groups are described.

3.2.2.1. **Retigabine (ezogabine)**

Retigabine or ezogabine, previously known as D-23129 (Scheme **14**), was recently approved by FDA under the trade names **Potiga** and **Trobalt** as an anticonvulsant for the treatment of partial epilepsies.[137] It was identified in 1994, based on flupirtine, a centrally acting analgesic that was discovered to have anticonvulsive activity.[138] Retigabine was found to activate neuronal potassium channels in different cell preparations.[139,140] The channel targeted was later identified as a member of the KCNQ channel, lately renamed the K_v7 channel.[141] This channel has long been known to control excitability of neuronal cells. Furthermore, mutation of the K_v7 channel subunits has been identified in a hereditary epilepsy syndrome, benign familial neonatal convulsions (BFNC).[70]

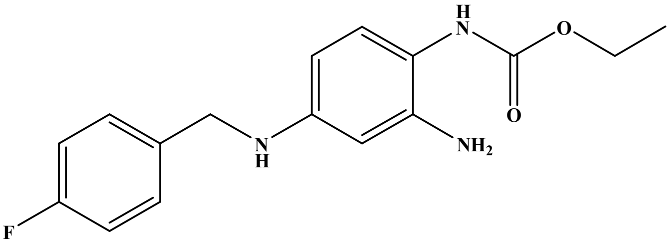

Scheme 14: Retigabine, ethyl-4-(4-fluorobenzylamino)-2-aminophenylcarbamate

Retigabine has been shown to activate human $K_v7.2$ and $K_v7.3$ expressed either alone or as a heterotetramer in *Xenopus* oocytes, and it appears highly selective for neuronal $K_v7.2$-$K_v7.5$ channels over cardiac $K_v7.1$, but it has much lower selectivity among the neuronal family members.[142-144] The exact molecular mechanism of retigabine is $K_v7.2$ activation by binding of lipophilic fluorophenyl ring of retigabine to tryptophan in the cytoplasmic end of S5 (W236) in $K_v7.2$ channel. Consequently, the open form of $K_v7.2$ is stabilised.[145] Retigabine is considered as the prototype KCNQ activator and has the triggered pursuit of new K_v activators.

3.2.2.2. **Benzamides and ICA-27243**

Generally, several studies[63,146-148] have shown that *N*-pyridylbenzamides or the pyridinecarboxamide scaffold, where two aromatic moieties are linked *via* an amide bridge, play a critical pharmacological role in the activation of potassium channels. It is important to emphasize that the same scaffold was used in our structural research.

In series of studies[63,146-148] simple *N*-pyridylbenzamides and pyridinecarboxamides (Scheme **15**), are found to be activators of BK potassium channels. The BK potassium channels play a fundamental role in the regulation of the tone of smooth muscle cells. Therefore, the availability of exogenous compounds able to activate BK channels can guarantee an innovative pharmacological tool for the clinical management of many pathological states, due to a cell hyperexcitability, such as asthma, urge incontinence and bladder spasm, gastric hypermotility, neurological and psychiatric disorders. Examples of isolated BK activators are shown in Scheme **15.**

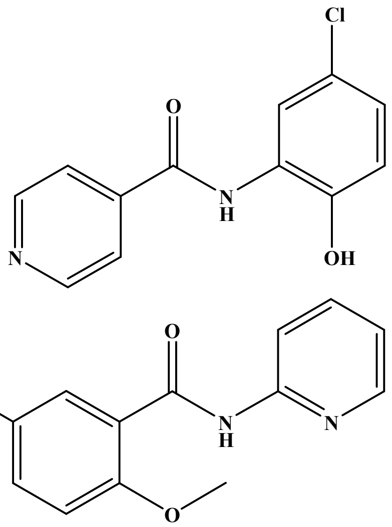

Scheme 15: Typical BK activators

Recently, a report[63] was published about the discovery of a K_v7 channel activator possibly representing a new class of K_v7.2 highly selective activators, with code name ICA-27243 (Scheme **16**). This new molecule appears to be a selective activator of the K_v7.2/3 channels. In human neuroblastoma cells, ICA-27243 produced membrane potential hyperpolarization that could be prevented by co-administration with the M-current inhibitors XE-991 and linopirdine. This compound enhanced both $^{86}Rb^+$ efflux (EC_{50} = 0.2 µM) and whole-cell currents in Chinese hamster ovary cells stably expressing heteromultimeric K_v7.2/3 channels (EC_{50}=0.4 µM). Activation of K_v7.2/3 channels was associated with a hyperpolarizing shift of the voltage dependence of channel activation.

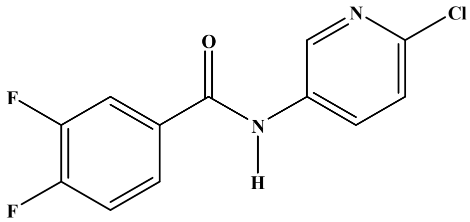

Scheme 16: ICA-27243

In contrast, the compound has no effect on cardiac K_v7.1 channels. The compound was found to reversibly suppress seizure-like activity in an *ex vivo* model of epilepsy and demonstrated *in vivo* anticonvulsant activity (ED_{50} = 8.4 mg/kg) in the mouse maximal electroshock epilepsy model.

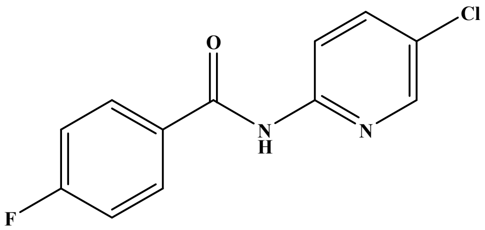

Scheme 17: *N*-(5-chloropyridin-2-yl)-4-fluorobenzamide, ZTZ240

The next step in the quest for new K_v7.2/3 activators was a recent study[32] that revealed new types of benzamide, *N*-(5-chloropyridin-2-yl)-4-fluorobenzamide (ZTZ240, Scheme **17**), as an effective activator of K_v7.2/3. The potentiation of outward current was dose-dependent, with a half-maximal value (EC_{50}) of 5.8±0.9 µM and, more dramatically, it slowed the deactivation. The molecular mechanism of the ZTZ240 effect is unique, mediated by specific molecular determinants, and hence consistent with recognizing a new site.[32]

3.2.2.3. **Acrylamides**

An important group of K_v7 activators are the acrylamides or cinnamic amides. The lead compound **8** ((S)-1, Scheme **18**), has an improved pharmacokinetic profile and is able to produce a remarkable increase (163±9%) in the $K_v7.2$ current at 10 µM (the estimated EC_{50} value appears to be 6.0 µM).[149] The compound (S)-1 enhances currents through all human neuronal K_v7 channels expressed in *Xenopus laevis* oocytes[150] with partially stronger preference towards $K_v7.4$ and $K_v7.5$ subunits.

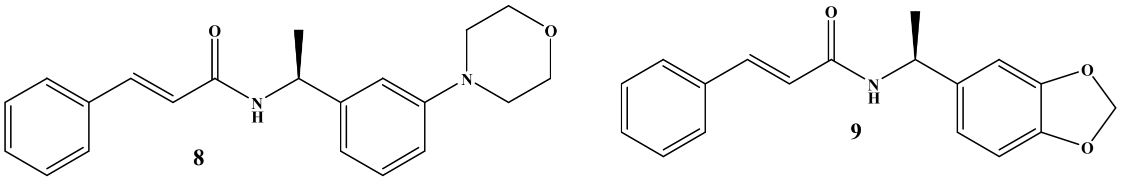

Scheme 18: Molecule **8** or (S)-1 ((S)-*N*-(1-[3-morpholin-4-yl-phenyl]-ethyl)-3-phenyl-acrylamide) and **9** ((S)-*N*-(1-(benzo[*d*][1,3]dioxol-5-yl)-ethyl))-3-phenyl-acrylamide).

The (S)-1 has hydrophobic binding site at S5 segment of $K_v7.2$ channel. Interestingly, the stereoisomeric centre of (S)-1 plays a fundamental role in the biological activity. Further lead optimisation efforts by restriction of the conformation, led scientists to conformationally-resticted analogues include the methylene dioxybenzene (compound **9** in Scheme **18**), with an EC_{50} value on $K_v7.2$ of approximately 20 nM (retigabine shows an EC_{50} of about 1 mM).[151] A number of these acrylamides have shown to have positive effects *in vivo* studies involving animal models of migraine, anxiety and neuropathic pain. Further research on this group of compounds potentially may bring new molecules that would have enhanced selectivity toward particular member of K_v7 channel family with clinical use as therapy for BFNC, DFNA2 or age-related deafness.

3.2.2.4. **Diphenylurea derivatives**

The diphenylurea group is a recently established group of $K_v11.1$ (HERG, KCNH2) channel activators, potential anti-arrhythmia therapeutics suitable for treatment of LQT2.[152-154] This group comprises two members, NS1643[152] and

NS3623[153] (structures **10** and **11**, Scheme **19**). In the experimental model with cardiomyocytes of guinea pig application of 10 μM of NS1643 activated K_V11.1 and significantly decreased the action potential duration to 65% of the control values. Exposure of K_V11.1 channels to NS3623 affected the voltage-dependent release from inactivation, resulting in a half-inactivation voltage that is rightward-shifted by 17.7 mV.

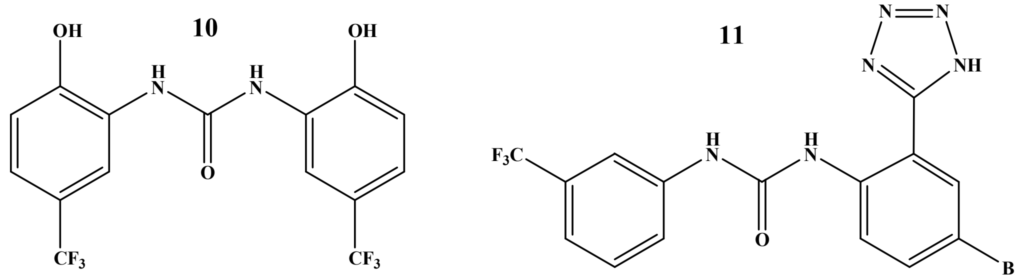

Scheme 19: Structures **10** (NS1643, 1,3-bis-(2-hydroxy-5-trifluoromethyl-phenyl)-urea) and **11** (NS3623, N-(4-bromo-2-(1H-tetrazol-5-yl)-phenyl)-N'-(3'-trifluoromethyl phenyl) urea)

Experiments[154,155] explained the mechanism of action of diphenylurea derivatives NS1643 and NS3623: they were found to be both activators and inhibitors of K_V11.1 channels, *e.g.* partial agonist of K_V11.1 channels and that the mechanism of activation is reduced channel inactivation. Another study[156] found that NS1643 also activates the K_V11.2 channel. Taken together, the present data strongly support the concept of using K_V11.1 activators as a treatment for certain kinds of arrhythmias and suggest further investigation of this new approach.

3.2.2.5. **Fenamates**

The fenamate group has the same *N*-phenylanthranilic acid structural basis, however, regarding their pharmacological activity they are diverse; different members possess K_V channel activation activity against different K_V channel types, including K_V7.1, K_V7.2/3 and K_V11.1.

The fenamate scaffold has served as a template for the development of new K_V channel modulators. Fenamates has been reported[157] with two prominent members, lead compound PD-118057 (**12** in Scheme **20**) and PD-307243 (**13** in Scheme **20**). PD-118057 produced increase of 111.1±21.7% in the peak tail K_V11.1 current at 10 μM and showed satisfactory selectivity and prevented action potential duration and QT prolongation caused by dofetilide.

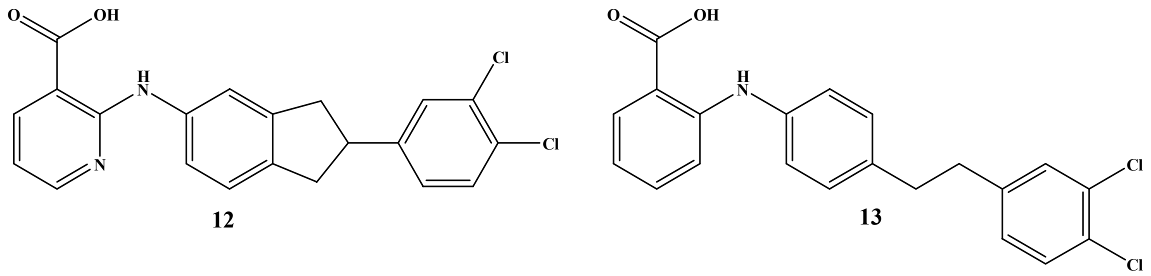

12 **13**

Scheme 20: PD-118057 (**12**) and PD-307243 (**13**)

The similar compound PD-307243 has been shown to increase the $K_v11.1$ tail current by 58% at 1 µM; this was more potent than PD-118057. A recent study[158] describes the mechanism of action of PD-307243. In experiments with $K_v11.1$, channel-transfected CHO cells PD-307243 increased tail currents by slowing the channel deactivation, but had no effect on channel activation, *e.g.* markedly slowed $K_v11.1$ channel deactivation and inactivation. Further optimisation could pave the way towards new pharmaceuticals for patients with inherited or acquired long QT syndrome, congestive heart failure, and diabetes.

3.2.2.6. **$K_v1.1$ disinactivators**

Another recent publication[159] described a new chemically diverse class of K_v activators (Scheme **21**) that can be regarded as $K_v1.1$ disinactivators, compounds that specifically target $K_v\beta1$-mediated inactivation of $K_v1.1$ channels in the brain. This was accomplished by testing compounds selected by high-throughput reverse yeast two hybrid based primary screening (among 500,000 random compounds), structure similarity searches, and engineering on $K_v1.1/K_v\beta1$ channels. The identified compounds blocked inactivation by several different mechanisms or sites of action, apparently including direct and indirect mechanisms.

These disinactivators are the first small molecules reported to specifically interfere with the protein–protein interaction of the K_v ball-and-chain N-type inactivation process. It is likely that these disinactivators act directly on the $K_v\beta1$ N-terminus or its receptor site on $K_v1.1$, thus preventing it from blocking $K_v1.1$ channels.

They are effective in blocking seizure activity both *in vitro* and *in vivo*. Many of the disinactivators are efficacious in the PTZ-induced seizure model, and some are also active in the MES-induced seizure model. Small molecule $K_v1.1$ channel disinactivators thus represent a new class of potential anticonvulsant drugs, and as such they may have unique properties and usefulness in various diseases as epilepsy, episodic ataxia-1 and neuropathic pain.

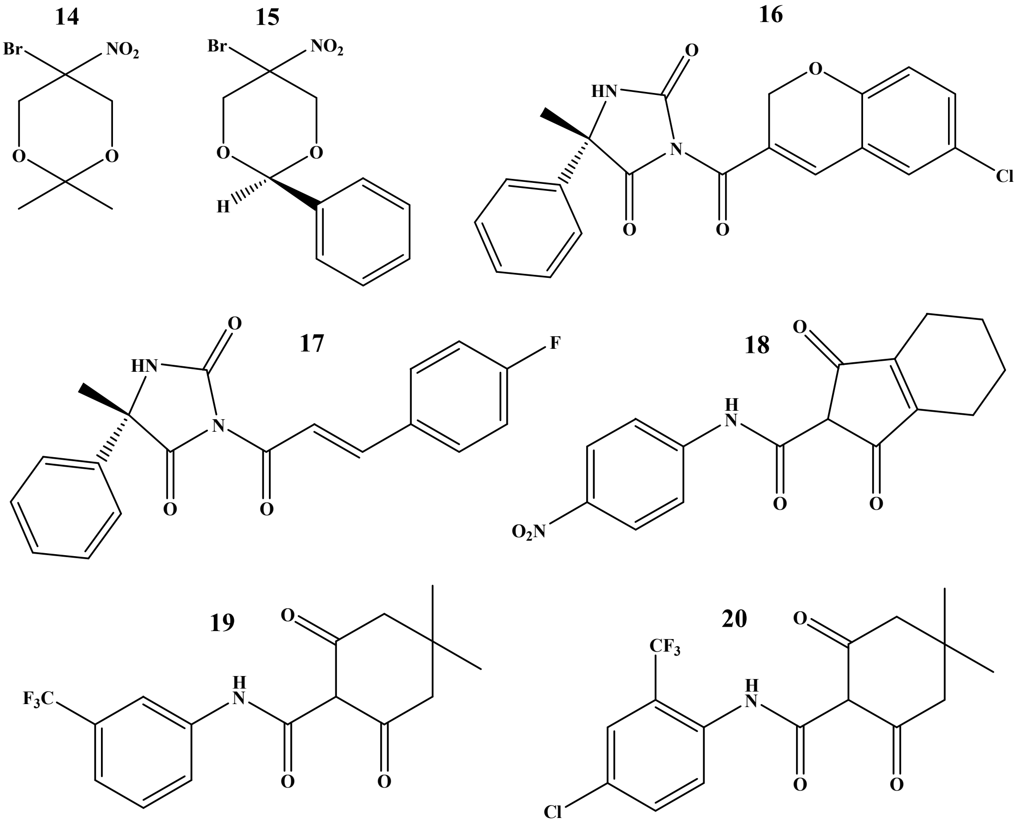

Scheme 21: Structures of K_V1.1 disinactivators: cyclohexadiones (**14**, **15**), hydantoins (**16**, **17**) and 1,3-dione-2-carboxamides (**18**, **19** and **20**)

4. Summary

The therapeutical needs for K_V channels modulators are still to be answered, bringing both potent and selective compounds. This is especially important for the peripheral neural Kv channels involved in pathophysiology of multiple sclerosis and spinal cord injuries. Currently, extracellular K_V blockers do not meet desired requirements regarding the potency, selectivity, and toxicity. Furthermore, internal blockers, based on 4-AP are still in basic development and future screening of many libraries of potential derivatives are still mandatory. The carbamate[53] and benzamide[63,146-148] blockers provide a solid ground for expansion of libraries involving both simple and advanced derivatives. Also, new approaches have to be explored in order to develop and design new scaffolds that might be a basis for the design of new, extracellular blockers of potassium channels.

Compound libraries for targeting of K_v channels formed on basis of isomer grids can be used for extensive structural systematic studies involving solid state investigation, *ab initio* molecular modelling and conformational analysis. This quest is not directly related to pharmacological success of a particular drug candidate, but rather uses *drug-like* compound libraries and the concept of isomer grids as a tool for an independent structural systematics survey. Therefore, the purpose of this study is to synthesise benzamide, pyridinecarboxamide and carbamate isomer grids, characterise them spectroscopically, determine their molecular and crystal structure, investigate their optimised structures, perform conformational analysis, correlate solid state structures with the modelled ones analysing differences and patterns as well as analysis and correlations of solid state crystal packing with *physico*-chemical properties. Finally, another important task is to explore and develop new scaffolds for future extracellular targeting of potassium channels.

CHAPTER I: BENZAMIDES AND PYRIDINECARBOXAMIDES

1. Benzamides

1.1. Mxx isomer grid

1.1.1. General description of synthesis

The classical nucleophilic acyl substitution reactions (Schotten–Baumann, **Scheme 22**) between the 4-, 3- or 2-aminopyridines and 4-, 3- or 2-toluoyl chlorides were used to produce a set of the nine methyl-*N*-(pyridinyl) benzamides (**Mxx**) (where **x** = *para-*/*meta-*/*ortho-*). Reactions were performed in anhydrous conditions in CH_2Cl_2 (under N_2), initially at 5°C and then at room temperature. A by-product was HCl, and Et_3N was employed, to move the reaction equilibrium towards the product; in total, one molar equivalent of Et_3N was added. The 4-, 3- or 2-aminopyridine (0.9411 g, 10.0 mmol) was added to a 250 ml round bottom flask placed on an ice bath with stirring. Then, 30 ml of solvent (CH_2Cl_2) was added to the flask, followed by addition of Et_3N (1.5 ml, 10.76 mmol). Finally, the 4-, 3- or 2-toluoyl chlorides (~1.5 ml, 11.0 mmol) were added in excess directly into the solution mixture. The reaction mixture was allowed to warm to room temperature and stirred overnight.

The standard washing was the same for all groups of compounds: the organic reaction phase was washed with 30 ml of $KHCO_3$ (0.1 M) solution *ca*. 3-7 times. Then, 1.5 g of anhydrous $MgSO_4$ was added to the organic solutions for 20 minutes. The flask contents were filtered through a Büchner funnel (under vacuum) to remove $MgSO_4$. The filtrate was evaporated under vacuum and the product dissolved in minimal volumes of warm $CHCl_3$. A saturated solution was placed on ice and re-crystallization induced. The resulting product was dried overnight and weighed. Silica was used as the stationary phase and mixture of $CHCl_3$, ethyl acetate and cyclohexane (4:2:1) was used as the mobile phase.

Table 6: Quantities, yields and melting points of **Mxx** compounds

Mxx	m/g	yield/%	m.p./ºC
Mpp	0.662	31.1	180.2-180.8[†]
Mmp	0.235	11.1	73.8-74.5[‡]
Mop	0.412	19.4	128.6-129.1
Mpm	0.416	19.5	128.2-128.8[*]
Mmm	1.490	70.0	90.0-91.0
Mom	0.903	42.5	107.5-108.5
Mpo	0.581	39.6	104.0-106.0
Mmo	0.498	37.6	78.8-80.0
Moo	0.504	38.2	115.0-117.1

[†] lit. 178.5-181°C[28]; [‡] partial melting, total melting occurs at 106.7°C; [*]lit.126.5°C[27]

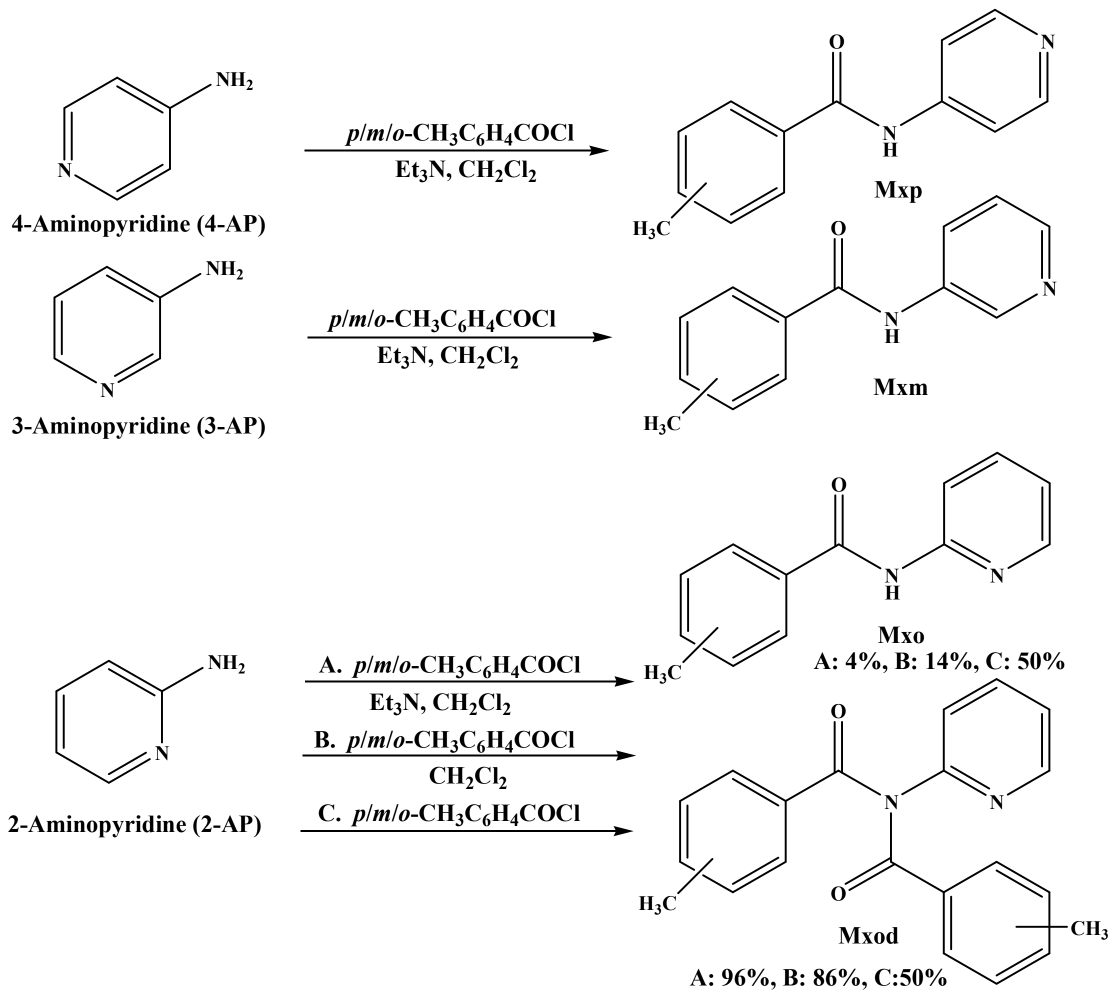

Scheme 22: The synthesis of the **Mxx** isomer grid and **Mxod** by-products

Since the purity of 3-aminopyridine was poor, column chromatography was employed for the **Mxm** compounds with success. This procedure was appropriate for the first six isomers (**Mxp** and **Mxm**), however, if 2-aminopyridine was used the products were almost exclusively imides, 4-/3-/2-methyl-*N*-(4-/3-/2-toluyl)-*N*-(pyridin-2-yl) benzamides (**Mxod**). The formation of imides with 2-aminopyridine has been well described,[160-162] and depends on the *ortho*-pyridine nitrogen atom that destabilises and weakens the neighbouring N-H bond, with a second substitution by an acyl moiety yielding the **Mxod** series, depending on the reaction conditions.[163,164]

Exclusion of the Et_3N improved formation of **Mxo** but not in sufficient ratio (14% of **Mxo**). Finally, the **Mxo** compounds were synthesised by performing the reaction without solvent and Et_3N by simply mixing 2-aminopyridine and toluoyl chlorides in a round bottom flask until a crude product is formed, containing 50% of **Mxo** and 50% **Mxod.** After standard washing, separation of the compounds was performed using column chromatography.

In most cases, yields were modest to good (19-70%), with the exception of **Mmp** (11%). All **Mxx** products are white, odourless, crystalline solids, insoluble in water, but readily soluble in organic solvents such as CH_2Cl_2 and $CHCl_3$, though less so in cyclohexane and isopropyl alcohol. The **Mxx** isomer characterisation data show a degree of modularity and patterns will be discussed below. Spectroscopic data including ^{1}H-NMR, ^{13}C-NMR and IR are listed in Appendix I (Sections 1.1), while the spectra are shown in the ESI I (Section 1.1)

1.1.2. General materials and equipment

All chemicals, including reagents, solvents and supplies were purchased from Sigma Aldrich except for 2-pyridinoyl chloride (Fluorochem). TLC alumina and silica plates were purchased from Fluka. Melting points were analysed using a Stuart Scientific SMP40 automated melting point apparatus. The solid state IR spectroscopy was performed using the attenuated total reflection (ATR) method on a Perkin-Elmer Spectrum 100 FT-IR Spectrometer. NMR spectroscopy was performed on Bruker BioSpin UltraShield NMR spectrometers at 293±1 K, operating at 400 or 600 MHz for ^{1}H, 100.62 MHz for the ^{13}C (on both instruments) and 376.46 MHz for ^{19}F resonances (on 400 MHz only). The ^{1}H spectra were recorded in two solvents: in $CDCl_3$ and DMSO-d_6 (in $CDCl_3$ and acetone-d_6 for carbamates) while the ^{13}C and ^{19}F spectra were only recorded in DMSO-d_6 (acetone-d_6 for carbamates); in $CDCl_3$ and while the ^{13}C spectra were only recorded in acetone-d_6. The NMR chemical shifts values (δ) are expressed in ppm and referenced to TMS (Cl_3FC for ^{19}F NMR) and coupling constants (J) are quoted in Hz. *Ab initio* molecular modeling and conformational analysis for the *gas phase* was performed at the B3LYP/6-311++G level using the Gaussian 03[25] package (version E.02) for the MS Windows XP SP3 operating system running on a PC (Intel Core i7-940 2.93 GHz, 8GB). The solvated form computations (PCM-SMD/B3LYP/6-311++G), conformational analyses and high accuracy energy (CBS-QB3) calculations were undertaken using Gaussian 09[25] for Linux/Unix operating on a Bull Novascale R422-E2 system provided by the Irish Centre for High-End Computing.

1.1.3. X-ray crystallography methods

The single crystal X-ray data for eight **Mxx** isomers were collected on an Enraf-Nonius κ-CCD diffractometer at 150(1) K and for **Mpo** on a Bruker ApexII: θ range from 2-27.5° with 100% data coverage to 25°.[165,166] Data reduction procedures are standard and details have been published previously.[167] All structure solutions were obtained using the SHELXS97 direct methods program and refined by full matrix least squares calculations on F^2 with all non-H atoms having anisotropic displacement parameters (except for the minor component C in **Mop**).[3] The H atoms were treated as riding atoms in SHELXL97 (150 K defaults) except for the amide N-H (isotropic refinement) using the OSCAIL suite of programs[168] with selected crystallographic and structural data in Tables **7** and **8** and in the ESI I (Section 2.1). Molecular and hydrogen bonding diagrams were generated using Mercury or PLATON (Figs. **6-11**).[169] All CSD searches on the Cambridge Structural Database (CSD) were performed with the November 2009 release (version 5.31).[8]

1.1.4. Computational methods

Ab initio calculations have been used to predict and optimize the nine methyl-*N*-(pyridyl)benzamide (**Mxx**) structures and energies, both in *gas phase* and solvated forms (CH_2Cl_2 and H_2O) to ascertain the energetically preferable conformations, global minima and rotational energy barriers between conformations.[25] The nine **Mxx** isomer structures were generated using GaussView with optimizations performed using the B3LYP/6-311++G method. Optimizations using CH_2Cl_2 (non-polar) or H_2O (polar) were performed using the PCM-SMD model[170] in Gaussian 09.

The **Mxx** compounds contain two aromatic rings linked by the amide group. A total of four distinct conformations are possible for the aromatic N atom and methyl group positions relative to the amide: this is relevant for **Mxx** isomers with a *meta*-/*ortho*-pyridine N atom or CH_3 group (Scheme **23**). The rings can have ***syn*** (**P-*syn*** or **M-*syn***) or ***anti*** (**P-*anti***, **M-*anti***) conformations (Scheme **23**): logically **Mpp** is not subject to this convention.

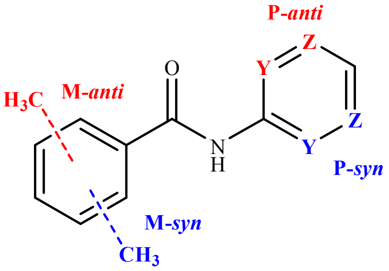

Scheme 23: The four possible **Mxx** conformations

Conformational analysis was performed by rotation of the C16-C11-C1=O1 (α dihedral, **Mx**-ring) and C26(N22)-C21-N1-C1 dihedral angles (β dihedral, ***p*/*m*/*o*-**

pyridine ring), respectively, by 5° increments from their optimised points through ±180°. Local relaxation (optimisation) was performed at every point and single point energies were calculated using the methods and basis sets detailed above. Potential energy surface (PES) diagrams were obtained where energy values are plotted against dihedral angle (°) in Figs. **7** and **8**. Differences ($\Delta\theta$) between the α and β dihedral angles and corresponding solid-state angles marked (•) can be ascertained in each isomer PES diagram for comparison purposes. The $\Delta\theta$ represents the deviation of the solid-state angle from the optimised angle as a basis point.

In addition, high accuracy energies including electronic energy and Gibbs free energy values were calculated using the Complete Basis Set (CBS-QB3) compound method[171] (ESI I, Section 3.1.1). Absolute energies are expressed in Hartrees, while relative energies are expressed in kJ.mol^{-1}.

1.1.5. Molecular and crystal structure data

The principal intermolecular feature for eight of the **Mxx** crystal structures (**x** = *para-/meta-/ortho*) is that they aggregate in the solid-state *via* N-H···N$_{\text{pyridine}}$ hydrogen bonds, but in different space groups. The O=C carbonyl group only participates in weak intra- and intermolecular C-H···O contacts in the majority of structures. Only for the **Mpm** structure is the N-H···O=C interactions the primary hydrogen bonding feature. However, in the **Mxo** series cyclic $R^2_2(8)$ rings of N-H···N intermolecular interactions are the main hydrogen bonding feature.

Table 7: Selected crystallographic data for the nine **Mxx** isomers[†]

Mxx	**Space group**	***Z'***	***Volume* (Å^3)**	***R*-factors**
Mpp	$P2_1/n$	1	1038.49(12)	0.066, 0.202
Mmp	$P\bar{1}$	2	1056.41(16)	0.066, 0.183
Mop	Pc	2	1123.65(12)	0.056, 0.161
Mpm	$P1$	4	1071.37(8)	0.059, 0.154
Mmm	$P\bar{1}$	2	1079.21(9)	0.076, 0.254
Mom	$Pca2_1$	1	1109.94(5)	0.041, 0.096
Mpo	$P\bar{1}$	1	525.04(5)	0.039, 0.109
Mmo	$P2_1/c$	1	1065.04(15)	0.065, 0.195
Moo	$P\bar{1}$	1	546.42(6)	0.063,0.184

[†] Complete crystallographic, refinement and structural details for all nine **Mxx** isomers ($C_{13}H_{12}N_2O$) are listed in the ESI I (Section 2.1).

The N-H···N interactions form *C*(6) chains in the **Mxp** series, *C*(5) chains in **Mmm**, **Mom** and cyclic $R^2_2(8)$ hydrogen bonded rings in the **Mxo** triad. In **Mpm**, $_{\text{amide}}$N-H···O=C interactions form classical *C(4)* chains. Diagrams highlighting the main features are presented in Figs. **6-11** and salient features of the nine **Mxx** structures are provided in Tables **1** and **2**. The α, β torsion angles for each **Mxx** isomer are plotted with *gas-phase* conformations (Fig. **12**).

1.1.5.1. **Mxp isomer series**

Mpp molecular and crystal structure

Apart from rotational disorder in the CH_3 group, the molecular structure is as expected for benzamides. The crystal structure in space group $P2_1/n$ is similar to the reported **Fpp**[162] structure in terms of the N-H···$N_{pyridine}$ bonding (N···N is 3.105(3) Å) and is isostructural with the series of five molecules in Table **5**.[172]

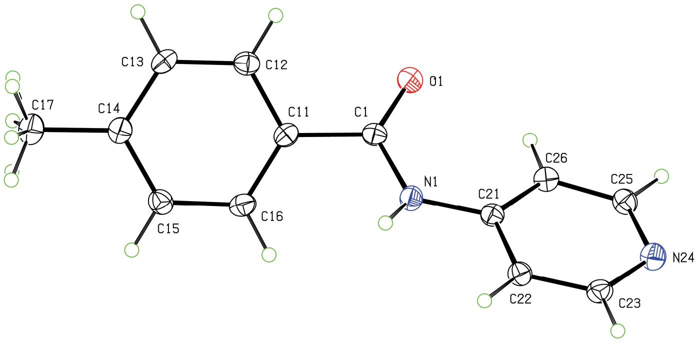

Fig. 6: An ORTEP diagram of **Mpp**

It is not isomorphous with **Fpp** but for the *a b, c* cell swop (Unit cell parameters for **Fpp** = *a* = 5.65, *b* = 11.39, *c* = 15.43 Å, *β* = 95.60°; transformed unit cell parameters for **Mpp** = *a* = 5.70, *b* = 16.89, *c* = 11.34 Å, *β* = 107.88°).

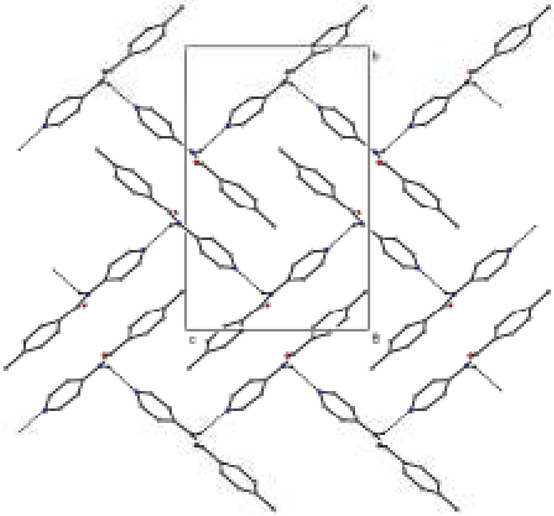

Fig. 7: The primary N-H···N hydrogen bonding along the *c*-axis direction in **Mpp** and isostructural with the related fluoro derivative **Fpp**

The N-H···N$_{\text{pyridine}}$ hydrogen bonding dominates the primary interactions in the **Fxp** structures where the pyridine N atom is *para*-substituted. **Mpp** (Fig. **6**) differs from **Fxp** by having a CH$_3$ group and the parent benzamide in Table **5**.[172] The N-H···N interactions in **Mpp** form a one-dimensional chain along the *c*-axis direction as *C(6)* chains (and parallel to the [$\bar{1}$01] plane) and augmented by weak C-H···O and C-H···π(arene) interactions involving the C26-H26 atoms. The C$_6$/C$_5$N interplanar angle is 46.03(9)°.

Mmp molecular and crystal structure

The **Mmp** structure crystallizes in $P\bar{1}$ with Z' = 2 and with differences between the O1-C1-C11 angles of [121.2(2)°, 119.7(2)°] and C1-N1-C21 [127.6(2)°, 125.5(2)°] for molecules A and B, respectively. Torsion angle differences of *ca.* 8° are evident by different A, B molecular data values for C1-N1-C21-C22 of 12.9(4)°, 20.2(4)°, respectively. Aggregation is driven by N-H···N$_{pyridine}$ hydrogen bonding. This involves alternating $_{\text{A/B}}$N···N$_{\text{B/A}}$ distances of 3.058(3), 3.059(3) Å, but with N-H···N angles of 142(3)° (for A→B), 172(3)° (for B→A). This highlights the strain and distortions in incorporating two molecules within the asymmetric unit and with the molecular packing as the A→B molecules link by *C(6)* chains and *vice versa*. The two N-H···N hydrogen bonds combine and aggregate as a one-dimensional column parallel to the (110) plane.

Table 8: Salient structural features in the nine **Mxx** isomers[†]

Mxx	C$_6$/C$_5$N (°)	C$_6$/amide	C$_5$N/amide	N···N/O (Å)[‡]	Packing
Mpp	46.03(9)	28.99(11)	17.40(13)	3.105(3)	1-D chains
Mmp	4.84(15)	15.70(13)	10.94(13)	3.058(3)	2-D sheets
	5.47(12)	19.88(10)	17.73(9)	3.059(3)	
Mop	81.79(15)	54.60(17)	28.34(17)	2.952(5)	1-D chains
	81.58(14)	54.85(15)	27.96(16)	2.950(5)	
Mpm[*]	65.13(11)	29.45(15)	35.83(14)	3.029(6)	1-D chains
	64.04(10)	29.70(15)	34.57(13)	3.016(5)	
	1.5(2)	24.47(16)	24.16(16)	3.085(6)	
	1.9(2)	24.79(16)	24.79(16)	3.085(5)	
Mmm	55.57(10)	25.55(8)	31.33(14)	2.998(4)	1-D chains
	65.70(10)	36.43(10)	29.54(14)	3.006(4)	
Mom	71.20(5)	57.33(6)	13.91(10)	2.946(2)	1-D chains
Mpo	45.34(4)	35.93(5)	17.51(8)	3.1081(15)	Dimers
Mmo	70.55(7)	35.99(8)	35.05(11)	3.106(3)	Dimers
Moo	84.79(5)	77.28(6)	10.93(10)	3.076(3)	Dimers

† Full structural details are in the ESI I (Section 2.1).

‡ The primary $_{\text{amide}}$N-H···N$_{\text{pyridine}}$ or N-H···O=C[*] interaction distances.

These 1-D columns interlock with symmetry related columns along the *c*-axis direction forming 2-D sheets *via* C-H···O interactions (involving C17A). The 3-D crystal structure assembles between parallel sheets with weak interactions *via* C-H···O (involving C23A) and short C-H···π(arene) interactions involving C25A···[C11B,…,C26B], with a H25A···Cg distance of 2.65 Å, where Cg is the aromatic ring centroid. Unlike the **Mpp** structure, the C_6/C_5N interplanar angles are essentially co-planar at 4.84(15)°, 5.47(12)° for molecules A and B, respectively.

Mop molecular and crystal structure

Mop crystallises in *Pc* with *Z'* = 2 and with molecular disorder in one of the molecules. The solution of the **Mop** structure failed in space group $P2_1/c$ despite the systematic absences indicating that this was a favourable choice. However, attempts to solve and refine in both *Pc* and $P2_1$ proved successful. The *Pc* structure provides the better solution and refinement to an R-factor of 0.076, a WGHT card of 0.14 and residual electron density for the top 26 peaks of +0.57 e.Å^{-3} to +0.26 e.Å^{-3} and indicating possible molecular disorder at molecule A. Refinement of these residual peaks as sensible chemical sites as a minor conformation of molecule A labelled as C drops the *R*-factor from 0.076 to 0.057 and a final *R*-factor of 0.056, WGHT of 0.09 and a range of residual electron density from +0.18 e.Å^{-3} to -0.20 e.Å^{-3}. The minor component C has 10.1(6)% site occupancy and occupies the same molecular volume element as the major A sites. Of the nine **Mxx** isomers the volume of the **Mop** is the largest and this is almost certainly due to the disordered A/C component.

Molecules A and B are identical and with practically no differences in molecular geometric data. The only difference between the two molecules is the disorder (A/C) at the molecule A location. The N-H···$N_{pyridine}$ interactions (intermolecular N···N distances of 2.952(5) Å, 2.950 Å) dominates the hydrogen bonding with additional C-H…O contacts. The N···N interactions aggregate as A/C→A/C and B→B molecules in *C(6) zig-zag* chains and parallel to the $(\bar{1}02)$ plane. The C_6/C_5N planes are almost orthogonal and due to the steric hindrance from the *ortho*-methyl groups and are at angles of 81.79(15)° and 81.58(14)°. Differences between the major orientation (A) and molecule (B) for C1-N1-C21-C22 are -155.2(4)° and -27.4(6)°.

1.1.5.2. **Mxm isomer series**

Mpm molecular and crystal structure

Mpm crystallizes with 4 molecules in *P1*. The crystallization of four molecules in *P1* is unusual (Fig. **8**) but all four molecules differ in their molecular conformations and can be distinguished as two distinct sets with molecules A, B and C, D, whereby the C_6/C_5N interplanar ring angles are oriented at angles of *ca*. 65° for molecules A, B at [65.13(11)°, 64.04(10)°] (with differences $> 3\sigma$) and close to co-planarity at 0° in C, D at [1.5(2)°, 1.9(2)°]. The bond lengths and angles are normal and are all similar and $<3\sigma$ level for the related geometric data. However, there are subtle differences in the torsion angles and intermolecular hydrogen bonds. For example with respect to distances across the molecules [intramolecular distances], the N23···C17 molecular distances vary and differ from 10.134(6) Å (in A), 10.118(6) (in B), 9.985(6) Å (in C) to 9.940(6) Å (in D), a difference of 0.2 Å.

The molecules aggregate as A···A···, B···B··· *etc.* 1-D chains *via* four separate and distinct N-H···O=C interactions and along the *b*-axis (010) direction with N···O distances of 3.029(6), 3.016(5), 3.085(6) and 3.085(5) Å for molecules A to D, respectively. Apart from weak C-H···π(arene) contacts – these are the primary interaction in the crystal structure. Two weak $CH_3 \cdots N_{pyridine}$ interactions with H···N 2.60 Å and angles of 159°/156° are also present involving C to D and D to C linking the independent C, D chains in two-dimensions. **Mpm** is unusual in that it is the only **Mxx** molecule which crystallizes with N-H···O=C as the primary interaction and not N-H···N_{pyridine} and given its unusual *Z'* = 4 in *P1* should at some stage be the subject of a thorough variable temperature study.

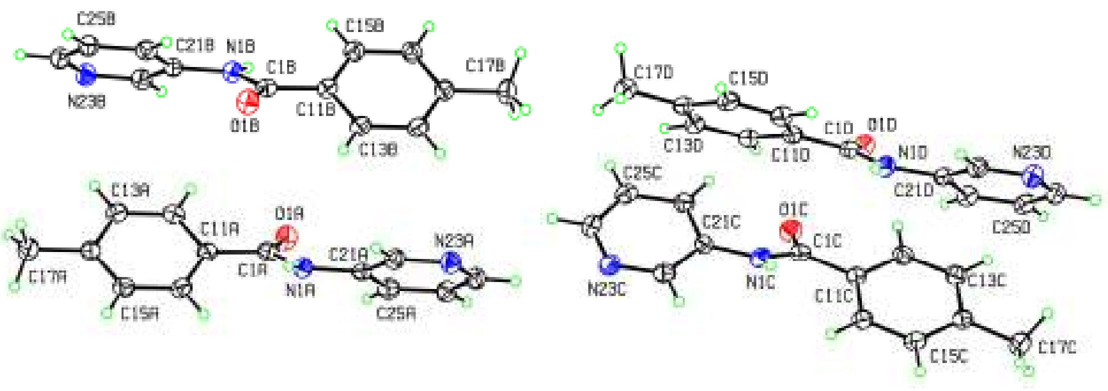

Fig. 8: The four molecules (A) to (D) in the asymmetric unit of **Mpm**.

The crystallization of four molecules in the asymmetric/unit cell is interesting in the absence of disorder and with clear and subtle distinctions between the four molecules (there are NO matrix correlation coefficients above 0.5). A solution can be obtained in space group $P\overline{1}$ (No. 2), but one of the molecules is disordered and the *R*-factor remains stubbornly high and at $R = 0.2$.

Mmm molecular and crystal structure

The **Mmm** structure crystallizes in $P\overline{1}$ with $Z' = 2$ with the two molecules differing by 10° in their corresponding dihedral angles. For example the C_6/C_5N interplanar angles are 55.57(10)° and 65.70(10)° in molecules A and B while the O1-C1-C11-C16 angles are 156.8(3)° and 146.1(3)°, for A and B, respectively. It is a *non-merohedral* twinned crystal and there is no discernible disorder in the molecular components. Molecules aggregate *via* $_{A/B}$N-H···N$_{B/A}$ hydrogen bonding as *C(5)* chains along the *b*-axis or (010) direction [at distances of 2.998(4) Å and 3.006(4) Å]. Two C-H···π(arene) interactions are present involving C22A and C22B. Of the carbonyl O atoms, only O1B is involved in a weak CH_3···O=C interaction. Both A and B molecules have their **P**-ring in the **P-*anti*** conformation, while both **M**-rings are **M-*syn***.

Mom molecular and crystal structure

The **Mom** structure crystallizes in $Pca2_1$ with $Z' = 1$. The primary interaction is the N-H···N$_{\text{pyridine}}$ intermolecular interaction forming 1-D *C(5)* chains along the *a*-axis direction with a N···N distance of 2.946(2) Å and two C-H···O interactions complete the interactions. There is also a weak C-H···π(arene) interaction. The C_6/C_5N rings are mutually oriented at 71.20(5)°. This is one of the most regular of the **Mxx** structures without disorder, twinning or potential pseudosymmetry problems. As in **Mmm** the **P**-ring is in the **P-*anti*** conformation.

1.1.5.3. Mxo isomer series

The primary hydrogen bonding in all three **Mxo** derivatives is cyclic, symmetrical $_{\text{(amide)}}$N-H···N$_{\text{(pyridine)}}$ with graph set $R^2_2(8)$ that is remarkably similar for all three **Mxo** structures. In tandem with this hydrogen bonded ring there are also intra- and intermolecular C-H···O=C contacts present. The principal difference between all three structures is the presence of an intra-dimer C-H···π(arene) interaction which is shortest in **Moo**. **Mpo**, **Mmo**, **Moo** are isostructural but they are not isomorphous.

Mpo molecular and crystal structure

The cyclic hydrogen bonded dimer (Fig. **9**) forms about inversion centres with an N···N distance of 3.1081(15) Å. The dimers are further linked into a 1-D *zig-zag* chain *via* C-H···O interactions about inversion centres and parallel to the $(11\overline{2})$ plane. Chains stack and are linked *via* weak contacts. The shortest C-H···π(arene) contacts have C···Cg distances of 3.5556(14) and 3.7056(14) Å with C-H···Cg angles of 123°, 134° and too long to be a meaningful interaction. The room temperature study of **Mpo** (XIFNIK[8]) has been reported and archived. **Mpo** is similar to XIFNIK[8] and only differs in interaction data due to the difference in the experimental data collection temperature. The interplanar angle between the C_6 and C_5N rings is 45.34(4)°.

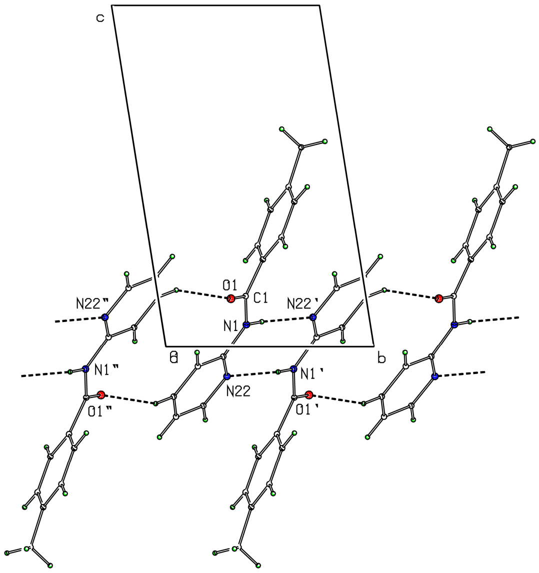

Fig. 9: The primary hydrogen bonding in **Mpo** with the cyclic N-H···N dimers.

Mmo molecular and crystal structure

The cyclic hydrogen bonded dimer forms about inversion centres with an N···N distance of 3.106(3) Å. Dimers are arranged and linked *via* weak C-H···O and C-H···π(arene) contacts. The interplanar angle between the C_6 and C_5N rings is 70.55(7)°. The major difference between **Mpo** and **Mmo** is the angle of the intradimer C-H···π(arene) contact.

Moo molecular and crystal structure

The cyclic hydrogen bonded dimer forms about inversion centres with N···N = 3.076(2) Å. In tandem is the formation of a C-H···π(arene) interaction, as C23-H23···[C11,…,C16] about inversion centres, such that all six C23···$C_{11\text{-}16}$ interaction distances are in the range 3.472(2) to 3.836(3) Å (and with six H23···$C_{11\text{-}16}$ from 2.71 to 2.92 Å): this highlights the symmetrical nature of this interaction (Figs. **10**, **11**). The short interaction C-H…π(arene) details are H23···Cg1 = 2.46 Å, C23…Cg1 = 3.3875(18) Å and C23-H23···Cg1 = 167°. Dimers are further linked *via* weak C-H···O and C-H···π(arene) contacts. There are very few examples[8,173-175] available in the literature that contain shorter C-H···π(arene) geometric data apart from analogous interactions in ionic structures, whereby the interaction is charge-based or assisted.[8,173-175] For overall comparisons, the interplanar angle between the C_6 and C_5N rings is 84.79(5)° showing an increasing trend towards aromatic rings that are perpendicular along the **Mxo** series.

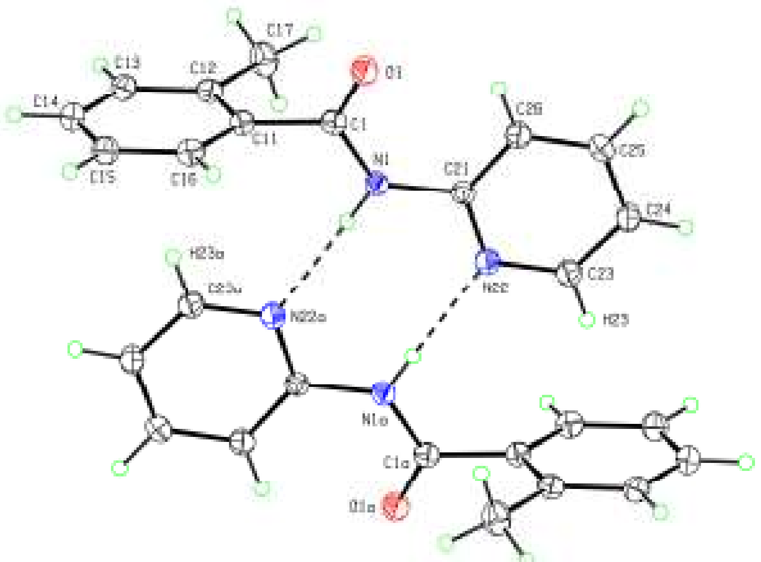

Fig. 10: An ORTEP diagram of the hydrogen bonded dimer in **Moo** (graph-set $R^2_2(8)$).

1.1.5.4. A CSD search for interactions related to Moo

A 'restricted' search was performed on normalised aromatic C-H···π(arene) interactions (C-H = 1.083 Å) with the following limits of H···Cg (2 → 2.5 Å), C···Cg (3→ 3.4 Å) and C-H···Cg (160 → 180°) (Cg is the aromatic ring centroid).

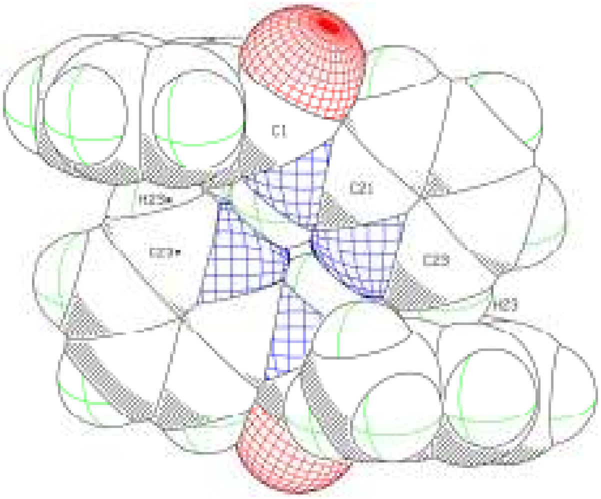

Fig. 11: The **Moo** ‘dimeric’ unit with N-H···N and C-H···π(arene) intermolecular interactions.

For version 2.30 + 4 updates a total of 41 ‘hits’ were obtained (of which 38 contain a metal): a total of 51 ‘hits’ are obtained when ‘normal’ bond lengths of C-H = 0.95 Å are used. The majority of these ‘hits’ are organometallic/metal-organic and are intramolecular in nature and principally due to the orientation of the aromatic ring towards another aromatic ring within the same molecule and typically separated by 5-7 bonds. The search was conducted to find short, symmetrical C-H···π(arene) interactions. In **Moo** with C23-H23 normalised to 1.083, the short interaction details are H23···Cg1 = 2.33 Å with C23-H23···Cg1 = 166°. The range of H23···[C11,…,C16] distances span from 2.61 to 2.80 Å.

The CSD codes for structures with short intermolecular C_6-H···π(C_6) interactions include ICEXUJ (a Zr complex) and LEXJOO (Au derivative): whereas in LETYUE the solvent is disordered with large displacement ellipsoids. In ICEXUJ, the geometric data are 2.32 Å, 3.373 Å, 163, involving indenyl group C_6 rings, whereas, in LEXJOO or triphenylphosphine-(3H-5-phenyl-1,2,3-triazol-4-yl)-gold(I) the geometric data are even shorter with data of 2.26 Å, 3.303 Å, 161° and this interaction forms in tandem with the ‘tight’ N-H···N interaction between the triazole moieties. The **Moo** data are comparable to the geometric data in these structures.

Examples with intramolecular interactions include both QEZRAO (2.25 Å, 3.32 Å, 171°) and TEGJOF (2.23 Å, 3.31 Å, 178°), which with WIXHIV (2.20 Å, 3.26 Å, 168°) are where the H atom direction is constrained by ligand geometry and steric bulk. In VAGFIS10 the interaction is constrained by the geometrical demands within the molecule. In **Moo** the interaction is intermolecular in nature and comparable in geometric terms with the shortest analogous C-H···π(arene) intramolecular interactions present in metal complexes (Figs. **10**, **11**).[8,173-175]

1.1.5.5. **Overall trends in Mxx**

Within each of the **Mxp**, **Mxm** and **Mxo** series, the primary N···N/O* interaction contracts along each **x** = *p*- > *m*- > *o*- and notably by 0.15 Å for the **Mxp** triad. This presumably is facilitated by increasing C_6/C_5N interplanar angles that allow molecules to pack more closely: the influence of repulsive H···H contacts and steric clashes (from CH_3) decreases on C_6/C_5N rotation from 0°, and as evidenced in **Mpm**. The **Mop** and **Mom** structures have the shortest N···N intermolecular distances (Table **7**) and the **Mxm** series the shortest average N···N/O* distances. The variation is small within **Mxo** as the primary interaction is responsible for the cyclic hydrogen bonded dimer formation and not chain formation.

A trend in molecular volume (unit cell *V/Z*) is noted (Table **8)** whereby the more symmetrical **Mpx** isomers have the smallest volume ($Å^3$), smaller than **Mmx** and especially the **Mox** triad (*i.e.* increasing in *V/Z* with **Mpp** < **Mmp** < **Mop**). The effect is greatest when the CH_3 group position changes from *para*-, *meta*- to *ortho*- with **Mpp**, **Mpo** having the smallest and **Mop**, **Mom** the greatest molecular volumes. The trend in pyridine N atom location is not as dramatic and the *V/Z* is greatest for the **Mxm** triad. Of interest is the decreasing N···N/O* distance (***o***- < ***m***- < ***p***-) within each **Mxp**, **Mxm**, **Mxo** triad correlating inversely with increasing molecular volume (Tables **7**, **8**). Distortion from co-planarity of the C_6 and C_5N rings allows closer molecular interaction along the primary interaction axis though with less efficient overall packing in 3-D. The trend is smallest in **Mxo** where dimer formation occurs.

Melting point analysis shows distinct patterns such as the *meta*- < *ortho*- < *para*- substitution m.p. trend in di-substituted benzenes.[10,11] The **Mmp**, **Mmo** isomers with the lowest melting points are 100°C less than the symmetrical **Mpp** isomer (50°C higher than any of the other eight **Mxx**). The pattern is distinct within **Mxp** (106°C variation), smaller in **Mxm** and reversed as *meta*- < *para*- < *ortho*- in the **Mxo** triad (a variation of 37°C). This m.p. reversal in **Mxo** is influenced by the tighter dimer formation in **Moo** due to the additional C-H···π(arene) interaction that is not present in **Mpo** or **Mmo**. In addition, the behaviour of **Mmp** should be noted where a partial melting occurs at 74°C and complete melting at 107°C.

1.1.6. *Ab initio* calculations

1.1.6.1. Structure optimisation

The three torsion angles that define the most important conformation angles of the **Mxx** isomers (optimised in *gas phase* and solvated as CH_2Cl_2, H_2O) are detailed in the Table **9**. The torsion angles are $_{\text{aromatic}}$C-C-C=O (α) between the toluoyl ring and amide group (equivalent to the C16-C11-C1=O1 solid-state angle), C-N-C-C$_{\text{aromatic}}$ (β) between the pyridine ring and amide group (equivalent to the C26(N22)-C21-N1-C1 angle) and the O=C-N-C amide linkage angle (δ).

In general, all calculated **Mxx** structures are partially planar with the α torsion angles deviating from co-planarity. Moreover, the α angle in **Mox** is smaller than in the **Mpx**, **Mmx** series due to the sterically repulsive interaction between the CH_3 group and C=O group (***M-anti*** conformation) as seen in the **Mxo** crystal structures.

Table 9: Torsion angles (°) of the optimised **Mxx** structures [a]

	optimised in gas phase			optimised in CH_2Cl_2			optimised in H_2O		
	α	β	δ	α	β	δ	α	β	δ
Mpp	153.29	-3.22	-4.76	152.24	-5.23	-4.12	152.34	-8.89	-4.88
Mmp	152.58	-2.95	-4.73	151.88	-3.73	-4.35	152.86	-5.76	-3.92
Mop	135.27	-2.19	-4.24	131.33	-2.50	-4.19	128.73	-2.13	-3.46
Mpm	153.50	-3.00	-4.39	152.26	-5.77	-3.82	152.50	-12.15	-4.36
Mmm	152.81	-2.94	-4.33	151.94	-4.08	-3.92	152.80	-8.01	-2.88
Mom	134.94	-1.96	-3.94	130.89	-2.54	-3.79	127.80	-4.97	-2.92
Mpo	156.74	-1.88	-3.94	153.07	-4.66	-3.34	153.61	-5.11	-4.06
Mmo	155.95	-1.71	-4.04	153.73	-1.86	-3.26	152.17	-5.58	-3.99
Moo	137.12	-1.19	-3.98	132.61	0.37	-4.45	128.63	-1.28	-2.91

[a] The angle C16-C11-C1=O1 is referred as α, the angle C26(N22)-C21-N1-C1 as β and O1=C1-N1-H1 angle (amide link) as δ. All geometries are based on B3LYP/6-311++G optimizations with or without the PCM-SMD solvation model.

In the *gas phase*, average α angles in **Mpx**, **Mmx** are 154.15±1.75° and 135.78±1.18° for the **Mox** triad. For solvation in CH_2Cl_2 (H_2O) the α angles are similar for **Mpx**, **Mmx** with $\alpha = 152.52\pm0.73°$ (152.71±0.51°) and 131.61±0.89° ($\alpha = 128.38\pm0.51°$) for **Mox**. The more polar solvent has little impact on the α angle in the **Mpx**, **Mmx** isomers, while in **Mox** there is additional rotation.

The β and δ torsion angles are essentially planar with β (*gas phase*) having an average of -2.34±0.71°, from **Mpp** (-3.22°) to **Moo** (-1.19°). The β angle decreases towards 0° and mainly due to the favourable, though weak intramolecular $_{\text{aromatic}}$C-

H…O interaction, with the **Mxo** series closest to 0°. The **Mxx** solvent optimisations are similar with CH_2Cl_2 (H_2O) averages of -3.33±1.99° (-5.54±3.17°) and a decrease towards 0° for **Moo**, though with high deviation for the **Mxm** (**Mpm**) triad in H_2O. The δ angle (*gas phase*) deviates slightly from planarity by -4.40±0.31° and similar to the solvent averages of -4.03±0.22° (-4.40±2.27°). The optimisation results can be compared directly with the solid-state torsion angles plotted for direct comparison in Fig. **12**.

1.1.6.2. **Conformational analysis**

Fig. **12** depicts the nine **Mxx** PES *gas phase* optimisations with both toluoyl ring (**M**-ring, blue dashed line) and pyridine rings (red, full line). A high degree of modularity of all nine **Mxx** isomers is present. Each **Mx** or **x** group displays a typical PES form, and for each molecule an **Mx-x** combination representative of both PES scans. Analysis of the amide linkage connecting the two groups shows a minor neighbouring ring influence.

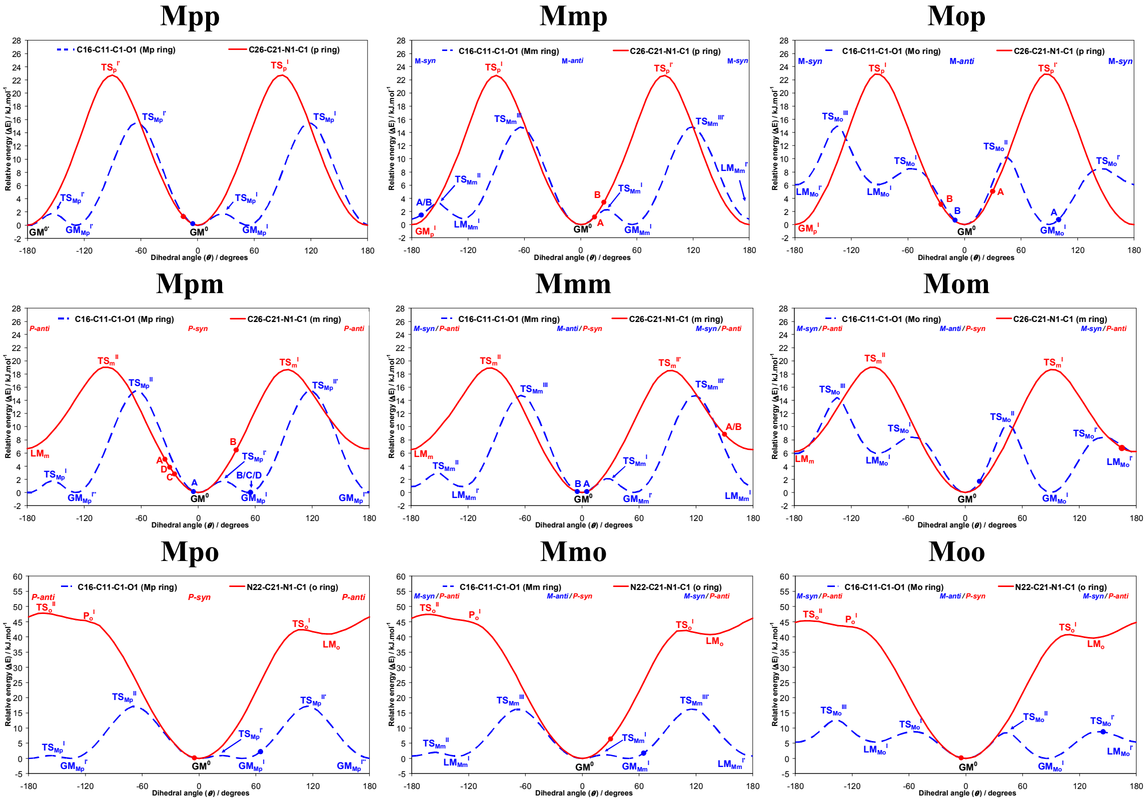

Mpp **Mmp** **Mop**

Mpm **Mmm** **Mom**

Mpo **Mmo** **Moo**

Fig. 12: The PES conformational analysis diagrams for the nine **Mxx** isomers optimised in *gas phase*: the equivalent solid state angle is depicted as a (●).

All optimised structures whether in the *gas phase* or in solvent have **M-*anti*/P-*syn*** conformations (if applicable) as the most stable. However, in the **Mmx** triad, the difference between the **M-*anti*/P-*syn*** and **M-*syn*/P-*syn*** conformations is as small as 0.84±0.05 kJ.mol^{-1} and implying a practical conformatial equivalence. The *ab initio* results are summarized as follows:

Conformational analysis of the *para*-toluoyl (**Mp**) ring gives a PES profile with two global maxima located *ca*. -60° and 120° (TS$_{\mathbf{Mp}}^{\mathrm{II}}$[**Mpm**] = 15.48 kJ.mol^{-1} to TS$_{\mathbf{Mp}}^{\mathrm{II}}$[**Mpo**] = 17.22 kJ.mol^{-1}), two local maxima *ca*. 25° and -155° (TS$_{\mathbf{Mp}}^{\mathrm{I}}$[**Mpo**] = 0.94 kJ.mol^{-1} to TS$_{\mathbf{Mp}}^{\mathrm{I}}$[**Mpp/m**] = 1.73 kJ.mol^{-1}). The four global minima are near 0°, 55°, ±180° and -130°.

Rotation of the *meta*-toluoyl (**Mm**) ring gives a PES profile with two global minima *ca*. 55° and 0°, two global maxima at *ca*. -65° and 120° (TS$_{\mathbf{Mm}}^{\mathrm{III}}$[**Mmm**] = 14.07 kJ.mol^{-1} to TS$_{\mathbf{Mm}}^{\mathrm{III}}$[**Mmo**] = 16.20 kJ.mol^{-1}), two local minima *ca*. -125° and ±180° with increases of (LM$_{\mathbf{Mm}}^{\mathrm{I}}$[**Mmo**] = 0.79 kJ.mol^{-1} to LM$_{\mathrm{Mm}}^{\mathrm{I}}$[**Mmm**] = 0.89 kJ.mol^{-1}). The two local maxima are at -155° and 25° (TS$_{\mathbf{Mm}}^{\mathrm{I}}$[**Mmo**] = 1.18 kJ.mol^{-1} to TS$_{\mathbf{Mm}}^{\mathrm{I}}$[**Mmp**] = 3.20 kJ.mol^{-1}).

Rotation of the *ortho*-toluoyl (**Mo**) ring gives a PES profile with one global maximum at -135° (TS$_{\mathbf{Mo}}^{\mathrm{II}}$[**Moo**] = 12.63 kJ.mol^{-1} to TS$_{\mathbf{Mo}}^{\mathrm{II}}$[**Mop**] = 14.99 kJ.mol^{-1}), one isolated local maxima at 45° (TS$_{\mathbf{Mo}}^{\mathrm{II}}$[**Moo**] = 8.40 kJ.mol^{-1}, TS$_{\mathrm{Mo}}^{\mathrm{II}}$[**Mop/m**] = 10.32 kJ.mol^{-1}), two local maxima *ca*. -55° and 145° (TS$_{\mathbf{Mo}}^{\mathrm{II}}$ = 8.55±0.19 kJ.mol^{-1}), two local minima at ±180° and -90° (LM$_{\mathbf{Mo}}^{\mathrm{II}}$[**Moo**] = 5.38 kJ.mol^{-1} to LM$_{\mathbf{Mo}}^{\mathrm{II}}$[**Mop**] = 6.06 kJ.mol^{-1}) and two global minima at 0° and *ca*. 90°.

Rotation of the *para*-pyridyl (**p**) ring gives a PES profile with two global maxima at ±90° (TS$_{\mathbf{p}}^{\mathrm{I}}$=22.75±0.08 kJ.mol^{-1}) and two global minima at 0° and ±180° whereas the *meta*-pyridine (**m**) ring has a PES profile with two global maxima *ca*. ±95° (TS$_{\mathbf{m}}^{\mathrm{I}}$ = 18.81±0.21 kJ.mol^{-1}), two local minima at ±180° (LM$_{\mathbf{m}}^{\mathrm{I}}$ = 6.48±0.23 kJ.mol^{-1}), and one global minimum. Rotation of the *ortho*-pyridine (**o**) ring gives an asymmetrical PES profile. One global maximum is located at -165° (TS$_{\mathbf{o}}^{\mathrm{II}}$[**Moo**] = 45.26 kJ.mol^{-1} to TS$_{\mathbf{o}}^{\mathrm{II}}$[**Mmo**] = 47.39 kJ.mol^{-1}), one local maxima at around 110° (TS$_{\mathbf{o}}^{\mathrm{I}}$[**Moo**] = 40.69 kJ.mol^{-1} to TS$_{\mathbf{o}}^{\mathrm{I}}$[**Mpo**] = 42.32 kJ.mol^{-1}), one local minimum at 135° (LM$_{\mathrm{o}}^{\mathrm{I}}$[**Moo**] = 39.62 kJ.mol^{-1} up to LM$_{\mathrm{o}}^{\mathrm{I}}$[**Mmo**] = 40.77 kJ.mol^{-1}) and of note, a *plateau* at -125° (P$_{\mathbf{o}}^{\mathrm{I}}$[**Moo**] = 43.27 kJ.mol^{-1} up to P$_{\mathbf{o}}^{\mathrm{I}}$[**Mpo**] = 45.34 kJ.mol^{-1}).

The conformational analyses in the solvents CH_2Cl_2 and H_2O (PCM-SMD model)[170] with comparisons between *gas phase* and solvents are depicted as PES scans in Fig. **13**.

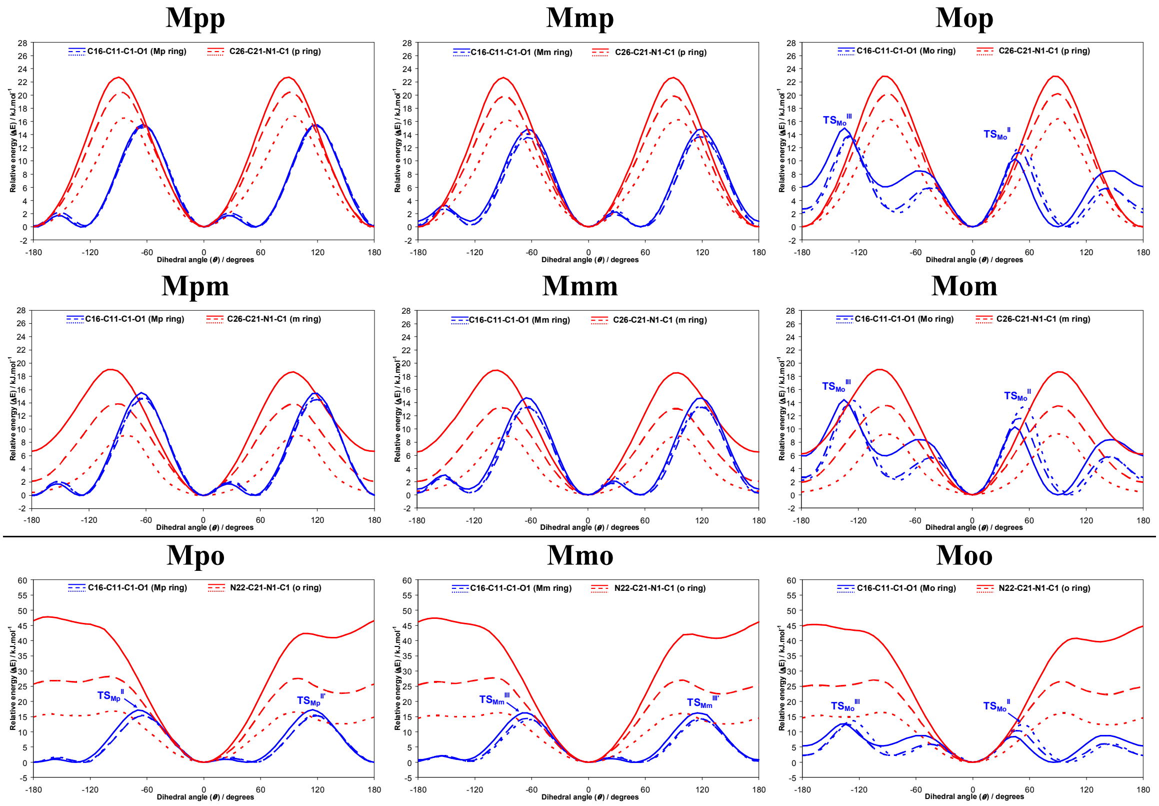

Fig. 13: The PES conformational analysis diagrams for the nine **Mxx** isomers optimised in *gas phase* (full line), CH_2Cl_2 (dashed line) and in H_2O (dotted line) using the PCM-SMD solvation method.

Comparisons between the *gas-phase* and solvated conformational analyses show small differences: all **Mxx** isomers have the **M-*anti*/P-*syn*** conformations at the stationary point regardless of the medium. Furthermore, the PES curve patterns are similar, but there are differences in the rotational barrier heights where the solvent dielectric constants influence significant changes (usually decreases, sometimes increases) in the rotational energies necessary for aromatic ring flipping. Large decreases in the rotational barriers in high dielectric solvents (methanol, DMSO) can facilitate ring rotation and conformational changes. This can influence the ability to (*a*) isolate more than one molecular conformation, (*b*) promote molecular disorder in the solid state and (*c*) obtain more than one polymorph depending on solvent choice and range.

Decreases of the rotational barriers for the *p-/m-/o-* rings are distinct and consistent with the *gas-phase*. For **p-** the decrease is greater in H_2O (~35%) than in CH_2Cl_2 (~12%). A related decrease is noted in **m-** (~32% in CH_2Cl_2: ~ 65% in H_2O) and in the **o**-rings (~33% in CH_2Cl_2: ~60% in H_2O).

The rotational barrier data for the **Mx** rings display different patterns than for the *p/m/o*- rings and the nine **Mxx** isomers can be assigned to three groups. The 1st group with **Mpp**, **Mmp**, **Mpm** and **Mmm** have small energy differences between the *gas phase* and solvated forms suggesting minor or negligible influence of the solvents on **Mx** ring rotation. The rotational barrier decreases in **Mp** are ~2% in CH_2Cl_2 and H_2O, but ~10% in CH_2Cl_2 and ~8% in H_2O for **Mm**. The 2nd group comprising **Mpo** and **Mmo** show negligible energy decreases over most of the curve but with a greater decrease approaching $TS_{\mathbf{Mp}}^{II}$ and $TS_{\mathbf{Mm}}^{III}$. This decline of ~26% is similar in both **Mp** and **Mm** rings regardless of the solvent. The 3rd group comprises the **Mo** ring (**Mox**) triad having an unusual increase and shift of the rotational barrier $TS_{\mathbf{Mo}}^{II}$ and $TS_{\mathbf{Mo}}^{III}$. At $TS_{\mathbf{Mo}}^{II}$ the molecules are planar and the CH_3 group is near the C=O group. On **Mo** ring rotation from 0° the solvated state electronic energy remains high in CH_2Cl_2 from ~9% (**Mop**) to ~23% (**Moo**); in H_2O from ~20% (**Mop**) to ~46% (**Moo**) when compared with the *gas phase* baseline curve, and to a minimum energy conformation. The higher dielectric solvent destabilizes the planar molecular conformation. The remainder of the curve shows a decrease by ~44% (CH_2Cl_2) and ~49% (H_2O). A similar rotation energy increase when the **Mx** ring is planar or rotating from 0° is seen in **Mp** and ~25% in CH_2Cl_2 and ~19% (H_2O), and in **Mm**, just for **Mmo** (~37% in CH_2Cl_2 and ~32% in H_2O). Overall, conformations are similar in all three media though with smaller rotational energy barriers for the solvated forms and the more polar solvent H_2O.

1.1.6.3. **Energy results**

The energy calculation results (CBS-QB3) (Table **10**) comprise the electronic energies (δE_{SCF}) and Gibbs free energies (δG) in all three media, including ΔG_{solv} (for CH_2Cl_2 and H_2O) and $\Delta\Delta G_{solv}$ (CH_2Cl_2 *vs*. H_2O). The differences among each molecule are presented as δE_{SCF} (δG) and the differences between media as ΔE_{SCF} (ΔG). The **Mom** energies were used as reference points for the *gas phase* and solvents. Detailed results including absolute values for E_{SCF} and G; zero point energies and thermal energies are provided in the ESI I (Section 3.1.1).

The electronic energy results (*gas phase*) show that the **Mxo** series is the most stable, with **Mxm** the least stable triad: **Mmo** is the most stable and **Mom** the least stable of the **Mxx** isomers. The results demonstrate that an *ortho*-N atom has a stabilising effect with an *ortho*-methyl having a slight destabilising effect.

Table 10: The energy calculation results for **Mxx** in kJ.mol^{-1}

	gas phase		**CH_2Cl_2**		**H_2O**		***gas phase*→ CH_2Cl_2**		***gas phase*→ H_2O**		**H_2O → CH_2Cl_2**	
	δE_{SCF}	δG	δE_{SCF}	δG	δE_{SCF}	δG	ΔE_{SCF}	ΔG_{solv}	ΔE_{SCF}	ΔG_{solv}	$\Delta\Delta E_{SCF}$	$\Delta\Delta G_{solv}$
Mpp	-22.31	-11.35	-27.34	-11.96	-26.62	-12.64	-74.73	-63.36	-58.06	-45.15	-16.67	-18.21
Mmp	-20.70	-11.34	-24.62	-13.26	-24.53	-10.24	-73.62	-64.67	-57.59	-42.76	-16.03	-21.91
Mop	-11.48	-3.89	-14.34	-6.46	-14.16	-6.82	-72.55	-65.31	-56.43	-46.79	-16.12	-18.53
Mpm	-10.85	-7.46	-12.88	-5.81	-12.18	-6.94	-71.73	-61.09	-55.09	-43.33	-16.64	-17.76
Mmm	-9.29	-7.45	-10.29	-7.40	-10.35	-4.12	-70.70	-62.69	-54.82	-40.52	-15.88	-22.17
Mom	0.00	0.00	0.00	0.00	0.00	0.00	-69.70	-62.75	-53.75	-43.86	-15.94	-18.89
Mpo	-45.89	-33.60	-44.15	-29.52	-35.82	-22.87	-67.96	-58.67	-43.69	-33.12	-24.27	-25.55
Mmo	-44.16	-33.38	-41.73	-29.61	-33.39	-21.61	-67.26	-58.98	-42.98	-32.09	-24.28	-26.89
Moo	-34.32	-24.74	-30.75	-23.03	-22.99	-14.73	-66.13	-61.03	-42.42	-33.84	-23.70	-27.19

[a] Only the differences between each molecule (δ) and media (Δ, ΔΔ) are shown, **Mom** is the reference molecule for the *gas phase* (E_{SCF} = -683.2650 E_h, G = -686.2042 E_h) and for solvents (CH_2Cl_2: E_{SCF} = -683.2915 E_h, G = -686.2281 E_h; H_2O: E_{SCF} = -683.2855 E_h, G = -686.2209 E_h). Full data including zero-point energies (E_0) and thermal energies (E) are provided in the Appendix III.

Calculations using the CBS-QB3 compound method with PCM-SMD solvation model provided theoretical values of ΔG_{solv} in CH_2Cl_2 (and H_2O), including theoretical $\log K_{D/W}$ (in the ESI I, section 3.1.1.4). These results are consistent with our experimental observations and with no unexpected values. All compounds should be 10^3-10^4 times more soluble in CH_2Cl_2 as compared to H_2O, while the **Mxo** series are expected to be the least soluble in water.

1.1.7. Comparisons of the solid state and modelling data

The molecular conformations of the **Mxx** series from X-ray diffraction data and *ab initio* calculations (*gas phase* and solvated) share similarities but exhibit distinct differences especially in a subset of cases. In each PES diagram, the corresponding torsion angles from the crystal structures data are incorporated as (●) and for **Mmp**, **Mop**, **Mpm** and **Mmm** two or more (●) are depicted where more than one independent molecule is present in the asymmetric unit ($Z' > 1$).

For five of the nine **Mxx** isomers the torsion angle data derived from *ab initio* calculations are reasonably consistent with the crystallographic geometric data and the global minima (GM) similar and within 10-15° (Fig. **12**). However, for **Mmp**, **Mmm**, **Mom** and **Moo**, the crystallographic torsion angles differ from their respective *ab initio* results and are not located in an energetically favourable conformation and based on our *ab initio* results. Three solid-state conformations **Mmp**, **Mmm** and **Mom** adopt *meta*-

stable conformations (relative to calculations using the *gas-phase* energy baseline) whereas **Moo** adopts an *unstable* conformation. However, in the solid-state the conformations adopted by the **Mxx** isomers are more than compensated for by strong intermolecular hydrogen bonds and packing forces driving the molecular packing and structure aggregation in the crystal. The PES scans (CH_2Cl_2, H_2O) (Fig. **13**) indicate that more polar solvents can facilitate aromatic ring rotations and may predispose **Mxx** isomers crystallising from such solvents to adopt unexpected conformations. The ability of a more polar solvent (usually through hydrogen bonding) to interact with the solute may provide an indication of a possible tendency towards polymorphism (or at least to steer towards this possibility).

The optimised **Mmx** triad shows a trend with their tolyl rings in an ***M-anti*** conformation (in close proximity to the C=O group), whereas the **Mmp** crystal structure is ***M-syn*** with the tolyl ring rotated by -170° from the optimized **Mmp** conformation (A/B in Fig. **12**). Patterns also emerge in the optimised **Mxm** triad with the pyridyl rings in the ***P-syn*** conformation (on the amide N-H side), whereas in the **Mmm** and **Mom** (LM_m in Fig. **12**) crystal structures the ***P-anti*** conformation is observed and presumably due to aggregation events. Crystals of **Mom** (***M-anti***/***P-anti***) proved elusive and only obtained after many attempts and from ethyl acetate. The CBS-QB3 calculations indicate **Mom** as the least stable isomer and PES scans show several possible conformations and geometries, four for the **Mo** and two for the **m** (*meta*-pyridyl) ring within 10-15 kJ.mol^{-1} which can easily be achieved in solution and may influence the crystallisation event and our inability to easily crystallize **Mom**.

In **Moo** the tolyl ring dihedral angle is suggestive of an energetically unfavourable conformation as ***M-syn***/***P-syn*** (Fig. **12**, $TS_{\mathbf{Mo}}^{I}$). The stability of **Moo** as a dimer in the solid-state {*via* N-H···N and two short C-H···π(arene) interactions} highlights the dimerisation driven by cyclic $R^2_2(8)$ ring formation and this more than compensates for twisting of the tolyl torsion angle in the crystal structure of **Moo**. The observation of the **Mxo** isomers as the most stable triad may be due to delocalised system N22-C21-N1-C1=O1; the *ortho*-pyridine ring conformation with one deep energy minimum at GM_0 illustrates this stability.

1.2. Fxx isomer grid

1.2.1. General description of synthesis

All nine **Fxx** compounds were synthesised using standard nucleophilic acyl substitution reaction (Schotten-Baumann reaction, Scheme **24**) between 4-/3-/2-aminopyridines and 4-/3-/2-fluorobenzoyl chlorides. In general, the procedure was as described for **Fxp** compounds in our previous publication.[162] However, a different procedure was applied to the **Fxo** compounds. The **Fxm** compounds were prepared by the condensation reaction of 3-aminopyridine (3-AP) with 4-/3-/2-fluorobenzoyl chlorides in CH_2Cl_2 in the presence of one equivalent of Et_3N.

In 100 ml round bottom flask 3-aminopyridine (0.6219 g, 6.6 mmol) was dissolved with stirring in 50 ml of CH_2Cl_2 and Et_3N (1.394 ml, 10 mmol) was added. The flask with reaction mixture was placed on an ice bath and allowed to cool. Under an inert atmosphere of N_2, 4-/3-/2-fluorobenzoyl chlorides (6.6 mmol) were added and the reaction mixture stirred overnight. The reaction mixture was washed three times with an aqueous $KHCO_3$ solution and the organic layer was dried with anhydrous $MgSO_4$. The solvent was evaporated and the product left for crystallization. A crystalline product was purified with column chromatography with silica as stationary phase and a mixture of $CHCl_3$, ethyl acetate and acetone (2:2:1).

Table 11: Product quantities, yields and melting points of **Fxx** compounds

Fxx	m/g	yield/%	m.p./ºC
Fpp	1.160	81.3	186.1-187.8
Fmp	1.133	79.4	185.0-186.6
Fop	3.711	86.7	134.7-135.6
Fpm	1.097	76.9	148.8-149.1
Fmm	1.046	73.3	149.7-152.2
Fom	1.926	67.5	89.2-89.6
Fpo	0.771	54.0	117.2-123.1
Fmo	1.275	59.0	76.7-77.4
Foo	1.567	36.2	84.0-86.1

Since 2-aminopyridine has increased reactivity due to the *ortho* nitrogen and readily undergoes dibenzoylation reaction giving imides[160-162] syntheses of **Fxo** was based on nucleophilic acyl substitution reaction between 2-AP and fluorobenzoyl chlorides, employing pyridine as reaction medium and without catalytic base, at -10ºC. The detailed procedure was as follows.

The 2-aminopyridine (0.9412 g, 10 mmol) were added to a 100 ml two-neck round bottom flask placed on an ice bath (ice/water/NaCl/NH_4Cl) with stirring. Then, 30 ml of solvent (pyridine) was added. The flask was placed on ice bath and reaction mixture was allowed to cool to -10ºC. Finally, the 4-/3-/2-fluorobenzoyl chloride (5 mmol) were added slowly into the solution mixture. The reaction mixture was allowed to warm to room temperature and stirred overnight. Into the reaction mixture 100 ml of purified water was poured and *conc.* HCl was gradually added until pH = 5-6. A white precipitate formed, and filtered on a Buchner's funnel. The precipitate was washed with copious amounts of water and allowed to dry. The pale yellow products were purified with column chromatography (**Fpo** and **Fmo**: silica// $CHCl_3$/ethyl acetate/n-hexane = 4:2:1, **Foo**: $CHCl_3$/ethyl acetate/*n*-hexane = 4:5:1).

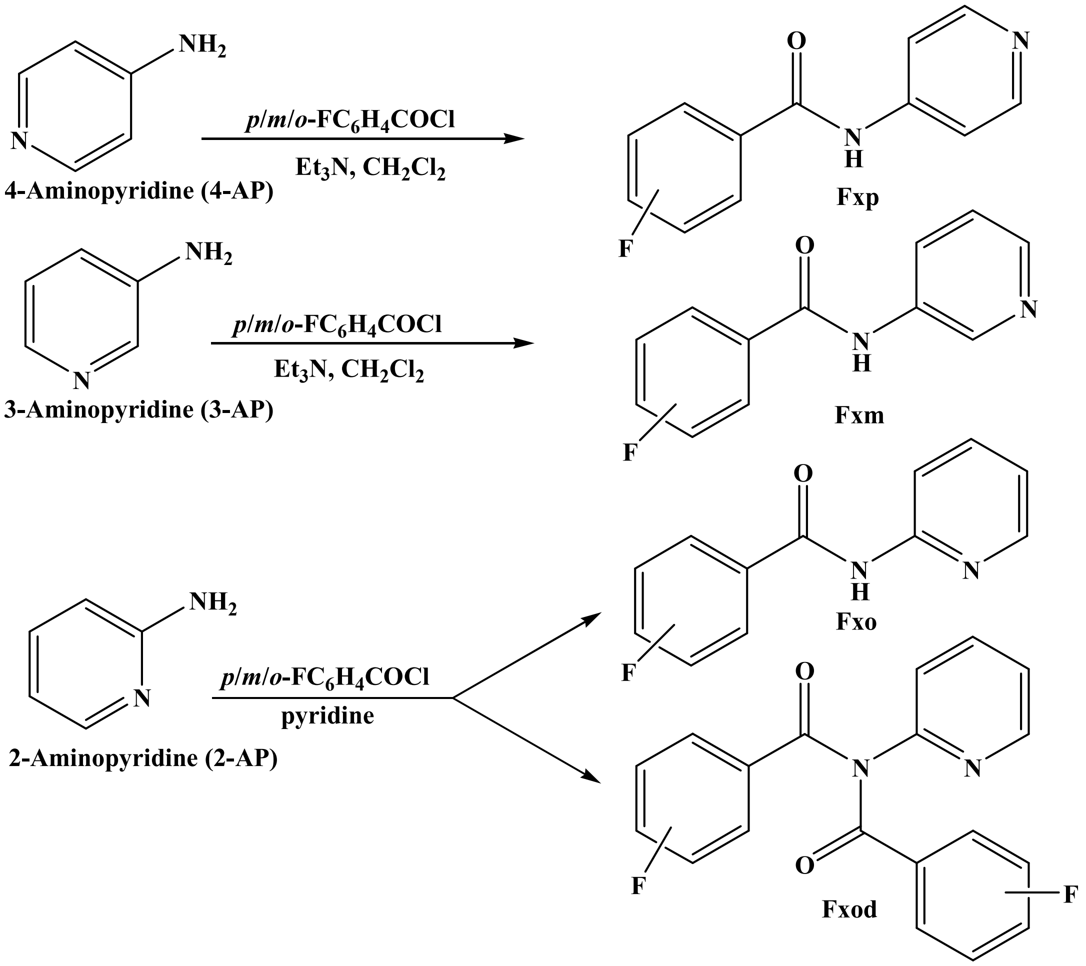

Scheme 24: Schematic diagram of the **Fxx** reactions

1.2.2. X-ray crystallography methods

Single crystals of the **Fxx** isomers including the three **Fxp** compounds[162] were obtained by slow evaporation at 4ºC or 21ºC and typically from ethyl acetate, while **Fmo** was grown from $CDCl_3$. The only **Fxx** isomer that proved difficult to crystallise as diffraction quality crystals was **Fom**: decent quality crystals were obtained only after a series of crystal growth experiments from mixtures of methanol and diethyl ether. The

X-ray data were collected on a Gemini S Ultra diffractometer at 294(1) K, with a θ range from 2-25° minimum and 100% data coverage to 25° (on θ).[176]

Data reduction procedures and absorption corrections are standard and comprehensive details have been published elsewhere.[176] All structures were solved using the SHELXS97 direct methods program[3] and refined by full matrix least squares calculations on F^2 with all non-hydrogen atoms having anisotropic displacement parameters. Hydrogen atoms were treated as riding atoms using the SHELXL97 defaults[3] (at 294 K) except for the amide N-H (isotropic refinement) using the OSCAIL software[168] with selected crystallographic and structural information in the ESI I, Section 2.2. Molecular and hydrogen bonding diagrams (Figs. **15-22)** were generated using PLATON.[169] All searches on the Cambridge Structural Database (CSD) were performed with the November 2010 release (version 5.32+4 updates).[8]

1.2.3. Computational methods

The computational methods and procedures reported herein are similar to previous isomer grid (**Mxx**) using Gaussian03/09.[25] The *ab initio* DFT (B3LYP) geometry optimisations in *gas phase* were performed with and without polarisation functions (as 6-311++G, 6-311G**, 6-311++G**) in order to probe the influence of polarisation functions on the overall structure and conformation. The B3LYP/6-311++G** basis set is close to optimal for the **Fxx** isomer series in terms of both accuracy of geometry and computational costs. As polarisation functions are important in molecular geometry optimisation and especially when hydrogen bonds are involved, we rigorously examined the influence of both diffuse and polarisation functions on key structural parameters by *gas phase* optimisation of the **Fxx** isomers using three distinct basis sets (as above). Solvated geometry optimisations and conformational analyses were performed in two solvents, CH_2Cl_2 and H_2O (PCM-SMD solvation model)[170] specifically using the B3LYP/6-311++G** basis set. Additionally, high accuracy energy calculations including ΔG_{solv} were obtained using the CBS-QB3 compound method.[171]

The conformational analysis of each **Fxx** structure was undertaken using PES scans of the two key dihedral angles over ±180° both in *gas phase* and solvents: the angles used are C12-C11-C1=O1 (α, **F**-ring), and C1-N1-C21-C26 (β, **P**-ring). Each asymmetric (*meta* or *ortho*) ring, can adopt, relative to the amide linker, two conformations (***syn*** or ***anti***) (Scheme **25**). Therefore, the fluorophenyl (**F**-ring) or pyridine (**P**-ring) rings can be either in the ***syn*** (**F-*syn***, **P-*syn***) or ***anti*** (**F-*anti***, **P-*anti***) conformation. Rings with *para*-pyridine N or *para*-phenyl F atoms are not subject to this convention. The results provide PES diagrams highlighting conformation preferences (***syn***/***anti***) and rotational barriers in kJ.mol^{-1}.

The computational analyses were performed to (*i*) investigate the effect of the polarisation functions (** or d,p) with the B3LYP/6-311++G basis set on molecular geometry and conformation, (*ii*) facilitate comparisons of the optimised structures and conformations with the solid state structural results and (*iii*) examine the influence of the solvation model (CH_2Cl_2, H_2O; PCM-SMD method) on the **Fxx** molecular geometry and conformations.

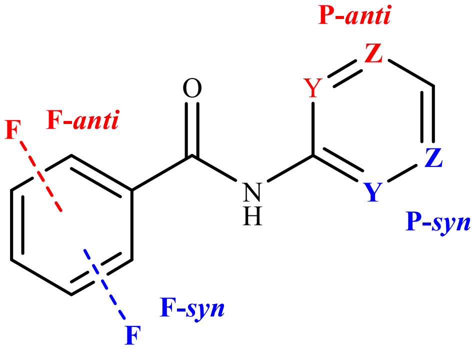

Scheme 25: The four possible **Fxx** conformations

1.2.4. Comment on synthesis and general characteristics

The **Fxx** compounds (as expected for benzamides) are crystalline, colourless, odourless solids, readily soluble in most organic solvents, less soluble in cyclohexane and diethylether but insoluble in water. The yields (Table **11**) were excellent for the **Fxp**/**Fxm** isomers, but lower for **Fxo** due to the competing reaction (and strategies were employed to prevent a significant formation of (2:1) imide products). The compound purities, following standard purification and chromatography, were excellent as analysed by TLC. In related benzamides we have noted similar trends with the melting point ranges and median values dropping from the symmetrical **Fpp** to the less symmetrical isomers, with **Fmo** having the lowest melting point. The melting points of **Fop** and **Fom** are ~50ºC lower than the related isomers in the **Mxx** series (Section 1.1).

1.2.5. Comment on spectroscopic data

All spectroscopic data, including ^{1}H, ^{13}C and ^{19}F NMR, as well as IR spectra are listed in the Appendix I (Section 1.2), while the spectra are presented in the ESI I, Section 1.2. There is a high degree of modularity within the **P**- and **F**-rings as noted previously in **Mxx**.

The amide proton (δ_{N-H}) resonance at *ca.* 8.37 ppm ($CDCl_3$) shifts to 10.62 ppm (DMSO-d_6) in the six **Fxp**/**Fxm** isomers. However, the average δ_{N-H} for **Fxo** is *ca.* 8.94 ppm ($CDCl_3$) and shifted to ~10.85 ppm in DMSO-d_6. The smaller difference for the δ_{N-H} in **Fxo** ($CDCl_3$) as compared to **Fxp**/**Fxm** results from the higher acidity of the amide proton and influenced by the *ortho*-pyridine N atom. The most distinct feature in the **Fxx** NMR spectra is the splitting of the N-H peak into a broad doublet in the **Fox** triad (**Fop**, **Fom**, **Foo**) when using aprotic solvents such as $CDCl_3$ (ESI I, Section 1.2).[162] This splitting results from the strong through-space nuclear spin–spin couplings ($^{1h}J_{N-H...F}$ = 13-15.5 Hz), caused by the formation of a strong N-H···F interaction between the *ortho*-F atom and amide proton.[177] The N-H peak is present as a broad singlet in polar solvents (DMSO-d_6, ESI I, Section 1.2) suggesting that the intramolecular N-H···F hydrogen bonding is disrupted with resulting conformational change. Our detailed studies of conformational analyses using both *gas phase* and solvated models for the **Mxx** analogues suggests that the use of highly polar solvents (high dielectric constants) decreases the rotational barriers so as to facilitate ring rotation and conformational changes. This is what is observed when the N-H···F_{ortho} interaction is disrupted in the **Fox** triad in polar solvents such as DMSO. The IR spectra for **Fxo** triad are similar with typical strong and diffused stretching bands between 3333 and 2700 cm^{-1} with prominent peaks distinctly present at 3078, 3175 and 3112 cm^{-1}.

1.2.6. Crystallographic data and analysis

1.2.6.1. General comments

The salient features of the **Fxx** structures are provided in Tables **12** and **13**; all other important crystallographic details are included in the ESI II (Section 2.2). The 3 × 3 isomer grid of nine **Fxx** compounds is augmented by two pairs of polymorphs for **Fpm** and **Fom**. For **Fpm**, one polymorph as **Fpm_O** exhibits N-H···C=O intermolecular interactions as amide···amide *C(4)* chains, while **Fpm_N** aggregates by the $_{amide}$N-H···$N_{pyridine}$ interactions (both in space group $P2_1/n$, Z' = 1). In **Fom**, both polymorphs **Fom_O** and **Fom_F** exhibit N-H···O=C intermolecular hydrogen bonding but in different space groups, with different conformations and disorder (**Fom_O**). For the remaining isomers, **Fmm** aggregates *via* N-H···N interactions while all **Fxo** isomers crystallise as twisted dimers [$R^2_2(8)$ rings] *via* $_{\text{amide}}$N-H···N$_{\text{pyridine}}$ interactions. **Fxx** has one strong N-H donor and two O=C/N acceptors and both types of interactions are possible.

Table 12: Selected crystallographic data for the **Fxx** isomers [a]

Structure[a]	**Space group**	***Z*/*Z'***	**Volume/Å^3**	***R*-factors**
Fpp[b]	$P2_1/c$	4/1	1006.40(3)	0.034, 0.090
Fmp[b]	$P2_1/c$	4/1	995.76(3)	0.034, 0.092
Fop[b]	$P2_1/c$	4/1	1009.72(3)	0.037, 0.103
Fpm_O	$P2_1/n$	4/1	992.74(3)	0.042, 0.114
Fpm_N	$P2_1/n$	4/1	1009.69(9)	0.053, 0.120
Fmm	$Pca2_1$	4/1	1019.67(5)	0.033, 0.084
Fom_O	$P2_1$	12/6	2999.41(12)	0.059, 0.176
Fom_F	$P2_1/n$	4/1	987.35(7)	0.044, 0.122
Fpo	$Pbcn$	8/1	2100.58(6)	0.042, 0.113
Fmo	$P\bar{1}$	4/2	1034.48(6)	0.046, 0.124
Foo	$P\bar{1}$	4/2	1048.88(7)	0.044, 0.114

[a] **Fxx** = $C_{12}H_9N_2OF$, $M = 216.21$, T = 294(1) K.

[b] **Fxp** = LOCREB, LOCLEV, LOCRAX at 150(1) K[8,162]

1.2.6.2. **Fxp isomer series**

The crystal structures of the three **Fxp** (Fig. **14**) compounds are published (data collected at 150(1) K[162]). Nonetheless, new crystal samples were grown from ethyl acetate with data collected at 294(1) K in order to examine the possibility of polymorphism and confirm previous results (Tables **12, 13**). All three **Fxx** isomers have similar crystal structures and are isomorphous in space group $P2_1/c$.

Table **13.** Salient structural features of the **Fxx** isomers (Å, °)

Structure[1]	**C_6/C_5N**	**C_6/amide**[2]	**C_5N/amide**[2]	**N···N/O**	**Packing**[3]
Fpp	52.14(4)	33.51(5)	18.93(6)	3.0581(15)	*C*(6) chains
Fmp	48.86(4)	32.37(5)	17.56(6)	3.0786(14)	*C*(6) chains
Fop	46.14(4)	31.65(5)	15.20(7)	3.0587(16)	*C*(6) chains
Fpm_O	1.02(9)	31.25(6)	30.32(6)	3.0575(13)	*C*(4) chains
Fpm_N	28.95(8)	20.73(9)	8.40(9)	3.151(3)	*C*(6) chains
Fmm	43.97(6)	35.95(7)	8.02(9)	3.077(3)	*C*(5) chains
Fom_F[1]	2.35(10)	18.36(8)	16.14(8)	3.3321(17)	*C*(4) chains
Fpo	44.41(5)	39.56(5)	6.19(5)	3.0608(18)	$R^2_2(8)$ rings
Fmo	65.30(6)	49.48(7)	3.0721(17)	3.0721(17)	$R^2_2(8)$ rings
	47.92(6)	43.00(8)	3.0502(18)	3.0502(18)	
Foo	66.31(5)	69.18(6)	3.0460(14)	3.0460(14)	$R^2_2(8)$ rings
	52.02(5)	38.12(6)	3.0408(15)	3.0408(15)	

[1] **Fom_O** ($Z' = 6$) is discussed in the *section 1.2.4.3.3.*

[2] Amide plane calculated as a 5 atom plane as [C-(C=O)N-C].

[3] Primary packing descriptors; chains are 1-D (*zig-zag*); $R^2_2(8)$ rings, cyclic (as N-H···N).

Bond lengths and angles are normal and the difference in C-F bond lengths noted previously is evident with 1.3591(14) Å (**Fpp**), 1.3517(16) Å (**Fmp**) and 1.3420(15) Å (**Fop**), presumably arising from the influence of the secondary interactions/contacts and intramolecular N1-H1···F12 in (**Fop**).

Of note is the expanding list of structures isomorphous with the **Fxp** triad (Table **5**)[172] including the parent *N*-(4-pyridyl)benzamide [MOHQOP][178] and 2,5-difluoro-(4-pyridyl)benzamide [HOFVUU].[172] This series of five compounds is unusual in that the compounds are isomorphous (with similar unit cell parameters, packing and alignment) but differ in their F/H peripheral atom-site position and interactions/contacts at the secondary level. This arises principally due to the *ca.* 0.4 Å difference between typical organic C-F/C-H bond lengths and the resulting directional influence on weaker interactions and contacts. The **Fxp** details are not discussed further except for comparisons (Tables **12**, **13**).

1.2.6.3. **Fxm isomer series**

Fpm polymorphs molecular and crystal structures

The **Fpm** isomer was isolated as two polymorphs **Fpm_O** and **Fpm_N** (suffix **O**/**N** based on the primary hydrogen bonding interactions), both of which crystallise in space group $P2_1/n$ with $Z' = 1$.[179,180] The IR spectra of both polymorphs show prominent differences in the N-H stretching region (2800-3400 cm^{-1}) with **Fpm_O** showing a sharp peak at 3325 cm^{-1} and characteristic for all amide···amide (N-H···O=C) hydrogen bonded benzamides/pyridinecarboxamides, while **Fpm_N** has a diffuse pattern of N-H stretching bands indicative of N-H···N bonded benzamides/pyridinecarboxamides.

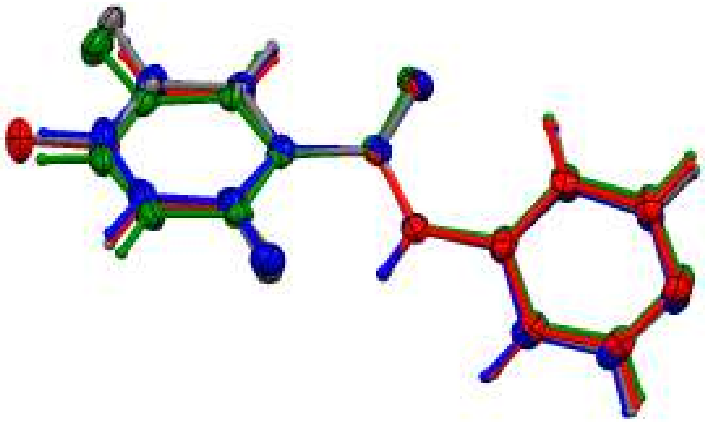

Fig. 14: An overlay of the **Fxp** isomorphous series with **25_F$_2$**

The IR spectrum of the bulk **Fpm** powder shows a diffuse peak pattern suggesting a prevalence of the **Fpm_N** polymorph. This polymorph seems to be preferred as the **Fpm_O** polymorph was isolated by chance. Crystals of the **Fpm_O** polymorph grow from CH_2Cl_2 have N-H···O=C primary hydrogen bonding as *C*(4) chains, while **Fpm_N** (from ethyl acetate) has intermolecular N-H···N interactions. It is rather unusual (though not unknown) that both polymorphs crystallise in the same space group and differing primarily in their main hydrogen bonding interactions.[181]

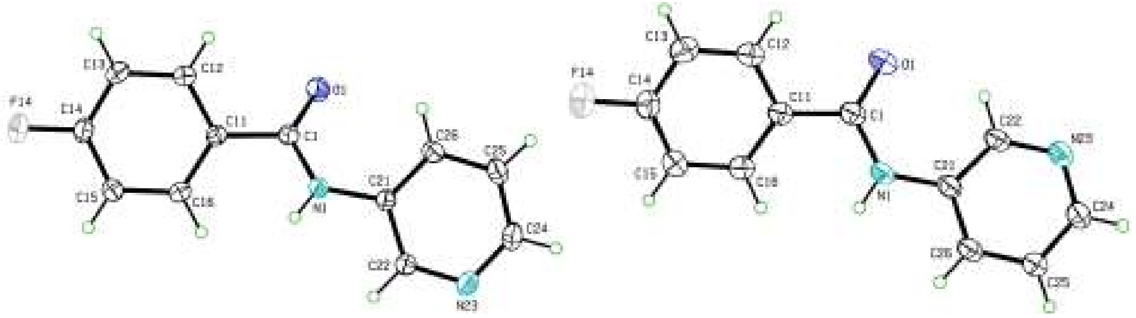

Figs. 15, 16: Views of **Fpm_O** and **Fpm_N**

The **Fxx** series with a strong N-H donor and two O=C/pyridine N acceptors offers the possibility of obtaining at least two different structures with either or both N-H···N/N-H···O=C interactions though in practice one type is clearly favoured for a particular **Fxx** isomer. In **Fpm_O** the N-H···O=C interaction (N1···O1$^{\boldsymbol{i}}$ = 3.0575(13) Å; ***i*** = x,y+1,z) links **Fpm** molecules into 1-D chains along the *b*-axis direction and parallel to the (101) plane. The remaining interactions are weak with 1-D chains (running anti-parallel) linked by C15-H15···N23 (C15···N23$^{\boldsymbol{ii}}$ = 3.5891(17) Å, ***ii*** = 1-x,1-y,-z) contacts into columns, with additional C14-F14···F14-C14$^{\boldsymbol{iii}}$ = 2.8982(18) Å, ***iii*** = 2-x,-y,-z) contacts. The pyridine **P**-ring conformation in **Fpm_O** is **P-*syn*** and the two aromatic rings are almost parallel though with the amide group twisted away from both rings (Table **13**). The **Fmp_O** molecular geometry (torsion angles) differs considerably from **Fmp_N** (Table **13**). However, the most significant bond length/angle difference is for C1-N1-C21 = 125.76(10)° in **Fpm_O** and 127.7(2)° in **Fpm_N**.

Aggregation in **Fpm_N** is principally by N1-H1···N23 interactions (N1···N23$^{\boldsymbol{i}}$ = 3.151(3) Å, ***i*** = -1/2+x,1/2-y,1/2+z) forming 1-D *zig-zag* chains along the *c*-axis direction and parallel to the (-101) plane. This primary N-H···N interaction is augmented by flanking C16-H16···N23$^{\boldsymbol{i}}$ and C26-H26···N23$^{\boldsymbol{i}}$ interactions {with C16/C26···N23$^{\boldsymbol{i}}$ = 3.403(3)/3.390(3) Å} and similar to the **NmpF** and **NmpM** structures (Sections 2.1 and 2.2). The 1-D chains are linked into 2-D sheets by weak C-H···F interactions (H24···F14^{ii} = 2.57 Å, C24···F14^{ii} = 3.107(3) Å, ***ii*** = 3/2-x,-1/2+y,1/2-z) along the [010] direction. There are no other direction specific interactions in **Fpm_N**.

The most striking difference between **Fmp_N** and **Fmp_O** is the **P-*anti*** conformation which is opposite to the **P-*syn*** in **Fmp_O**. This conformation change in the pyridine ring orientation is essential for intermolecular N-H···N hydrogen bonding in **Fmp_N**. The **Fpm_O** structure resembles the related methyl isomer derivative **Mpm** (Section 1.1). However, and in contrast to **Fpm_O**, the **Mpm** isomer crystallises in space group P1 with *Z′* = 4 and contains four distinct hydrogen bonded chains aggregating *via* N-H···O=C interactions.

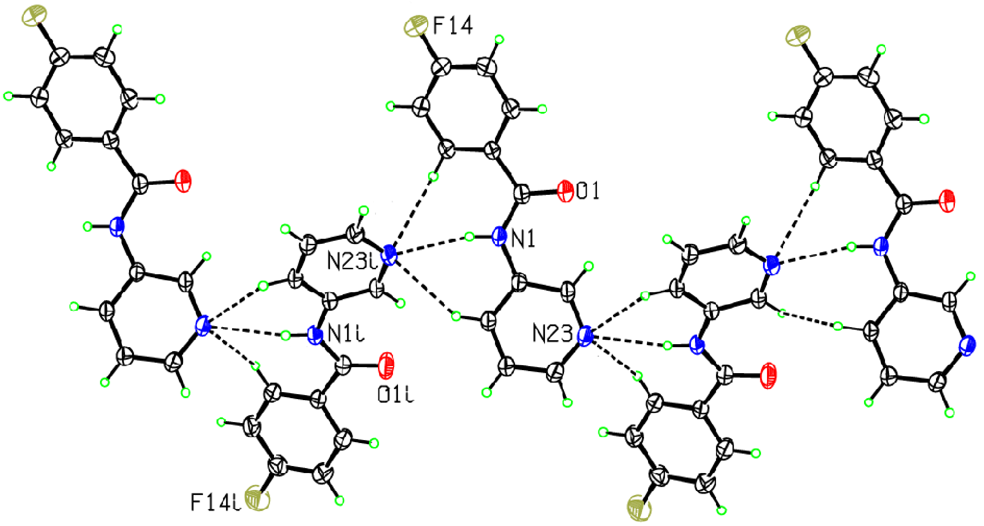

Fig. 17: Aggregation in **Fpm_N**

Fmm molecular and crystal structure

The **Fmm** isomer shows some similarities with **Fpm_N** in terms of aggregation and conformation. As in **Fmp_N**, the conformation of **Fmm** is **F-*anti***/**P-*anti*** and as noted above the **P-*anti*** conformation is crucial for formation of the $_{\text{amide}}$N-H···N$_{\text{pyridine}}$ hydrogen bond. The principal interaction in **Fmm** is N1-H1···N23^{i} (N1···N23^{i} = 3.077(3) Å, ***i*** = x+1/2,1-y,z) and augmented by a flanking C26-H26···N23^{i} (C26···N23 = 3.444(3) Å) interaction linking **Fmm** molecules into 1-D chains along the *a*-axis (100) direction. A secondary interaction involves π···π stacking (C26···C22^{ii} = 3.366(3) Å, ***ii*** = -1/2+x,1-y,z) along the *c*-axis direction weakly connecting the 1-D chains into 2-D sheets parallel to (010) plane. There are no other interactions in **Fmm**.

Fom polymorphs molecular and crystal structure

The **Fom** isomer was isolated as two polymorphs with **Fom_O** grown as poor quality single crystals from ethyl acetate (amongst other solvents and mixtures) after many attempts. A second polymorph, **Fom_F** crystallised subsequently as fine diffraction quality single crystals by very slow evaporation from MeOH in long tubes. The **Fom_O** polymorph crystallises in space group $P2_1$ ($Z' = 6$). The structure solves easily in $P2_1$ using default settings in common structure solution programs and even at this juncture it is obvious that there is considerable disorder in **Fom_O**. On refinement the **Fom_O** structure is revealed to be completely disordered with the six individual molecules having varying levels of disorder, from four molecules with a minor component (~10%) and two having complete 50% molecular disorder.

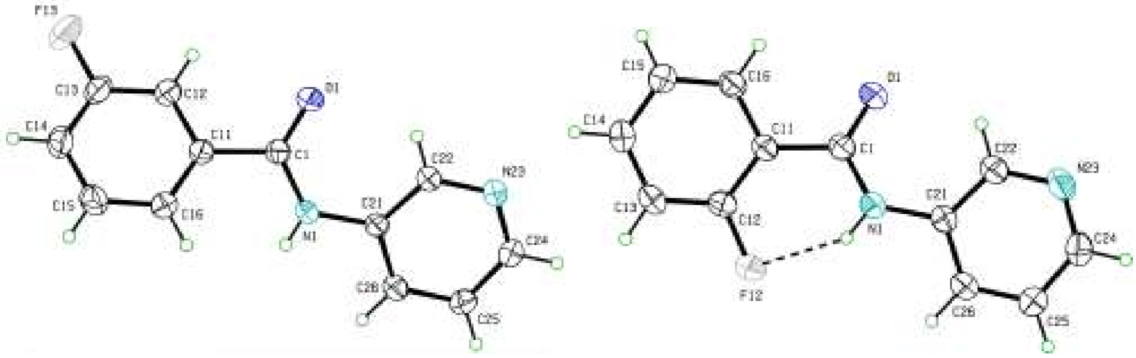

Figs. 18, 19: Views of **Fmm** and **Fom_F**

All six **Fom_O** molecules are **F-*syn*** as this facilitates the favourable intramolecular N-H···F_{ortho} interaction as noted in the ^{1}H NMR of related benzamides.[177] The N···F distances for (A) to (D) range from 2.722(5) to 2.753(6) Å. The *meta*-pyridine ring is mostly **P-*syn*** with evidence for the **P-*anti*** conformation in at least one of the 50:50 disordered molecules (F/H). The possibility of a second conformation of the pyridine ring in the crystal structure may be needed to effect a repeat unit on crystallisation but at the cost of a crystal structure with $Z' = 6$.

The primary interaction consists of six distinct N-H···O=C $C(4)$ chains of all six molecules in the *b*-axis direction. The intermolecular N···O distances range from 3.066(8) Å to 3.111(9) Å and C_6/C_5N interplanar angles range from 4.5(4)° to 9.1(4)° for (A) to (D). The four largely ordered molecules (A) to (D) stack in a column along the *a*-axis direction with the remaining two molecules as 50:50 disordered components (E/G) and (F/H) stacking as a column in the (100) direction adjacent to (A) to (D).

Alternating columns of (A) to (D) and (E/G), (F/H) are linked by weak interactions/contacts. The assembly of the structure is perplexing and our analysis suggests that the *ortho*-F atom plays a major role in the molecular conformation. The **Fom_O** crystal structure as a completely disordered system can be viewed as the kinetic product of imperfect crystallisation. **Fom_O** is worthy of a more detailed study over a range of temperatures.

A review of the CSD[8] for structures with $Z' = 6$ in space group $P2_1$ reveals 42 compounds of which bis[4-(dimethylamino)phenyl]diazene oxide [XIYZOV][182] is a representative planar molecule. It is described as a commensurate modulation of a $P2_1/c$ parent with ⅓ of the *b*-axis, and comprising two disordered molecules with an indication of disordered components in two of the remaining azoxybenzene molecules

The **Fom_F** polymorph crystallises in $P2_1/n$ and is isostructural with **Fpm_O** and has similar geometry features, but the conformation as (**F-*syn*/P-*anti***) is similar to **Fpm_N**. The primary **Fom_F** interaction is the long N-H···O=C hydrogen bond ($N1\cdots O1^{i}$ = 3.3322(17) Å, ***i*** = x+1,y,z) as *C*(4) chains linking molecules into 1-D chains along *a*-axis. Apart from the intramolecular $N\text{-}H\cdots F_{ortho}$ interaction, the N-H···O=C is the only intermolecular interaction of consequence in **Fom_F** apart from the repulsive $C16\text{-}H16\cdots H16\text{-}C16^{ii}$ interaction ($H16\cdots H16^{ii}$ = 2.33 Å) and a weak $C14\text{-}H14\cdots N23^{iii}$ interaction linking chains (***ii*** = -1-x,1-y,-z; ***iii*** = 1/2+x,1/2-y,1/2+z). Examination of both structures allows us to understand the difficulty **Fom** has in forming quality crystals.

1.2.6.4. Fxo isomer series

The **Fxo** triad form twisted dimers as $R^2_2(8)$ rings *via* cyclic $_{amide}N\text{-}H\cdots N_{pyridine}$ interactions denoted by $(N\text{-}H\cdots N)_2$. Formation of dimers with the pyridine N atom located *ortho* (a mandatory **P-*syn*** conformation) has already been discussed in the related **Mxo** isomers (Section 1.1). In these **Mxo** isomers the central hydrogen bonded $R^2_2(8)$ ring is essentially planar while the **Fxo** dimers as twisted dimers have interplanar C_5N/C_5N or [NCNH/NCNH] angles of 39.12(4)°, [34.63(15)°] in **Fpo**, 43.66(7)°, [30.9(16)°] in **Fmo**, and 22.18(5)°, [21.6(6)°] in **Foo**. In the **Fxo** triad (on dimer formation) the N-H and pyridine N are excluded from further intermolecular interactions and the three crystal structures rely on weaker C-H···O/F/π or π···π secondary interactions.

Fpo molecular and crystal structure

Fpo (Fig. **20**) crystallises as a hydrogen bonded $R^2_2(8)$ dimer *via* N1-H1···N22 interactions (N1···N22^{i} = 3.0608(18) Å, ***i*** = -x,y,1/2-z) but in tandem with a C16···C23^{i} = 3.285(2) Å contact. Pairs of dimers are connected into tetramers by C16-H16···O1 interactions (C16···O1^{ii} = 3.266(2) Å, ***ii*** = x,1-y,1/2+z) and enhanced by a C15-H15···C12 contact. Tetramers are linked into a 1-D column by C25-H25···O1^{iii} (***iii*** = -x,y,3/2-z) interactions along the *c*-axis direction. The weak C12-H12···F14^{iv} (***iv*** = 1/2+x,-1/2+y,1/2-z) interaction alternatively interconnects 1-D columns into a 3-D structure.

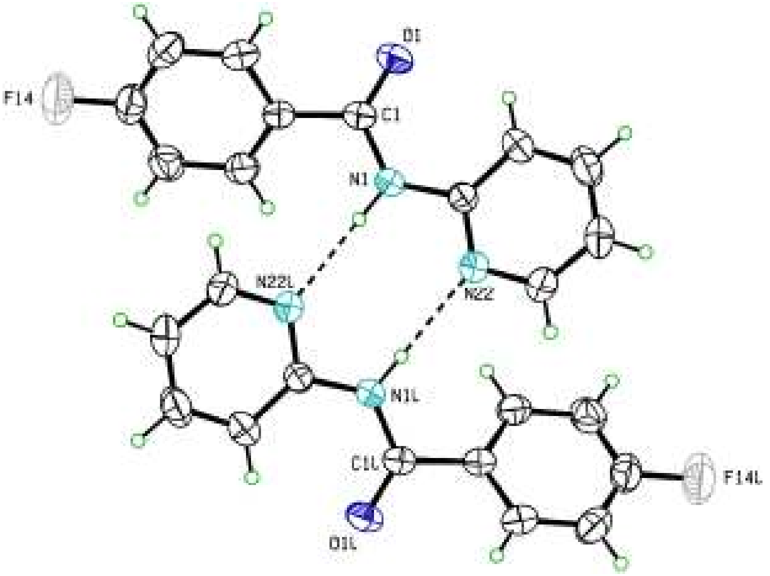

Fig. 20: A view of the **Fpo** hydrogen bonded dimer

Fmo molecular and crystal structure

Fmo (Fig. **21**) forms a twisted dimer through two distinct N1-H1···N22 interactions [N1A···N22B = 3.0721(17) Å and N1B···N22A = 3.0502(18) Å] as the two **Fmo** molecules (A/B) are not identical (*Z′* = 2). Therefore all three major torsion angles differ as well as the C_6/C_5N interplanar angles (Table **13**).

Dimer formation also occurs with additional $C16_{A/B}\cdots C23_{B/A}$ contacts [both contacts = 3.237(2) Å]. Dimers are linked into tetramers by two weak C-H···O contacts (C16A-H16A···O1B^{ii}, C15B-H15B···O1A^{iii}; ***ii*** = 1-x,1-y,1-z, ***iii*** = 1-x,2-y,1-z). Tetramers are interconnected into a 1-D column by stronger C25A-H25A···O1B [C25A···O1B^{i} = 3.235(2) Å, ***i*** = x,1+y,z] interactions in the *b*-axis direction. Columns are further linked into a 2-D sheet parallel to the [10-1] plane by double π···π stacking

(C13A···C15A^{iv}, ***iv*** = -x,1-y,-z) and C14B···C14B^{v} (***v*** = 2-x,2-y,2-z) contacts. It is unusual that the fluorine atoms F13A/B (**F-*anti***) do not play a significant role in the **Fmo** crystal structure apart from influencing π···π stacking interactions.

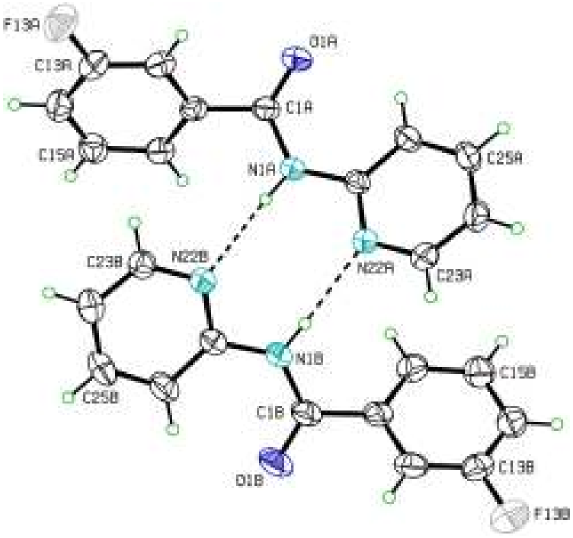

Fig. 21: A view of the **Fmo** hydrogen bonded dimer

Foo molecular and crystal structure

The **Foo** crystal structure (Fig. **22**) assembles in a similar fashion to **Fmo** at the primary level (with $Z' = 2$). The interplanar angle between the two pyridinyl rings C_5N_A/C_5N_B) is 22.18(5)º; the smallest among the **Fxo** dimers.

The **Fo** rings are oriented as **F-*syn*** allowing the formation of three contacts as N1-H1B···F12B [N1B···F12B = 2.7981(15) Å] and C23-H23···π(C11,…,C16) with H23A···Cg1$_B$ = 2.82 Å, C23A-H23A···Cg1$_B$ = 138°, while H23B···Cg1$_A$ = 2.70 Å, C23B-H23B···Cg1$_A$ = 149° and stabilising the dimeric unit. In **Foo** these C23-H23$_{A/B}$···π(arene)$_{B/A}$ interactions are similar though not as significant as the analogous C-H···π(arene) interactions described in **Moo** (Section 1.1). Dimers aggregate into tetramers by two π···π contacts with C21A···C24B^{i} = 3.257(2) Å, (***i*** = -x,-y,2-z) and C24B-H24B···π(C21A,…,C26A)^{i}. These are interconnected along the *b*-axis into a 1-D column by weak C-H···O contacts (H25B···O1A^{ii} = 2.62 Å, ***ii*** = x,-1+y,z) and (C26A···O1A^{iii} = 3.225(2) Å, ***iii*** = -x,1-y,2-z). Further aggregation is accomplished *via* weak contacts. In **Foo** the **Fo** rings have interplanar angles of 69.56(5)º and as both are **F-*syn*** the F12A···F12B atoms are separated by a distance of 4.7995(15) Å.

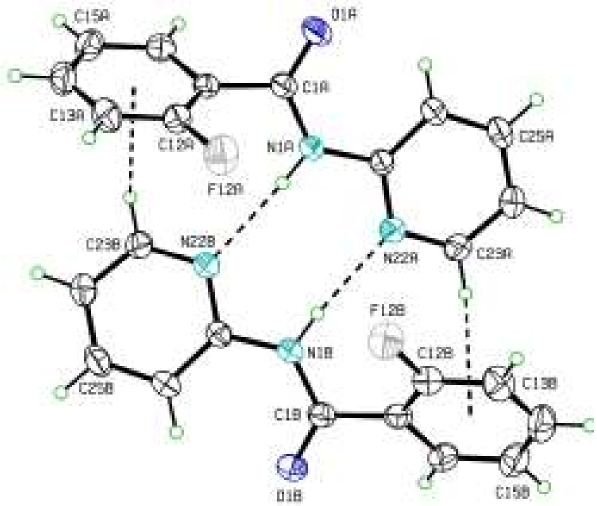

Fig. 22: A view of the **Foo** hydrogen bonded dimers.

1.2.7. *Ab initio* calculations

1.2.7.1. Structure optimisation results

The main geometric parameters of the **Fxx** isomers (optimised in the *gas phase* with different basis sets), for torsion angles C12-C11-C1=O1 (α), C1-N1-C21-C26 (β) and O1-C1-N1-C21 (δ) are presented in the Table **14.** Torsion angles (α, β and δ) of the *gas phase* and solvated forms (CH_2Cl_2, H_2O) obtained with implicit solvation model PCM-SMD and B3LYP/6-311++G** basis set are listed in Table **15**.

In general when examining geometry, the *relative* and *absolute* benzamide geometry should be differentiated depending on whether the (***syn***-/***anti***-) conformation is neglected or endorsed. If the conformation is taken into account then the given geometrical parameter values (torsion angles) are regarded as absolute geometry. In the reverse case, if conformation is neglected then the relative values of the geometry are provided, in order to give emphasise the relative molecular shape and for comparisons with other isomers having different conformations.

For **Fxx**, the additional polarisation function (6-311++G**) does not yield a significant change in the relative geometric parameters in *gas phase* as compared to the standard (6-311++G) basis set (ESI I, Section 3.2.). The most significant change is for the β and δ angles (Table **14**). However, the polarisation function changes the preferred conformation of the **Fm** ring making the **F-*anti*** slightly preferable to **F-*syn***. Alternatively the exclusion of diffuse functions (from the standard set but with added polarisation functions as 6-311G**) slightly changes the α dihedral angle (**F**-ring). Analysis of the **Fxx** isomers reveals the 6-311++G** basis set to be optimal in terms of time and computational expense and does not significantly influence relative geometry (apart from the **Fm** ring).

The most prominent feature of the modelled **Fxx** isomers is the planarity of the **Fox** triad. Optimisation of the **Fox** isomers suggests the existence of intramolecular hydrogen bonding between *ortho*-fluorine and amide group (as N-H···F) regardless of the basis set. The N-H···F interaction (according to models) is responsible for the **Fox** triad planarity. Optimisation (using the solvation model) shows that the **Fox** triad are less planar in low polar solvents (CH_2Cl_2, $CDCl_3$), while in highly polar solvents (H_2O, DMSO) the N-H···F interaction may distort from planarity (**Fom**/**Foo**: α = -7.14±0.73°; β = -4.22±0.36°; δ = -0.26±0.60°).

Table 14: Torsion angles (°) of **Fxx** isomers[a] optimised with different basis sets

	6-311++G**			6-311++G			6-311G**		
	α	β	δ	α	β	δ	α	β	δ
Fpp	-24.45	-5.33	-3.10	-25.75	-3.74	-4.69	-22.27	-4.24	-2.87
Fmp	-24.95	-4.70	-2.85	151.63	-3.69	-4.24	-23.52	-4.24	-2.37
Fop	-0.03	0.01	0.03	0.00	0.00	0.00	0.00	0.00	0.00
Fpm	-24.27	-5.67	-2.51	-25.54	-3.45	-4.30	-22.07	-4.14	-2.34
Fmm	-24.62	-4.79	-2.29	151.90	-3.68	-3.84	-23.20	-4.15	-1.84
Fom	0.01	0.00	-0.02	-0.05	0.02	-0.02	0.02	0.01	-0.03
Fpo	-21.73	-3.44	-2.66	-22.36	-2.06	-3.86	-19.05	-3.68	-2.10
Fmo	-22.08	-2.96	-2.55	-21.95	-1.75	-3.68	-19.69	-3.34	-2.09
Foo	-0.01	0.00	0.00	-0.02	-0.02	0.04	-0.01	0.00	0.00

[a] The angle C12-C11-C1=O1 (**F**-ring) is α; angle C1-N1-C21-C26 angle (**P**-ring) is β and O1-C1-N1-C21 angle (amide linkage) is δ.

Table 15. Torsion angles (°) of optimised **Fxx** isomers[a]

	optimised in *gas phase*			optimised in CH_2Cl_2			optimised in H_2O		
	α	β	δ	α	β	δ	α	β	δ
Fpp	-24.45	-5.33	-3.10	-25.49	-6.72	-3.14	-26.21	-12.01	-3.10
Fmp	-24.95	-4.70	-2.85	-24.78	-4.47	-2.93	-24.43	-6.72	-3.40
Fop	-0.03	0.01	0.03	0.01	0.00	0.00	-0.01	0.00	0.00
Fpm	-24.27	-5.67	-2.51	-25.36	-7.76	-2.71	-25.52	-16.41	-2.10
Fmm	-24.62	-4.79	-2.29	-24.62	-5.38	-2.43	-23.91	-12.62	-1.64
Fom	0.01	0.00	-0.02	-0.05	0.00	0.00	-6.62	-4.48	-0.68
Fpo	-21.73	-3.44	-2.66	-25.54	-7.43	-2.10	-25.08	-6.11	-3.06
Fmo	-22.08	-2.96	-2.55	-24.27	-3.76	-2.17	-24.16	-5.63	-3.66
Foo	-0.01	0.00	0.00	-7.51	0.79	0.48	-7.65	-3.96	0.16

[a] The angle C12-C11-C1=O1 (**F**-ring) is α; angle C1-N1-C21-C26 angle (**P**-ring) is β and O1-C1-N1-C21 angle (amide linkage) is δ. All geometries are based on B3LYP/6-311++G** optimisation with PCM-SMD solvation model.

The hypotheses (from calculations) are shown by ^{1}H NMR ($CDCl_3$; DMSO) that the N-H···F interaction and **Fox** triad planarity exists in low polarity solvents but can be disrupted in highly polar solvents.

The remaining **Fpx/Fmx** isomers optimised in *gas phase* have relatively uniform geometries with the **F**-ring rotated (α = -23.68±1.40º), **P**-ring slightly rotated (β = -4.48±1.06º) and planar amide dihedral angle (δ = -2.66±0.28º). The **Fpx/Fmx** isomers optimised in CH_2Cl_2 agree (α = -25.01±0.52º; β = -5.92±1.64º; δ = -2.58±0.42º) but in H_2O the **F**-ring and amide dihedral angle are similar for *gas phase* and CH_2Cl_2 (α = -24.88±0.88º, δ = -2.83±0.79º), however the **P**-ring differs. In **Fpp**, **Fpm** and **Fmm** the **P**-ring exhibits increased rotation (β = -13.68±2.38º) while for **Fmp**, **Fpo** and **Fmo** it is similar in CH_2Cl_2 (β = -6.15±0.55º). A similar increased rotation under the influence of a high dielectric field was noted for **Mxx** (Section 1.1).

1.2.7.2. **Conformational analysis**

Fig. **23** shows nine PES diagrams for conformational analyses of the **Fxx** isomers (in *gas phase* with 6-311++G** basis set). High resolution PES diagrams are provided in the ESI I (Section 3.2.2). The **F-ring** (α dihedral angle) is depicted as a **blue dashed line**, whereas the **P-ring** (β dihedral angle) is a **full red line**. At θ = 0 and ±180º, the conformation of the asymmetric **F**- or **P**-ring is noted as ***syn*** or ***anti***.

The **Fxx** and **Mxx** isomer girds are congeneric derivatives of the same *N*-pyridinylbenzamide template (Scheme **5**). Comparisons of the **Fxx** and **Mxx** PES diagrams (Section 1.1) reveal a high degree of similarity and especially for **Fpx** and **Fmx** triads. As expected and due to the modelled **Fox** triad planarity, the **Fo** rings in **Fox** isomers have symmetrical PES profiles and very different to the **Mo** ring (**Mxx**), but similar to the PES profile of the **oF** ring in the **NxoF** isomers (Section 2.1). As in all related isomer grids the modularity of the **Fxx** isomers allows a modular approach in the analysis and classification of the PES profiles depending on substituent position (*para*-/*meta*-/*ortho*-), and for direct comparison with **Mxx** (Section 1.1).

The asymmetric **Fxx** isomers (having at least one non-*para* ring) show a preference for the **F-*syn*/P-*syn*** conformation, except for **Fmx** where the **F-*anti*** conformation is found to be slightly more stable. The *para*-fluorophenyl (**Fp**) ring gives a PES profile with two global maxima located *ca*. -65° and 120° (TS_{Fp}^{II}[**Fpp/m**] = 13.61±0.03 kJ.mol^{-1}, TS_{Fp}^{II}[**Fpo**] = 15.01 kJ.mol^{-1}), two local maxima *ca*. 25° and -155° (TS_{Fp}^{I}[**Fpp/m**] = 1.73±0.03 kJ.mol$^{-1,}$ TS_{Fp}^{I}[**Fpo**] = 0.94 kJ.mol^{-1}). The four global minima are near 0°, 55°, ±180° and -130°.

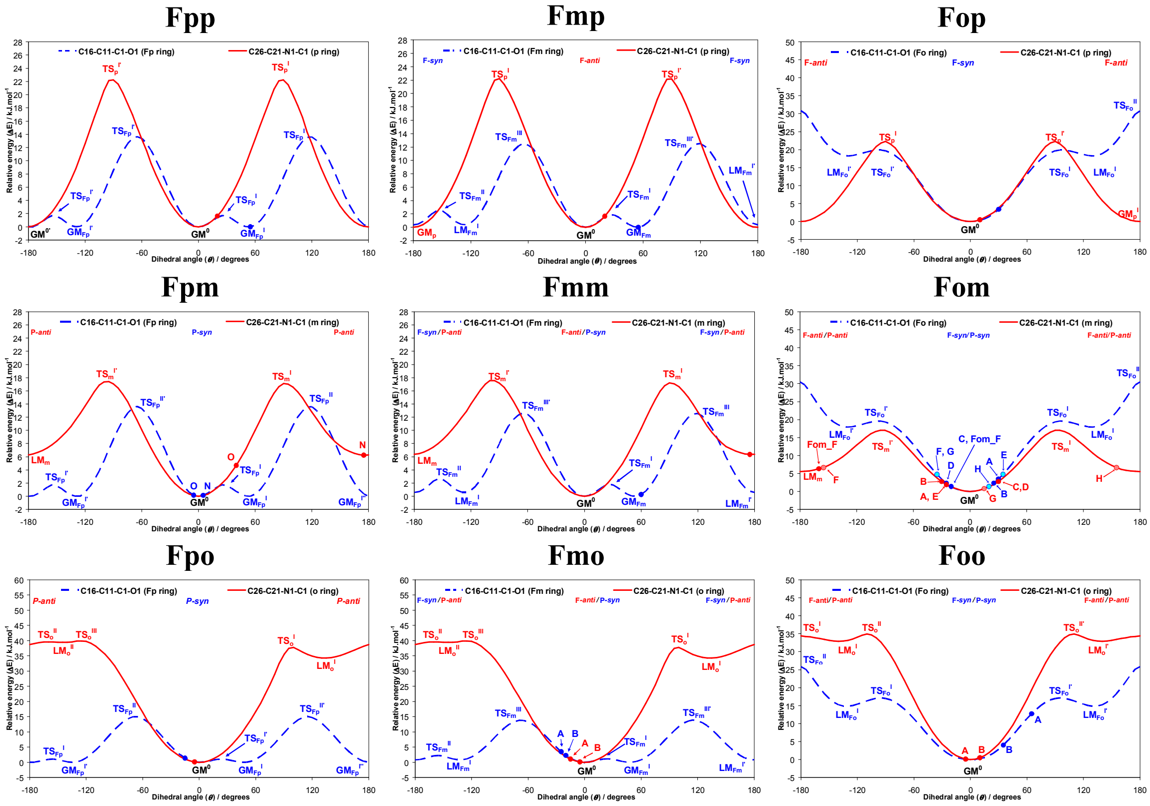

Fig. 23: The PES conformational analysis for the nine **Fxx** isomers optimised in *gas phase*: the equivalent solid state angle is depicted as a (•), with, if applicable, assigned identification letter and/or polymorph designation.

The *meta*-fluorophenyl (**Fm**) ring has two global minima (**F-*anti*** conformation) *ca*. 55° and 0°, two global maxima at *ca*. -65° and 120° (TS_{Fm}^{III} = 13.00±0.66 kJ.mol^{-1}), two local minima (**F-*syn*** conformation) *ca*. -130° and ±180° with increases of (LM_{Fm}[**Fmp**] = 0.37 kJ.mol^{-1} to LM_{Fm}[**Fmo**] = 0.83 kJ.mol^{-1}**)**. The two local maxima are at -155° (TS_{Fm}^{II} = 2.46±0.17 kJ.mol^{-1}) and 25° (TS_{Fm}^{I}[**Fmp/m**] = 1.83 kJ.mol^{-1}, TS_{Fm}^{I}[**Fmo**] = 1.14 kJ.mol^{-1}). As expected, the difference between the two conformations is small (~0.6 kJ.mol^{-1}) and from Boltzmann distribution (Fig. **1**) at ambient temperatures, *ca*. 57% of molecules have the thermodynamically preferred **F-*syn*** conformation. In reality, a kinetic equilibrium between the **F-*syn***/**F-*anti*** conformations exists. Although the **Fmp** and **Fmm** isomers optimised with the 6-311++G basis set have **Fm** rings as **F-*syn***, their PES scans overwhelmingly correspond with those obtained with the polarisation function (ESI I, Section 3.2.2). Conformational analyses with the 6-311++G basis set reveal that the **Fm** ring difference between the **F-*syn*** and **F-*anti*** conformation is even smaller (~0.1 kJ.mol^{-1}), suggesting, in this specific case, the dependence of the optimised model and conformation on a particular basis set and function choice, together with the existence of **F-*syn***/**F-*anti*** equivalence. Alternatively, optimisation and conformational analyses with the 6-311G** basis set shows a preference for **F-*anti*** in the **Fm** ring for all **Fmx** isomers.

The *ortho*-fluorophenyl (**Fo**) ring has a symmetric PES profile with one global maximum at ±180° ($\mathrm{TS_{Fo}^{II}}$[**Fop/Fom**] = 30.65±0.23 kJ.mol^{-1}, $\mathrm{TS_{Fo}^{II}}$[**Foo**] = 25.82 kJ.mol^{-1}), two local maxima at ±95° ($\mathrm{TS_{Fo}^{I}}$[**Fom/Fom**] = 19.73±0.17 kJ.mol^{-1}, $\mathrm{TS_{Fo}^{I}}$[**Foo**] = 17.16 kJ.mol^{-1}), two local minima at ±130° ($\mathrm{LM_{Fo}^{I}}$[**Fop/Fom**] = 18.07±0.19 kJ.mol^{-1}, $\mathrm{LM_{Fo}^{I}}$[**Foo**] = 14.83 kJ.mol^{-1}) and one global minimum at 0°.

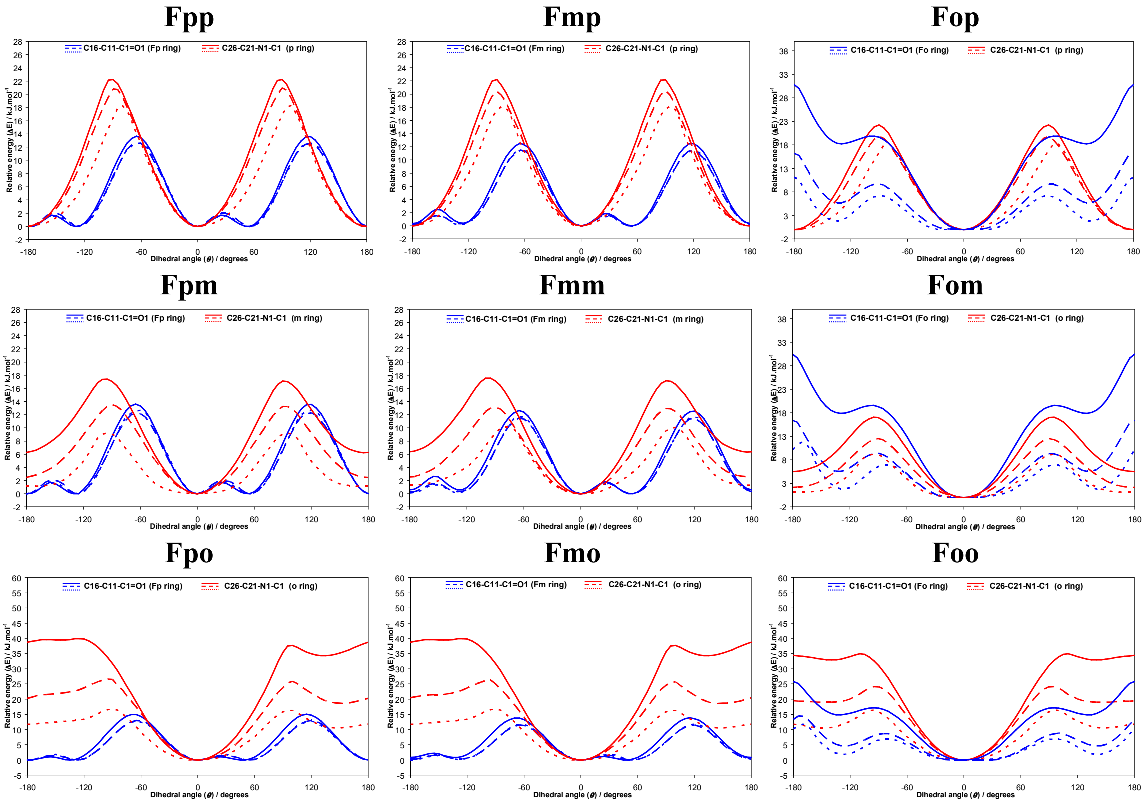
Fpp Fmp Fop
Fpm Fmm Fom
Fpo Fmo Foo

Fig. 24: The PES conformational analysis diagrams for the nine **Fxx** isomers optimised in *gas phase* (full line), CH_2Cl_2 (dashed line) and in H_2O (dotted line) using the PCM-SMD solvation method.

The **Fox** triad optimisation gives planar models regardless of the basis set and provides evidence for a 6-membered ring formed *via* N-H···F interactions. In **NooF**, a similar 5-membered ring and with a symmetrical **oF** ring PES profile has been noted (Section 2.1). In comparison to **NooF**, it was expected that the 6-membered ring in **Fox** with a better oriented donor/acceptor would provide stronger hydrogen bonding. However, a comparison of the **Fo** and **oF** PES diagrams (using the 6-311++G basis set) shows that TS_{oF}^{I} in **NooF** and TS_{Fo}^{I} in **Fox** are equal (~25.25 kJ.mol^{-1}) suggesting similar N-H···F hydrogen bonding strength.

Conformational analyses of the pyridinyl rings show similar results to the **Mxx** series. The *para*-pyridinyl ring (**p**) has two global maxima at *ca.* ±90° (TS_{p}^{I} = 22.23±0.04 kJ.mol^{-1}) and two global minima at 0° and ±180°. The *meta*-pyridinyl ring (**m**) has two global maxima *ca.* ±95° (TS_{m}^{I}=17.21±0.22 kJ.mol^{-1}), one global minimum at 0° (**P-*syn*** conformation) and one local minimum at ±180° (**P-*anti*** conformation) with a difference of ~6 kJ.mol^{-1} between the two conformers. The conformer preference is not altered by excluding the polarisation or diffuse functions from the basis set (6-311++G**) (ESI I, Section 3.2). Rotation of the *ortho*-pyridyl (**o**) rings in **Fpo** and **Fmo** give asymmetrical PES profiles, while in **Foo** isomer the PES profile of the **Fo** ring is symmetrical. In **Fpo** and **Fmo** one global maximum (**P-*syn*** conformation) is located at *ca.* -125° (TS_{o}^{III}= 39.86 kJ.mol^{-1}), two local maxima at *ca.* 100° (TS_{o}^{I}= 37.73 kJ.mol^{-1}) and *ca.* -160° (TS_{o}^{II} = 39.58 kJ.mol^{-1}), two local minimum at *ca.* 135° (LM_{o}^{I} = 34.26 kJ.mol^{-1}) and *ca.* -145° (LM_{o}^{II} = 39.44 kJ.mol^{-1}) and global minimum at 0°. However, in the symmetrical **Foo** there is two global maxima at ±110º (TS_{o}^{II}[**Foo**] = 34.95 kJ.mol^{-1}), one local maximum at ±180º (TS_{o}^{I}[**Foo**] = 34.39 kJ.mol^{-1}), two local minima at ±140º (LM_{o} = 32.89 kJ.mol^{-1}) and one global minimum (**P-*syn*** conformation) at 0°.

Conformational analyses without the polarisation (**/d,p) or diffuse (++) functions (ESI I, Section 3.2) generally give analogous PES diagrams with an increase of the main rotational barriers and energies at conformational states that are far from stable. The PES scan without polarisation function (as 6-311++G) gives, in general, higher rotational barriers, except for the **p** ring where a decrease arises. These changes are insignificant in **Fp** (~6%), **Fm** (~11%), **p** (~-4%) and **m** rings (~2%), while in the **Fo** (~37%) and **o** (~16%) rings the rotational barrier increase is more pronounced with a slight change in the PES curve shape. This reflects the polarisation influence on the interactions of electronegative atoms (F) and protons in molecules, as well as on intramolecular interactions (N-H···F). In contrast, conformational analyses without the diffuse function (as 6-311G**) substantially increases the main rotational barriers but the pattern is opposite to the 6-311++G basis set. This increase is relatively high in the **Fp** (~20%), **Fm** (~20%), **p** (~16%) and **m** (~20%) rings but weaker in the **Fo** (~16%) and **o** (~8%) rings suggesting the importance of the diffuse function in energy estimation in transition states of these molecular systems. As there is no conformational change (***syn***/***anti***) in any ring with the 6-311G** basis set it may be concluded that polarisation functions represent an important auxiliary addition for model stability if flexibility and conformational change are important.

The main feature of the **Fx** ring PES in different solvents (Fig. **24**) compared with *gas phase* is the uneven difference in the decrease/increase of the rotational barriers and local minima throughout the **Fxx** series as noted in the **Mxx** isomers In the PES of solvated **Fx** rings, the isomers can be divided in three main groups: **Fpp**/**m**, **Fmp**/**m**, **Fox**, while in **Fpo** and **Fmo** the influence of solvation is more pronounced. However, it is obvious that the influence of solvents is minor in the **Fp** and **Fm** rings (especially in **Fpp**/**m** and **Fmp**/**m**) while in **Fo** a strong decrease is present.

In **Fpp**/**m**, where the influence of the solvation model is minor (Fig. **24**), the main rotational barrier TS_{Fp}^{II} decreases by ~9% in CH_2Cl_2 (~7% in H_2O). In contrast the TS_{Fp}^{I} increases by ~14% in CH_2Cl_2 (decrease by ~7% in H_2O). This phenomenon noted in **Mxx** can be explained partially by the fact that the TS_{Fp}^{I} has molecules in a planar conformation and a higher dielectric field can destabilise this conformation.

The PES behaviour of the **Fm** ring in the **Fmp**/**m** isomers is slightly different to **Fp** with a similar small drop in the main rotational barrier TS_{Fm}^{III}. Regardless, there is a significant decrease of LM_{Fm} and TS_{Fm}^{II} that effectively equalises the **F-*syn*** and **F-*anti*** conformations and especially in a high dielectric solvent: the **F-*syn***/**F-*anti*** difference for all **Fmx** isomers solvated in CH_2Cl_2 is 0.38 $kJ.mol^{-1}$ (0.16 $kJ.mol^{-1}$ in H_2O). In **Fpo** and **Fmo** a decrease at TS_{Fm}^{III} is more pronounced (~16%) as well as the increase at $TS_{Fm}^{I/II}$ (~36% in CH_2Cl_2, ~65% in H_2O).

For the **Fo** ring, the behaviour in solvents (Fig. **24**) is even for all three **Fox** isomers with a strong decrease of the rotational barriers. These results reflect the influence of the dielectric field in impeding the internal interactions (N-H···F) whereas spectroscopic data support the existence of hydrogen bond obstruction in polar solvents (^{1}H-NMR in DMSO-*d₆* *vs.* $CDCl_3$, Appendix I, Section 1.2).

Conformational analyses of the pyridinyl rings with the solvation model (Fig. **24**) show significant decreases of rotational barriers and local minima in both solvents. In the *para*-pyridinyl ring (**p**) the rotational barrier TS_p decreases by 8% in CH_2Cl_2 (18% in H_2O), while the *meta*-pyridinyl ring decrease of the TS_m rotational barrier is 25% (45%). The significant result is that the LM_m decreases by 60% in CH_2Cl_2 (80% in H_2O). According to the Boltzmann distribution it signifies (at ambient temperature in polar solvents such as water, DMSO or methanol) that ~38% of all **Fxm** molecules are predicted to have their **m** rings as **P-*anti***, while in less polar solvents (CH_2Cl_2, EtOAc) some ~25% of all **Fxm** molecules are **P-*anti***. Finally, the rotational barriers of the *ortho*-pyridine rings (**o**) evenly decrease by ~40% in CH_2Cl_2 and ~63% in H_2O.

1.2.7.3. **Energy results**

The energy calculation results (CBS-QB3) (Table **16**) comprise the electronic energies (δE_{SCF}) and Gibbs free energies (δG) in all three media, including ΔG_{solv} (for CH_2Cl_2 and H_2O) and $\Delta\Delta G_{solv}$ (CH_2Cl_2 *vs*. H_2O). The differences among each molecule are presented as δE_{SCF} (δG) and the differences between media as ΔE_{SCF} (ΔG). The **Fmm** (**Fpm**) absolute energies values were used as reference points for the *gas phase* and **Fom** values for solvents. Detailed results including absolute values for E_{SCF} and G, zero point energies and thermal energies are provided in the ESI I (Section 3.2.1). The energy results show that generally the most stable compounds are **Fxo**, similarly to the **Mxx** isomer grid where **Mxo** compounds were the most stable. The **Fxo** compounds have at least 20 kJ.mol^{-1} lower energies in *gas phase* that the remaining isomers. The strong stabilisation comes from N atom moving into *ortho* position. This causes delocalisation across both the *ortho*-pyridine ring and the amide linkage group, and, as seen in the modelled as well as solid state structures of the **Fxo** and **Mxo** compounds, consequent co-planarity of the *ortho*-pyridine ring and the amide linkage group.

Table 16: The energy calculation results[a] for **Fxx** in kJ.mol^{-1}

	gas phase		CH_2Cl_2		H_2O		*gas phase*→ CH_2Cl_2		*gas phase*→ H_2O		H_2O → CH_2Cl_2	
	δE_{SCF}	δG	δE_{SCF}	δG	δE_{SCF}	δG	ΔE_{SCF}	ΔG_{solv}	ΔE_{SCF}	ΔG_{solv}	$\Delta\Delta E_{SCF}$	$\Delta\Delta G_{solv}$
Fpp	-14.18	-3.70	-26.35	-11.14	-28.89	-17.02	-72.97	-63.81	-59.25	-47.66	-13.72	-16.15
Fmp	-10.84	-3.77	-22.38	-12.92	-25.31	-16.35	-72.34	-65.52	-59.01	-46.92	-13.33	-18.60
Fop	-11.36	-5.37	-13.56	-0.92	-13.58	-3.10	-63.00	-51.92	-46.75	-32.07	-16.24	-19.85
Fpm	-3.12	0.00	-12.17	-5.22	-14.67	-11.06	-69.85	-61.59	-56.09	-45.40	-13.76	-16.19
Fmm	0.00	-0.22	-8.51	-7.48	-11.57	-9.45	-69.31	-63.63	-56.10	-43.58	-13.21	-20.05
Fom	-0.35	-1.74	0.00	0.00	0.00	0.00	-60.45	-54.63	-44.19	-32.60	-16.26	-22.03
Fpo	-38.81	-26.44	-43.50	-29.50	-38.19	-27.11	-65.48	-59.43	-43.91	-35.01	-21.57	-24.42
Fmo	-35.44	-26.49	-39.56	-31.34	-34.38	-26.80	-64.91	-61.22	-43.47	-34.65	-21.45	-26.57
Foo	-32.36	-24.26	-30.25	-20.24	-22.98	-15.18	-58.69	-52.35	-35.16	-25.26	-23.53	-27.10

[a] Only the differences between each molecule (δ) and media (Δ, ΔΔ) are shown, **Fmm** (**Fpm**) is the reference molecule for the *gas phase* [E_{SCF}(**Fmm**)= -743.1048 E_h, G(**Fpm**)= -746.1007 E_h] and for solvents **Fom** was taken (CH_2Cl_2: E_{SCF}= -743.1279 E_h, G= -746.1632 E_h; H_2O: E_{SCF}= -743.1218 E_h, G= -746.1548 E_h). Full data including zero-point energies (E_0) and thermal energies (E) are provided in the ESI, Section 3.2.

The least stable triad is **Fxm**. In the **Mxx** isomer grid the most unstable isomer was **Mom**. However, due to the additional stabilisation from the intermolecular N-H···F hydrogen bond the most unstable isomer in *gas phase* is not **Fom** but **Fmm**. The hydrogen bonding is hampered in the solvated form and therefore, **Fom** is the most unstable isomer in solvent. The theoretical values of ΔG_{solv} in CH_2Cl_2 and H_2O, including theoretical $\log K_{D/W}$ (ESI I, Section 3.2.1) are consistent with experimental observations and with no unexpected values. The **Fxo** series are expected to be the least soluble in water.

1.2.8. Comparisons of the solid state and modelling data

Comparison of the **Fxx** isomer structures from crystal structure data and calculations is shown by difference marks (●), marking the torsion angle differences ($\Delta\theta$) between the experimental and theoretical structures on the corresponding *gas phase* PES diagram curves (Fig. **23**). For structures with $Z' > 1$ (**Fom_O**, **Fmo**, **Foo**) the data from each molecule is labelled with corresponding capitals. The data for particular polymorphs are labelled as **O**, **N (Fpm)** and **Fom_F**. For the **Fom_O** polymorph only the angles of the main components are assigned labels.

In general, most of the crystal structure conformations and dihedral angles correlate well with their modelled equivalents and especially **Fxp** and **Fxo** where the average deviation from the nearest global minimum (GM) is 11 to 24° for both rings.

The **Fxp** isomers are isomorphous and their solid-state geometries are almost identical with minor differences. However, while the **Fpp** and **Fmp** have difference spots (•) on similar positions close to the global minima, in **Fop** the dots are shifted as the modelled **Fop** structure is supposed to be planar, and different from **Fpp** and **Fmp**. **Fop** in the solid state adopts a similar geometry to **Fpp** and **Fmp**, and partially retaining the N1-H1···F12 hydrogen bond. The **F**-ring rotation from planarity is necessary in order to facilitate N1-H1···N24 hydrogen bonding. In contrast, **Fpp** and **Fmp** at their global minima are in an almost ideal position for crystal structure formation. Crystal growth of the **Fxp** triad was easy in most organic solvents and their high melting point ranges reflect the stability and strength of the **Fxp** crystal structures. Their physical behaviour might be influenced by similarities between the geometry of the optimised models and solid state structures.

The **Fxm** triad (comprising all polymorphs) reveals some interesting features. One key feature is the frequent occurrence of the *meta*-stable **P-*anti*** conformation (in

Fpm_N, **Fmm** and **Fom**). This result is in accordance with similar structures (**Mom**, **Mmm**) that have their *meta*-pyridine rings in a **P-*anti*** conformation. It is clear that the **P-*anti*** conformation is favourable for the formation of the primary intermolecular N-H···N hydrogen bonds as it positions the pyridine N atom and the amide N-H into opposite orientations suitable for molecular aggregation into 1-D N-H···N *zig-zag* chains.

Fpm_O has the same conformation **P-*syn*** as the optimised structure with the **P**-ring slightly rotated towards co-planarity with the **Fp** ring. The stable **P-*syn*** conformation arranges molecules in the correct conformation for N-H···O=C hydrogen bond formation. Co-planar rings can form additional contacts between the 1-D chains. The more common **Fpm_N** polymorph has the **P**-ring as **P-*anti*** which is suitable for N-H···N interactions. Of note is that the energy levels of the **P**-rings are similar for both polymorphs while their **F**-rings are located at the global minimum (GM).

As expected, **Fmm** is **F-*anti***/**P-*anti*** and almost strictly lying in global/local minima without significant deviations from the stationary points. The same conformation is present in the **Mmm** isomer, both of the *meta*-pyridinyl and *meta*-substituted phenyl rings (regardless of the nature of substituents) prefer the ***anti*** conformation in combination with N-H···N primary interactions.

The **Fom** isomer is isolated as two polymorphs, the disordered **Fom_O** and ordered **Fom_F**. The **Fom_F** conformation is **F-*syn***/**P-*anti***, while for **Fom_O**, only one molecule (F/H) among six ($Z' = 6$) has the **F-*syn***/**P-*anti*** with all other **Fom_O** molecules having the **F-*syn***/**P-*syn*** conformation. In the solid state all molecules from both **Fom** polymorphs are relatively planar with rings rotated by ±15-35° which partially complies with modelling results as **Fom** is predicted to be planar both in *gas phase* and solvents (Section *1.2.5.1*, Table **15**). **Fom_F** has essentially the same shape as **Fpm_N**, but with conformation and space group as for **Fpm_O**. However, since F is located *ortho*, an additional intramolecular N-H···F interaction forms. It is clear that the *ortho*-fluorine prevents any conformation other than **F-*syn***, and influences disorder in **Fom_O** (with mostly **P-*syn***) preventing the same supposed structural organisation as in **Fpm_O** (**P-*syn***). If only the **P**-ring is allowed to assume the **P-*anti*** conformation. The main factors influencing different polymorph formation experimentally are solvent and crystallisation rate. The **Fom_F** polymorph crystallises from MeOH by very slow evaporation. In the modelling analysis, solvents with higher polarity can facilitate the necessary conformational changes (from **P-*syn*** → **P-*anti***) while slower evaporation is often known to produce better quality crystal growth. The **Fom_O** polymorph crystallises from a less polar solvent (ethyl acetate) at a faster evaporation rate. Therefore, it seems that under these conditions the **Fom** molecules cannot fully adopt the favourable **P-*anti*** conformation, but rather aggregate (where possible) with a high level of disorder. Nevertheless, a comparison of both polymorphs gives the impression that the **Fom_O** polymorph is, in fact, an imperfect variant of **Fom_F**.

In the **Fxo** triad, all crystal structure conformations correspond closely with the calculated models with similar dihedral angles and small but moderate distortions from the global minima (25-5°). The only major difference is in **Foo** where the **Fo** rings are rotated by 65° (molecule A) and 35° (molecule B). This rotation is primarily due to steric reasons as formation of the hydrogen bonded $R^2_2(8)$ rings does not allow the **Fo** ring to adopt a planar geometry. The intramolecular N1-H1B···F12B interaction decreases the dihedral angle in molecule B, while in molecule A increased rotation allows the formation of favourable C-H…π interactions. This is a trade-off between N-H···F/C-H···π(arene) that does not arise in **Moo** as dimer formation by N-H···N interactions is exclusively augmented by very short C-H···π(arene) interactions.

2. Pyridinecarboxamides

2.1. NxxF isomer grid

2.1.1. General description of synthesis

Nucleophilic acyl substitution reactions between the fluoroanilines and pyridinoyl chlorides produced the nine N-(fluorophenyl)pyridinecarboxamides (**NxxF,** Table **17**) in modest to high yields (20-70%).

Condensation reactions were performed with the 4-, 3- or 2-fluoroanilines (1 ml, 10.41 mmol) added to a 250 ml flask placed on an ice bath and with subsequent stirring. Then, 30 ml of CH_2Cl_2 was added to the flask followed by addition of Et_3N (1.5 ml, 10.76 mmol). Finally, the 4-, 3- or 2-pyridinoyl chlorides (2 g, 11.23 mmol) were added in portions directly into this solution mixture. Another 30 ml of CH_2Cl_2 and 1.5 ml of Et_3N was added to accelerate the dissolution of any solids and the reaction mixture was allowed to warm to room temperature and stirred overnight.

As acyl chlorides are very reactive, the reactions were performed in anhydrous conditions in CH_2Cl_2 (under N_2), initially at 5°C and then at room temperature. A by-product is HCl, and Et_3N was employed to drive the reaction equilibrium towards the **NxxF** product. The pyridinoyl chlorides technically were used in the form of hydrochlorides so an additional mole of Et_3N was used to enhance their solubility in CH_2Cl_2 so that in total, two molar equivalents were added.

Organic washing and work-up was as standard: the organic reaction phase was washed with 20 ml of $KHCO_3$ (0.1 M) solution *ca.* 3-7 times and during purification, glassware was warmed to *ca.* 35°C. Then, 1.5 g of anhydrous $MgSO_4$ was added to the organic solutions for 20 minutes. The flask contents were filtered through a Büchner funnel (under vacuum) to remove $MgSO_4$. The filtrate was evaporated under vacuum and the product dissolved in minimal volumes of warm $CHCl_3$. A saturated solution was placed on ice and re-crystallization induced. The resulting product was removed by filtration under vacuum, washed with cold $CHCl_3$ and dried overnight: the dry product was weighed and total yield calculated.

Yields were modest to good (30-70%) in most cases with the exception of the **NoxF** isomers with lower yields of 20-30%. The product purity was mostly high (~99%), therefore crystallization and separation of the respective products from impurities was successful for most cases.

Table 17: Amounts, yields and melting points of the **NxxF** compounds

NxxF	m/g	yield/%	m.p./°C
NppF	1.059	47	135.0-136.5
NmpF	1.556	69	131.2-133.6
NpoF	1.000	44	139.0-140.0
NmpF	0.750	33	131.5-133.8
NmmF	1.352	60	121.2-122.6
NmoF	1.261	56	116.7-118.2
NopF	0.823	18	92.0-96.0
NomF	0.451	20	77.2-78.0
NooF	0.653	29	105.0-108.0

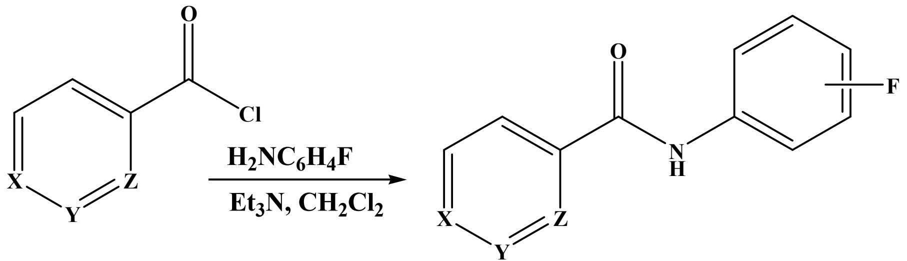

para (4-pyridinoyl): (X=N, Y=C, Z=C)
meta (3-pyridinoyl): (X=C, Y=N, Z=C)
ortho (2-pyridinoyl): (X=C, Y=C, Z=N)

Scheme 26: Schematic diagram of the **NxxF** reaction

However, for the **NoxF** isomers, the accessible starting material (2-pyridinoyl chloride) was of technical grade purity containing 5-chloro-2-pyridinoyl chloride (a by-product of the 2-pyridinoyl chloride synthesis with $SOCl_2$) and solubility of the products in $CHCl_3$ was greater: re-crystallization was accomplished using *iso*-propanol to give reasonably pure **NoxF** products.

The physical appearance and properties (solubility and melting points) are broadly similar for all nine **NxxF** isomers and especially for the six **NpxF** and **NmxF** isomers. All **NxxF** are white, odourless, crystalline solids, soluble in $CHCl_3$, CH_2Cl_2, CH_3CN, DMSO, acetone and ethyl acetate, insoluble in water, though sparingly soluble in cold MeOH and *iso*-propanol but, with increased solubility when warmed. A substantial difference in solubility in $CHCl_3$ is evident with the **NoxF** isomers more soluble in $CHCl_3$ than the remaining six **NpxF** and **NmxF** isomers.

2.1.2. Comment on spectroscopic data

All spectroscopic data, including NMR and IR spectra, are listed in the Appendix I (Section 2.1), while the spectra are provided in the ESI I section 1.3.

The ^1H and ^{13}C NMR data reveal a considerable degree of similarity (as expected) and a high level of modularity (in the pyridine and fluorophenyl rings) for all nine **NxxF** isomers. Distinct trends and salient features in the series will be discussed further. The ^{19}F NMR spectra in DMSO reveal distinct differences (δ values) with the **NxpF** series at -118 ppm and the **NxmF** triad at -112 ppm. The **NxoF** triad has both **NpoF** and **NmoF** at -121 ppm with **NooF** at -127.4 ppm highlighting the additional intramolecular hydrogen bonding in the **NxoF** series, but especially for **NooF** (Fig. **32**).

The ^1H NMR δ values of the amide N-H proton lie in the range 7.91-8.15 ppm (**NpxF**) and 8.23-8.75 ppm (**NmxF**) in $CDCl_3$ and from 10.38-10.68 ppm for the six **NpxF**/**NmxF** isomers in DMSO-d_6 showing the increased effect of the hydrogen bonding influence (and deshielding effect) of the S=O group on the N-H proton in DMSO. The distinct location of the amide proton δ values for the three **NoxF** isomers at lower-field values [10.04-10.36 ppm ($CDCl_3$) and 10.37-10.86 ppm (DMSO-d_6)] and shifting from 8→10 ppm in $CDCl_3$ (from **NpxF**/**NmxF**→**NoxF**) is due to the position and effect of the *ortho*-substituted N atom in forming intramolecular amide $N\text{-}H\cdots N_{pyr}$ interactions and $N\text{-}H\cdots O{=}S$ hydrogen bonding. However, for **NooF** the intramolecular hydrogen bonding is at a maximum with the N-H proton at 10.36 ppm ($CDCl_3$) and 10.37 ppm (DMSO-d_6) and the N-H proton is little influenced by DMSO. Overall, the spectroscopic data for the **NoxF** triad show distinct differences with the nine **NxxF** isomers and highlighting the **NoxF** $_{amide}N\text{-}H\cdots N_{pyridine}$ intramolecular interaction.

2.1.3. X-ray crystallography methods

Single crystals of the **NxxF** compounds were grown from ethyl acetate or $CHCl_3$ by slow evaporation of the **NxxF** solutions at room temperature (294 K). Single crystal X-ray data for all nine **NxxF** isomers were collected as described for the **Mxx** isomer grid (Section 1.1.2), except for **NppF** a non-merohedral twinned crystal [89:11 components] at 200(1) K), θ range 2-27.5° with 100% data coverage to 25° (on θ). Data reduction procedures are standard and SORTAV was used for the absorption corrections.[166,167] Structure solution methods, diagrams generation and CSD searches were as described for **Mxx** (Section 1.1.2). Selected crystallographic and structural information are in Tables **18**, **19** and the ESI I, Section 2.3.

2.1.4. Computational methods

The nine **NxxF** isomers were analysed using the same methods and techniques as described in the **Mxx** isomer grid section. The **NxxF** isomer optimisation and conformational analysis was performed using *ab initio* calculations (B3LYP/6-311++G) on isolated (*gas-phase*) and solvated molecules (PCM-SMD[170] solvation model with CH_2Cl_2 or H_2O as solvents) using Gaussian03/09.[25] As additionality high accuracy energy calculations (CBS-QB3)[171] are performed obtaining ΔG of solvation.

Conformational analysis of the optimised **NxxF** isomers was achieved by rotation of (*a*) the C26-C21-C1=O1 dihedral angle (α dihedral, **N**-ring), and (*b*) the C1-N1-C11- C12 dihedral angle (β dihedral, **F**-ring) both in the *gas phase* and solvated forms in order to analyse and predict the energetically favourable conformations in the *gas phase* (or as the solvated forms).

As the **NxxF** isomers have two aromatic rings connected *via* an amide linkage a total of four conformations are possible for the aromatic pyridine **N** and **F** site positions relative to the amide linkage. The rings can have the ***syn-*** (**N-*syn*** or **F-*syn***) or the ***anti-*** (**N-*anti***, **F-*anti***) conformations (Scheme **27**). This is relevant only for **NxxF** having an aromatic **N** or **F** in the *meta-* or *ortho-* position (**x** = **m** or **o**).

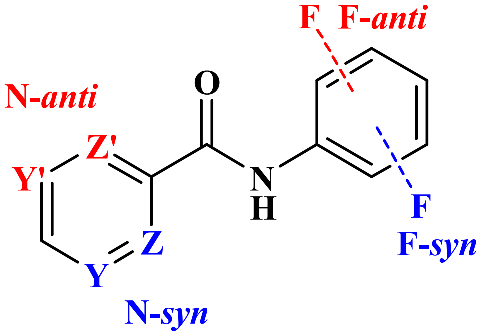

Scheme 27: Possible conformations of the **NxxF** isomers

2.1.5. Molecular and crystal structure data

The distinct intermolecular feature for eight of the **NxxF** crystal structures (Table **18**) (where **x** = *para-/meta-/ortho*) is that they aggregate in the solid-state *via* $_{\text{amide}}$N-H···N$_{\text{pyridine}}$ hydrogen bonds, but in different crystal systems and space groups. The **NppF** isomer is the only **NxxF** structure where the primary hydrogen bonding is *via* N-H···O=C interactions. Of the nine **NxxF** structures there are only three, **NpmF**, **NmmF** and **NmoF** that crystallize with *Z'* = 1 and with no disorder: the remaining six **NxxF** crystallize with one or more of the following: (*i*) more than one molecule in the asymmetric unit, (*ii*) disorder in the orientation of the C_6H_4F ring and/or (*iii*) have a minor Cl component of impurity (derived from the original **NoxF** synthesis). The **NmpF** structure is of further interest as it forms a $_{\text{amide}}$N-H···N$_{\text{pyridine}}$ hydrogen bonded tetrameric assembly and further linked by C-H···F and C-H···O=C interactions.

Table 18: Selected crystallographic data for the nine **NxxF** isomers[a]

NxxF	**Space group**	***Z'***	***Volume*** **(Å^3)**	***R*-factors**
NppF	$P\bar{1}$	2	963.94(6)	0.051, 0.142
NpmF	*Cc*	1	1032.22(10)	0.042, 0.113
NpoF	*Cc*	1	1027.33(8)	0.051, 0.135
NmpF	$P\bar{1}$	4	1995.47(9)	0.050, 0.124
NmmF	$P2_1/n$	1	999.42(12)	0.044, 0.118
NmoF	$P2_12_12_1$	1	989.44(9)	0.049, 0.125
NopF	$P2_1/c$	1	993.10(16)	0.063, 0.166
NomF	$P2_1/n$	2	1999.17(18)	0.074, 0.223
NooF	$P2_1/n$	1	986.32(14)	0.057, 0.154

[a] Complete crystallographic, refinement and structural details for all nine **NxxF** isomers ($C_{12}H_9N_2OF$) are listed in the ESI I (Section 3.1).

2.1.5.1. **NpxF isomer series**

The three **NpxF** compounds aggregate *via* two different primary hydrogen bonding intermolecular interactions (*i.e.* the typical amide···amide as N-H···O=C for **NppF** and N-H···N$_{pyridine}$ for **NpmF**, **NpoF**).

NppF molecular and crystal structure

The **NppF** crystal structure crystallizes in $P\overline{1}$ and with $Z' = 2$ at 200(1) K. The crystal and molecular structure solution of **NppF** is interesting in that crystals analysed at 150(1) K would not yield a solution: therefore by increasing the temperature to 200(1) K a meaningful result was obtained whereby the unit cell was halved. It is a non-merohedral twinned crystal with two components of 0.89:0.11. Metrically, it suggests a unit cell change to the monoclinic system but this does not seem appropriate for the results at 200(1) K. There are several distinct differences between the two independent (A) and (B) molecules in the asymmetric unit; an example is the F14$_{A/B}$···N24$_{A/B}$ intramolecular of 9.800(3) in (A) and 9.769(3) Å in (B).

The molecules aggregate along the *a*-axis [100] direction as amide N-H···O=C chains [*C*(4) chains] with rather long intermolecular distances of 3.203(2) and 3.216(2) Å for molecules (A) and (B), respectively, and in tandem with this is a rather weak C16-H16$_{A/B}$···O1$_{A/B}$ contact forming $R^1_2(6)$ rings, together with an intramolecular C-H···O contact (Fig. **25**). The molecules aggregate as weakly interacting A···A···, and B···B··· chains with similar N···O distances (the aggregation is principally 1-D). Interestingly, the pyridine N24(A/B) atoms do not participate in hydrogen bonding or even in weak contacts which is rather unusual.

The two *para*-fluorine atoms [F14$_{A/B}$] form contacts and interact with symmetry related fluoro atoms with F···F distances of 2.86 Å, some 0.10 Å < van der Waals contact radii distance: this enables the formation of *zig-zag* chains of F atoms along the *a*-axis direction. The larger two molecule wide columns stack *via* C-H···π(arene) interactions and manifesting as a chain of weakly interacting F atoms along [100].

The aromatic C_6/C_5N interplanar angles in molecules A and B are 56.74(5)° and 57.93(5)°, respectively, and differing by only 1°. However, the biggest angle difference is for the C_6/five-atom amide group and two linker C atoms [C11/C1/O1/N1/C21] and differing by 4° with 29.24(7)° for (A) and 33.16(6)° (B). Using a structural overlay, it can be observed that the differences are small and in an opposite sense to the amide group. Torsion angle differences of 2-3° are noted in **NppF** for C1-N1-C11-C16 as 150.9(2)° in (A) and -148.1(2)° in (B).

Table 19: Relevant structural features (Å,°) in the nine **NxxF** isomers [a]

NxxF	C_6/C_5N (°)	C_6/amide	C_5N/amide	N···N/O[b]	Packing[b]
NppF[*]	56.74(5)	29.24(7)	27.63(7)	3.203(2)	1-D chains[*]
	57.93(5)	33.16(6)	24.93(7)	3.216(2)	
NpmF	65.93(10)	39.16(10)	27.39(13)	2.991(4)	1-D chains
NpoF	76.99(12)	51.39(12)	27.06(15)	2.930(4)	1-D chains
NmpF	5.42(9)	3.38(9)	2.04(9)	3.193(2)	Tetrameric
	0.77(10)	1.99(9)	2.13(9)	3.224(2)	assembly
	5.39(9)	3.21(9)	2.18(9)	3.171(2)	
	0.74(9)	1.56(9)	1.82(9)	3.254(2)	
NmmF	50.16(5)	27.47(5)	24.00(7)	3.1146(18)	1-D chains
NmoF	22.67(14)	33.09(12)	10.75(13)	3.182(4)	1-D chains
NopF	30.34(10)	27.74(11)	4.75(15)	2.679(3)	Intramolecular
NomF	4.4(2)	5.5(2)	2.0(2)	2.675(4)	Intramolecular
	4.6(2)	6.4(2)	4.2(2)	2.655(4)	
NooF	9.69(14)	8.67(14)	2.53(14)	2.630(3)	Intramolecular
				2.654(2)[c]	

[a]Full structural details are provided in the ESI I (Section 3.1). [b] The $_{amide}$N-H···$N_{pyridine}$ or N-H···O=C[*] interaction distances. [c] The N···F intramolecular distance.

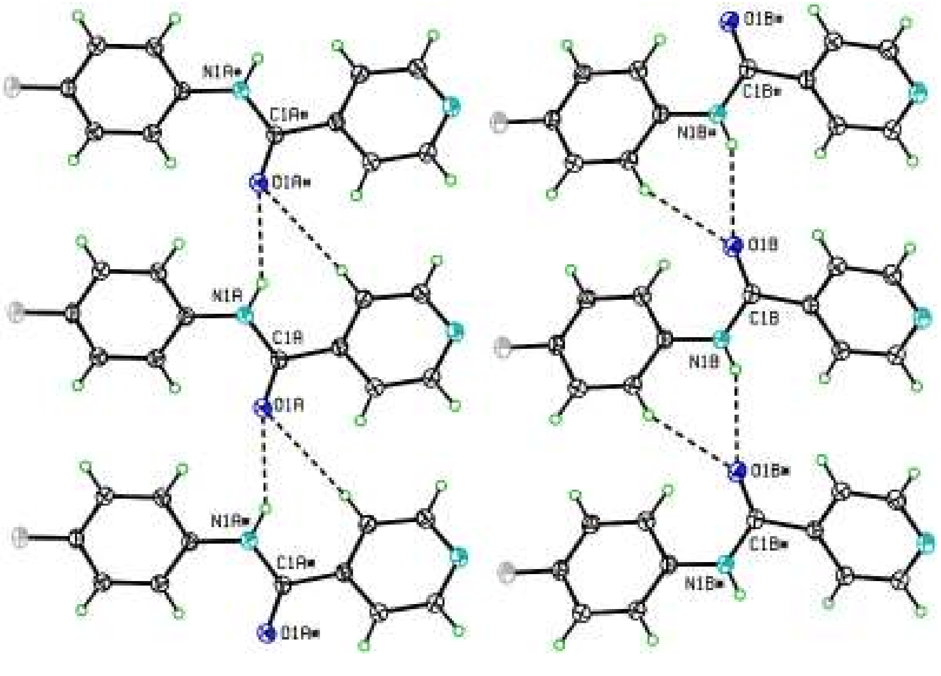

Fig. 25: An ORTEP diagram of the N-H···O=C and C-H···O=C interactions in **NppF**. The symmetry codes # and * refer to 1+x,y,z and x-1,y,z, respectively.

NpmF molecular and crystal structure

The **NpmF** crystal structure (Fig. **26**) is a regular structure with intermolecular N–H···$N_{pyridine}$ interactions and without molecular disorder: the N1···N24 intermolecular distance is typical at 2.991(4) Å and the aggregation is *via* 1-D C(7) *zig-zag* chains. The conformation of the **mF** ring in **NpmF** is **F-*syn***. The only other interactions of note are an intramolecular C-H···O=C interaction, a weak intermolecular C-H···O and a short C-H···π(arene) interaction. The arene interaction has a H25···Cg distance of 2.65 Å and with C25…Cg = 3.484(3) Å and a C25-H25···Cg angle of 147° [Cg = centroid]. This is not as short as the C-H···π(arene) interaction in **Moo**. The fluorine atoms in **NpmF** do not participate in interactions apart from some weak contacts. The angle between the C_6/C_5N planes is 65.93(10)°, whereas the C_5N/amide and C_6/amide are intermediate at 27.39(13)° and 39.16(10)°.

NpoF molecular and crystal structure

The **NpoF** structure (Fig. **27**) has C_6 and C_5N aromatic rings that are almost mutually orthogonal at 76.99(12)°. There is a minor component of disorder present in the fluorobenzene at 8.3(9)% and involves a 180° rotation about the N1-C11 axis with H/F atoms interchanging (**F-*anti***/**F-*syn***): this type of H/F interchange and disorder is not uncommon. A key reason in performing the conformational analyses is to attempt to ascertain factors (energy) which may predispose why one isomorph **NpmF** is ordered and why **NpoF** is disordered (see Section 2.1.8).

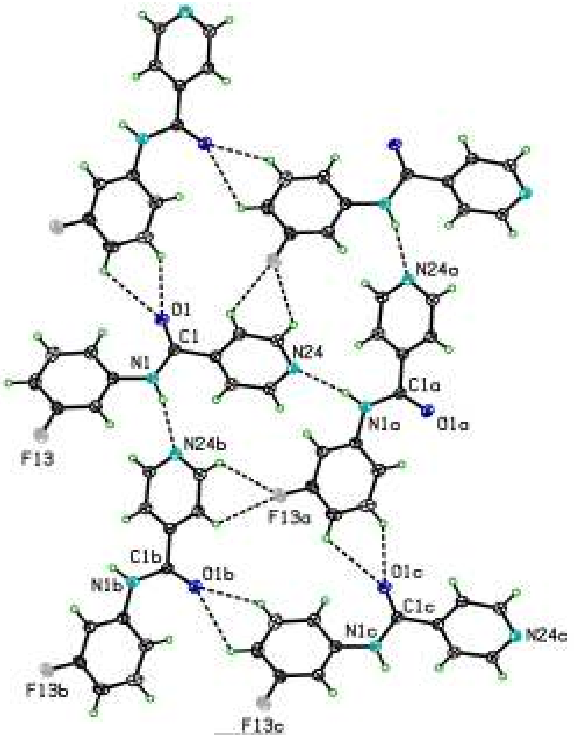

Fig. 26: The primary intermolecular interactions in **NpmF** (*a* = 1/2+x,-1/2-y,1/2+z;, *b* = -1/2+x,-1/2-y, -1/2+z and *c* = x,y-1).

Isomorphous relationships are seen in the related **Fxx** benzamides (Section 1.2) while disorder is a common phenomenon in fluorobenzamides given the isosteric relationships between H and F atoms and small energy differences between the **F-*syn***/**F-*anti*** conformations of the C_6 aromatic rings both in solution and the crystalline state.[13,162]

The N···N hydrogen bonding is short and forms a 1-D *zig-zag* *C*(7) chain parallel to the $(10\bar{1})$ plane: this N…N distance is short compared to related systems with similar N-H···N interactions *e.g.* as in **NpmF**. The C-H···N contact is rather long and does not augment the interactions. There are two weak C-H···O and a C-H···π(arene) interaction per molecule and have little overall effect on the packing apart from weakly linking columns into sheets and a 3-D structure. The **NpmF** and **NpoF** structures are isomorphous and are isostructural (Fig. **28**). The C_5N/amide and C_6/amide angles are 27.06(15)° and 51.39(12)°.

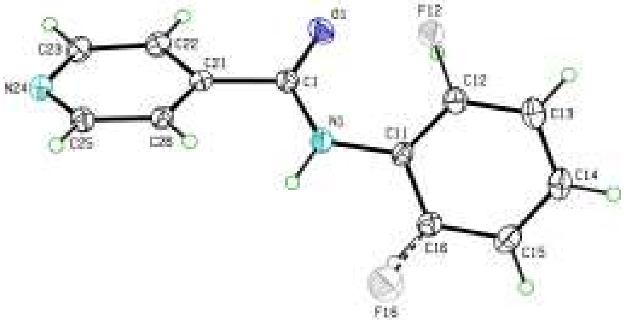

Fig. 27: The **NpoF** molecular structure with group disorder for F12

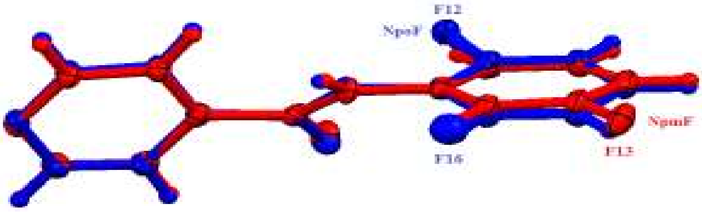

Fig. 28: A molecular overlay of the isomorphous molecules of **NpmF** (in red) and **NpoF** (in blue) in space group *Cc*. The F-atom positional disorder in **NpoF** is depicted where the major component has the **F-*anti*** conformation.

2.1.5.2. **NmxF isomer series**

The three **NmxF** compounds all aggregate *via* intermolecular N-H···$N_{pyridine}$ interactions. The **NmpF** crystal structure assembles as unusual hydrogen bonded tetramers linked by rather long N-H···N hydrogen bonds in addition to flanking but weaker intramolecular C-H$\cdots$N interactions, while aggregation in form of $C(6)$ chains is found both **NmmF** and **NmoF** isomers.

NmpF molecular and crystal structure

The **NmpF** isomer crystallizes as a cyclic hydrogen bonded tetrameric assembly in the space group $P\bar{1}$ with $Z' = 4$, and in the overall shape of a '*St. Brigid's*' cross (Fig. **29**) which is quite unusual and rather unexpected. The four molecules (A) to (D) form a tetrameric assembly with four independent molecules within the asymmetric unit and *via* long N-H$\cdots$N$_{\mathrm{pyridine}}$ hydrogen bonds. There are distinct differences between the $_{\mathrm{amide}}$N-H…N$_{\mathrm{pyridine}}$ intermolecular distances of 3.171(2), 3.193(2), 3.224(2), 3.254(2) Å (a difference of 0.08 Å) with all of the N$\cdots$N distances significantly different. In all four molecules the **Nm** ring is in the ***N-syn*** conformation.

In tandem with each of the four N-H$\cdots$N$_{\mathrm{pyridine}}$ interactions are two slightly longer and weaker flanking C-H$\cdots$N$_{\mathrm{pyr}}$ interactions forming $R^1_2(6)$ and $R^1_2(7)$ rings with an overall size of $R^1_3(9)$. The molecules aggregate as four-membered molecular rings as [A→D→B→C→A] (Fig. **29**) to give a compact four molecule assembly as a hydrogen bonded $R^4_4(24)$ ring. The four C22$_{\mathrm{A\text{-}D}}\cdots$N23$_{\mathrm{A\text{-}D}}$ distances are from 3.366(2) to 3.403(2) Å [and similar to C16$_{\mathrm{A\text{-}D}}\cdots$N23$_{\mathrm{A\text{-}D}}$]. These are the only C-H$\cdots$N interactions of significance in the **NmpF** tetramer and subtle differences between the various interactions allow us to easily distinguish and note the differences between the four independent molecules. The closest overlap of aromatic groups and $\pi\cdots\pi$ stacking is 3.40 Å. Of interest is that the tetramers are further linked by C-H$\cdots$F/O=C interactions. The four rather short C-H$\cdots$F interactions are in the range of 3.266(2) to 3.281(2) Å and there are also some C-H$\cdots$O=C interactions present in the crystal structure linking the tetramer moieties.

The four molecules (A) to (D) can be grouped into the A/C and B/D molecular pairs within which are close similarities. The C_6/C_5N interplanar angles are 5.42(9)°/5.39(9)° for the (A)/(C) and 0.77(10)°/0.74(9)° for the (B)/(D) pairs. There are however significant differences within each pair and molecules (A) and (C) have the closest fit. It is possible that a phase transition can occur at a different temperature although the **NmpF** RT (294 K) structure is similar. The unusual **NmpF** geometry (though unexpected) and assembly can be attributed to the ***N-syn*** conformation and directional arrangement of both the N-H donor and pyridine N acceptor groups. Cyclic hydrogen bonded dimers/catemers almost certainly exist in solution but the presence of cyclic tetramers probably drives the crystallization process in a *pseudo*-macrocyclic chelation process and with the assembly held together by four N-H···N and eight C-H···N interactions.

Crystallization with $Z' = 4$ is rather unusual but there are many cases available on the CSD, [495 examples with 3-D coordinates and $R < 0.1$ in space group $P\overline{1}$ or 1705 'hits' for the entire CSD (version 4.29 + 3 updates)]. Molecules (A) to (D) differ slightly within the tetrameric assembly and without molecular disorder.

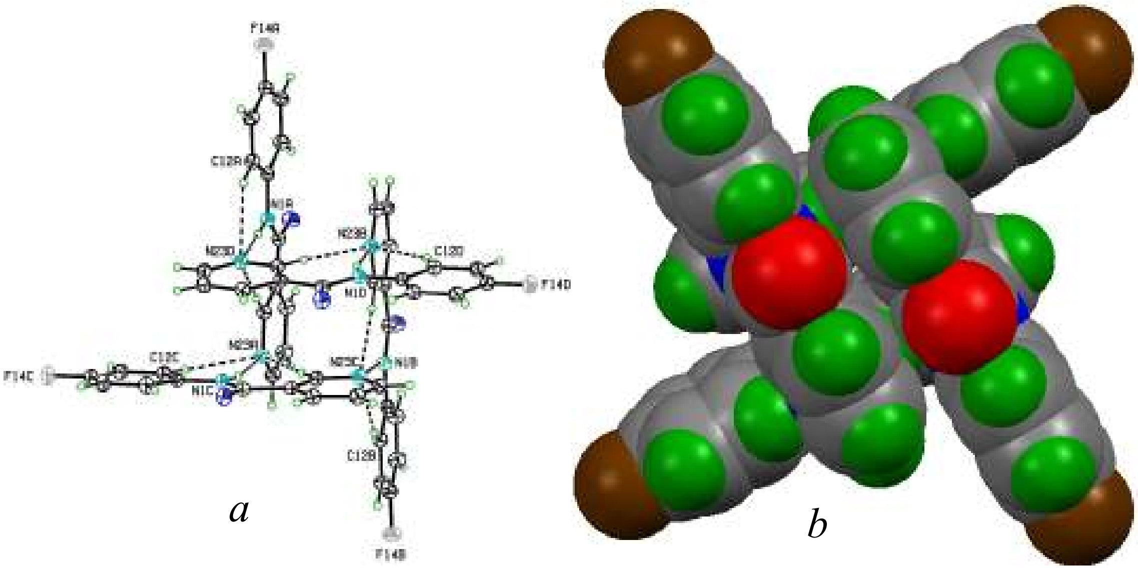

Fig. 29: *a*) The N-H···N and flanking C-H···N intermolecular interactions in the tetrameric assembly of **NmpF**; *b*) CPK view of the **NmpF** tetramer.

The N-H and pyridine N are oriented in the same direction and this facilitates either dimer or chain formation at least. The transformation could be metrically monoclinic but the unit cell data would be transformed from 9.759 Å, 9.764 Å, 21.170 Å, 96.14°, 95.74°, 90° to 13.805 Å, 13.804 Å, 21.170 Å, 89.71°, 98.41°, 90.03° which is NOT close to being monoclinic. This **NmpF** structure should be the subject of further investigation and especially to see if there is a temperature dependence on the crystal structure and a phase transition below 150(1) K or between 150 and 300 K.

Comparable examples of hydrogen bonded tetrameric units occur in both Ph_3COH and Ph_3GeOH where tetramers are linked by a relay of $[O\text{-}H\cdots O\text{-}H\cdots]_2$ interactions.[183,184] The crystal structure of 3-(CF_3),5-(Ph)PzH [ESUJOR: CSD[8]] forms *tub-shaped* tetramers *via* N-H···N interactions as hydrogen bonded $R^4_4(12)$ rings comparable to **NmpF** in space group $P\overline{1}$ with $Z' = 4$; tetramers though are the least common structural motifs found amongst the N-unsubstituted pyrazoles.[185] The four

N···N distances in ESUJOR are in the range from 2.844 to 2.866 Å and the tetramer is smaller than in **NmpF**.[185] Another series of tetrameric structures are the $[AgXL]_4$ complexes {with X = halide, L = tertiary phosphine *e.g.* $P(4\text{-}MeC_6H_4)_3$} though the structures of $[AgXL]_4$ are very different to **NmpF**, with the *cubic vs. stella quadrangula* $[MX]_4$ cores recently discussed.[186]

NmmF molecular and crystal structure

The **NmmF** crystal structure is regular with intermolecular N–H···$N_{pyridine}$ interactions as *C*(6) *zig-zag* helical chains and without disorder: the N1···N23 distance is longer than for **NpmF** at 3.1146(18) Å (the flanking C-H···N with H···N23 = 2.67 Å is not significant). In **NmmF** the pyridyl N23 and fluoro F13 atoms are *cisoid* with respect to one another and *transoid* to the N-H group giving a ***N-anti*/*F-anti*** conformation. A similar conformation in already seen in both **Mmm** (pyridine ring only, Section 1.1.2.2) and **Fmm** (Section 1.2.6). The combination of the primary N-H···N interaction, C-H···O=C and two weaker interactions gives rise to a rumpled 2-D sheet parallel to the $(10\bar{1})$ plane. The C_6/C_5N interplanar angle is 50.16(5)° with C_5N/amide and C_6/amide intermediate at 24.00(7)° and 27.47(5)° (Table **19**).

NmoF molecular and crystal structure

The **NmoF** structure crystallizing in $P2_12_12_1$ is regular. In **NmoF** the orientation of the pyridinyl N23 and fluoro F12 atoms are *cisoid* with respect to one another (***N-syn*/*F-syn*** conformation) and *transoid* to the carbonyl oxygen atom O1. In **NmoF** the C_5N and C_6 aromatic rings are mutually oriented at an angle of 22.67(14)°, whereas the C_5N/amide and C_6/amide angles are 10.75(13)° and 33.09(12)°. Of further significance is that, in addition to the expected twisting, there is also some slight bending of the amide group with respect to the two terminal aromatic rings, with atom C11 by 0.139(11) Å and atom C21 by 0.009(13) Å from the three atom amide group (O/C/N) and positioned on the same side (to emphasize the overall bending), though the bending especially manifests at C11 and is presumably due to crystal packing forces. The {C11,…,C16} rings overlap slightly on stacking along the [100] direction with a close contact between C12···$C15^i$ of 3.307(5) Å, and this is 0.10 Å less than the C atom radii sum {symmetry code *i* = 1+x,y,z}. In **NmoF**, the N1-H1···N23 primary interaction (with intramolecular N1-H1···F12 *ortho* contact: another contact C16-H16···O1 is also present) is assisted by an intermolecular C22-H22···N23 interaction forming $R^{1}_{2}(7)$ rings with C22···N23 = 3.348(4) Å (Fig. **30**).

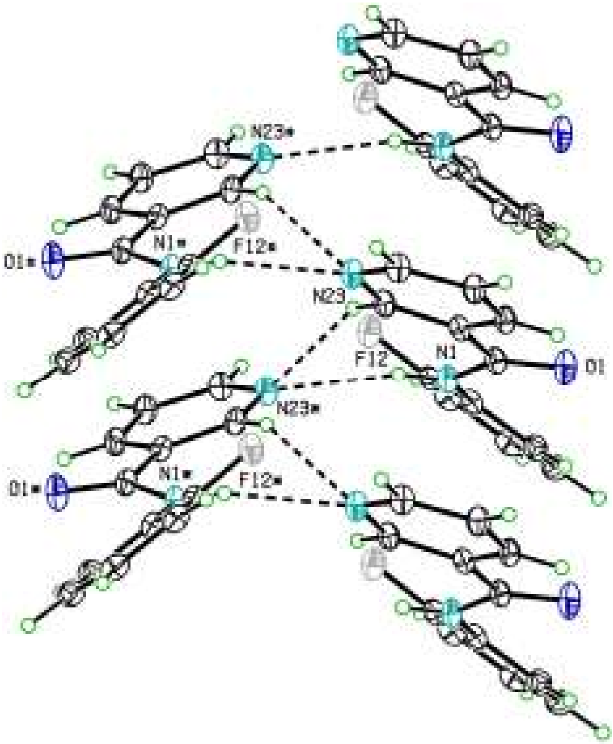

Fig. 30: The N-H···N hydrogen bonding in **NmoF**: molecules with labels # and * are positioned at the symmetry equivalent positions 1/2+x,-1/2-y,-z and -1/2+x,-1/2-y,-z.

The N-H···N interaction [being the shortest N1···N23* distance among **NxxF** structures of 3.182(4) Å] generates a *zig-zag* 1-D helical chain in the [100] direction as a stacked herringbone column (along a 2_1 axis); longer C-H···N/O/F intermolecular interactions generate a 3-D network. Aromatic π···π stacking occurs with overlap of symmetry related [C11,…,C16] rings along the [100] direction [C12···C15^{i} = 3.307(5) Å (i = 1+x,y,z)]. For comparison the **NmoF** conformation when '*docked*' in *Leishmania* sirtuin (Fig. **5A**)[37] is similar to our **NmoF** but with the amide plane twisted by ~30°.

2.1.5.3. **NoxF isomer series**

The primary hydrogen bonding in all three **NoxF** derivatives is aggregation *via* N-H···N$_{pyridine}$ interactions but these are *intramolecular* interactions. There is a clear lack of strong hydrogen bonding in these three **NoxF** systems apart from the intramolecular N-H···N$_{pyr}$. Disorder is observed in **NomF** and a minor Cl atom component is present as an impurity with site occupancies of 4.2(3)% and 3.2(3)% at the *meta*-C25-H25 site in **NopF** and **NooF**, respectively, and is a contaminant in the original synthesis from the acyl chloride.

The minor Cl atom site component is not seen in the **NomF** structure, but there is rotational disorder in one of the C_6 rings with a minor F atom site at C15A having 6.1(5)% site occupancy (Z' = 2): this group disorder is similar to that described in **NpoF**. In the **Mxx** and **Fxx** isomer grids the **Mxo** and **Fxo** triads (with an *ortho*-pyridine N atom) all aggregate using intermolecular N-H···N interactions forming hydrogen bonded dimers by centrosymmetric $R^2_2(8)$ rings. However, for the **NoxF** triad the additional C atom between the pyridyl-N and amide N-H (amide group is reversed) facilitates the additional intramolecular N-H···N_{pyr} interaction as $S(5)$ rings but mitigates against cyclic dimer formation (Figs. **31**, **32**). This intramolecular interaction drives **No** ring in all **NoxF** compounds to be in the **N-*syn*** conformation.

NopF molecular and crystal structure

The **NopF**[39] structure crystallizes in $P2_1/c$ and refines to an R-factor of 7%. In the latter stages of refinement it was detected that a minor peak was present in close proximity to H25 with a peak height of 0.55 e.Å^{-3}: the next highest peak is at 0.20 e.Å^{-3}. This atom site is situated at a distance of only 1.20 Å from the C25 atom. Refinement initially with a minor F atom site was finalised with a Cl atom to give site occupancy of 4.2(4)%. This is the optimum site value although the apparent bond length is very short for a C-F or C-Cl and this can be attributed to many factors not least the fact that librational motion could be important. The minor C atom sites were not modelled accordingly as it is such low occupancy that it is essentially background 'noise'. The chloro atom site is treated as if it were part of the principal molecule given that it is not practical to refine 4% of the C/N/O molecular backbone as a minor component. In **NopF** the angle between the C_6/C_5N planes is 30.34(10)° whereas the C_5N/amide are co-planar at 4.75(15)°. The structure is remarkable for the lack of strong hydrogen bonds and the only hydrogen bond of consequence is the intramolecular N1-H1···N22 hydrogen bond [N···N 2.679(3) Å] that enforces quasi-parallel alignment of the aromatic rings in tandem with an intramolecular C-H···O interaction. A C-H···O interaction further links the **NopF** molecules into 1-D chains along the *b*-axis direction and weak C-H···F interactions link chains into sheets and complete the structure with molecules forming weak interactions along the *b*-axis direction and parallel to the $(10\bar{2})$ plane. On the CSD[8], **GEPQIC**[187] is the parent chloro derivative [as **NopCl**] instead of containing an F atom as for **NopF**. **WUVYIV** (Br)[188] is isomorphous with the Cl derivative **GEPQIC** although this is not stated on the CSD. The molecular overlay between the Cl/Br analogues is within 0.005 Å.

NomF molecular and crystal structure

The **NomF** structure contains two molecules (Z' = 2) which are similar. One of the molecules is disordered with a major *meta*-F atom site of 0.939(5) at F13A (**N-*syn***/**F-*anti*** conformation) and the minor site at F15A (**N-*syn***/**F-*syn*** conformation, Scheme **27**) with 0.061(5) unit site occupancy. The disorder is simple in that it only involves 180° rotation about the N1-C11 bond and there are no other unusual artefacts of disorder in the structure [no minor chloro site component was detected in the *meta*-position as for **NopF**]. The other differences between the two molecules are in the bond lengths and angles *e.g.* the C1-N1-C11-C16 torsion angle is 177.6(3)° in molecule (A) and 172.0(3)° in (B).

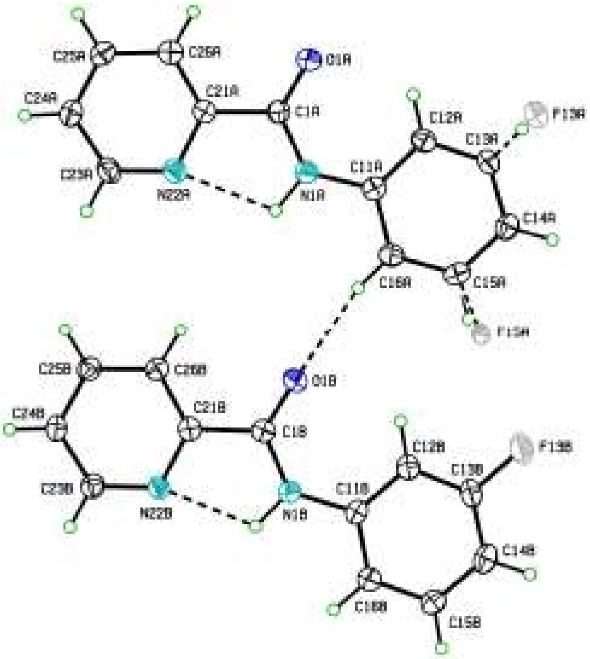

Fig. 31: An ORTEP diagram of molecules (A) and (B) in. The minor component of disorder in molecule (A) is shown at C15-H15 (as in Fig. **27)**.

As for **NopF**, the **NomF** structure is remarkable for the lack of strong hydrogen bonds in that the strongest hydrogen bond is the intramolecular N-H···$N_{pyridine}$ at 2.675(4) Å in (A) and 2.655(4) Å in (B). Two intramolecular C-H···O interactions are also present involving C12A/B at 2.845(4) Å and 2.895(4) Å. Otherwise, there are no other direction specific interactions (Fig. **31**) apart from a C-H···O=C interaction that links (A) and (B) molecules within the asymmetric unit. The angles between the C_6/C_5N

planes is 4.4(2)/4.6(2)° for molecules (A) and (B), whereas the C_5N/amide and C_6/amide are 2.0(2)/4.2(2)° and 5.5(2)/6.4(2)°.

NooF molecular and crystal structure

In **NooF** the molecular structure (Fig. **32**) is essentially planar with only a small twist (<10°) of the three principal groups from co-planarity (Table **19**). A minor impurity of a chloro atom is present in a *meta* position on the pyridinyl ring. As in **NmoF**, there is molecular bending in the amide group with respect to the two terminal aromatic rings in **NooF**, with C11 at 0.087(9) Å and C21 at 0.033(11) Å from the O1/C1/N1 amide group plane and with C11, C21 positioned on the same side. In **NooF** there are two distinct intramolecular interactions from the amido group as (*a*) N1-H1···F12 with the *ortho*-F atom (N1···F12 = 2.655(3) Å, N1-H1···F12 = 103°) and (*b*) N1-H1···N22 with the *ortho*-N atom [N1···N22 = 2.630(3) Å and N1-H1···N22 = 115(2)°]: C16-H16···O1 is an additional intramolecular contact. These intramolecular interactions give the **NooF** molecule a **N-*syn*/F-*syn*** conformation.

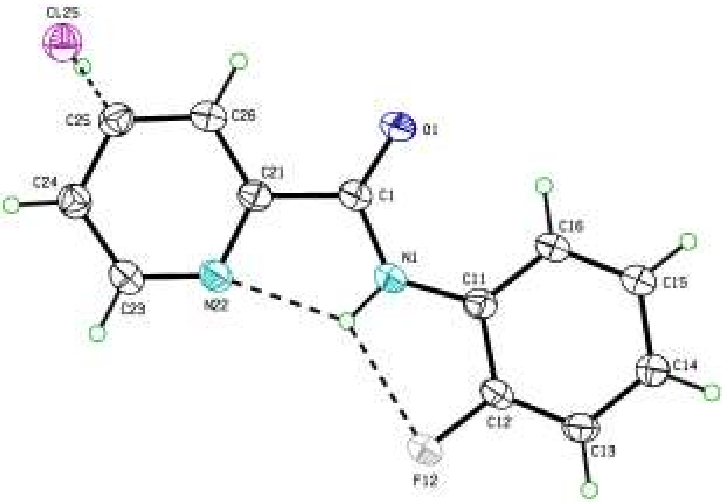

Fig. 32: A view of **NooF** with intramolecular N-H···N/F interactions

Surprisingly, there are no intermolecular N1-H1···X interactions (where **X** = **C**/**N**/**O**/**F**) in **NooF** with the two closest N1···C atoms at 3.539(3) Å (C16 positioned at the symmetry equivalent position 1+x,y,z) and at 3.577(3) Å for C23 (at x-1,y,z). The closest H···N1 atom contact is H23 at 3.30 Å (at -x,-y,-z). The lack of H bonding involving the amide N1-H1 is interesting as it is the strongest donor group in **NooF**. The dominance of the two intramolecular N-H···F and N-H···N interactions with intermolecular steric packing effects prevents the close approach of suitable of acceptor atoms/groups. This effect is also observed in the ^{1}H-NMR in DMSO-d_6. A minor stacking contact is present with C1···C23 (at x-1,y,z) = 3.335(4) Å which manifests along the *a*-axis direction. Furthermore **NooF** is of interest as it has potential as a ligand for exploitation in coordination chemistry using a N_2F donor set.[40]

2.1.6. Comments on molecular volumes and melting points

The symmetrical **NppF** isomer has the smallest volume per molecule [241 Å^3] at 150(1) K (**Mpp** has the smallest with **Mop** the largest *V/Z* in the **Mxx** series), whereas **NpmF** [258 Å^3] and **NpoF** [257 Å^3] have the largest molecular volumes in space group *Cc*. The range of volumes for the remaining six **NxxF** molecules is narrow from 247 Å^3 for **NooF** to 250 Å^3 for **NmmF**/**NomF**. The average molecular volume is 250 Å^3 for all nine **NxxF** isomers as compared to 268 Å^3 for **Mxx**, the difference being replacement of F with CH_3 in the latter.

Melting points continue to be largely ignored in solid-state chemistry[10,11] apart from documenting data values and ranges. Within an isomer series with identical molecular weights and numbers of each elemental component, some general trends can be discerned and compared with literature data.[10,11] This will be of additional use in comparing isomers and by ~30-40°C: these six **NpxF**, **NmxF** isomers have melting points within a 23°C range. The highest melting point is for **NpoF** (139-140°C), expanding studies of related isomer series[10,11] Melting point trends show the three **NoxF** compounds have the lowest melting points compared to the other six **NpxF**, **NmxF** the lowest is **NomF** (77.2-78°C). The trends show as (*a*) the **NpxF** triad (136°C average) > **NmxF** (124°C) > **NoxF** (93°C) and (*b*) within each of the **NxxF** triads there is a tendency for the **NxmF** to have the lowest melting points. These differences are not as dramatic as noted in the related **Mxx** series where a range of 100°C is observed for the nine **Mxx** isomers: therein, **Mmo** has the lowest melting point (78.8-80.0°C) and similar to **NomF** (77.2-78.0°C). The **Mxx** and **NxxF** series differ by a reversed amide bridge and substitution of a CH_3 group for an F atom on the C_6 ring with **Mxx** following the *meta*- < *ortho*- < *para*-substitution melting point trend in disubstituted benzenes.[10,11,189] A rationalisation as why the melting point range is much greater in the **Mxx** grid in comparison to the **NxxF** series may be due to the weaker interactions. The methyl group in the **Mxx** series forms weak but favourable and cumulative secondary C-H…O/π(arene) interactions and reinforced especially in the high melting point of **Mpp** (180.2-180.8°C). In **NxxF** the effect of the F atom is smaller and weaker in supramolecular aggregation (as weak C-H···F interactions and contacts) and does not justifiably preserve aggregation especially at the melting point event. Only in **NmpF** and **NmoF** are the C-H···F interaction distances considerably shorter (0.2 to 0.3 Å) than the contact radii. For comparisons of the **Mxo** and **NoxF** series, the *ortho*-pyridine N atom facilitates dimer formation as $R^2_2(8)$ rings in **Mxo**, but only as intramolecular $_{\text{amide}}$N-H···N$_{\text{pyridine}}$ interactions in **NoxF** and in both series only weak additional aggregation interactions are observed. These factors may explain why the **NoxF** triad has the lowest melting point data in the **NxxF** series, but the **Mxo** triad as hydrogen bonded 'dimers' exhibit relatively higher average melting points.

2.1.7. *Ab initio* calculations

2.1.7.1. Structure optimisation results

The main structural aspects of the optimised **NxxF** structures are presented in Table **20**. The three most important torsion angles are the C26-C21-C1=O1 angle (α) between the pyridine ring and amide group, the C1-N1-C11-C12 angle (β) between the fluorophenyl ring and amide group and the O1=C1-N1-C11 amide linkage angle (δ).

Table 20: Torsion angles (°) of optimised **NxxF** isomers

	optimised in *gas phase*			optimised in CH_2Cl_2			optimised in H_2O		
	α	β	δ	α	β	δ	α	β	δ
NppF	26.67	3.72	3.20	30.35	4.04	3.27	29.47	12.09	2.43
NpmF	26.34	3.13	3.31	27.69	2.94	2.49	27.53	4.39	2.78
NpoF	23.84	1.54	3.46	30.18	3.28	3.90	27.58	3.31	2.35
NmpF	24.36	3.64	3.55	29.56	4.34	3.81	29.76	11.89	3.22
NmmF	23.81	2.68	3.74	27.28	2.57	3.23	27.29	3.15	3.79
NmoF	22.27	2.11	3.82	30.04	4.32	4.64	27.94	4.00	3.77
NopF	-0.02	0.01	-0.01	0.02	0.00	-0.02	0.01	0.01	0.00
NomF	0.00	0.00	0.01	0.06	0.02	-0.03	0.00	0.00	0.00
NooF	0.00	-0.01	0.01	0.01	-0.01	0.00	-0.02	-0.04	-0.01

[a] The angle C26-C21-C1=O1 (**N**-ring) is referred to as α; angle C1-N1-C11-C12 angle (**F**-ring) as β and O1=C1-N1-C11 angle (amide linkage) as δ. All geometries are based on B3LYP/6-311++G optimisation with PCM-SMD solvation model.

In general, all of the **NxxF** structures can be regarded as nearly planar. The **NoxF** triad are essentially planar with no discernible differences regarding the medium (*gas phase* or solvation). The remaining six (**NpxF**, **NmxF**) isomers have torsion angles deviating from planarity. In the *gas phase* the α torsion angles of **NpxF** and **NmxF** are rotated from planarity by 24.55±1.67°, the δ angle by an average of 3.51±0.24° and a small deviation from planarity for β by 2.80±0.86°.

In CH_2Cl_2, the six (**NpxF**, **NmxF**) isomers have α torsion angles rotated by 29.18±1.34° and the β angles by an average of 3.58±0.76°: the δ angle twists by 3.56±0.73°. In H_2O, the **NpxF** and **NmxF** structures have α torsion angles twisted by 28.26±1.07° and δ angles by 3.06±0.64°. However, the β torsion angle is 11.99±0.14° for **NppF** and **NmpF** but in **NpmF**, **NpoF**, **NmmF** and **NmoF** is smaller at 3.71±0.58°. Overall, optimisation of the **NxxF** isomers predicts that the three **NoxF** isomers are stabilised by the intramolecular amide N1-H1···N22 interaction (as demonstrated by the crystallographic and spectroscopic evidence for the relatively planar **NoxF** series (see Table **19** and Figs. **31, 32**). The other six **NpxF** and **NmxF** isomers distort from co-planarity mainly through pyridine ring rotation from unfavourable intramolecular H···H contacts. For the **NpxF** and **NmxF** series the only notable differences between the structures optimised in different media are the α angles (at -4.64±2.28° if optimised in CH_2Cl_2 and at -3.71±1.67° in H_2O); larger deviations occur for the β angle for **NppF** and **NmpF** optimised in water.

2.1.7.2. **Conformational analysis**

Conformational analyses in the *gas phase* establish those conformations that are favourable and Fig. **33** (high resolution diagrams are provided in the ESI I, Section 3.3.2) highlights the nine **NxxF** PES optimized in the *gas phase* including both the **N-ring** (full line) and **F-ring** (dashed line). The high modularity of all nine **NxxF** isomers is obvious, (as observed in the NMR data). Each pyridine (**N**) or fluorophenyl (**F**) group has a typical PES shape, and as each **NxxF** molecule is a combination of **Nx** and **xF** moiety, the expected arrangement is easy to visualise with the amide link as a linker group separating both aromatic rings.

The *para*-pyridine (**Np**) ring gives a PES profile with two global maxima located at *ca.* 60°, -120° (TS_{Np}^{II} = 12.01-13.43 kJ.mol^{-1}), two local maxima near -25°, 155° (TS_{Np}^{I} = 1.08-2.05 kJ.mol^{-1}). The four global minima are located at or near 0°, 125°, ±180° and -55°. The *meta*-pyridine (**Nm**) ring gives a PES profile with two global minima *ca.* -50°, 0°, two global maxima near 65°, -120° (TS_{Nm}^{III} = 15.04±0.15 kJ.mol^{-1}) and two local minima *ca.* 125°, ±180° (LM_{Nm}^{I} = 3.33-5.00 kJ.mol^{-1}). The two local maxima are located at -25° (TS_{Np}^{I} = 0.83-1.55 kJ.mol^{-1}) and 155° (TS_{Np}^{II} = 5.15-7.90 kJ.mol^{-1}). The *ortho*-pyridine (**No**) ring has a symmetrical PES profile with one global maximum at ±180° (TS_{No}^{II} = 52.70-60.24 kJ.mol^{-1}), two local maxima at ±105° (TS_{No}^{II} = 47.55-51.84 kJ.mol^{-1}), two local minima at ±135° (LM_{No}^{II} = 45.57-50.91 kJ.mol^{-1}) and one global minimum.

The *para*-fluorophenyl (**pF**) ring gives a PES profile with two global maxima at ±90° (TS_{pF}^{I} = 13.46-17.94 J.mol^{-1}) and two global minima at 0°, ±180°. The *meta*-fluorophenyl (**mF**) ring shows a PES profile with two global maxima near ±90° (TS_{mF}^{I} = 16.12-20.58 kJ.mol^{-1}), one local minimum at ±180° (LM_{mF}^{I} = 0.23-0.58 kJ.mol^{-1}) and one global minimum. The *ortho*-fluorophenyl (**oF**) ring gives an asymmetrical PES profile in **NpoF** and **NmoF**, but symmetrical for **NooF**. There is a global maximum at ±180° (TS_{oF}^{II} = 46.69-52.17 kJ.mol^{-1}). **NpoF** and **NmoF** have one local maximum at -95° (TS_{oF}^{I} = 24.22±0.53 kJ.mol^{-1}), one local minimum at -120° (LM_{oF}^{II} = 23.17±0.48 kJ.mol^{-1}) and of note, a point of inflexion at 110° (TS_{oF}^{II} = 25.68±0.15 kJ.mol^{-1}). However, the symmetrical **NooF** has two local minima near ±120° (LM_{oF}^{I} = 24.09 kJ.mol^{-1}) and two local maxima at ±100° (TS_{oF}^{I} = 25.23 kJ.mol^{-1}).

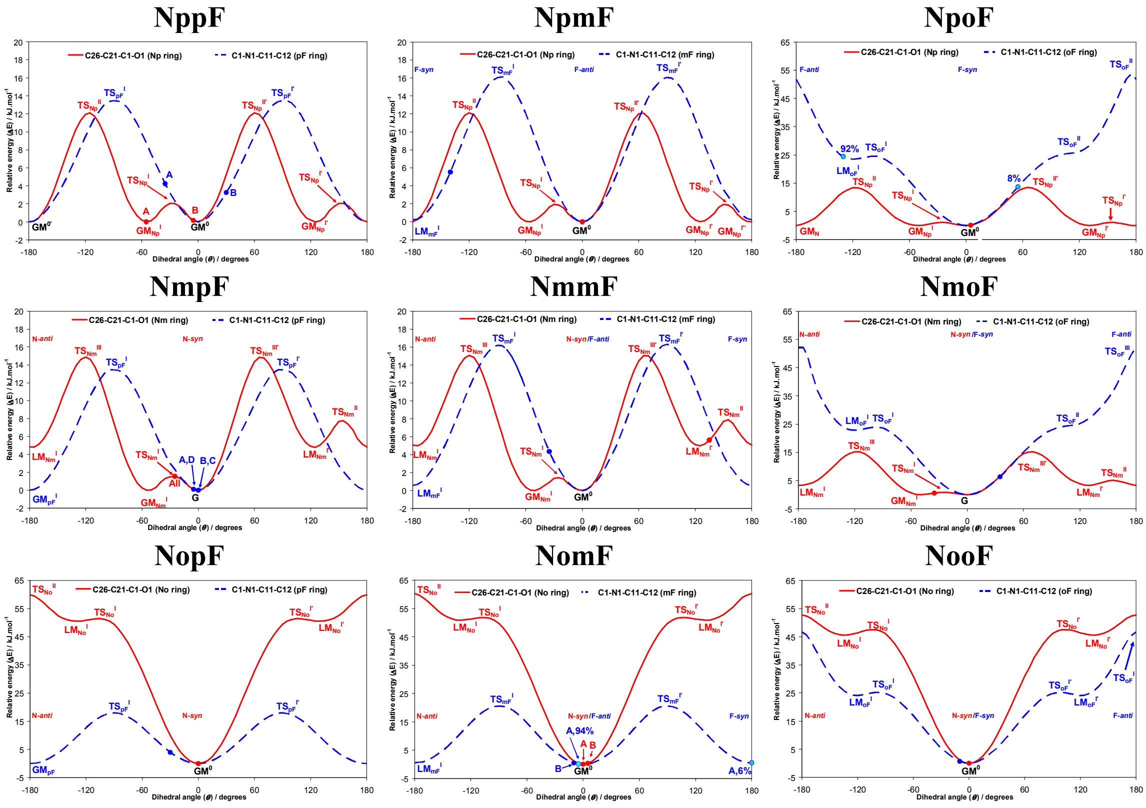
NppF
NpmF
NpoF
NmpF
NmmF
NmoF
NopF
NomF
NooF

Fig. 33: The PES conformational analysis for the nine **NxxF** isomers optimised in the gas phase: the equivalent solid state angle is depicted as a (●), with, if applicable, assigned identification letter and/or partial occurrence (%).

For the **Np** and **pF** rings all conformations at their minima are energetically identical; for the **Nm** ring the **N-*syn*** conformation is the most stable, although the **N-**

anti conformation is possible, but less likely. The **No** ring exists only in the **N-*syn*** conformation, while for **oF** the **F-*syn*** conformation is preferred. This supports the **NoxF** intramolecular N1-H1···N22 interaction supported by the weaker N1-H1···F12 hydrogen bond in **NooF** (the local maxima positions of both **No** and **oF** curves show that the N-H···N interaction energy is *ca*. twice the strength of the N-H···F interaction). In comparison, the conformational diagrams of the **mF** ring show that the difference between the preferred **F-*syn*** and **F-*anti*** conformations is small (0.58 kJ.mol^{-1}), and both conformations are possible. This possibility is demonstrated in two cases. Firstly, the **NpmF** crystal structure ($Z' = 1$) (Fig. **26)** is in the **F-*syn*** conformation. Secondly, the **NomF** structure (Fig. **31**) has a minor component of disorder at F15A with an occupancy of 6.1(5)% and averaged over both molecules the **mF** rings have *ca*. 3% in the **F-*syn*** and 97% occupancy in the **F-*anti*** conformation.

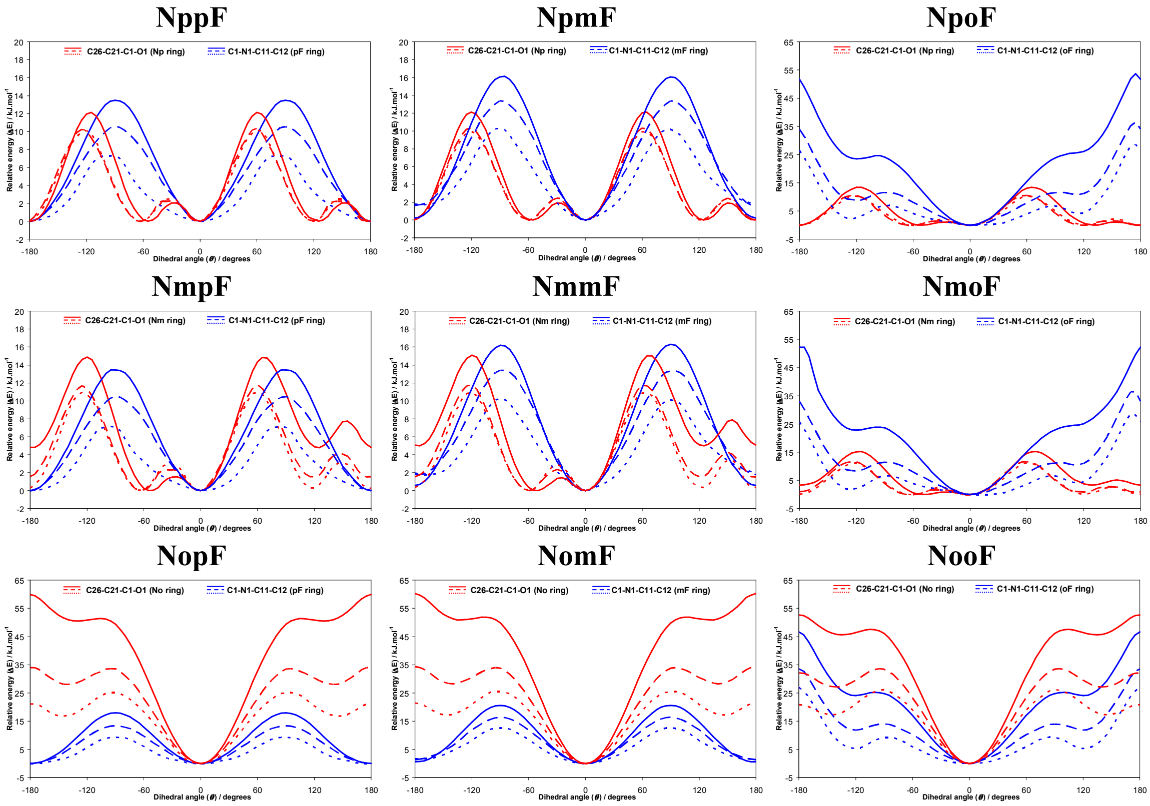

Fig. 34: The PES conformational analysis diagrams for the nine **NxxF** isomers optimised in gas phase (full line), CH_2Cl_2 (dashed line) and in H_2O (dotted line) using the PCM-SMD solvation method.

In summary, the optimised structures (*gas phase*) typically have **N-*syn*/F-*syn*** conformations but the exceptions are **NxmF** where the **N-*syn*/F-*anti*** conformation is the most stable. Differences between the **N-*syn*/F-*syn*** and **N-*syn*/F-*anti*** conformations are small with both conformations being plausible.

The conformational analysis results in the solvents CH_2Cl_2 and H_2O using the implicit PCM-SMD model are shown as PES scans in Fig. **34**, while in the ESI I high resolution diagrams are provided (Section 3.3.2). Comparisons between the *gas phase* and solvents reveals no conformation changes with all **NxpF** and **NxoF** molecules (at the stationary point) having the **N-*syn*/F-*syn*** conformation, while **NxmF** have the **N-*syn*/F-*anti*** conformations regardless of medium. Furthermore, the patterns of maxima and minima are similar, but there are significant decreases in the rotational energy necessary for aromatic ring flipping from one conformation to another.

Rotational barriers (for conformational analysis under PCM-SMD solation model) decrease almost linear for the **pF** (~23% in CH_2Cl_2, ~59% in H_2O), **mF** (~19% in CH_2Cl_2, ~43% in H_2O) and **oF** rings (by ~46% in CH_2Cl_2, ~70% in H_2O) when compared with *gas phase* rotational barriers. There is a dramatic decrease for the **oF** ring with a change in the overall curve shape. For **Np** (~27%) and **Nm** (~28%) the decrease is similar for both solvents and for the **No** ring the rotational barrier drops by ~36% in CH_2Cl_2 and ~52% in H_2O. Another effect is the additional linear drops of LM_{Nm}^{I} and TS_{Nm}^{II} (by ~28% in CH_2Cl_2, ~45% in H_2O) and elevation of LM_{mF}^{I} (by an average of 1.24 ± 0.27 $kJ.mol^{-1}$ in both solvents) and a shift of some of the minima in the **Np** and **Nm** rings by ±10°.

The implicit dielectric field incorporated in the PCM-SMD model of solvation will predict decrease of the rotational barriers and conformational change would be more likely. This model can be applicable only for solvents in which the **NxxF** isomers are fairly soluble. The high dielectric constant of water ($\varepsilon_r = 80$) is supposed to significantly reduce the rotational barriers and disrupt the **NoxF** intramolecular interactions. However as is evident from their insolubility in water and the calculated ΔG_{solv} (given in the ESI I section 3.3.1) this solvation in water is not favoured thermodynamically. Spectroscopic data (ESI I, Section 1.3) shows that a solvent with a high dielectric constant such as DMSO disrupts the intramolecular hydrogen bonds in **NoxF** and supports the *ab initio* predictions and results.

2.1.7.3. **Energy results**

The energy calculation results (CBS-QB3) (Table **21**, comprehensive information is given in the ESI I, Section 3.3.1) comprise the electronic energies (δE_{SCF}) and Gibbs free energies (δG) in all three media, including ΔG_{solv} for CH_2Cl_2 and H_2O, as well as $\Delta\Delta G_{solv}$ (CH_2Cl_2 *vs*. H_2O). Differences between each molecule are given as

δE_{SCF} (δG) and differences between media as ΔE_{SCF} (ΔG). The **NppF** energies are the *gas phase* reference points (least stable isomer) and **NpoF** energies for the solvents (as least stable). The large energy decrease for the **NoxF** triad is due to the intramolecular N1-H1···N22 interaction thus stabilising the **NoxF** molecular series. In addition, a weak stabilisation effect of the *meta*-F atom is discernible and these two effects make **NmoF** the most stable of the **NxxF** isomer grid.

The solvation of the **NxxF** isomers in CH_2Cl_2 is stabilizing and favourable, much more than solvation in H_2O. Differences in stabilisation among the nine isomers are considerable (Table **21**). From **NppF** to **NooF** the stability gain (on solvation) decreases consistently. This solvation effect is greatest in the six **NpxF**, **NmxF** isomers compared to the **NoxF** triad which gain less stabilisation (in terms of energy decrease).

Table 21: The energy calculation results for the **NxxF** isomers in $kJ.mol^{-1}$

	gas phase		CH_2Cl_2		H_2O		*gas phase*→ CH_2Cl_2		*gas phase*→ H_2O		CH_2Cl_2→ H_2O	
	δE_{SCF}	δG	δE_{SCF}	δG	δE_{SCF}	δG	ΔE_{SCF}	ΔG_{solv}	ΔE_{SCF}	ΔG_{solv}	$\Delta\Delta E_{SCF}$	$\Delta\Delta G_{solv}$
NppF	0.00	0.00	-4.62	-3.17	-7.25	-3.73	-70.81	-62.30	-57.08	-42.27	13.73	20.03
NpmF	-5.43	-1.68	-9.80	-5.12	-11.79	-7.78	-70.56	-62.57	-56.19	-44.64	14.37	17.93
NpoF	-3.50	-3.13	0.00	0.00	0.00	0.00	-62.69	-56.00	-46.33	-35.40	16.35	20.59
NmpF	-6.08	-2.30	-10.40	-4.02	-13.46	-5.39	-70.50	-60.86	-57.21	-41.63	13.29	19.23
NmmF	-11.79	-3.86	-15.81	-6.31	-18.61	-8.08	-70.21	-61.59	-56.66	-42.76	13.55	18.83
NmoF	-9.36	-4.91	-5.98	-1.02	-6.88	-1.97	-62.80	-55.24	-47.35	-35.60	15.45	19.64
NopF	-30.99	-28.26	-24.36	-22.73	-20.22	-16.11	-59.56	-53.61	-39.06	-26.39	20.50	27.22
NomF	-36.84	-29.83	-29.68	-25.82	-25.20	-19.49	-59.03	-55.13	-38.19	-28.20	20.84	26.93
NooF	-31.66	-28.11	-19.69	-17.57	-14.22	-15.57	-54.22	-48.59	-32.39	-26.00	21.83	22.60

[a] Only the differences between each molecule (δ) and media (Δ,ΔΔ) are shown, the reference molecule for the gas phase is **NppF** (E_{SCF} = -743.1027 E_h, G = -746.1394 E_h) and for solvents is **NpoF** (CH_2Cl_2: E_{SCF} = -743.1279 E_h, G = -746.1620 E_h; H_2O: E_{SCF} = -743.1217 E_h, G = -746.1541 E_h).

The calculated $\Delta\Delta G_{solv}$ for CH_2Cl_2/H_2O (D/W) system are strongly positive, illustrating insolublity in H_2O (provisional $\log K_{D/W}$ values based on $\Delta\Delta G_{solv}$ are 3-5: ESI I, Section 3.3.1). The **NoxF** triad should be the least soluble in H_2O (~$\log K_{D/W}$ = 4-5); empirical observations confirm these calculated predictions.

2.1.8. Comparisons of the solid state and modelling data

The nine **NxxF** isomers derived from calculations and crystal structures were compared by showing the differences in the corresponding torsion angles ($\Delta\theta$) as (●) for each crystal structure in each PES diagram (Fig. **33**). For **NppF**, **NmpF** and **NomF** with *Z*' > 1, the molecules are labelled as A, B *etc*. and for disordered systems (**NomF**, **NpoF**) the symbol (●) has the assigned identification letter and partial occupancy (%).

In general, most solid state **NxxF** conformations correspond with their *gas phase* or solvated structures without significant deviations of the torsion angles from the *gas phase* optimised minima ($\Delta\theta$). Thermodynamically, formation of intermolecular bonds and contacts in the crystallisation process brings stabilisation that is more than sufficient to overcome destabilisation caused by torsion angle deviations.

Conformational differences amongst the **NxxF** isomers include **NpmF** having the **F-*syn*** conformation in crystal structure, **NmmF** with an **N-*anti*/F-*anti*** conformation, as well as the disordered molecule A in **NomF** where a minor F component is present in the **N-*syn*/F-*syn*** conformation and surprisingly **NpoF** where the main molecular conformation at 91.7(9)% occupancy has the **F**-ring in a *meta*-stable form with the **F-*anti*** conformation.

In almost all cases the data values for the solid-state torsion angles of the **N**-rings are on or near their calculated global minima (Fig. **33**), and often with only small deviations. The only exceptions include the **Nm** rings in **NmpF** and **NmmF**. For **NmpF** with *Z*' = 4 (Fig. **29**) all four independent molecules are planar in this *unusual* hydrogen bonded tetrameric assembly and the **Nm** ring torsion angles are similar and located near TS_{Nm}^{I} which represents a relatively unstable position (*gas phase*). However, the solid-state conformation allows the *meta*-pyridine N atom to engage in intermolecular N-H···N_{pyr} hydrogen bonding with one relatively long N-H···N_{pyr} and augmented by two flanking C-H···N intermolecular interactions. Ultimately the **NmpF** supramolecular structure represents a hydrogen bonded tetramer that aggregates from a series of weak but cumulatively important N/C-H···N interactions (Fig. **29**).

For the **NmmF** structure the **Nm** ring torsion angle is in the **N-*anti*** conformation in a *meta*-stable $LM_{Nm}^{I'}$ potential well. Despite this *unusual* conformation, examination of the crystal packing shows that the **N-*anti*** conformation facilitates the 1-D chain of N1-H1…N23 hydrogen bonding that is essential as the crystal structure backbone.

In contrast to the **N**-ring, the solid state **F**-ring torsion angles usually do not overlap with the corresponding *gas phase* model pendant angle: the deviation $\Delta\theta$ is around ±30-50º, excluding the structures that are planar or close to planarity (**NmpF**, **NomF**, **NooF**) and the **NpoF** structure. The **NomF** and **NooF** are the only structures where the solid state structures correspond closely with only a slight $\Delta\theta$ deviation from the model structures.

The minor presence of the **N-*syn*/F-*syn*** conformation in **NomF** (at 3%) is interesting where conformational analysis of the **mF** ring demonstrates that the **F-*syn*** conformation is similar to **F-*anti***, and allowing the **F-*syn*** conformation to appear statistically probable. An overview of the **NomF** crystal structure shows that the fluorine atoms at their thermodynamically favoured, major occupation site (F13, **F-*anti***) are in a position to interact with neighbouring molecules, a making network comprised of weak C-F···H-C and C-F···F-C bonds, like F13A···H24A-C24A [3.339(4), -1/2+x, 1/2-y, 1/2+z] and F13A···F13A [2.896(3), -x,-y,2-z]. The **F-*syn*** conformation gives fewer possibilities for F···H/F/C interactions, but even those interactions contribute to the overall crystal structures. Taking the fact that the difference between **F-*syn*** and **F-*anti*** is 0.58 kJ.mol^{-1}, the minor **F-*syn*** conformation is presumably statistical disorder, driven by kinetic factors.

Another phenomenon is observed in **NpmF** where the solid state conformation of the **F**-ring is **F-*syn***, although the **F-*anti*** conformation is slightly thermodynamically favoured from calculations. The main backbone of the **NpmF** crystal structure is the short N1-H1···N24 hydrogen bond that drives the formation of *C*(7) *zig-zag* chains. As the **F**-ring adopts the **F-*syn*** conformation, H15 atom forms a very important contact [C15-H15…O1, 3.202(5) Å] with O1 (at -1/2+x, 1/2-y,-1/2+z) that links up the 1-D *zig-zag* chains into 2-D sheet. The fluorine atom (F13) forms weak contacts (C22/23-H22···F13, 3.212(4)/3.222(4) Å) with neighbouring molecule (at -1+x, y,-1+z), supporting the main *zig-zag* backbone, as well as weak contacts [C22/23···F13, 3.166(4)/3.222(4) Å] with C22/C23 (at -1+x,-y,-1/2+z) which participates, along with H25···Cg interaction, in joining the 2-D sheets into the 3-D network. All these contacts (Fig. **26**) would not be possible if the F-ring was in the **F-*anti*** conformation. Therefore, the **F-*syn*** conformation, despite its *meta*-stability in *gas phase,* is essential for **NpmF** crystal structure assembly.

The **NpoF** structure is atypical with 91.7(9)% of the **NpoF** molecules in a thermodynamically unfavourable *meta*-stable local minimum LM_{oF}^{I} with the *ortho*-F atom at F12. The **NpoF** isomer is isomorphous with **NpmF** in space group *Cc*. A study of the crystal packing of **NpoF** shows that with the minor F16 atom site [8.3(9)%] located as **F-*syn*** it is directed near the N1-H1···N24 primary intermolecular interaction [with F16···N24 = 2.84(4) Å] and effects a measure of steric hindrance. It is possible that the **F-*anti*** (F12 site) conformation even though it is relatively thermodynamically unstable allows for stabilisation of the N-H···N interaction in the crystal structure.

NpoF can obviously cope with a measure of steric strain in the minor conformation incorporating the F16 atom site.

Overall, there are a few differences between the **NxxF** solid state molecular structures and the *ab initio* models and for those cases (as discussed above) this arises where conformational change is essential in the promotion of favourable formation of stable intermolecular hydrogen bonds in the solid state.

2. 2. NxxM isomer grid

2.2.1. General description of synthesis

As acyl chlorides are very reactive, the reactions were performed in anhydrous conditions in CH_2Cl_2 (under N_2), initially at 5°C and then at room temperature. A by-product was HCl, and Et_3N was employed to drive the reaction equilibrium towards the **NxxM** product. The pyridinoyl chlorides technically were used in the form of hydrochlorides so an additional mole of Et_3N was used to enhance their solubility in CH_2Cl_2 so that in total, two molar equivalents of Et_3N were added.

Table 22: Amounts, yields and melting points of the **NxxM** compounds

NxxM	m/g	yield/%	m.p./ºC
NppM	1.578	78.9	161.0-162.5
NmpM	1.847	92.3	140.2-142.9
NpoM	1.747	87.3	123.9-125.9
NmpM	1.863	93.1	147.6-148.3
NmmM	1.530	76.5	113.0-114.7
NmoM	1.390	69.5	106.1-107.0
NopM	1.340	67.0	104.7-105.2
NomM	0.876	43.8	49.2-50.5
NooM	1.134	56.7	64.1-64.9
5-Cl-NopM	0.250	12.5	125.5-129.5
5-Cl-NomM	0.224	11.2	70.2-73.9
5-Cl-NooM	0.332	16.6	128.3-128.6

Condensation reactions were performed with the 4-, 3- or 2-toluidines (1 ml, 10.41 mmol) added to a 250 ml flask placed on an ice bath and with subsequent stirring. Then, 30 ml of CH_2Cl_2 was added to the flask followed by addition of Et_3N (1.5 ml, 10.76 mmol). Finally, the 4-, 3- or 2-pyridinoyl chlorides (2 g, 11.23 mmol) were added in portions directly into this solution mixture. Another 30 ml of CH_2Cl_2 and 1.5 ml of Et_3N was added to accelerate the dissolution of any solids and the reaction mixture was allowed to warm to room temperature and stirred overnight.

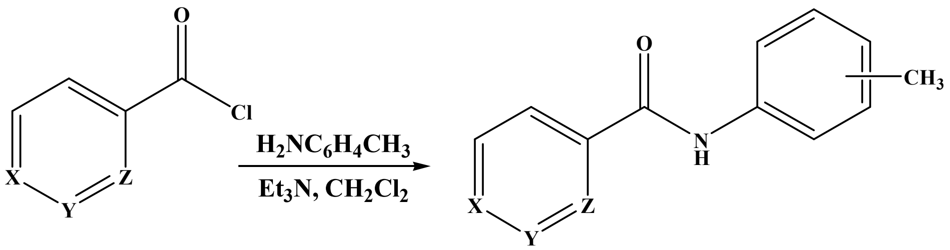

para (4-pyridinoyl): (X = N, Y = C, Z = C)
meta (3-pyridinoyl): (X = C, Y = N, Z = C)
ortho (2-pyridinoyl): (X = C, Y = C, Z = N)

Scheme 28: Schematic diagram of the **NxxM** reactions

Organic washing and work-up was as standard: the organic reaction phase was washed with 20 ml of $KHCO_3$ (0.1 M) solution *ca.* 3-7 times and during purification, glassware was warmed to *ca.* 35°C. Then, 1.5 g of anhydrous $MgSO_4$ was added to the organic solutions for 20 minutes. The flask contents were filtered through a Büchner funnel (under vacuum) to remove $MgSO_4$. The filtrate was evaporated under vacuum and the crystallization induced giving the desired product.

Generally, the yields (30-70%) and purity were modest to excellent with the exception of the **NoxM** triad where **5-Cl-NoxM** compounds were by-products (Table **22**), as the picolinoyl chloride starting material contains a small quantity of 5-chloro-picolinoyl chloride. This impurity is an inevitable by-product of the original 2-pyridinoyl chloride synthesis using $SOCl_2$. The same impurities are present in the **NoxF** compounds, however only simple re-crystallisation purification was employed in the **NoxF** triad, without intention of isolation, characterisation or structural survey of the **5-Cl-NoxF** compounds.

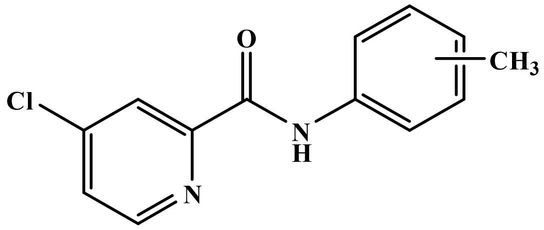

	para-tolyl	*meta*-tolyl	*ortho*-tolyl
ortho (5-chloro-2-pyridinoyl)	**5-Cl-NopM**	**5-Cl-NomM**	**5-Cl-NooM**

Scheme 29: Structures and nomenclature of the three **5-Cl-NxxM** isomers

The **NoxM** compounds were successfully separated from of the **5-Cl-NoxM** compounds by column chromatography using silica gel as stationary phase and a mixture of $CHCl_3$, ethyl acetate and cyclohexane (4:2:1) The three **5-Cl-NoxM** compounds were isolated in low yield and characterised by both spectroscopic methods and single crystal X-ray diffraction. In addition, the structure of **NmpFM** (isolated from a 50:50 mixture of **NmpF** and **NmpM**) is compared with both **NmpF** and **NmpM**.

All **NxxM** compounds are white, odourless solids, soluble in various organic solvents (MeOH, ethyl acetate, CH_2Cl_2, $CHCl_3$, 2-propanol, DMSO), poorly soluble in cyclohexane, hexane, toluene and insoluble in water. The overall yields were moderate to good and the **NxxM** and **5-Cl-NxxM** compound purity was excellent after column chromatography. The **NpxM**, **NmxM** and **NopM** isomers crystallize easily from a range of solvents. However, after purification by column chromatography **NomM** proved reluctant to crystallise from several solvents using different crystallization conditions. Crystals were finally obtained using stress cooling with liquid N_2 followed by re-crystallisation from cyclohexane. Solid **NomM** differs from the other **NxxM** isomers and looks ceraceous rather than crystalline. **NooM** crystals were obtained after several trials from CH_3OH. In general, melting points decrease (Table **22**) consecutively from the symmetrical **NppM** to the unsymmetrical **NomM**. The lowest melting point for **NomM** (~50ºC) is unusual, suggesting, together with other macroscopic characteristics, weak and unusual intermolecular interactions in the **NomM** crystal structure. The **5-Cl-NoxM** derivatives have higher melting points as compared to their **NoxM** relatives and by > 20°C; this effect is due to replacement of H by Cl.

2.2.2. X-ray crystallography methods

All nine **NxxM** crystal samples and three **5-Cl-NoxM** single crystals were obtained by slow evaporation at 4ºC, typically from either $CHCl_3$ or ethyl acetate. However, for **NomM**, suitable single crystals were grown from cyclohexane and for **NooM**, crystals were eventually grown from methanol after many crystallization attempts from several solvents under a wide range of crystallization conditions.

Single crystal X-ray data for all nine **NxxM** isomers, the three **5-Cl-NoxM** and **NmpFM** collection and data reduction,[176] structure solution and refinement[3,168] was as described for the **Fxx** isomer grid (Section 1.2.2). Selected crystallographic and structural information are detailed in Tables **23**, **24** and the ESI I (Section 2.4). Molecular and hydrogen bonding diagrams (Figs. **35-44**) were generated as for the other isomer grids.[169]

2.2.3. Computational methods

The computational methods and procedures used are identical to the previous isomer grids. Each asymmetric (*meta*- or *ortho*-) ring can adopt (relative to the amide linker) two conformations (either ***syn*** or ***anti***) (Scheme **30**). The pyridine (**N**) or tolyl (**M**) rings can be either ***syn*** (**N-*syn***, **M-*syn***) or ***anti*** (**N-*anti***, **M-*anti***) and this does not apply for *para*-substitution. Conformational analysis was undertaken using PES scans of the two key dihedral angles over a range ±180º both in *gas phase* and solvents, as the C26-C21-C1=O1 dihedral (α, **N**-ring), and C1-N1-C11-C12 dihedral (β, **M**-ring). The results provide PES diagrams showing the conformational preferences either as (***syn***/***anti***) and the rotational barriers in kJ.mol^{-1}.

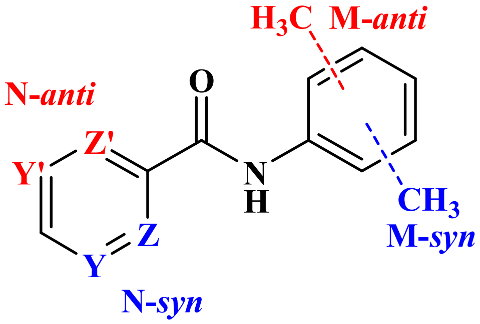

Scheme 30: Possible conformations of the **NxxM** isomers

2.2.4. Comment on spectroscopic data

All spectroscopic data, including NMR and IR spectra, are listed in the Appendix I (Section 2.2), while the spectra are given in the ESI I (Section 1.4). The NMR data (^{1}H, ^{13}C) show a high level of modularity within the pyridine and tolyl rings across the **NxxM** isomer grid as expected. As for the **NxxF** series the spectroscopic data reveal the presence of the intramolecular N-H···N$_{pyr}$ interactions in the **NoxM** and **5-Cl-NoxM** triads. The shifts for the amide hydrogen (N-H) in the six **NpxM**/**NmxM** isomers in $CDCl_3$ are *ca*. 8.0 ppm, while in DMSO-*d$_6$* are shifted to *ca*. 10.3 ppm from interacting with the S=O group. In the **NoxM** triad the shifts are ~10.0 ppm (in $CDCl_3$) and 10.5 ppm (in DMSO-*d$_6$*) indicating the presence of additional internal de-shielding of the amide hydrogen as a result of interacting with the neighbouring N$_{pyr}$ atom. The intramolecular N1-H1···N22 interaction in the **NoxM** triad is also noted in the ATR-IR with one sharp N-H stretching band at 3336 (**NopM**), 3286 (**NomM**), 3343 cm^{-1} (**NooM**) and contrasting with weaker, more diffuse N-H vibrations in the **NpxM**/**NmxM** series.

2.2.5. Crystallographic data and analysis

2.2.5.1. General comments

The nine **NxxM** and three **5-Cl-NoxM** crystal structures crystallise in seven common space groups with only CH_3 methyl group rotational disorder of the H atom sites in six of the twelve structures (treated with AFIX 127). Seven **NxxM** and three **5-Cl-NoxM** isomers crystallise with *Z'* = 1 and **NmmM**, **NomM** with *Z'* = 2 (Table **23**). The twelve compounds can be classified into two distinct (**NpxM**, **NmxM**) and (**NoxM**, **5-Cl-NoxM**) groups.

The distinct intermolecular feature of the **NxxM** crystal structures is aggregation in the solid state either *via* $_{amide}$N-H···N$_{pyridine}$ or N-H···O=C hydrogen bonds, and usually in different space groups. The primary hydrogen bond in **NpmM**, **NmpM** and **NmmM** is $_{amide}$N-H···N$_{pyridine}$ usually in tandem with a much weaker C-H···O=C interaction (*ca*. 0.2 Å longer). In **NppM**, **NpoM** and **NmoM**, the primary interaction is $_{amide}$N-H···O=C$_{amide}$ with additional weak contacts (*ca*. 2.70 Å for C-H···N) involving the pyridine-N atom and pyridine ring. In the related **NxxF** series, only **NppF** has $_{amide}$N-H···O=C$_{amide}$ interactions as the primary interaction [as typical *C*(4) chains] and with no additional longer C-H···N interactions.

Table 23: Selected crystallographic data for **NxxM**, **NmpFM**, **5-Cl-NoxM**

Structure	**Space group**	***Z'***	**Volume (Å^3)**	***R*-factors**
NppM	$P2/c$	1	1089.98(9)	0.051, 0.141
NpmM	$P2_1/n$	1	1133.67(6)	0.034, 0.083
NpoM	Cc	1	1123.84(11)	0.030, 0.081
NmpM	$P2_1/c$	1	1074.47(8)	0.036, 0.073
NmmM	$P\bar{1}$	2	1085.36(7)	0.057, 0.179
NmoM	$Pbca$	1	2239.48(10)	0.040, 0.107
NopM	$P2_1/c$	1	1100.40(7)	0.035, 0.083
NomM	$P2_1$	2	1178.92(8)	0.029, 0.045
NooM	$P2_1/c$	1	1099.41(5)	0.037, 0.093
NmpFM	$Pna2_1$	0.5:0.5	1062.66(18)	0.035, 0.093
5-Cl-NopM	$Pca2_1$	1	1189.24(3)	0.026, 0.065
5-Cl-NomM	$P2_1/c$	1	1204.0(5)	0.066, 0.233
5-Cl-NooM	$P2_1/n$	1	1171.93(15)	0.038, 0.103

In the three **NoxM** crystal structures, the intramolecular N-H···N interaction dominates with additional longer C-H···O interactions in **NopM** (+2) and **NooM** (+1), but in **NomM** an additional N-H···O=C interaction (H···O = 2.32(3), 2.41(2) Å) with C-H···O=C forms a hydrogen bonded $R^1_2(6)$ ring (Fig. **42**). The **NomM** crystals provide the poorest quality structure with a high R_{int} (0.096) and unexpected aggregation;

NomM has the lowest melting point range of just 49-50°C. Three **5-Cl-NoxM** structures also display the intramolecular N1-H1···N22 interaction and are similar to **NoxM** except for **5-Cl-NomM** with N-H···O=C/π···π stacking interactions being atypical of either the **NoxM** or **NoxF** structures. In addition, the mixed fluoro/CH_3 system as **NmpFM** is isolated from a 50:50 mixture of **NmpF**/**NmpM** and is compared with the tetrameric assembly in **NmpF** and catemeric **NmpM** structure.

Table 24: Salient structural features (°, Å) of **NxxM**, **NmpFM** and **5-Cl-NoxM**

Structure	C_6/C_5N	**C_6/amide**[a]	**C_5N/amide**[a]	**N···N/O**	**Packing**[b]
NppM	66.45(3)	34.96(5)	31.54(5)	**3.0529(14)**	1-D chains
NpmM	4.50(10)	14.73(7)	19.19(7)	**3.1265(18)**	2-D sheets
NpoM	83.90(6)	68.04(7)	28.26(9)	**2.825(2)**	1-D chains
NmpM	4.11(9)	4.11(9)	1.06(9)	**3.223(2)**	1-D catemers
NmmM	57.23(6)	24.69(6)	33.93(8)	**3.090(2)**	1-D chains
	64.31(6)	36.68(6)	28.23(8)	**3.078(2)**	
NmoM	89.99(5)	60.63(5)	29.55(6)	**2.8978(15)**	1-D chains
NopM	33.63(4)	29.45(5)	4.33(4)	**2.6548(18)**	1-D chain
NomM[c]	14.61(14)	15.39(14)	4.63(15)	**3.241(3)**[c]	2-D sheets
	9.71(17)	6.54(15)	16.03(16)	**3.132(3)**	
				2.683(4)	
				2.703(4)	
NooM	1.91(5)	1.47(5)	1.70(5)	**2.6209(15)**	Dimers
NmpFM	5.00(14)	3.21(13)	1.93(13)	**3.207(2)**	2-D Cat sheets
5-Cl-NopM	26.42(2)	22.25(2)	4.20(3)	**2.6514(9)**	2-D sheet
5-Cl-NomM[c]	4.35(13)	8.98(12)	12.79(12)	**3.035(4)**[c]	1-D chains
				2.683(4)	
5-Cl-NooM	2.30(5)	4.38(6)	2.80(5)	**2.6690(15)**	1-D tape

[a] Amide plane calculated as a five atom plane *i.e.* $_{Ar}C-C(=O)N-C_{Ar}$

[b] Packing is noted as primary packing unless for competing strengths and for **NoxM** and **5-Cl-NoxM**, additional interactions are considered where the primary interaction is intramolecular **N-H···$N_{pyridine}$**.

[c] For **NomM** and **5-Cl-NomM** both intramolecular **N-H···N** and intermolecular **N-H···O=C** interactions are quoted.

As noted above, the primary hydrogen bonding in the **NxxM** isomers can be classed into three groups, each with distinctive IR spectra in the N-H stretch region between 3600 cm^{-1} and 2800 cm^{-1}. The **NpmM**, **NmpM** and **NmmM** isomers with $_{amide}$N-H···$N_{pyridine}$ as the main intermolecular interaction exhibit two principal N-H stretch vibrations at 3274 cm^{-1} and 3066 cm^{-1} with several smaller peaks. The second group comprising **NppM**, **NpoM** and **NmoM** with $_{amide}$N-H···O=C_{amide} interactions has a smaller band at 3073 cm^{-1} and one close to 3322 cm^{-1} (3237 cm^{-1} for **NpoM** and **NmoM** as the proximity of the *ortho*-CH_3 moiety clearly changes the frequency of the N-H stretching vibration). The third group consisting of **NoxM** and **5-Cl-NoxM** display the intramolecular N1-H1···N22 interaction as the main hydrogen bond and exhibit a typical sharp peak at around 3335 cm^{-1} (3286 cm^{-1} for **NomM** due to the additional interaction of the amide N-H with a neighbouring carbonyl oxygen). Therefore, IR spectroscopy provides a useful indicator of the type of N-H hydrogen bonding in these and related crystal structures and has been especially useful in identifying polymorphs.

2.2.5.2. **The NpxM isomer series**

The three **NpxM** isomers aggregate *via* $_{\mathrm{amide}}$N-H···O=C *C*(4) chains for both **NppM** and **NpoM** isomers and through $_{\mathrm{amide}}$N-H···N$_{\mathrm{pyridine}}$ *C*(7) chains for **NpmM**.

NppM molecular and crystal structure

The **NppM** isomer crystallizes in *P*2/c and refined initially to an *R*-factor of 0.15. Application of the twin law [100, 0-10, 00-1] results in an *R*-factor of 5% without any non-hydrogen atom disorder apart from the CH_3 rotational disorder. The hydrogen bonding as $_{\mathrm{amide}}$N-H···O=C$_{\mathrm{amide}}$ 1-D *C*(4) chains forms along the *b*-axis [010] direction (Fig. **35**) (Table **24**). There are no other strong interactions of note in an otherwise regular structure (with similarities to **NppF**). The pyridine N24 atom does not participate in hydrogen bonding, with the closest intermolecular H···N24 contact distance > 2.90 Å (similar to the lack of interactions for the pyridinyl N24 in **NppF**).

NpmM molecular and crystal structure

NpmM (with a **M-*anti*** tolyl ring conformation) aggregates *via* intermolecular N1-H1···N24 hydrogen bonds and assisted by a flanking C22-H22···N24 interaction forming a ring with graph set $R^1_2(7)$ (Fig. **35**). This tandem effect links as a 1-D column in the [010] direction; columns are linked reciprocally by longer C23-H23···O1 interactions parallel to the ($\bar{1}$01) plane into 2-D rumpled sheets. All interplanar angles are < 20° highlighting the near co-planarity of all atoms in **NpmM** in contrast to both of the **NppM** and **NpoM** crystal structures (Table **24**).

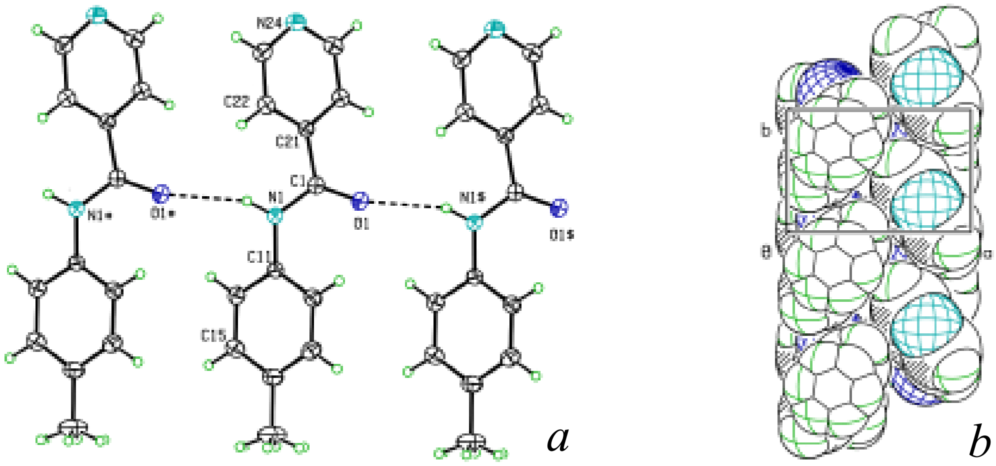

Fig. 35: *(a)* An ORTEP diagram of **NppM** as a chain of three molecules with the primary N-H···O=C interaction aggregating along the *b*-axis direction and (*b*) two chains with atoms as van der Waals spheres and parallel to the (001) plane.

NpoM molecular and crystal structure

NpoM with the tolyl ring in the **M-*syn*** conformation although almost orthogonal to amide linker (Table **24**) crystallizes in space group *Cc* with N-H···O=C as the primary hydrogen bond linking along the *c*-axis or [001] direction (Fig. **36)**. The short N1···O1^{i} = 2.825(2) Å is augmented by an *ortho*-$CH_3\cdots(O{=}C)^{i}$ interaction involving the methyl group interacting with the neighbouring C=O group (symmetry code i = x,-y,z-½) (Fig. **36)**. The closest intermolecular contact involving pyridyl N24 is with the aromatic H22 atom [H22···N24 = 2.72 Å]. The isomorphous **NpmF** and **NpoF** systems also crystallise in space group *Cc* but differ from **NpoM** by having N-H···$N_{pyridine}$ as the primary interaction.

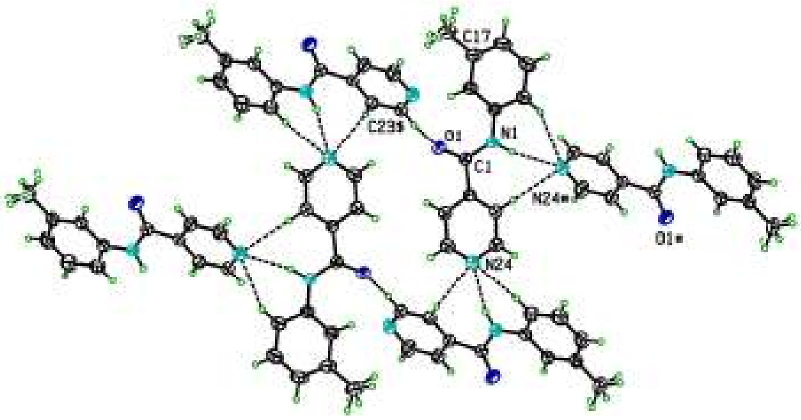

Fig. 35: An ORTEP diagram of **NpmM** as two chains with *zig-zag* primary N-H···N hydrogen bonds, C-H···N interaction/contacts and linked by C-H···O=C. The suffix labels # and $ are for symmetry related sites ½-x,½+y,3/2-z and -½+x,½-y,-½+z.

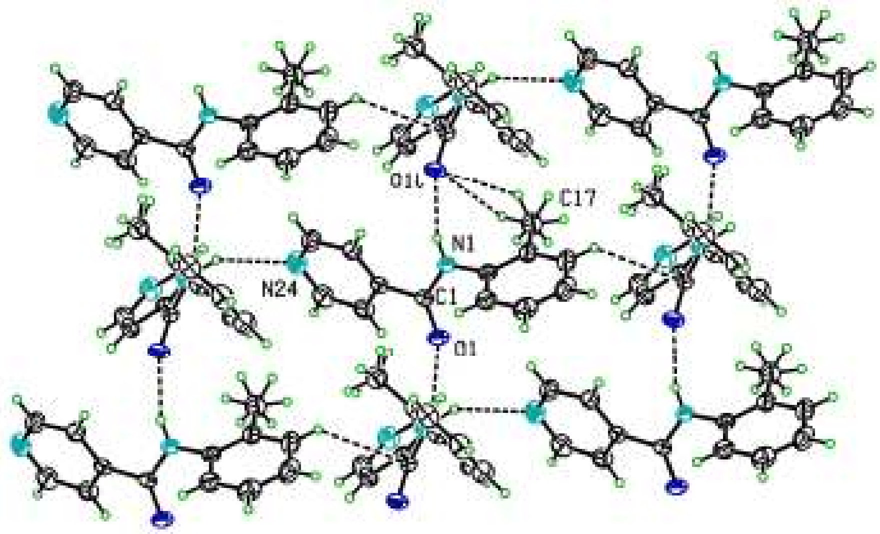

Fig. 36: An ORTEP diagram of **NpoM** with three molecules in three chains showing the primary N-H···O=C interaction propagated along the *c*-axis with weaker contacts at $O1^i$.

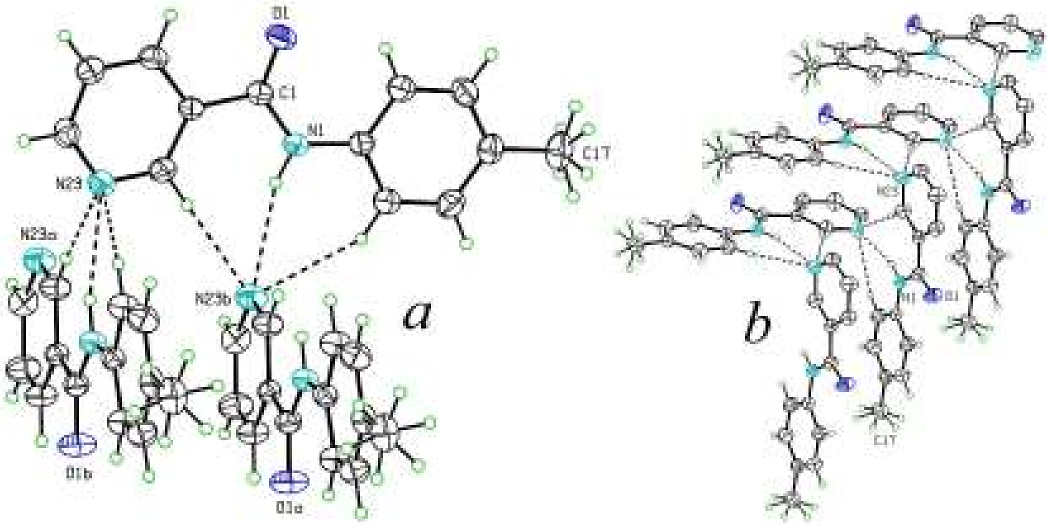

Fig. 37: An ORTEP diagram of **NmpM** as (*a*) three molecules with N/C-H···$N_{pyridine}$ interactions (at sites *a* = -x,½+y,½-z; *b* = -x,-½+y,½-z), (*b*) a catemeric linked column and with pyridyl H atoms omitted for clarity.

2.2.5.3. The NmxM isomer series

The three **NmxM** isomers aggregate by $_{amide}$N-H···$N_{pyridine}$ interactions for **NmpM** (**NmpFM**), **NmmM** and through $_{amide}$N-H···O=C interactions in **NmoM**.

NmpM and the NmpFM mixed molecular and crystal structure

NmpM crystallises as fine needles that splinter easily. The **NmpM** crystal structure (Fig. **37**) contrasts with **NmpF** (a hydrogen bonded tetramer). In **NmpM** the primary interaction that drives aggregation is also $_{\text{amide}}$N-H···N$_{\text{pyridine}}$ but is catemeric (Fig. **37**) and in the form of a stepped column with an intermolecular N···N distance of 3.223(2) Å and N-H···N angle of 164.7(12)°; the pyridinyl (**Nm**) ring has the **N-*syn*** conformation. In **NmpM** the assembly process as an N-H···N relay generates an alternating two molecule column along the *b*-axis [010] direction, linked by weaker C-H···O=C interactions along the [001] direction (2-D) and the C-H···C/π(arene) contacts along the [100] direction forming a 3-D structure. The key difference is that the CH$_3$ groups in **NmpM** form C-H···π(arene) interactions and link the stacked columns [with six C···C(arene) distances from 3.68 to 4.03 Å], whereas this does not arise as donor C-F···(arene) interactions in **NmpF**. The intermolecular data indicate that (at the primary interaction level) the **NmpM** and **NmpF** molecules are similar and differences between the remotely positioned CH$_3$/F groups influence the overall aggregation and packing. Catemeric/tetrameric aggregation interchange is known in pyrazole chemistry.[185] As both **NmpM** and **NmpF** contrast in their aggregation modes, their solution mixtures and resulting solid-state structure **NmpFM** were analysed.

A 50:50 solution of **NmpF**, **NmpM** (recrystallized from ethyl acetate) yields the crystal structure of **NmpFM** which differs from either **NmpF** or **NmpM**. The molecules occupy the same site in the asymmetric unit of space group $Pna2_1$ differing only by the 50:50% occupancy of the F14 atom and CH$_3$ group (Fig. **38)**.

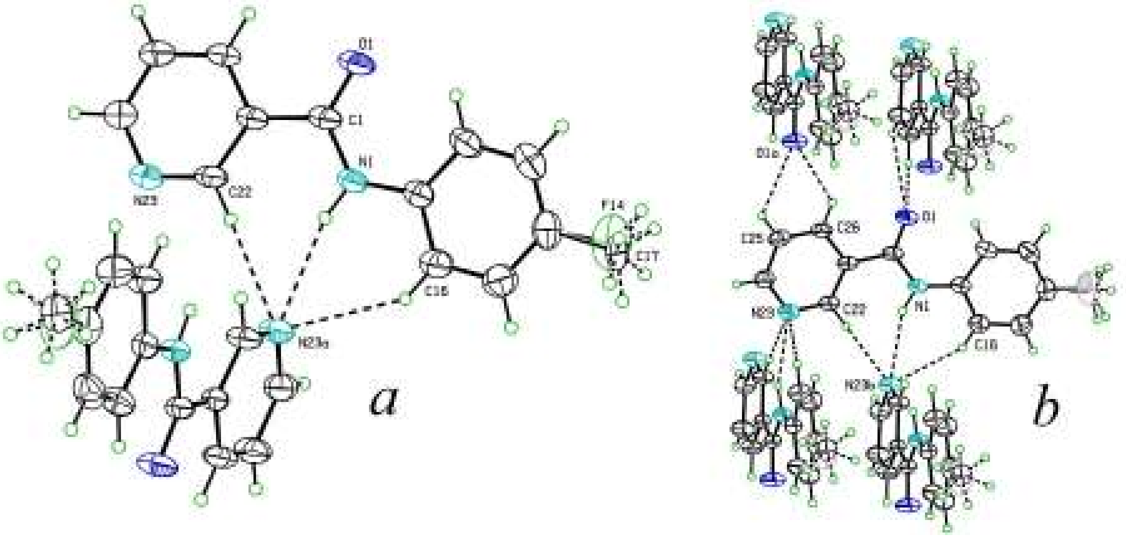

Fig. 38: An ORTEP view of two **NmpFM** molecules: *a*) the primary C/N-H···N$_{\text{pyridine}}$ [$R^1_2(6)$, $R^1_2(7)$ rings] and *b*) C-H···O=C interactions [$R^1_2(5)$ rings] in **NmpFM**.

NmpFM is comparable to both **NmpF** and **NmpM** structures in basic geometry. However, **NmpFM** is similar to **NmpM** in the primary intermolecular N-H···N/C-H···N hydrogen bonding mode but aggregation differs *via* weaker C-H···O=C by linking the columns into 2-D sheets which interlock *via* weaker C-H/F···C contacts (Fig**. 38)**. For comparison, the N···N intermolecular distances change from 3.2205(19) to 3.285(2) Å in **NmpF**, 3.223(3) Å in **NmpM** and 3.207(3) Å in **NmpFM**. The interchangeability of F/CH_3 moieties in crystal structures has been reported in the 5-fluorouracil:thymine crystalline solid solution.[190,191]

NmmM molecular and crystal structure

The **NmmM** structure ($Z' = 2$) is *essentially* isomorphous and isostructural with **Mmm**, the *amide reversed* or *'bridge-flipped*' related isomer (Fig. **39**). The **NmmM** unit cell parameters of 9.38, 9.92, 12.34 Å, 86.96°, 86.98°, 71.41° [RT] are similar to the unit cell data of **Mmm** (a *non- merohedral* twin) of 9.59, 9.99, 12.51 Å, 85.83°, 85.77°, 68.56° [at 294(1) K]. The ring conformations in **NmmM** are **N-*anti*/M-*anti*** (Figs. **12** and **46**) and for **Mmm** are **M-*anti*/P-*anti***. Comparisons between molecules A and B reveal C_6/C_5N interplanar angles of 57.23(6)°, 54.76(6)° in **NmmM**, and 55.57(10)°, 65.70(10)° in **Mmm**. For **NmmM** the primary N-H···N hydrogen bonding distances are 3.090(2), 3.078(2) Å and longer than 2.998(4) Å, 3.006(4) Å in **Mmm**. In **NmmM**, 1-D chains are linked by C-H···O interactions into 2-D sheets parallel to (110). Analysis of structural isomers differing by a '*bridge flip*' (with **NmmM** and **Mmm** as reversed amides) provides a perspective beyond analysis of the individual molecules. Comparisons of two $n \times m$ isomer grids can *potentially* yield invaluable structural information especially when *isomorphous* pairs are found.

Ojala and co-workers[192] have reported that isostructural relationships exist with halogen replacement (**X** = **F**, **Cl**, **Br**, **I**) in a benzylideneaniline series, but not with the *bridge flipped* isomers (as -CH=N- *vs*. –N=CH-). They stated that *'in general isostructuralism between bridge flipped isomers is rare. Differences between the isomers with respect to their molecular conformations and solid-state intermolecular interactions tend to differentiate their solid-state molecular packing arrangements*.' Herein, **NmmM** and **Mmm** provide a rare example of *isostructuralism* in *bridge-flipped* isomers (Fig. **39**). The melting point range is 113.0-114.7°C in **NmmM** and 90.0-91.0°C in **Mmm**, a difference of *ca*. 23°C.

However, **Mmm** is twinned (0.844:0.156) and despite the isostructural nature of these isomers, **Mmm** has fewer interactions and contacts due the absolute and specific nature of the packing. This may account for the disparity in mp ranges. Comparisons of *bridge flipped* isomers can provide information that polymorphs often cannot, as polymorphic forms *usually* differ substantially in packing and *often* with different Z'.[8,22]

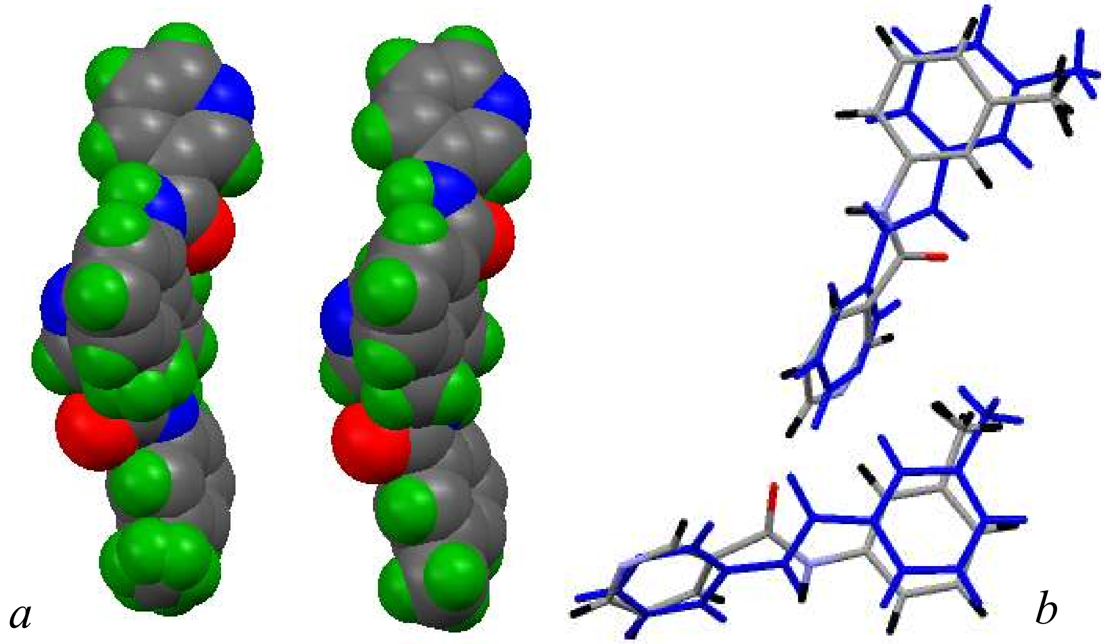

Fig. 39: (*a*) **NmmM** and **Mmm** molecules as their van der Waals spheres and highlighting the similarity of the asymmetric unit. (*b*) **NmmM** overlaid with **Mmm** in blue.

The **3,4-F$_2$** and **3,5-F$_2$** difluorobenzamide isomers[193] are *essentially* isomorphous structures (similar unit cells and gross packing) but with distinctly different primary hydrogen bonding distances due to the packing at the atom/group/ring level arising from differences in the peripheral ring substitution patterns of the **3,4-F$_2$** and **3,5-F$_2$** systems. Increasing numbers of related structures will provide more examples for future analysis and correlation.

NmoM molecular and crystal structure

NmoM forms $_{\text{amide}}$N-H···O=C$_{\text{amide}}$ interactions along [010] as the primary hydrogen bond augmented by weaker C-H···π(arene) interactions from C24 and C26. The ring conformations in the crystal structure are **N-*anti*/M-*anti***. In **NmoM** the *meta*-pyridinyl N23 atom does not form hydrogen bonds (positioned where no donor atom can interact) with closest contact from N23···H25 = 2.95 Å [H25 at symmetry position -½-x,½+y,z].[169] **NmoM** is isostructural with related benzamides[41] [defined as C$_6$CONHC$_6$] that do not possess a pyridine acceptor group. This may explain the isostructurality of **NmoM** with benzamides [such as PIFLAS, QOVDOV, POPWUN][8] that all crystallise in space group *Pbca* (No. 61) with similar unit cell parameters.

Analysis of isomeric series of mono- and dichloro-/methyl benzamides[8,194] reveals a preponderence of C_6CONHC_6 structures in *Pbca* with similar unit cell parameters *i.e. a, b* = 6→10 Å, *c* = 20→30 Å. The **NmoM** structure (with pyridyl N23 atom) is expected to form intermolecular N-H···N/C-H···N interactions on crystallisation. The lack of N…N hydrogen bonding means that **NmoM** mimics the more common N-H…O=C hydrogen bonding motif in benzamides. Of further note is that **NmoM** with unit cell data of 8.07, 9.40, 29.53 Å and mp range of 106.1-107.0°C is *isomorphous* with the bromo derivative **TICDOZ**[195] [unit cell parameters of 8.15, 9.35, 29.59 Å; mp = 92°C]. Overlap of **NmoM** and **TICDOZ**[195] shows the main differences are due to the C-Me and C-Br moieties (Fig. **40**). Both structures have almost orthogonal C_6/C_5N rings and the **TICDOZ** torsion angles are all within 3° of the related angles in **NmoM**.

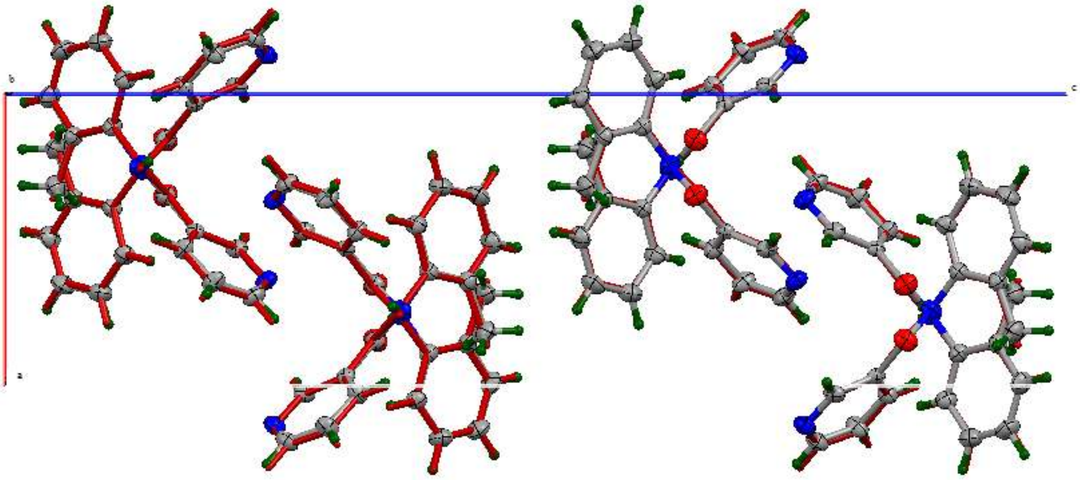

Fig. 40: A unit cell packing view along the *b*-axis direction of **NmoM** (ellipsoids) with **TICDOZ**[195] (related bromo derivative in **red**) as a ball and stick

2.2.5.4. **The NoxM isomer series**

A variation of 0.08 Å is noted in the intramolecular N1···N22 interaction distance from 2.6548(18) Å [torsion angle N1-C1-C21-N22 = 3.87(18)°, **NopM**], 2.683(4), 2.704(4) Å [angles (A) = 2.2(3)°, (B) = 17.5(4)°] in **NomM** and 2.6209(15) Å [0.45(14)°] in **NooM**. Aggregation typically occurs *via* C-H···O=C intermolecular interactions; however, the interaction mode in **NomM** is *rather* unexpected.

NopM molecular and crystal structure

NopM is a regular structure (having the **No** ring conformation as **N-*syn***) with N1-H1···N22 and a C-H···O=C intermolecular interaction (from C16) linking molecules into alternating 1-D columns along the *a*-axis parallel to the (001) plane (Fig. **41**), but stacked (in an alternating fashion) along [001]. Weaker C-H···O=C (from C23) link columns into 2-D sheets with *para*-substituted methyl groups interlocking with neighbouring sheets by van der Waals and π···π stacking contacts.

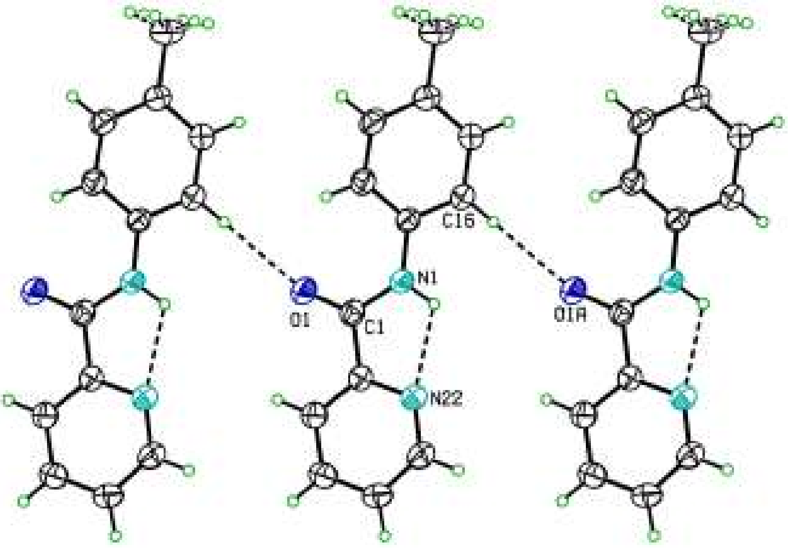

Fig. 41: Three molecules of **NopM** showing the N-H···N intramolecular and primary C-H···O=C interactions along the *a*-axis direction involving C16

NomM molecular and crystal structure

Two molecules in the asymmetric unit ($Z' = 2$) differ in **NomM** (Fig. **42**) (**Table 23**). The unexpected N-H···O=C intermolecular interactions with $N1_{A/B}\cdots O1_{B/A}$ = 3.241(3), 3.132(3) Å] are longer than the N···O distances in **NppM**, **NpoM** and **NmoM**. In **NomM** the amide···amide interaction (H···O = 2.32, 2.42 Å) in tandem with a C-H···O=C contact forms a hydrogen bonded $R^1_2(6)$ ring per molecule and overall as 2-D sheets. Molecules A and B differ significantly with torsion angles for O1-C1-C21-N22 = -176.0(3)°, -162.6(3)° (Table **24**); however, both molecules exhibit the **N-*syn*/M-*anti*** conformation. The aggregation in **NomM** is unusual compared to the other eight **NxxM** isomers and this is evident with **NomM** forming the poorest quality crystals of an isomer that proved reluctant to crystallise; the interactions are weak and often repulsive. Of the **NxxM** isomers it has the lowest mp range of 49-50°C and an explanation for the low mp is that molecules are positioned with only a modest amount of energy needed to force them to 'slip' or break the intermolecular N-H…O=C interactions near/at the melt event.

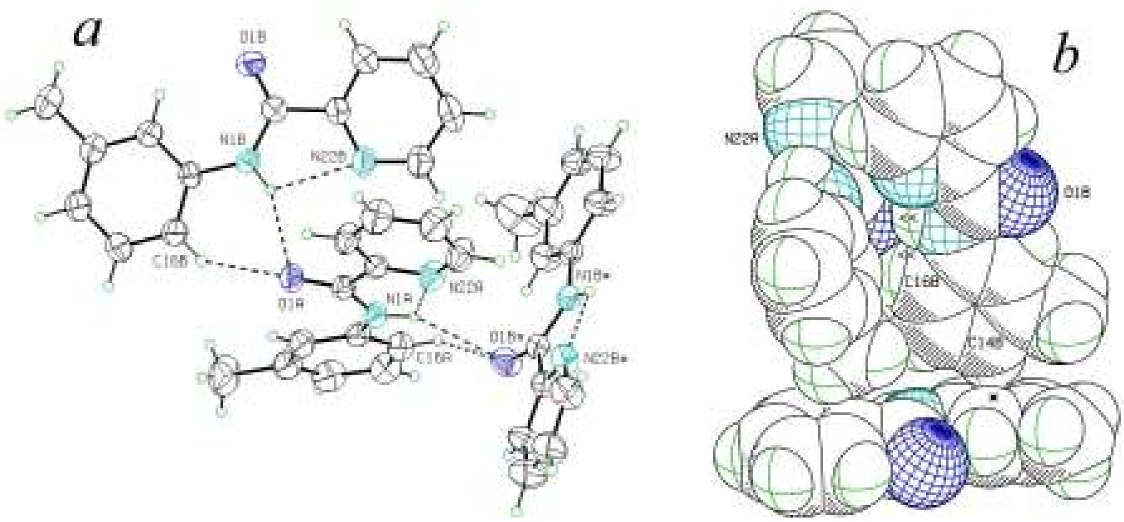

Fig. 42: (*a*) An ORTEP view of three **NomM** molecules highlighting the unusual packing and contacts with symmetry code # = -x,1/2+y,-z and (*b*) the intimate packing with << showing the orthogonal nature of the C16B-H16B/N1B-H1B···O1A=C1A interactions and with * for the C14B-H14B···π(arene) interaction.

NooM molecular and crystal structure

NooM crystals proved to be the most elusive of the nine **NxxM** isomers and were subject to many crystallisation attempts yielding gel-like, plastic spirals. Suitable crystals were eventually grown after several trials using methanol. **NooM** with the intramolecular N1-H1···N22 interaction forms a hydrogen bonded dimer *via* the C15-H15···O1a interaction about inversion centres [C15···O1a = 3.4720(16) Å] (Fig. **43**). Dimers do not pack efficiently and the effective *dimer* is only slightly *stepped* in appearance and there are no other interactions of note (the molecular volume is average for **NxxM**). The lack of interactions directly impacts on packing and obviously leads to the lack of initial success with obtaining quality crystals of **NooM**. The structure of **NooM** is planar with conformation ***N-syn*/*M-syn*** and C_6/C_5N interplanar angles of 1.91(5)° and all interplanar angles involving the aromatic rings and the amide linkage are <2°. The amide C1-N1-C11 angle of 131.02(11)° is larger than the equivalent C1-N1-C11 angles in the **NxxF** and **NxxM** isomers with C-N-C angles from 123° to 129° noted. The N1-C1-C21 angle in **NooM** is 112.71(11)° and acute compared with the 113 to 119° range in related **NxxM** isomers. These two angles are similar to the **5-Cl-NopM** and **5-Cl-NooM** molecules and primarily due to steric effects on adopting planarity.

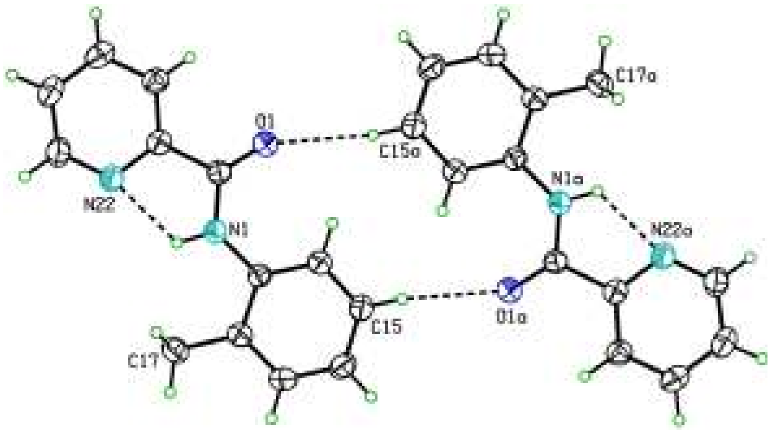

Fig. 43: An ORTEP view of the dimeric unit in **NooM** along the *a*-axis direction with centrosymmetric C-H···O=C interactions as dashed lines and suffix *a* = 1-x,1-y,1-z

2.2.5.5. **Three 5-Cl-NoxM isomers**

The **5-Cl-NoxM** compounds were isolated as minor components from their respective **NoxM** reactions and yielded crystalline solids. **5-Cl-NopM** crystallises as an inverted twin in space group $Pca2_1$ with twin component ratios of 0.87:0.13. The **5-Cl-NopM** molecule is not planar (Table **24**) and participates in weak interactions with the intramolecular N1···N22 = 2.6514(9) Å. Two additional weak C-H···O1=C1 interactions are present with C12···O1 = 2.9543(11) Å (intramolecular) and 3.4223(11) Å (C23, intermolecular and C16). A π···π stacking interaction is observed with C1···C24a = 3.3312(13) Å, and C17 forms a weak C-H···π(arene) interaction with the [C11,...,C16] aromatic group (Fig. **44**). The **5-Cl-NomM** crystal is also twinned with twin components of 0.972:0.028 and refinement drops the *R*-factor from 7.5% to 6.6%. The principal interaction is N-H···O=C at 3.035(4) Å and shortest stacking interaction is C21···C12^{a} at 3.338(4) Å [*a* = x,3/2-y,1/2+z].[169]

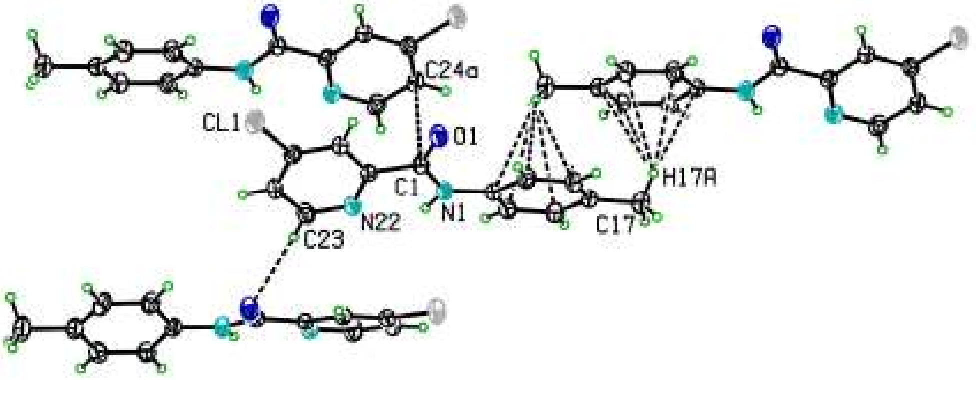

Fig. 44: The intermolecular interactions in **5-Cl-NopM** with label suffix *a* = 1/2+x,-y,z

The N-H···O=C hydrogen bond is unorthodox and the effect of the combination of N-H···O=C/π···π stacking interactions is to generate a stacked complex as a 1-D column propagating along the *c*-glide plane (Fig. **45**). Finally, the **5-Cl-NooM** structure contains the intramolecular N1···N22 = 2.6690(15) Å interaction with an intramolecular contact C16···O1 = 2.9128(19) Å. The other relevant interaction is C26-H26···Cl1^{i} where C26···Cl1^{i} = 3.7371(14) Å (*i* = 1/2-x, 1/2+y, 1/2-z). Molecules are linked along [100] as a 1-D molecular tape (Fig. **45**).

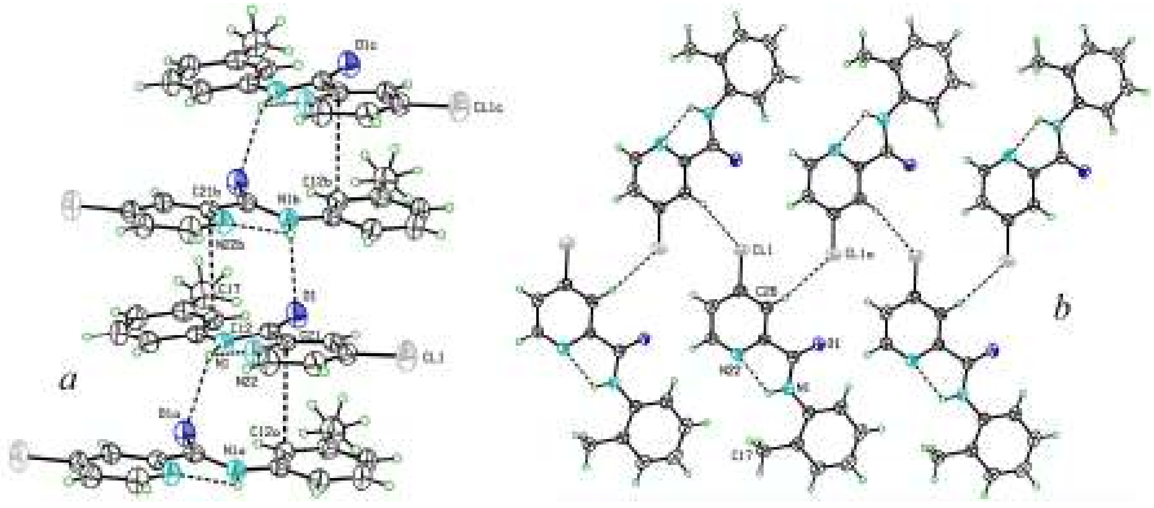

Fig. 45: (*a*) A view of the primary N-H···O=C intermolecular interactions in **5-Cl-NomM** with π···π stacking depicted for C21···C12a; suffixes *a*, *b*, *c* refer to the symmetry related sites: x,3/2-y,-1/2+z; x,3/2-y,1/2+z and x,y,1+z.; (*b*) A view of the C-H···Cl interactions along the *b*-axis in the 1-D molecular tape of **5-Cl-NooM**.

2.2.6. *Ab initio* calculations

2.2.6.1. Structure optimisation results

The key structural features of the **NxxM** isomers optimised in the *gas phase* and solvents are presented in Table **25,** including the *α*, *β* and amide linkage dihedral angles *δ* [O1=C1-N1-C11]. The most salient feature of the geometry analysis is the planarity of the **NoxM** triad in contrast to the **NpxM**, **NmxM** isomers, For **NoxM**, all dihedral angles are equal to or close to 0°, with or without the solvation model and therefore only the **NpxM** and **NmxM** triads are discussed. For the **NpxM**, **NmxM** isomers (*gas phase*) the dihedral angles exhibit a regular pattern. The *α* angle is 26.76±0.09° in **NpxM** and 24.56±0.09° in **NmxM**. The *β* angle is 5.69±0.07° in **NpoM** and **NmoM** while the remaining four structures have β = 3.65±0.43°. However, the δ dihedral angle increases slightly from 3.17° (**NppM**) to 3.77° (**NmoM**).

Table 25: Torsion angles (°) of the optimised **NxxM** isomers[a]

	optimised in *gas phase*			optimised in CH_2Cl_2			optimised in H_2O		
	α	β	δ	α	β	δ	α	β	δ
NppM	26.65	3.70	3.17	26.62	5.89	2.13	28.81	11.07	2.15
NpmM	26.80	3.58	3.18	27.57	3.14	2.06	28.39	8.34	2.32
NpoM	26.83	5.64	3.32	31.95	9.91	4.54	30.40	40.40	2.67
NmpM	24.60	4.19	3.39	29.63	5.15	3.54	29.90	12.59	3.11
NmmM	24.45	3.14	3.67	27.29	2.67	2.77	30.09	12.91	3.28
NmoM	24.62	5.75	3.77	31.37	10.10	5.24	30.38	40.42	3.44
NopM	0.00	0.00	0.00	0.00	0.00	0.00	0.00	0.00	0.00
NomM	0.00	0.00	0.00	0.00	0.00	0.00	0.00	0.00	0.00
NooM	-0.01	0.00	0.00	0.00	0.00	0.00	-0.01	0.00	-0.02

[a] The angle C26-C21-C1=O1 (**N**-ring) is designated as α; the C1-N1-C11-C12 angle (**M**-ring) as β and the O1=C1-N1-C11 angle (amide linkage) as δ. All geometries are based on B3LYP/6-311++G optimisation with PCM-SMD solvation model.

The dihedral angles optimised in CH_2Cl_2 display a different though somewhat less regular pattern. The α angle in **NpoM**, **NmoM** is 31.66±0.41° while the remaining four are 27.78±1.3°. The β angle in **NppM**, **NmpM** is 5.52±0.52°, for **NpmM**, **NmmM** = 2.91±0.33°, whereas in **NpoM**, **NmoM** β = 10.01±0.13°. The δ angle shows a small regular increase from 2.13° (**NppM**) to 5.24° (**NmoM**).

The α dihedral angle optimised in H_2O for all **NpxM**/**NmxM** isomers is 29.66±0.85°, while δ increases from 2.15° to 3.44°. For β, both **NpoM** and **NmoM** exhibit a deviation of 40.41±0.01° compared to the remaining four at 11.23±2.08°. For the **NxxM** isomers optimised in the *gas phase* this deviation is small, while slight deviations exist for the optimised structures in CH_2Cl_2. In general, the **NoxM** triad is planar (due to the intramolecular N-H···N) and the molecular distortion of the remaining **NxxM** structures occurs through rotation of the pyridine ring (*gas phase*) and both pyridine (**N**) and tolyl (**M**) rings (in solvents). Crystallographic and spectroscopic results support this interaction.

2.2.6.2. Conformational analysis

Fig. **46** depicts the nine PES conformational analysis diagrams of the **NxxM** modelled structures in the *gas phase*. The **N**-ring (pyridinoyl ring, α dihedral angle) is drawn as a **full red line**, with the **M**-ring (tolyl ring, β dihedral angle) as a **blue dashed**

line. At $\theta = 0$ and ±180°, the conformation of the asymmetric **N**- or **M**-ring is noted as ***syn*** or ***anti***. Higher resolution PES diagrams are provided in the ESI I (Section 3.4.2). The modularity of the **NxxM** isomer series is highly expressed, with each **N** or **M** ring (*p*-, *m*- or *o*-) having a distinctive PES curve as in previous analyses.

The *para*-pyridine (**Np**) ring is symmetrical, with all stable conformations energetically equal. The PES curve has two global maxima at *ca*. 65° and -120° (TS_{Np}^{II} = 11.94±0.18 kJ.mol^{-1}), two local maxima at around -30° and 150° (TS_{Np}^{I} = 1.98±0.05 kJ.mol^{-1}) and four global minima at *ca*. 0, -55, 125 and ±180°.

The *meta*-pyridine (**Nm**) ring has two global maxima at *ca*. -120° and 65°, (TS_{Nm}^{III} = 14.57±0.12 kJ.mol^{-1}), two local maxima at *ca*. -25° (TS_{Nm}^{I} = 1.48±0.05 kJ.mol^{-1}) and 150° (TS_{Nm}^{II} = 7.57±0.17 kJ.mol^{-1}), two local minima at *ca*. 125° and ±180° (LM_{Nm}^{I} = 4.70±0.17 kJ.mol^{-1}) and two global minima at 0° and -55°. The preferred conformation is **N-*syn*** while the difference on changing to **N-*anti*** is 4.70±0.17 kJ.mol^{-1}; Boltzmann distribution of the different conformers indicates that ~86% of all molecules at 294 K have the **Nm** ring in the **N-*syn*** conformation with the remainder in the **N-*anti*** conformation.

The *ortho*-pyridine (**No**) ring shows a symmetric PES curve with one global maximum at ±180° (TS_{No}^{II} = 59.07±0.53 kJ.mol^{-1}), two local maxima at ±105° (TS_{No}^{I} = 50.28±0.34 kJ.mol^{-1}), two local minima at *ca*. ±130° (LM_{No}^{I} = 49.44±0.41 kJ.mol^{-1}) and one global minimum at 0°. Strongly favoured is the **N-*syn*** conformation where the intramolecular N-H···N hydrogen bond forms. The *para*-tolyl (**pM**) gives a symmetric PES curve with two global maxima at *ca*. ±90° (TS_{pM}^{I} = 13.15±0.09 kJ.mol^{-1}, while TS_{pM}^{I}[**NopM**] = 17.33 kJ.mol^{-1}), and two global minima at 0° and ±180°. The *meta*-tolyl (**mM**) has a symmetric PES curve with two global maxima at *ca*. ±90° (TS_{mM}^{I} = 14.54±0.06 kJ.mol^{-1}, while TS_{mM}^{I}[**NomM**] = 8.79±0.11 kJ.mol^{-1}), one local minima at *ca*. ±180° (LM_{mM}^{I} = 0.37±0.02 kJ.mol^{-1}, while LM_{mM}^{I}[**NomM**] = 0.46 kJ.mol^{-1}) and one global minima at 0°.

Although the **M-*anti*** conformation in the **mM** ring is the slightly preferred conformation, the 0.37-0.46 kJ.mol^{-1} energy difference when compared to the **M-*syn*** conformation ensures both conformations are plausible. The *ortho*-tolyl (**oM**) shows a strong preference for the **M-*syn*** conformation. However, both **NpoM** and **NmoM** have asymmetric PES curves, whereas the planar **NooM** has a symmetrical curve. Although the **M-*syn*** conformation is preferred, deep potential wells at the local minima (LM_{oM}, 5-7.5 kJ.mol^{-1}) can cause another conformation closer to **M-*anti*** to occur to a minor extent.

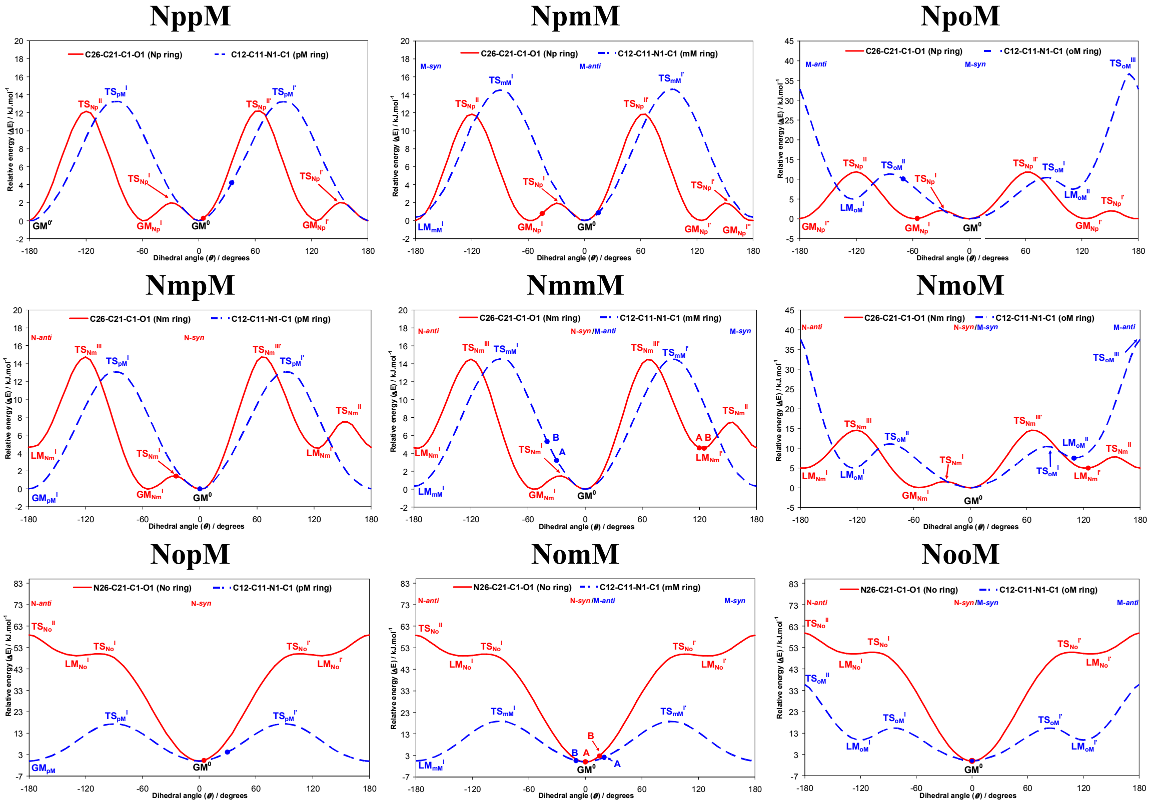

Fig. 46: The PES conformational analysis for the nine **NxxM** isomers optimised in the gas phase: the equivalent solid state angle is depicted by (●) with, if applicable, an assigned identification letter.

The PES in **NpoM** has one global maximum at 170°, while in **NmoM** it is at ±180° (TS_{oM}^{III} = 37.13±0.53 kJ.mol^{-1}). The PES curve has two local maxima at *ca*. 85° (TS_{oM}^{I} = 10.39±0.01 kJ.mol^{-1}) and -85° (TS_{oM}^{II} = 11.21±0.19 kJ.mol^{-1}), two local minima at *ca*. -125° (LM_{oM}^{I} = 4.97 kJ.mol^{-1}) and 110° (LM_{oM}^{II} = 7.47±0.03 kJ.mol^{-1}), and one global minimum (0°). The symmetric PES curve of the oM ring in **NooM** has one global maximum at ±180° (TS_{oM}^{II}[**NooM**] = 35.73 kJ.mol^{-1}), two local maxima at ±85° (TS_{oM}^{I}[**NooM**] = 15.31 kJ.mol^{-1}), two local minima at ±120° (LM_{oM}^{I}[**NooM**] = 9.73 kJ.mol^{-1}) and the global minimum at 0°.

Overall, the *gas phase* conformational analysis shows that the favoured **NxxM** conformation is **N-*syn*/M-*syn*** for the majority of asymmetric rings (structures), but excluding the **NxmM** triad, where the preferred conformation is **N-*syn*/M-*anti***, albeit the difference with **N-*syn*/M-*syn*** is small with both conformations possible.

The conformational analysis results using the PCM-SMD solvation model (CH_2Cl_2 and H_2O as solvents) are given in Fig. **47**. Introduction of the solvent model does not cause a major conformational change in the modelled **NxxM** structures (***syn*-*anti*** model) in the *gas phase*; asymmetric **NxxM** isomers have the **N-*syn*/M-*syn*** conformation with the **NxmM** triad being **N-*syn*/M-*anti***. As seen in previous cases (**Mxx**, **Fxx**, **and NxxF**) the general feature of the solvated conformational analysis is a decrease in rotational barriers. However, when specific rings are coplanar with the amide linker an increase is noticed. This is due to an increase in repulsion factors due to the higher dielectric field.

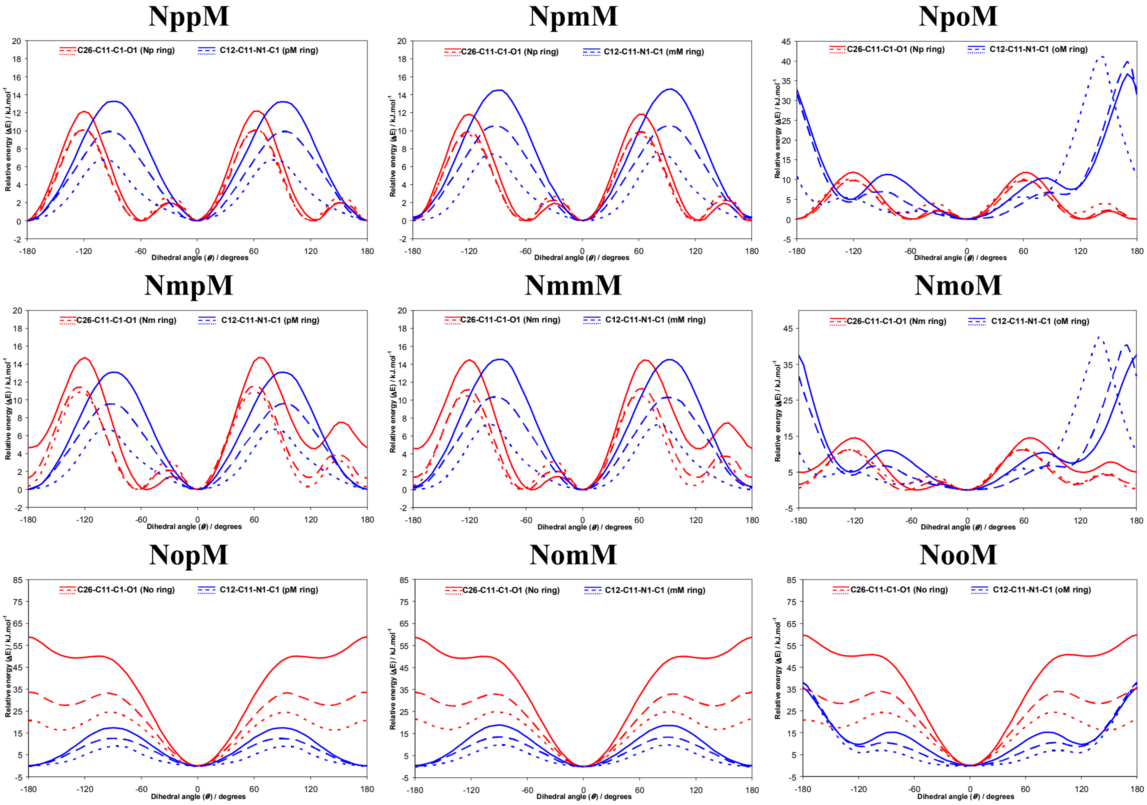
NppM
NpmM
NpoM
NmpM
NmmM
NmoM
NopM
NomM
NooM

Fig. 47: The PES conformational analysis diagrams for the nine **NxxM** isomers optimised in *gas phase* (full line), CH_2Cl_2 (dashed line) and in H_2O (dotted line) using the PCM-SMD solvation method.

When the *para*-pyridine (**Np**) ring rotates towards orthogonality (around TS_{Np}^{II}) the rotational barriers decrease by ~16.5% in CH_2Cl_2 (~17.2% in H_2O), whereas, in the areas of planarity (around TS_{Np}^{I}) the rotational barriers increase in CH_2Cl_2 by ~15% (~50% in H_2O). The decrease when orthogonal is almost the same in both solvents, while when planar the more polar solvent has the higher impact on the barrier increase. This is due to an increase in repulsion associated with the higher dielectric field.

The *meta*-pyridine (**Nm**) ring has a specific rotational barrier change pattern. In the **N-*syn*** conformation (from θ = -120º→60º) the **Nm** ring is similar to the **Np** ring with the decrease with orthogonal rings of ~22.4% in CH_2Cl_2 (~25% in H_2O) and an increase when the rings are co-planar is ~54.1% in CH_2Cl_2 (~133.6% in H_2O). In the **N-*anti*** conformation a linear decrease by ~3.35 kJ.mol^{-1} in CH_2Cl_2 (~3.87 kJ.mol^{-1} in H_2O)

is observed. This results in a small energy gap between the **N-*syn*** and **N-*anti*** conformations of the **Nm** ring, 1.45 kJ.mol^{-1} in CH_2Cl_2 (0.38 kJ.mol^{-1} in H_2O). From the Boltzmann distribution, at 294 K approximately 35% of the molecules in CH_2Cl_2 and approximately 47% of the molecules in H_2O have the **Nm** ring in the **N-*anti*** conformation. Therefore, conformational analysis with the PCM-SMD solvation model predicts the plausibility of the **N-*anti*** conformation of the **Nm** ring. The noticeable shift of barriers ($\Delta\theta$~5-10º) occurs due to the deviation of dihedral angles in solvents.

The rotational barrier for the *ortho*-pyridine (**No**) ring symmetrically decreases by ~41.7% (CH_2Cl_2) and ~63.2% (H_2O). Therefore, the solvent effect on the rotational barrier of the **No** ring is the most distinct, albeit as expected: the PCM-SMD model predicts the interaction of a strong solvent electric field with the intramolecular N-H···N hydrogen bond in the three **NoxM** isomers and weakening the interaction.

The *para*-tolyl (**pM**) ring shows a regular decrease by ~27% in CH_2Cl_2 (~49% in H_2O). In **NopM** all of the barrier peaks are symmetrical, but in **NppM** and **NmpM** the peaks are shifted by ~5º in CH_2Cl_2 (~10º in H_2O).

In the *meta*-tolyl (**mM**) ring the pattern is similar to the **pM** ring with decreases of ~28.5% in CH_2Cl_2 (~49% in H_2O), similar barrier shifts are noted as for the **pM** ring. The energy difference between **M-*anti*** and **M-*syn*** in CH_2Cl_2 decreases by ~43% (0.21 kJ.mol^{-1}), while in H_2O the difference is almost cancelled (93%, negligible 0.03 kJ.mol^{-1}), making both conformations energetically equal. Theoretically, this observation implies that the **mM** ring in polar solvents can adopt both **M-*anti*** and **M-*syn*** conformations equivalently.

The *ortho*-tolyl (**oM**) ring behaviour is more complex with the **NpoM/NmoM** isomers showing differences with **NooM**. The rotational barriers in the **M-*syn*** conformation decrease by ~37% (CH_2Cl_2) and in the **M-*anti*** conformation increase by ~8% in CH_2Cl_2, (~13% in H_2O). However, due to a strong additional rotation of the **oM** rings optimised in H_2O the PES curve shape exhibits significant deviations. An extra local maximum is positioned at -45º *only* and TS_{oM}^{III} is displaced (by $\Delta\theta = 40º$). For the symmetrical **NooM** the pattern is much simpler: as **M-*syn*** the conformation barrier decrease is ~31% in CH_2Cl_2 (~54% in H_2O) and in **M-*anti*** the increase is 6.7% in CH_2Cl_2 (5.6% in H_2O) because solvent induced high dielectric field can amplify repulsion of the methyl group and carbonyl oxygen.

Although the **NxxM** isomers are insoluble in H_2O, it was used as an example of a strong polar solvent (ε_r=80) to illustrate and amplify solvation effects with implicit polar solvent in the PCM-SMD model; extrapolations can be made for polar solvents where the **NxxM** isomers are soluble. Spectroscopic data demonstrate that solvents like DMSO can disrupt intramolecular hydrogen bonding in the **NoxM** series.

2.2.6.3. Energy results

The energy calculation results (CBS-QB3) (Table **26,** full data is given in the ESI I, Section 3.4.1) comprise the electronic energies (δE_{SCF}) and Gibbs free energies (δG) in all three media, including ΔG_{solv} for CH_2Cl_2 and H_2O, as well as ΔΔG_{solv} (CH_2Cl_2 *vs*. H_2O). Differences between each molecule are given as δE_{SCF} (δG) and differences between media as ΔE_{SCF} (ΔG). The least stable molecules are **NppM** and **NpoM**, while the most stable, regardless of media is **NomM**. The **NoxM** molecules due to their inherent stabilisation through intramolecular N-H···N_{pyr} hydrogen bonding are the most stable, with significant differences as compared to the other six **NpxM**/**NmxM** isomers.

Another stabilisation factor is the methyl group located in a *meta* position, although this effect is less pronounced. In total, the effects of the pyridine **N** atom and CH_3 group positions on stability is summarised as: **No**>**Nm**>**Np** with **mM**>**pM**>**oM**. The estimated ΔG_{solv} in CH_2Cl_2 and H_2O, along with theoretical log$K_{D/W}$ (given in the ESI I, Section 3.4.1) are consistent with our experimental observations and with no unexpected results.

Table 26: The energy calculation results for the **NxxM** isomers[a] in kJ.mol^{-1}

	gas phase		CH_2Cl_2		H_2O		*gas phase*→CH_2Cl_2		*gas phase*→H_2O		CH_2Cl_2→H_2O	
	δE_{SCF}	δG	δE_{SCF}	δG	δE_{SCF}	δG	ΔE_{SCF}	ΔG_{solv}	ΔE_{SCF}	ΔG_{solv}	ΔΔE_{SCF}	ΔΔG_{solv}
NppM	-4.38	0.00	-5.63	-0.69	-1.54	-1.83	-72.09	-67.33	-55.38	-47.53	16.71	19.80
NpmM	-6.63	-8.38	-7.63	-0.94	-3.33	-1.85	-71.84	-59.21	-54.93	-39.17	16.92	20.04
NpoM	0.00	-2.09	0.00	0.00	0.00	0.00	-70.84	-64.55	-58.22	-43.61	12.62	20.94
NmpM	-10.03	-6.64	-10.99	-1.57	-7.84	-2.81	-71.81	-61.58	-56.03	-41.87	15.77	19.70
NmmM	-12.36	-7.78	-13.16	-2.11	-9.69	-1.74	-71.64	-60.98	-55.55	-39.66	16.09	21.32
NmoM	-5.78	-4.23	-5.71	-1.69	-6.60	-1.16	-70.78	-64.10	-59.04	-42.64	11.73	21.47
NopM	-33.97	-27.00	-24.99	-16.98	-14.44	-8.28	-61.86	-56.62	-38.69	-26.98	23.17	29.64
NomM	-36.31	-27.31	-26.99	-20.21	-16.64	-15.08	-61.52	-59.54	-38.55	-33.48	22.97	26.06
NooM	-30.37	-29.93	-20.73	-17.29	-9.81	-8.31	-61.21	-54.00	-37.67	-24.08	23.54	29.92

[a] Only the differences between each molecule (δ) and media (Δ,ΔΔ) are shown. **NppM** and **NpoM** isomers are taken as basis point.

2.2.7. Comparisons of the solid state and modelling data

Comparison of the **NxxM** isomer structures from crystal structure data and calculations is made by marking (as ●) torsion angle differences (Δθ) between the experimental and theoretical structures on the corresponding *gas phase* PES diagrams (Fig. **46**). For **NmmM** and **NomM** with Z'>1 the corresponding angles are labelled as A or B. Most crystallographic dihedral angles correlate with their computational results by having similar conformations with an average offset of torsion angles of ±20-40º. This holds for the **NoxM** triad with **NooM** having both a planar crystal and calculated molecular structure. Generally, no significant differences ($\Delta\theta$) are seen in the **NoxM** isomers. The **5-Cl-NoxM** side products were not subjected to conformational analysis; their crystal structure conformations generally correspond with the optimised models of the related **NoxM** isomers.

In the **NpxM** crystal structures, the **Np**-ring conformation corresponds with its optimised *gas phase* model; however, it can found in either the GM_0 or GM_{Np} equivalent positions. In the case of the **NmxM** isomers the **Nm**-ring adopts the unstable $TS_{Nm}{}^{I}$ position in **NmpM** or $LM_{Nm}{}^{I'}$ in both **NmmM** and **NmoM**. The unstable planar conformation of the **Nm-**ring in both **NmpM** and **NmpFM** crystal structures is due to the catemeric chain formation driven by N-H···N/C-H···N hydrogen bonding. The **No-**ring conformations in the **NoxM** crystal structures correspond with their modelled equivalents.

In almost all molecules with the exception of **NpoM** and **NmoM**, the **M**-ring conformation is the same in both the solid state and optimised *gas phase* models with a maximum deviation of ±40º. In fact all **NxmM** crystal structures have the **mM**-ring as ***M-anti*** as predicted by conformational analyses despite the small differences with the ***M-syn*** structure (0.37-0.46 $kJ.mol^{-1}$). This is the reverse of the **NxmF** isomers where opposite conformations and/or disorders are noted.

Generally, for the **Nm**-ring the main conformational differences are seen in the **NmmM** and **NmoM** isomers. The calculated **NmmM** conformation is ***N-syn*/*M-anti***, whereas the solid state (Z' = 2) has a *meta*-stable ***N-anti*/*M-anti*** conformation for both molecules (Fig. **39**), with **A** and **B** residing in the $LM_{Nm}{}^{I'}$ potential well (Fig. **46**) There is a high probability of the ***N-anti*** conformation especially in polar solvents, allowing isolation of this conformation in the solid state. The reverse arrangement of the **N**-ring solid state conformation as ***N-syn*** would not facilitate the $_{amide}$N-H···$N_{pyridine}$ hydrogen bond and would introduce short H···H sterically hindered contacts in the crystal structure (if allowed); the N-H···N interactions are crucial for the formation of the crystal structure backbone. The same phenomenon exists for the structurally similar **Mmm** and **NmmF**.

For **NmoM** the crystallographic conformation is **N-*anti***/**M-*anti*** and opposite to the **N-*syn***/**M-*syn*** in the modelled structure (Fig. **46**, *meta*-stable potential wells at LM_{oM}^{II} and $LM_{Nm}^{I'}$). As for **NmmM**, conformational analysis shows the **N-*anti*** conformation is likely, especially in polar solvents, while the **M-*anti*** conformation can be expected as well. The primary interaction of **NmoM** is N-H···O=C which generates a 1-D chain along the *b*-axis. In this arrangement the *ortho*-CH_3 group is positioned as **M-*anti*** because the alternate **M-*syn*** conformation brings the CH_3 group closer to the N-H···O=C interaction and effects a steric clash. Therefore, the LM_{oM}^{II} potential well represents the only *niche* available for the relatively sterically bulky *ortho*-CH_3 group (compared to H). Similarly, the N_{pyr} is located as **N-*anti***, as the opposite **N-*syn*** conformation negates some weak but favourable C-H···π interactions and places it too close to the carbonyl C atom of a neighbouring molecule.

For comparison **NpoM** has N-H···O=C as the primary interaction (as in **NmoM**). In **NpoM** the *ortho*-CH_3 is positioned as **M-*syn*** but in a highly distorted and relatively *unstable* conformation, being almost orthogonal to the amide linker. However, conformational analysis with the PCM-SMD solvation model suggests that this conformation in polar solvents may be plausible. For **NpoM** the *ortho*-methyl group also participates in crystal structure formation making additional weak C-H···O=C contacts with the C=O of an adjacent **NpoM** molecule (C17 in Fig. **36**).

An overview of the benzamide and pyridinecarboxamide results is presented in the “Discussion and Conclusions”.

Chapter II: Carbamates

1. General description of carbamate syntheses

The simplest synthetic method for the formation of phenyl-*N*-pyridinyl-carbamates (**CxxR**) (**Scheme 32**) is the condensation reaction of aminopyridines with commercially available phenyl chloroformates in the presence of base (Et_3N) and solvent (CH_2Cl_2).[196-198] This method is analogous to the Schotten-Baumann reaction as applied to the previous isomer grids. The condensation reaction gives relatively pure products in high yields. Unfortunately only a limited number of phenyl chloroformates are commercially available, *i.e. para*-substituted and only two *ortho*-substituted phenyl chloroformates. Therefore, 14 compounds were synthesised using the condensation approach starting from the 3-/4-aminopyridines (**Method 1,** Section 1.1). Alternatively, if 2-aminopyridine is used, double carbamates are obtained where both hydrogen atoms in the amine moiety are substituted with chloroformates. The result is similar to the formation of the (2:1) **Mxod** and **Fxod** by-products (Chapter I, Section 1). As with the benzamides, this is due to the pyridine nitrogen in the *ortho* position. In order to minimise the formation of double carbamates, the reaction is carried out without solvent and base, applying only the mechanical mixing of two compounds at lower temperature (**Method 2,** Section 1.3). The resulting mixture was then purified by re-crystallisation.

There were several options available for the synthesis of the remaining **CxxR** compounds. One of these approaches is the use of an agent that transforms phenols into the desired chloroformates, phosgene or a substitute, diphosgene or triphosgene. Due to health and safety reasons these methods were not used. A simple and straightforward method for carbamates synthesis is the Curtius rearrangement reaction (or Curtius reaction or degradation),[199] a chemical reaction that involves the rearrangement of an acyl azide to an isocyanate (**Scheme 31**).[200] The acyl azide (pyridinyl azide) can be formed from the carboxylic acid by a suitable agent like diphenylphosphoryl azide (DPPA).[201]

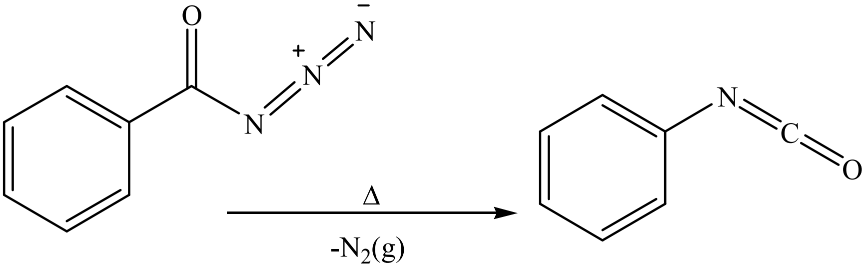

Scheme 31: Rearrangement of benzyl azide into a reactive benzylisocyanate molecule

Pyridinecarboxylic acids can be easily converted into pyridinyl azides using diphenylphosphoryl azide, at higher temperature (70°C) in the presence of a base. The pyridinyl azides spontaneously rearrange into reactive pyridinyl isocyanates. Reaction of pyridinyl isocyanate with phenol gives the phenyl-*N*-pyridinyl-carbamate (**CxxR**, Section 1.3).

Usually the Curtius rearrangement reaction (Curtius reaction, variant A, see section 1.3) is performed as a two step (one pot) reaction, with isonicotinic or nicotinic acids as starting materials, diphenylphosphoryl azide as converting agent, and Et_3N as base in anhydrous acetonitrile at 70°C. Immediately after the pyridinyl isocyanate is formed, the addition of a phenol starts the final condensation into a phenyl-*N*-pyridinyl-carbamate. Similar syntheses have been described in the literature.[202-204]

This method was convenient when isonicotinic or nicotinic acids (3-/4-pyridinecarboxylic acids) were used as starting materials, giving acceptable yields. However, if picolinic acid (2-pyridinecarboxylic acids) was used in order to synthesise phenyl-*N*-pyridin-2-yl-carbamates (**CoxR**) the yield was low (~2%). This was overcome by a longer reaction time, using toluene instead of acetonitrile as solvent and performing the reaction at 110°C (variant A, Section 1.3).[205]

1.1. Method 1. Condensation of AP's with phenyl chloroformates

1. To a stirring solution of 3-/4-aminopyridine (490 mg, 5.2 mmol) in 150 ml of CH_2Cl_2, triethylamine was added (0.740 ml, 5.2 mmol) and then ***R***-phenyl chloroformate [***R*** = 4-**F**, 4-**Cl**, 4-**Br**, 4-$\mathbf{OCH_3}$, 4-$\mathbf{CH_3}$, 2-**Cl** or 2-$\mathbf{OCH_3}$] (5.2 mmol) was added dropwise under an atmosphere of N_2. The resulting mixture was stirred for 3 hours.

2a. If a white product formed it was filtered and washed with CH_2Cl_2 (in most cases it was the pure product).

2b. The organic reaction mixture was washed three times with 250 ml of 3% $KHCO_3$, and dried with anhydrous $MgSO_4$. After removal of the solvent, the product was recovered.

If necessary, purification was accomplished by column chromatography using silica as stationary phase and a mixture of CH_2Cl_2 and MeOH (8:1) as mobile phase. This method (**Scheme 32**) was used for the synthesis and purification of the following 14 compounds: **CppF**, **CppCl**, **CppBr**, **CppOMe**, **CppM**, **CmpF**, **CmpCl**, **CmpBr**, **CmpOMe**, **CmpM**, **CpoCl**, **CmoCl**, **CpoOMe** and **CmoOMe**.

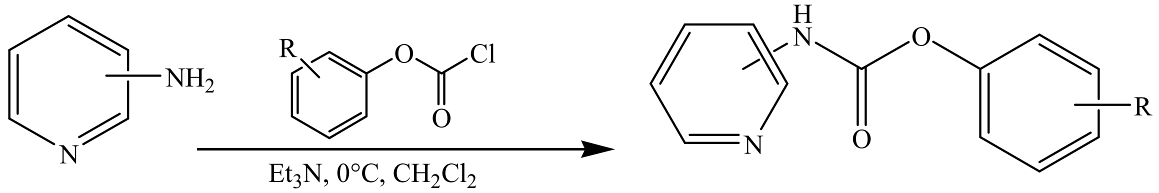

Scheme 32: Condensation of 3-/4-AP with phenyl chloroformates forming **CxxR**

1.2. Method 2. Condensation of 2-AP with phenyl chloroformates in solventless conditions

R-phenyl chloroformate [**R** = 4-**F**, 4-**Cl**, 4-**Br**, 4-**OCH$_3$**, 4-**CH$_3$**] (5.23 mmol) was added using a pipette to a cooled 2-aminopyridine solid (10.46 mmol) in a test tube (on an ice bath) and the mixture was vigorously agitated. The resulting solid was dissolved in a mixture of CH_2Cl_2 (250 ml) and aqueous $KHCO_3$ (1%, 250 ml). The emulsion was allowed to separate in a funnel, and the organic layer was washed three times with an aqueous solution of $KHCO_3$ and twice with brine. The organic layer was dried with $MgSO_4$ and the crude product obtained after evaporation of the solvent.

The crude product was washed with a cooled mixture of hexane, acetone and ethyl acetate (3:1:1). If necessary the precipitate was dissolved in warm CH_2Cl_2 and re-crystallisation induced. Crystals of pure product were collected on a Hirsch funnel. This method (**Scheme 33**) was used for the synthesis and purification of the following five compounds: **CopF**, **CopCl**, **CopBr**, **CopOMe** and **CopM** (**CopR**).

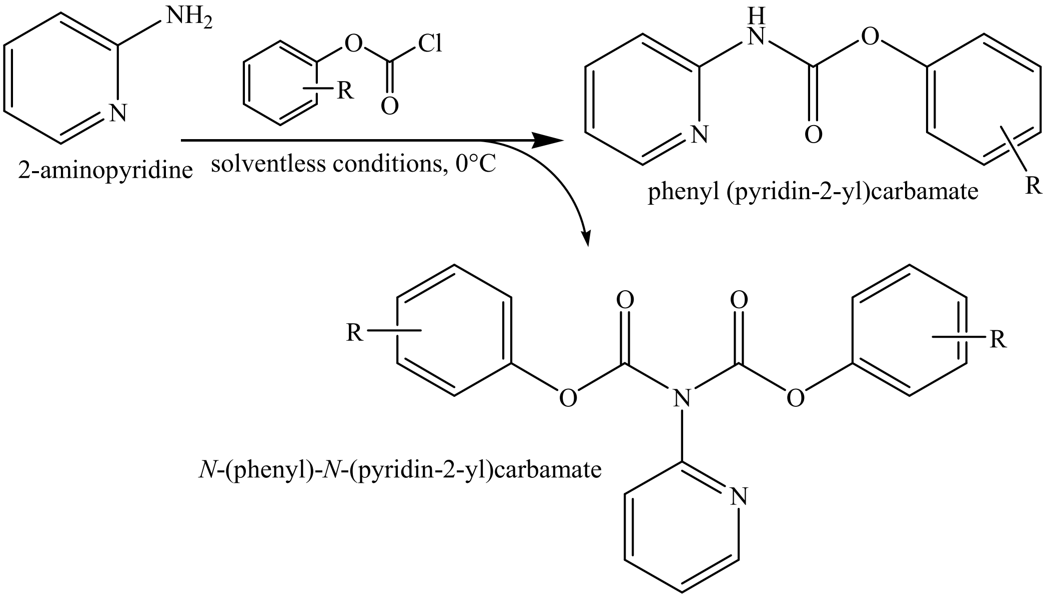

Scheme 33: Condensation of 2-aminopyridine with phenyl chloroformates

1.3. Method 3. Curtius rearrangement reaction, variant A

1. A mixture of isonicotinic or nicotinic acid (1.2877 g, 10.46 mmol), Et_3N (1.46 ml 10.46 mmol) and diphenylphosphoryl azide (2.258 ml, 10.46 mmol) was stirred for 1 hour in 30 ml of dry acetonitrile at room temperature (**Scheme 34**). The reaction mixture was carefully heated (water bath) to reflux for 1 hour and **R**-phenol (R = 3-**F**, 2-**F**, 3-**Cl**, 3-**Br**, 2-**Br**, 3-OCH_3, 2-CH_3 and 3-CH_3) (10.46 mmol) was added. The solution was refluxed for 7 hours and gradually cooled down and allowed to stir overnight.

2a. If a white precipitate formed it was filtered, washed with acetonitrile and dried (usually found to be the pure product).

2b. The solvent was removed from the reaction mixture under reduced pressure, the residue dissolved in CH_2Cl_2, washed thrice with a solution of $KHCO_3$ and Na_2CO_3 (pH=9) and twice with brine/ammonium chloride (pH=5). The organic fraction was evaporated and the compound re-crystallised from diethyl ether and CH_2Cl_2. If necessary, the purification was accomplished by column chromatography using silica and a mixture of CH_2Cl_2 and methanol (8:1) as mobile phase. There were 16 compounds obtained using this method: **CpmF**, **CmmF**, **CpoF**, **CmoF**, **CpmCl**, **CmmCl**, **CpmOMe, CmmOMe, CpmBr, CpoBr, CmmBr, CmoBr, CpmM, CpoM, CmmM, CmoM**.

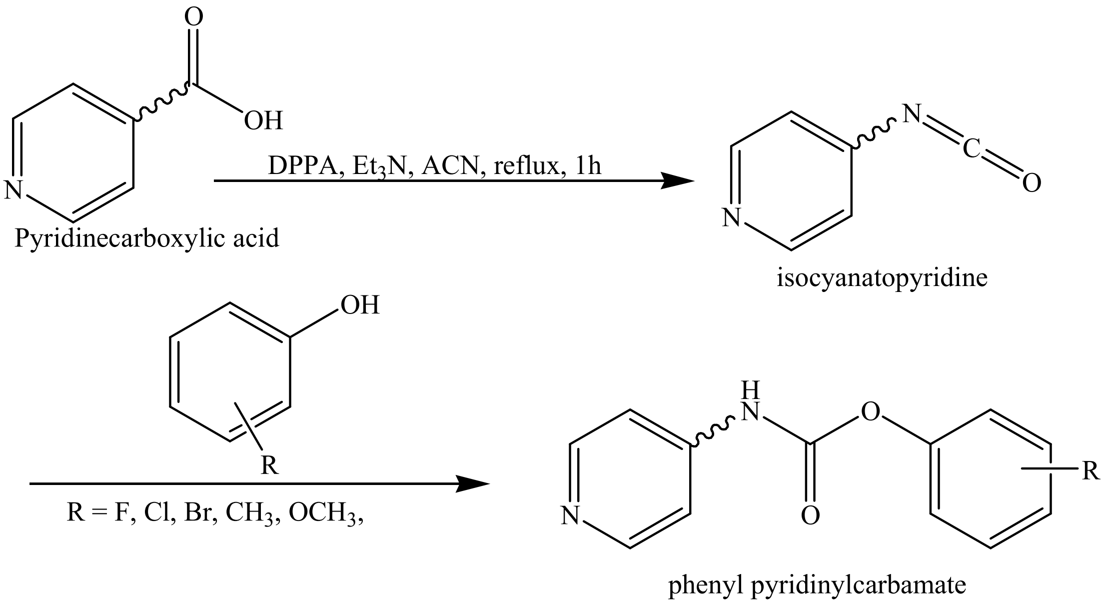

Scheme 34: Curtius rearrangement reaction, variant A, synthesis of the **CxxR** compounds.

1.4. Method 4. Curtius rearrangement reaction, variant B

A mixture of picolinic acid (2.5754 g, 20.92 mmol), Et_3N (2.92 ml 20.92 mmol), and diphenylphosphoryl azide (4.516 ml, 20.92 mmol) was refluxed in 40 ml of dry toluene at 100°C for 4 hours. The **R**-phenol (R = 3-**Cl**, 2-**Cl**, 3-**Br**, 3-OCH_3, 2-OCH_3, 3-CH_3 and 2-CH_3) (20.92 mmol) was added and the reaction mixture was refluxed (**Scheme 35**) for an additional 4 hours and left to cool overnight.

If a precipitate formed then it was filtered using a Hirsch funnel. The precipitate was found to contain the product. The filtrate was subjected to further purification. Into the filtrate 100 ml of CH_2Cl_2 was added and the organic mixture was washed thrice with a solution of $KHCO_3$ and K_2CO_3 (pH=9) and twice with brine. The organic fraction was dried with $MgSO_4$, filtered and solvent removed.

The black product was washed (re-crystallised) with diethyl ether and dark crystals were obtained. The presence of the product was confirmed by TLC and the combined products were purified by column chromatography (silica/$CHCl_3$). Seven compounds (**CoxR**) were obtained using this method: **ComM**, **CooM**, **ComOMe**, **CooOMe**, **ComBr**, **CooCl** and **ComCl**.

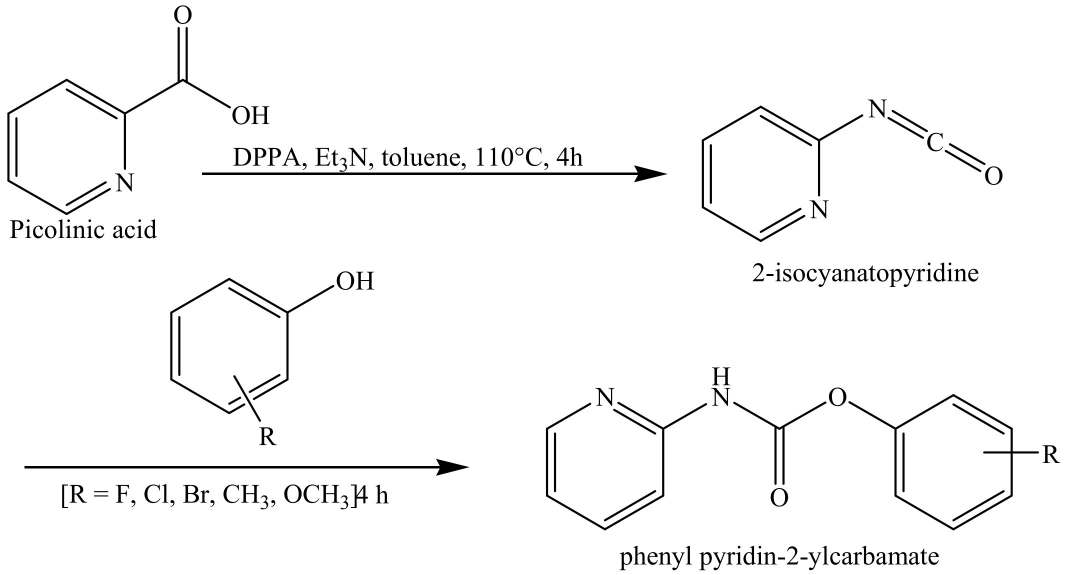

Scheme 35: Curtius rearrangement reaction, variant B, synthesis of some phenyl-pyridin-2-ylcarbamates (**CoxR**)

2. Comment on synthesis and general characteristics

Table **27** summarises the amounts, yields and melting points of the **CxxR** compounds.

Table 27: Yields and melting points of the **CxxR** compounds

	m/g	%	m.p./ºC		m/g	%	m.p./ºC
CppF	0.923	76	183.0-185.3	**CpoF**	0.404	16	166.3-169.0
CppCl	1.019	78	196.9-199.6	**CmoF**	0.806	33	134.1-136.5
CppBr	1.106	72	204.5-206.4	**CmmCl**	1.106	42	168.9-171.2
CppOMe	1.074	84	155.1-156.7	**CpmCl**	0.600	23	193.0-197.5
CppM	1.118	94	163.5-165.7	**CmmM**	1.700	71	112.5-113.0
CmpF	0.546	45	165.3-167.4	**CpmM**	0.474	20	131.3-134.6
CmpCl	0.971	37	173.2-175.4	**CmoM**	1.098	46	79.0-84.0
CmpBr	0.660	43	167.5-170.4	**CpoM**	0.863	36	128.0-131.0
CmpOMe	0.820	32	159.5-162.5	**CmmOMe**	1.164	45	139.5-142.5
CmpM	0.610	51	167.7-170.6	**CpmOMe**	0.870	34	130.1-134.7
CopF	0.450	29	178.9-179.9	**CmmBr**	1.208	39	152.2-154.7
CopCl	0.290	22	197.2-199.8	**CmoBr**	0.642	21	86.2-86.9
CopBr	0.200	13	194.3-196.6	**CpoBr**	0.700	23	167.6-168.5
CopOMe	0.350	27	182.3-184.7	**CpmBr**	1.212	39	191.6-193.4
CopM	0.362	30	190.0-191.8	**ComCl**	0.345	23	173.4-175.4
CpoCl	0.870	67	168.2-170.3	**CooCl**	0.243	20	144.4-146.1
CpoOMe	1.073	84	187.3-191.8	**ComM**	1.487	31	139.7-143.8
CmoCl	0.365	28	123.4-125.6	**ComOMe**	1.2269	24	144.2-145.4
CmoOMe	0.283	22	107.5-109.6	**CooM**	1.664	33	160.1-162.3
CpmF	0.300	25	160.5-162.9	**CooOMe**	0.697	14	157.3-159.8
CmmF	1.200	49	151.3-152.3	**ComBr**	0.32	5	175.1-175.5

The **CpxR** compounds synthesised with **Method 1** usually had a good to excellent yield, especially the methyl and methoxy derivatives (~73%, **CppM** = 94%). However, the **CmxR** compounds synthesised with the same method had a lower yield (~37%). Finally, compounds synthesised by **Method 2** (**CopR**) had, due to the losses during the re-crystallisation, lower yields (~24%). The compounds obtained by the Curtius rearrangement reaction (**Method 3**) had moderate yields (~35), while the **CoxR** compounds (**Method 4**) had lower yields (~21%). Attempts to synthesise **CooF**, **CooBr** and **ComF** were not successful, resulting in very small and unsatisfactory yields.

The **CxxR** compounds are usually white powders, less crystalline than the benzamides and pyridinecarboxamides (with the exception of some methyl and methoxy derivatives) and with a specific phenolic odour. Despite the rigorous purifications, the phenolic odour originates from a small amount of decomposition giving traces of phenols.

Two major characteristics of the **CxxR** derivatives that differentiate them from the previous groups of compounds are the relatively poor solubility of most of the compounds and their instability (spontaneous decomposition).

The **CxxR** carbamates are insoluble in water and cyclohexane, while their solubility is poor in solvents such as diethyl ether, CH_2Cl_2 (with the exception of most **CmxR** compounds), toluene, but slightly better in ethyl acetate. Solubility in CH_3CN, $CHCl_3$ and CH_3COCH_3 can be regarded as moderate, while solubility is good in MeOH (for most compounds) and excellent in DMSO.

Unfortunately, stability was approximately the reverse. The carbamates were found to be very unstable in polar solvents such as alcohols and DMSO with decomposition in DMSO found to be very fast (within hours). Hence, NMR data were not collected in DMSO-d_6, as was the case with the benzamides (Chapter I), but in acetone-d_6 affording a better solubility/stability ratio. Since stability in non-polar solvents was satisfactory while solubility was modest, crystal growth was tried from limited choices of solvents, such as CH_3COCH_3, $CHCl_3$, CH_3CN, or mixtures of these solvents.

3. Comment on spectroscopic data

All spectroscopic data including ^{1}H-, ^{13}C-, ^{19}F-NMR and IR are listed in Appendix I, Section 3 and the spectra are given in the ESI II, Section 1. Due to the insolubility/instability of the **CxxR** compounds, the NMR data were recorded in $CDCl_3$ (^{1}H-NMR) and acetone-d_6 (^{1}H-, ^{13}C- and ^{19}F-NMR).

As for the benzamide and pyridinecarboxamides (Chapter I), the chemical shift of the carbamate hydrogen changes position depending on the solvent. In the less polar $CDCl_3$ the carbamate proton of the **CpxR** and **CmxR** isomers ranges from 7.3-8.0 ppm, while in more polar solvents such as acetone, it is usually at 9.5-10 ppm. However, in **CoxR** the carbamate proton shifts are usually found around 10 ppm regardless of solvent. These findings are in agreement with hitherto observations in benzamides and pyridinecarboxamides where almost the same pattern was observed in all isomers where the pyridine nitrogen was located *ortho*. The cause of this effect is delocalisation of electrons between the carbamate and pyridine nitrogens.

With regard to the IR spectra, all compounds show a strong band *ca.* 1745 cm^{-1} that corresponds with the stretch of the carbonyl (C=O) bond. The N-H vibrations in the region between 3300 cm^{-1} and 2700 cm^{-1} are usually strongly linked to hydrogen bonding in the crystal structure. The relationship between this “N-H” region and primary intermolecular interactions in solid state will be discussed later.

4. X-ray crystallographic methods

All **CxxR** crystal samples were obtained by slow evaporation at room temperature or 4ºC, typically from $CHCl_3$, acetone, ethyl acetate, methanol, THF or solvents blends including *n*-hexane and toluene. The single crystal growths were successful for most of **CxxM** (except for **CmmM** and **ComM**) and **CxxOMe** (except **CmoOMe**) isomers. For the halogen derivatives (**CxxX**) success was limited, with only 10 out of 25 halogen-carbamates giving suitable single crystals, after many crystallization attempts from several solvents, under a wide range of crystallization conditions. These compounds are **CmpF**, **CmmF**, **CopF**, **CpmCl**, **CmpCl**, **CmmCl**, **CopCl**, **CmoBr**, **CmpBr** and **CopBr**.

Single crystal X-ray data collection and data reduction,[176] structure solution and refinement[3,168] for all **CxxR** compounds was as described for the **Fxx** and **NxxM** isomer grids (Chapter I). Selected crystallographic and structural information is detailed in the ESI II (Section 2). Molecular and hydrogen bonding diagrams (Figs. **48-54**, **56-64** and **66-75**) were generated as described for other isomer grids (with displacement ellipsoids drawn at the 30% probability level).[169]

5. Computational methods

A computational study similar to that carried out for the benzamides (**Mxx** and **Fxx**) and pyridinecarboxamides (**NxxF** and **NxxM**) was performed for all five phenyl-*N*-pyridinyl-carbamate (**CxxR**) isomer grids. The aim, as in Chapter I, was to investigate the optimised molecular geometry of the isomers, perform conformational analysis and elucidate conformational preference in *gas phase* and to investigate the flexibility of the main torsion angles and energies of rotational barriers. Finally the modelling information, presented in the form of PES diagrams, was directly compared with the solid-state molecular geometries in order to rationalise both similarities and differences of the modelled and solid state molecular structures, as well as problems with the crystallinity of carbamates.

Unlike the computational methods used in Chapter I, phenyl-*N*-pyridinyl-carbamate (**CxxR**) isomer grids were not subjected to optimisations using implicit solvent models (PCM-SMD, CH_2Cl_2 and H_2O); the modelling was limited to *gas phase* calculations since *gas phase* modelling affords the most significant information regarding optimised geometries and conformational behaviour. Furthermore, high accuracy energy calculations were not performed,

The optimisations and conformational analyses in *gas phase* are performed as described in Chapter I (Section 1) using the DFT method [B3LYP/6-311++G(d,p)]. All calculations were performed using Gaussian09[25] for Linux/Unix operating on a SGI Altix ICE 8200EX high performance computing system at the ICHEC.

The carbamates contain pyridinyl and phenyl rings joined by a carbamate linker moiety. In total there are four main torsion angles involved in the geometry: the angle C26-C21-C1=O1 (pyridinyl ring, **C**-ring, α torsion angle, **red** bond in Scheme **35**), the C1-O2-C11-C16 angle (**R**-phenyl ring, **F-/Cl-/Br-/O-/M**-ring, β torsion angle, **blue** bond), the O1=C1-N1-C21 torsion angle (δ, OCNC, **green** bond) and the O1=C1-O2-C11 torsion angle (γ, COCO, **brown** bond). For the methoxyphenyl-*N*-pyridinyl-carbamate (**CxxOMe**) isomer grid an additional, methoxy torsion angle (ω, **Me**) exists. As for the compounds described in Chapter I, *meta*- or *ortho*-pyridinyl (**C**) and phenyl (**R**) rings can theoretically be present in the **C-*syn*** or **C-*anti*** conformations depending on the position of the carbonyl moiety (Scheme **36**). However, optimisations and conformational analyses showed that in the **CxoR** isomers the **oR**-ring is found to be orthogonal to the pyridinyl (**C**) ring. Therefore, two conformations are equivalent and the ***syn***/***anti*** convention, cannot be applied to the *ortho*-phenyl isomers.

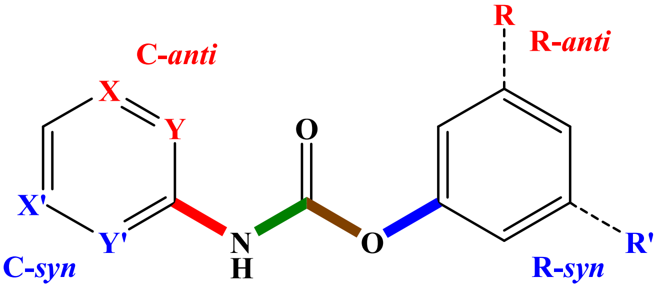

Scheme 35: Possible conformations in the **CxxR** compounds

The benzamide and pyridinecarboxamide (Chapter I) amide link torsion angle was not subject to conformational analysis, since it was considered to be rigid. However, for the **CxxR** isomer grids the decision was made to investigate the conformational behaviour of the carbamate linker torsion angles, namely the O1=C1-N1-C21 torsion angle (OCNC, δ) and the O1=C1-O2-C11 torsion angle (COCO, γ). Although considering their general rigidity, the aim was mainly to inspect the flexibility and energies of the rotational barriers. All PES diagrams are provided in the ESI II (Section 3).

6. CxxM isomer grid

6.1. Molecular and crystal structure data

Seven of the nine **CxxM** isomers gave single crystals suitable for single crystal X-ray diffraction. The **CmmM** and **ComM** isomers did not produce any suitable single crystals, even after numerous attempts with a range of organic solvents. Unexpectedly, the **CpoM** and **CmoM** were isolated as solvates, **CpoM** with a disordered molecule of chloroform and **CmoM** as a monohydrate.

All structures crystallise in the monoclinic system, with exception of **CmpM** (orthorhombic). Apart from the disordered solvent in the **CopM** crystal structure, no disorder was found in the solid state **CxxM** structures. Tables **28** and **29** summarise the basic crystallographic data and structural features.

Table 28: Selected crystallographic data for the seven **CxxM** isomers[†]

CxxM	*Space group*	*Z'*	*Volume* (Å^3)	$R[F^2 > 2\sigma(F^2)], wR(F^2)$
CppM	$P2_1/c$	1	1149.0(7)	0.065, 0.132
CpmM	$P2_1/n$	1	1150.42(8)	0.064, 0.095
CpoM	$P2_1/n$	2	2649.4(12)	0.075, 0.237
CmpM	$P2_12_12_1$	1	1182.66(3)	0.025, 0.068[a]
CmoM	$P2_1/c$	1	1268.09(4)	0.048, 0.134
CopM	$P2_1/c$	1	1164.39(11)	0.091, 0.338
CooM	$P2_1/n$	1	1176.92(3)	0.044, 0.127

† Complete crystallographic, refinement and structural details for the seven **CxxM** isomers ($C_{13}H_{12}N_2O_2$) are listed in the ESI II (Section 2.1.1). [a]Obtained with Cu *K*α radiation

Table 29. Relevant structural features (Å,°) in the eight **CxxM** isomers[a]

CxxM	C_6/C_5N	C_6/carbamate	C_5N/carbamate	N...N/O[b]	Packing
CppM	73.94(8)	62.89(10)	20.85(13)	2.955(3)	*C(6)* chains
CpmM	53.44(8)	55.24(7)	4.53(15)	2.972(3)	*C(6)* chains
CpoM	84.97(12) 82.38 (10)	87.68(14) 69.46(11)	8.10(24) 13.14(19)	2.900(4) 2.908(4)	2-D sheets
CmpM	52.33(5)	63.16(5)	11.38(11)	2.9138(17)	2-D sheets
CmoM	66.25(4)	86.55(4)	26.12(5)	2.8279(15)[c] 2.8269(16)[d]	$R^4_4(14)$ dimers /2-D Sheets
CopM	62.53(12)	67.60(11)	8.58(27)	3.003(4)	dimers
CooM	76.45(4)	81.68(4)	5.42(11)	2.9770(16)	dimers

[a] Full structural details are provided in the ESI II (Section 2.1.2).

[b] The $_{\text{carbamate}}N\ldots N_{\text{pyridine}}$ interaction distances.

[c] The $_{\text{carbamate}}N\cdots O_{\text{water}}$ interaction distances.

[d] The $_{\text{water}}O\cdots N_{\text{pyridine}}$ interaction distances.

6.1.1. **CpxM** isomer series

The main interaction in the **CpxM** isomers is the $_{\text{carbamate}}$N1-H1···N24$_{\text{pyridine}}$ hydrogen bond, with (**CppM**) or without (**CpmM**) significant C-H···O2 auxiliary interactions while in **CpoM** (*Z'* = 2) both types of bonding are present, alternately linking molecules as (···ABAB···). The **CpoM** isomer crystallises with a solvate with one disordered CHCl$_3$ molecule.

CppM molecular and crystal structure

Single crystals were grown from acetone. The primary aggregation is accomplished *via* N1-H1···N24 hydrogen bonding [N1···N24^{a} = 2.955(3) Å, *a* = -1+x,1/2-y,-1/2+z], enhanced by an auxiliary C25-H25···O2^{a} [C25···O2^{a} = 3.213(3) Å] interaction (Fig. **48**). The N1-H1···N24 hydrogen bond links molecules in a *zig-zag* manner into a *C(6)* chain, parallel with the (010) plane and perpendicular to the *b*-axis direction. A secondary interaction involves π-π stacking (C21···C25^{b} = 3.161(3) Å, *b* = x,1/2-y,-1/2+z), as well as the C16-H16···O1^{c} [C16···O1^{c} = 3.582(4) Å, *c* = 1+x,y,z] interaction. Of less importance are the weak C23-H23···C12^{d} (*d* = -1+x,y,-1+z) and C15-H15···H15-C15^{e} (*e* = -2-x,-y,-z) contacts. It is interesting that the disordered methyl group (around the bond axis) does not engage in any intermolecular interaction.

The carbamate linker atoms form a four atom carbamate plane (N1/C1/O1/O2). The angle between the carbamate plane and the **M**-ring (tolyl ring) is 62.89(10)°, while against the pyridinyl ring it is 20.85(13)°. The angle between the **M**-ring and the pyridinyl ring is 73.94(8)° (Table **29**). Compared with **Mpp** [46.03(9)°] and **NxxM** [66.45(3)°] the **M**-ring appears to be more rotated than in the benzamides.

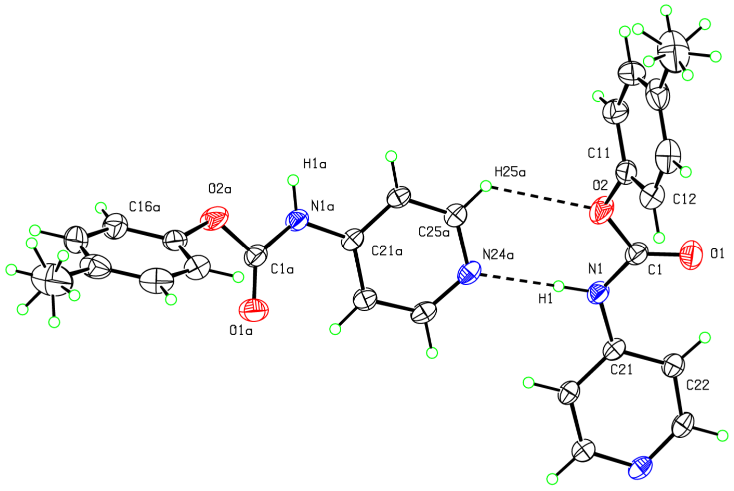

Fig. 48: An ORTEP diagram of **CppM** with N1-H1···N24^{a} hydrogen bonding (*a* = -1+x, ½-y,-½+z) and an auxiliary C25^{a}-H25^{a}···O2 interaction.

CpmM molecular and crystal structure

Suitable single crystals were grown from $CDCl_3$. As for **CppM,** the primary interaction is N1-H1···N24 hydrogen bonding (N1···N24^c = 2.972(3) Å, *c* = -x+1/2,y-1/2,-z+1/2), and contrary to **CppM,** no auxiliary bonding to O2 is present (Fig. **49**). However, a weak N1-H1…C23 contact is present.

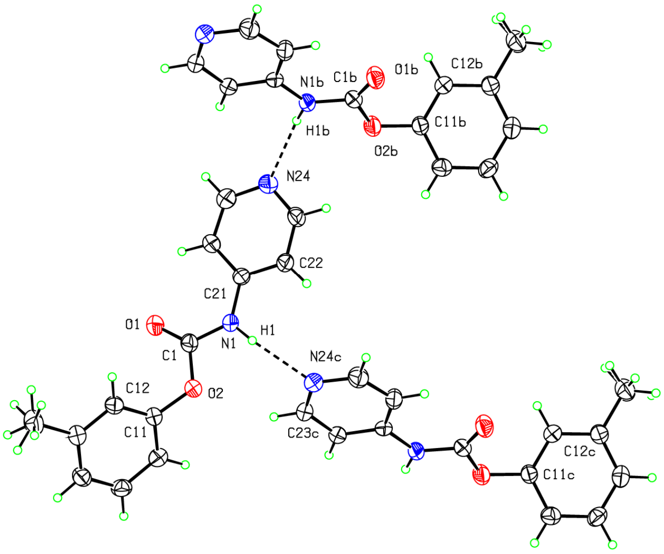

Fig. 49: An ORTEP diagram of **CpmM** showing aggregation *via* N1-H1···N24 hydrogen bonds (*b* = ½-x, ½+y, ½-z; *c* = ½-x,-½+y, ½-z)

The N1-H1···N24 hydrogen bonds form a *zig-zag C(6)* chain, along the *b*-axis direction and parallel to the (301) plane. A contact C14-H14···H17-C17 (H14···H17^a = 2.27 Å, *a* = -x,1-y,2-z) exists along the (301) plane. Finally, weak but double C16-H16···C1 contacts (C16···C1^d = 3.485(3) Å, *d* = -x,1-y,1-z) connect chains into a 3-D structure. The methyl group is disordered around the C14-C17 axis.

The angle between the carbamate plane and the pyridinyl ring (**C**-ring) is 4.53(15)°, therefore, most of the molecule is planar apart from the **M**-ring at an angle of 55.24(7)° to the carbamate plane. The interplanar angle between the **M**-ring and the **C**-ring is 53.44(8)°. The conformation of the **M**-ring is **M-*anti***.

CpoM molecular and crystal structure

The **CpoM** isomer is the only isomer isolated as a solvate as [$(\mathbf{CpoM})_4$:$CHCl_3$]. The molecule of $CHCl_3$ is disordered with total occupancy of 50%; the ratio between **CpoM** and $CHCl_3$ is 4:1 (Fig. **50**).

Two **CpoM** molecules (A and B) are connected into a pair with similar N1-H1···N$_{pyr}$ hydrogen bonding N1A-H1A···N24B [N1A···N24B = 2.900(4) Å] as in the **CpmM** molecule, with an additional weak N1A-H1A···C25B contact. The interplanar angle between the two pyridinyl rings (A and B) is 28.67(16)º. Two pairs of molecules (AB) are linked into an undulating *C(6)* chain (···ABAB···) through N1B-H1B···N24^{b} [N1B···N24^{b} = 2.908(4) Å, *b* = -3/2+x,1/2-y,-1/2+z] hydrogen bonding, augumented with flanking C23A-H23A···O2B^{b} [C23A···O2B^{b} = 3.222(4) Å] interactions (Fig. **50**) as described for the **CppM** isomer. The waving 1-D chain is perpendicular to the *b*-axis and parallel to the ($\bar{1}$03) plane. The secondary interaction is the C16B-H16B···O1B^{v} (C16B···O1B^{c}= 3.325(5) Å, *c* = -1+x,y,z) contact aggregating chains along the *a*-axis direction into a 2-D sheet parallel to the (010) plane.

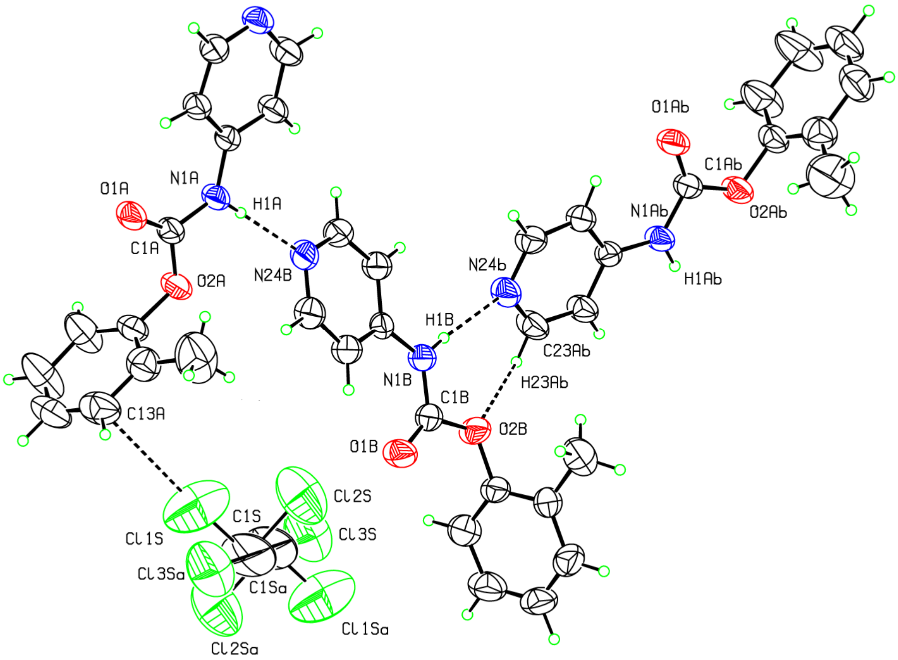

Fig. 50: An ORTEP diagram of **CpoM** showing the N1-H1···N24 hydrogen bonds and disordered molecule of CHCl$_3$ (*a* = 1-x,-y,-z; *b* = -$^{3}/_{2}$+x, ½-y,-½+z)

The disordered CHCl$_3$ molecules engage in a final aggregation through weak but double C13A···Cl1S [3.426(9) Å] and C17B-H17B…Cl(1S) interactions (Fig. **50**).

The *ortho*-tolyl ring (**M**-ring, C$_6$) in molecule A is almost orthogonal to the carbamate plane [87.68(14)°], while in the molecule B the **M**-ring/carbamate ring is 69.46(11)°. The pyridinyl rings (**C**-ring, C$_5$N) are generally planar with the carbamate plane (Table **29**). Both interplanar angles (C$_5$N/C$_5$) (Table **29**) are close to 90°, the rings are nearly orthogonal. The interplanar angle between the **M**-rings is 56.15(14)°.

6.1.2. **CmxM** isomer series

Since crystal growth of **CmmM** was not successful, only the **CmpM** and **CmoM** results are presented. **CmoM** is unique in the **CxxM** isomer grid since it was isolated as a monohydrate with a remarkable hydrogen bonding system. With the exception of **CmoM**, only **CmoBr** was isolated as monohydrate among all the carbamate grids.

CmpM molecular and crystal structure

The **CmpM** crystal structure data was collected with Cu Kα radiation, affording a structure solution with an *R*-factor of 0.025.

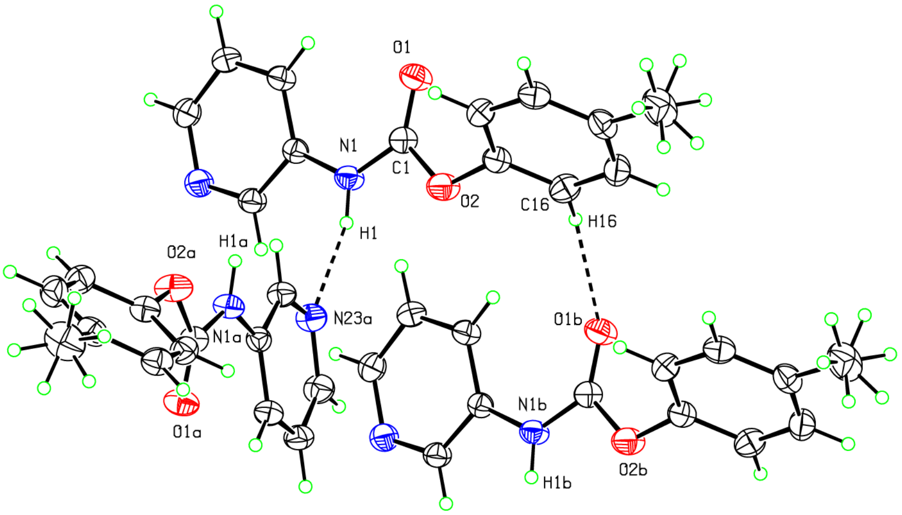

Fig. 51: An ORTEP diagram of **CmpM** (*a* = 1-x,-½+y,½-z; *b* = -1+x,y,z)

The single crystals were grown from acetone. The primary interaction is N1-H1···N23^a [N1···N23^a = 2.9138(17) Å, *a* = 1-x,-1/2+y,1/2-z] hydrogen bond, aggregating molecules into a spiral *C(5)* chain, along the *b*-axis direction, parallel with the (001) plane (Fig. **51**). The N1-H1···N23 hydrogen bond is supported by the weak N1-H1···C22^a side interaction [N1···C22^a = 3.3604(18) Å], as seen in **CpmM**.

The secondary interaction is C16-H16···O1^b [C16···O1 = 3.440(2) Å, *b* = -1+x,y,z] connecting the chains along the *a*-axis direction into a 2-D sheet, parallel with the (001) plane (Fig. **51**). Weak C-H···π(arene) contacts C24-H24···Cg1^c [C24···Cg1^c = 3.7300(16) Å, Cg1 = (C21,…,C26), *c* = 2-x,1/2+y,1/2-z] and C25-H25···Cg2^c [C25…Cg1^c = 3.4083(16) Å, Cg2 = (C11,…,C16)] support sheet formation. The conformation of the **C**-ring is **C-*syn***.

CmoM molecular and crystal structure

The **CmoM** isomer is the only compound in the **CxxM** isomer grid isolated as a hydrate (**CmoM**:H_2O). The single crystals were grown from a $CHCl_3$/acetone solvent mixture. Molecules of water play a crucial role in the aggregation of the **CmoM**:H_2O crystal structure. Two molecules of water and two molecules of **CmoM** form a complex structure through double N1-H1···O2W [N1···O1W = 2.8279(15) Å] and O1W-H2W···N23 [O1W···N23^a = 2.8269(16) Å, *a* = 2-x,1-y,-z] hydrogen bonds giving rise to a $R^4_4(14)$ ring (Fig. **52**).

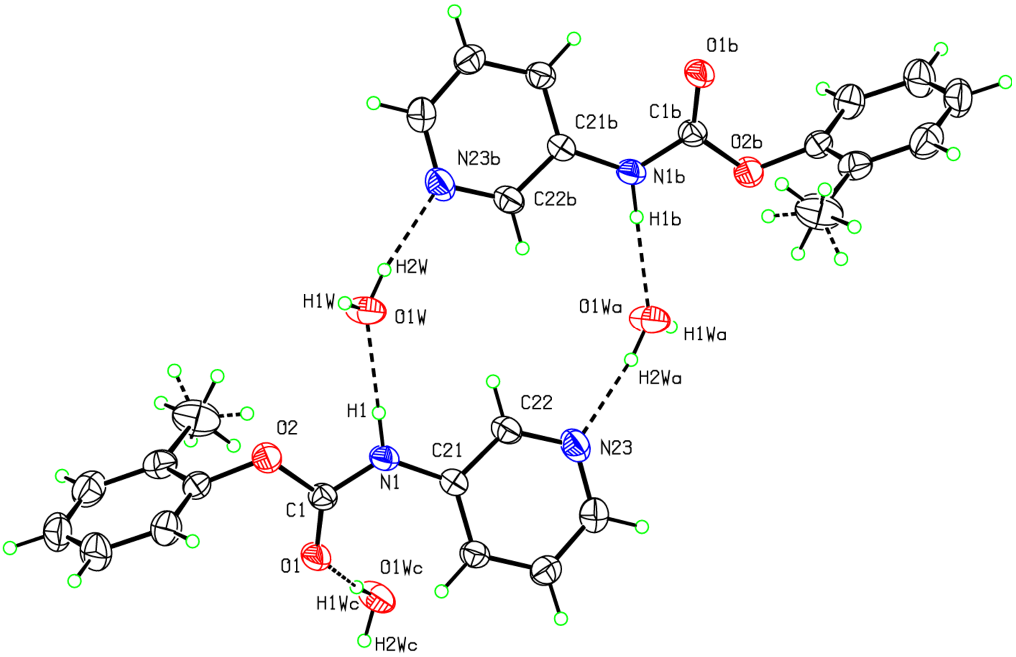

Fig. 52: An ORTEP diagram of the **CmoM** monohydrate (*a*, *b* = 2-x,1-y,-z, *c* = x,½-y,-½+z).

Two pyridinyl rings in the complex are coplanar with a minor offset; molecules of water are on either side of and below the pyridinyl ring planes. An auxiliary interaction O1W-H2W···C22^a [O1W···C22^a = 3.5219(16) Å] supports the O1W-H2W···N23 hydrogen bonding.

The secondary interaction is the O1W-H2W···O1^d [O1W···O1^d = 2.9126(15) Å, *d* = x,1/2-y,1/2+z] hydrogen bond (Fig. **52**). It is critical and even more important for aggregation, supported by weak but double C26-H26···O1^d [C26···O1^d = 3.3532(15) Å] interaction it links complexes directly into a 2-D sheet, parallel with the (100) plane. The 2-D sheets are connected into a 3-D crystal structure by weak C17-H17D…C14^e [H17D…C14^e = 2.82 Å, *e* = 1-x,-y,-z] contacts.

Within the molecule, a weak intramolecular C17-H17A…O2 (H17A…O2 = 2.65 Å) interaction is observed. The C_6/C_5N interplanar angle is 66.25(4)°, while the

C_6/carbamate angle is 86.55(4)°. The C_5N/carbamate angle is unusually large with a value of 26.12(5)°. The conformation of the **C**-ring is **C-*syn*.**

6.1.3 CoxM isomer series

The main feature of both **CoxM** isomers is dimer formation through double N1-H1…N22 hydrogen bonding as a primary intermolecular interaction, forming cyclic $R^2_2(8)$ rings. This interaction is essentially the same as in the **Fxo**/**Mxo** (Chapter I) benzamide isomers. However, in the **CoxM** isomers multiple additional interactions are involved in dimerisation, making the **CoxM** dimer linkage possibly stronger than in the benzamides. Since the strongest hydrogen bond forming moieties are engaged in dimerisation, the crystal structure relies mostly on weaker C-H···π/O interactions and contacts. All pyridinyl rings of the **CoxM** compounds are found to be in the **C-*syn*** conformation, as it is essential for dimer formation.

CopM molecular and crystal structure

The *R*-factor is high, due to the twinning; single crystals were grown from acetone. The main interaction in **CopM** is dimerisation (Fig. **53**) about inversion centres, forming cyclic $R^2_2(8)$ rings *via* double N1-H1···N22^a [N1···N22^a = 3.003(4) Å, *a* = 1-x,1-y,1-z] hydrogen bonds. Dimer linkage is enhanced by two auxiliary C23-H23···O2^a [C23···O2^a = 3.232(5) Å] interactions. In total, four interactions engage in this molecular recognition, giving a strongly bounded dimeric unit.

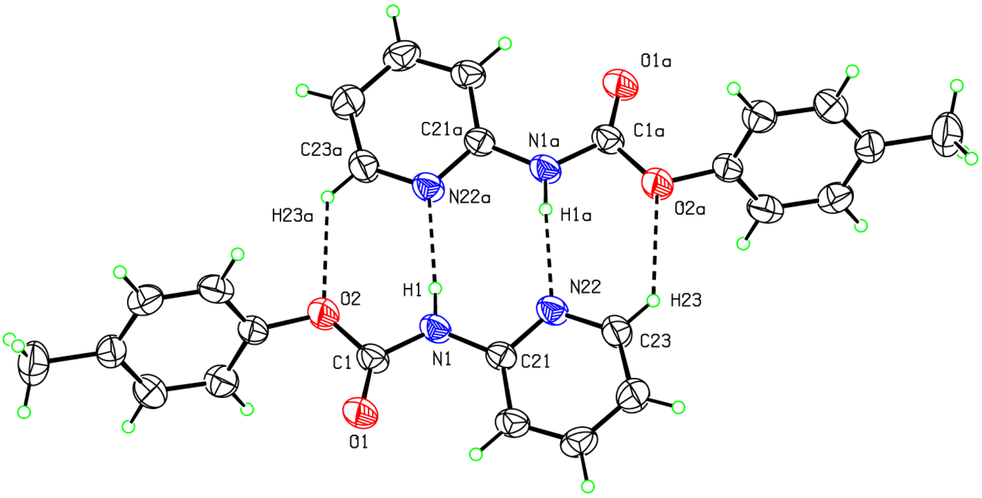

Fig. 53: Hydrogen bonding and auxiliary interaction in **CopM** isomer (*a* = -1-x,1-y,1-z).

The crystal structure formation depends on weak C-H···π(arene) contacts such as C25-H25···C15^b (C25···C15^b = 2.84 Å, b = -x,-1/2+y,1/2-z) and C15-H15···C26^c (C15···C26^c = 2.83 Å, c = 1-x,1/2+y,1/2-z). These contacts aggregate dimers directly into a 3-D crystal structure. It is interesting to note that both methyl and carbonyl moieties do not engage in any significant intermolecular interactions or contacts.

According to Table **29**, the pyridinyl ring is nearly planar with the carbamate linker plane [8.58(27)°], while the **M**-ring (C_6) is moderately rotated by 67.60(11)°. The interplanar C_6/C_5N angle is 62.53(12)°.

CooM molecular and crystal structure

A single crystal suitable for X-ray diffraction was grown from $CHCl_3$. As for the **CopM** isomer, the **CooM** molecules form dimers about inversion centres *via* two N1-H1···N22^a [N1···N22^a = 2.9770(16), a = 2-x,1-y,-z] hydrogen bonds giving cyclic $R^2_2(8)$ rings. These two hydrogen bonds are aided and augmented by two strong C23-H22…O2^a [C23···O2^a = 3.2560(19) Å] interactions as well as two weak N1-H1···C23^a [H1···C23^a = 2.897(17) Å] contacts. In total, six interactions per dimeric unit, two being hydrogen bonds, are engaged in this remarkable dimer (Fig. **54**).

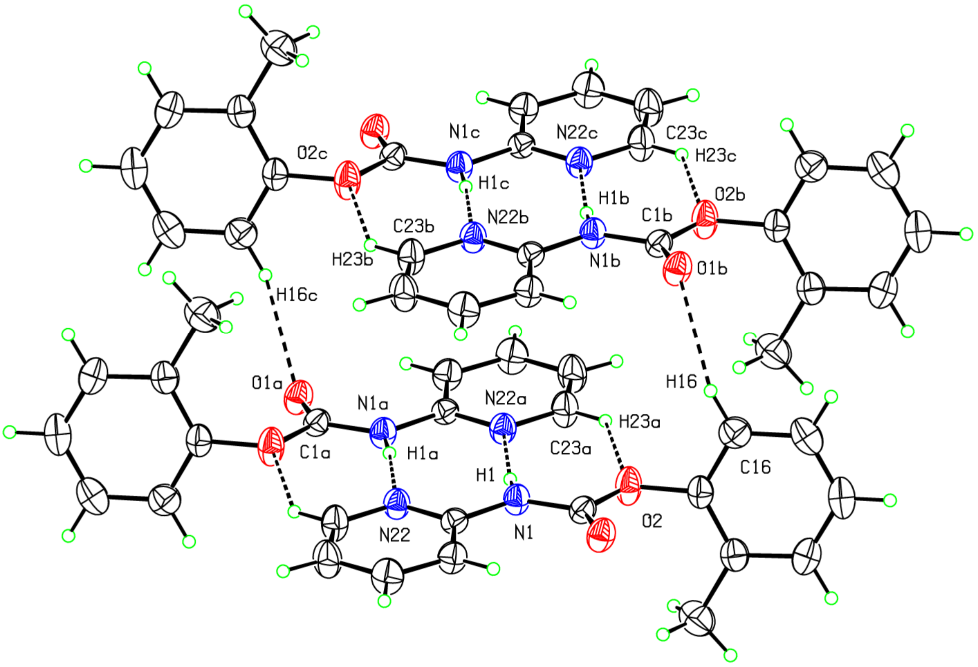

Fig. 54: Dimer formation in **CooM** (a = 2-x,1-y,-z; b = 1+x,y,z; c = 3-x,1-y,-z).

The secondary hydrogen bond C16-H16···O1^b [C16···O1^b = 3.370(2) Å, b = -1+x,y,z], aided with a long C-H···π(arene) interaction C17-H17A···C16^c [H17A···C16^c = 3.593(2) Å, c = 1+x,y,z] links dimers along the a-axis direction or (100) direction to form a column parallel to the (024) plane (Fig. **54**). There are no other interactions in the structure. Intramolecular geometry of the **CooM** isomer is as seen in the **CpoM** and **CmoM** isomers. The pyridinyl ring (**C**-ring, C_6) is nearly co-planar with the carbamate linker plane [5.42(11)°] while the *ortho*-methylphenyl ring (**M**-ring, C_6) is almost orthogonal to the carbamate linker [81.68(4)°]. The interplanar angle (C_6/C_5N) is 76.45(4)°.

6.2. *Ab initio* calculations and modelling data

6.2.1. Structure optimisation

The main structural features of the **CxxM** isomers optimised in the *gas phase* are shown in Table **30**.

The most evident characteristic of the modelled **CxxM** structures is the planarity of all dihedral angles except the β angle, related to the tolyl ring (**M**-ring). On average, molecules are mainly planar; the pyridinyl ring is tilted by -0.04±0.9°, the δ torsion angle (OCNC) is rotated by 0.06±1.26° and the γ torsion angle (COCO) is rotated by -0.6±2.8°. The planar OCNC and COCO torsion angles form the carbamate plane and the pyridine ring is coplanar with it. The only significant exception from planarity is the tolyl ring torsion angle. In Table **30**, absolute values of the β (**M**-ring) torsion angles are given, taking into account conformations.

Table 30: Torsion angles (°) of the optimised **CxxM** isomers[a]

	α	β	β^*	γ	δ
CppM	-0.32	62.00	62.00	-0.85	0.27
CpmM	-0.01	62.94	62.94	-0.68	-0.45
CpoM	-0.14	83.14	83.14	-0.91	-0.14
CmpM	-0.43	61.93	61.93	-0.91	-0.04
CmmM	0.49	63.02	63.02	0.93	0.64
CmoM	0.17	107.69	75.96	-2.02	-0.18
CopM	-0.03	61.51	61.51	-0.93	-0.15
ComM	-0.32	62.48	62.98	0.82	0.79
CooM	0.25	82.47	82.47	-0.73	-0.22

[a] The angle C26-C21-C1=O1 (**C**-ring) is designated as α; the C1-O2-C11-C16 angle (**M**-ring) as β, the O1=C1-N1-C21 angle as δ, and O1=C1-O2-C11 as γ. All geometries are based on B3LYP/6-311++G(d,p) optimisations.

However, if only the corresponding deviation from planarity is given (β^* in Table **30**), a specific pattern can be noted. In all compounds except for the **CxoM** triad, the **M**-ring is rotated by an average of 62.4±2.0°, whereas the **oM**-ring, due to the steric repulsion between methyl group and carbonyl moiety, is nearly orthogonal to the carbamate plane and pyridinyl ring with an average torsion angle of 80.5°.

The **mM**-rings in the **CxmM** triad are all found to be in an **M-*anti*** conformation. Due to the orthogonality of the **oM**-ring, the ***syn***/***anti*** conformational convention cannot be applied since both supposed conformations are equivalent. However, in **CmoM,** the **oM** ring is slightly rotated towards the **M-*syn*** conformation, and in **CpoM** and **CooM** there is a slight preference for the **M-*anti*** conformation.

6.2.2. Conformational analysis

Fig. **55** depicts the nine PES conformational analysis diagrams of the **CxxM** modelled structures in *gas phase*. The **C-ring** (pyridinyl ring, α dihedral angle) is drawn as a **full red line**, with the **M-ring** (tolyl ring, β dihedral angle) as a **blue dashed line**. At $\theta = 0$ and ±180º, the conformation of the asymmetric **C**- or **M**-ring is noted as ***syn*** or ***anti***.

As expected, modularity is present in the PES diagrams of the **CxxM** isomers and similar to the benzamides and pyridinecarboxamides (Chapter I). The preferred **C**-ring conformation in the **CmxM** and **CoxM** isomers is **C-*syn***, whereas for the **CxmM** isomer triad, the *meta*-tolyl ring is expected to prefer the **M-*anti*** conformation. As noted in Section 5 of the current Chapter, an *ortho*-tolyl ring cannot be subjected to ***syn***/***anti*** formalism, since its orthogonality makes any of the two conformations equivalent in steric and electronic terms. The same **C-*syn*** preference in pyridinyl rings is noted in the benzamide and pyridinecarboxamide (Chapter I) isomer grids.

The *ab initio* results are summarized as follows: Rotation of the *para*-pyridyl (**Cp**) rings give a PES profile with two global maxima at *ca.* ±90° ($\mathrm{TS_{Cp}}^{\mathrm{I}}$ = 24.56±0.15 kJ.mol^{-1}) and two global minima at 0° and *ca.* ±180°. As expected, the shape of the curve resembles a pyridinyl (**p**) ring with a PES profile of the **Mxx**/**Fxx** benzamides although the rotational barrier is slightly higher ($\mathrm{TS_{\mathbf{p}}}^{\mathrm{I}}$=22.75±0.08 kJ.mol^{-1}).

The *meta*-pyridine ring (**Cm**) PES scan profile is slightly asymmetric with one global maximum at *ca.* -90° ($\mathrm{TS_{Cm}}^{\mathrm{II}}$ = 18.02±0.09 kJ.mol^{-1}), one local maximum at *ca.* 90° (17.84±0.17 kJ.mol^{-1}), local minimum at *ca.* ±180° (5.63±0.03 kJ.mol^{-1}) and global minimum at 0°.

As mentioned previously, the **Cm** ring has the **C-*syn*** conformation and the difference in energy when compared to **C-*anti*** is 5.63±0.03 kJ.mol^{-1}. According to the Boltzmann distribution, around 91% of molecules are in the **C-*syn*** conformation. A similar PES profile was found in the *meta*-pyridinyl ring (**m**) of the benzamide isomer rings.

Conformational analysis of the *ortho*-pyridinyl ring (**Co**) gives an asymmetric PES profile that has one global maximum (36.93±0.28 kJ.mol^{-1}) at *ca*. -115°, one local maximum (TS_{Co}^{I} = 36.13±0.39 kJ.mol^{-1}) at *ca.* 110°, one local minimum (30.96±0.12 kJ.mol^{-1}) at *ca.* 150° and one global minimum (0°). Therefore, the mandatory conformation is **C-*syn***. The PES profile is similar to the *ortho*-pyridinyl ring (**o**) in **Mxx**/**Fxx** benzamides, but with lower energy rotational barriers.

The **pM** ring PES profile has two global maxima at *ca*. -120° and *ca*. 60° (4.06±0.07 kJ.mol^{-1}), two local minima at *ca*. -30° and 155° (0.43±0.05 kJ.mol^{-1}) and four global minima at -60°, 120°, ±180° and 0°.

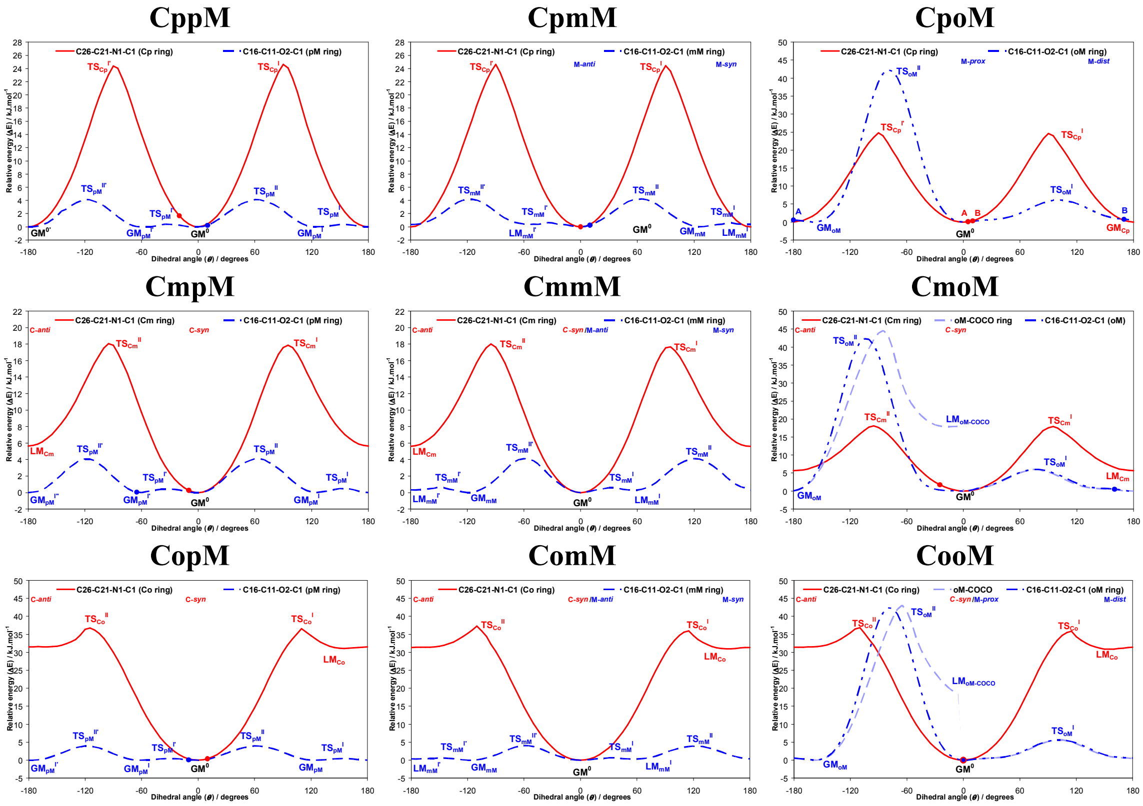

CppM

CpmM

CpoM

CmpM

CmmM

CmoM

CopM

ComM

CooM

Fig. 55: The PES conformational analysis for the nine **CxxM** isomers (*gas phase*): the equivalent solid state angle is depicted by (●) with, if applicable, an assigned identification letter.

The **mM** ring has a similar PES profile with two global maxima at *ca.* -60° and 120° (TS_{mM}^{II} = 4.10±0.11 kJ.mol^{-1}, at *ca.* -120° and 60° in **CpmM**), two local maxima at -150° and 35° (TS_{mM}^{I} = 0.62±0.02 kJ.mol^{-1}, at *ca.* -35° and 150° in **CpmM**), two local minima at *ca.* 60° and ±180° (LM_{mM}^{I} = 0.33±0.03 kJ.mol^{-1}, at *ca.* -60° in **CpmM**) and one global minimum at 0°.

The PES profiles of the **pM** and **mM** rings are similar to the equivalent PES profiles of the benzamide isomer grids, but the rotational barriers are significantly lower than in the benzamides (14-16 kJ.mol^{-1}) where partial delocalisation between the amide linker and the phenyl ring exists. In the carbamate backbone, however, due to the additional oxygen atom (O2), partial delocalisation does not exist and the phenyl ring can freely rotate. Therefore, the flexibility of the **pM** and **mM** rings in carbamates is significantly higher than in the benzamides and free rotation is possible. The preferred conformation of the **mM**-ring was found to be ***M-anti***. However, due to the low rotational barriers and very low energy difference (0.33±0.03 kJ.mol^{-1}) the ***M-syn*** conformation is very plausible (47% in *gas phase*).

A normal PES scan procedure of the *ortho*-methyl ring gave a simple result for the **CpoM** isomer, however in **CmoM** and **CooM**, a PES scan procedure ended with the COCO dihedral angle at its local minimum. When the **oM** ring is at *ca.* -120°, a collision between the carbonyl ring and methyl group occurs producing a very high rotational barrier (43.85±1.10 kJ.mol^{-1}). For the **ComM** and **CooM** isomers, the barrier cannot be crossed without the COCO dihedral angle being moved. Therefore, a normal PES scan procedure forces rotation of the **oM** ring, but this results in movement of both the **oM** ring and COCO dihedral in the area between *ca.* -120° and 0°. The resulting PES scan is shown in the **ComM** and **CooM** diagrams as pale blue dashed lines ending as a conformer with unusually deviated COCO ring and a very high relative energy of 18.20±0.30 kJ.mol^{-1} ($LM_{oM\text{-}COCO}$, Fig. **55**). This conformer is not probable under normal conditions.

In order to overcome the steric clash and accomplish the conformational analysis, the COCO dihedral angle was kept constrained while the PES scan of the **oM** ring is performed. The result is a continuous PES diagram (**oM** ring, **blue dashed** curve), performed in all three **CxoM** isomers and presented in Fig. **55**. This constrained PES profile is a non-realistic approximation of the **oM** rotation, but explains the inflexibility and behaviour of the **oM** ring during the hypothetical rotation. Despite that, the constrained PES profiles of the **oM** rings can be considered true PES scans. They have one global maximum at -80° (TS_{oM}^{II} = 42.32±0.04 kJ.mol^{-1}), one local maximum at 100° (TS_{oM}^{I} = 5.94±0.23 kJ.mol^{-1}) and two global minima at -155° (±180° in **CmoM**) and 0°.

In general, conformational analyses of the **oM** rings clearly show that collision of methyl and carbonyl groups limits rotation and flexibility of the **oM** rings – it can rotate by 180° only in one direction.

The PES profile of the COCO dihedral angle in **CxmM** and **CxpM** is symmetrical and has two global maxima at *ca.* ±100° (TS_{COCO}^{I} = 27.19±0.69 kJ.mol^{-1}), one local minima at ±180° (LM_{COCO}^{I} = 18.40±0.39 kJ.mol^{-1}) and one global minima at 0°. However, in **CxoM**, due to the steric interaction with the methyl ring, equivalent PES profiles are asymmetric and have one global maximum at *ca.* -95° (TS_{COCO}^{II} =36.84±0.62 kJ.mol^{-1}), one local maximum at *ca.* 105° (TS_{COCO}^{I} = 26.73±0.17 kJ.mol^{-1}), one local minimum at ±180° (LM_{COCO}^{I} = 17.72±0.54 kJ.mol^{-1}) and one global minimum at 0°. High rotational barriers prevent flexibility of the COCO dihedral angle, although some limited oscillations out of the global minimum are possible. The opposite conformation with COCO dihedral angles at its local minimum is very unlikely.

Finally, the PES profiles of the OCNC (δ) dihedral angles are the same in all **CxxM** isomers and are therefore independent of isomeric variations. It has two global maxima at *ca.* -65° and 115° (TS_{OCNC} = 69.63±2.14 kJ.mol^{-1}), one local minimum at ±180° (LM_{OCNC} = 11.37±0.88 kJ.mol^{-1}) and one global minimum at 0°. Very high rotational barriers prevent rotation of the OCNC dihedral angle and limit the flexibility although, as for the COCO dihedral angle, some very limited flexibility is possible. The existence of the opposite conformation is very unlikely too. Therefore the carbamate moiety in the **CxxM** isomers can be considered as rigid.

6.3. Comparisons of the solid state and modelling data

Comparison of the **CxxM** isomer structures from the seven available crystal structures and calculations is made by marking (as ●) torsion angle differences ($\Delta\theta$) between the available experimental and theoretical structures on the corresponding *gas phase* PES diagrams (Fig. **55**). For the **CpoM** isomer with *Z'* = 2 the corresponding angles are labelled as A or B. For the **CmmM** and **ComM** isomers whose crystal structure determination failed due to the poor quality of their single crystals, no $\Delta\theta$ was marked.

According to this comparison, experimentally derived solid state dihedral angles of all seven **CxxM** isomers positively corresponds with the global minima of the equivalent modelled **CxxM** isomers. This holds true for all four studied torsion angles (α, β, δ, γ). Eventual deviations from stationary points (global minima) are no larger than 25°, which is within the acceptable range. Therefore, it can be said that for the **CxxM** isomers, apart from the **CmmM** and **ComM** isomers, the solid state matches the modelled molecular structures.

These findings are substantially different from those made for the benzamides and pyridinecarboxamides where more than one third of solid state molecular structures do not match the optimised molecular structures. It is especially true for the **CmxM** compounds where a conformational change was expected as the **C-*anti*** conformation allows the formation of $_{\text{carbamate}}$N1-H1···N23$_{\text{pyridine}}$ hydrogen bonds linking the molecules into a *C(5)* chain. However, aggregation of **CmpM** in the orthorhombic $P2_12_12_1$ space group allows formation of $_{\text{carbamate}}$N1-H1···N23$_{\text{pyridine}}$ hydrogen bonds while the **Cm** rings are in the thermodynamically more stable **C-*syn*** conformation. Furthermore, the **CmoM** isomer was unexpectedly grown as a monohydrate, where the **C-*syn*** conformation allows complexation with a molecule of water. However, the IR spectrum of the **CmoM** isomer (ESI II, Section 1.1) does not show any band typical for a molecule of water, suggesting that the determined **CmoM** structure might not be representative of the bulk **CmoM** material.

7. CxxOMe isomer grid

7.1. Molecular and crystal structure data

Eight out of the nine synthesised **CxxOMe** isomers gave suitable single crystals. In most attempts the **CmoOMe** isomer decomposed and only in rare cases gave very fragile, poor, needle-like crystals. Nevertheless, despite the difficulties with the **CmoOMe** isomer, the **CxxOMe** isomer grid compounds proved to be the most crystalline among all of the studied carbamate grids.

All eight **CxxOMe** crystal structures crystallise with Z' = 1 and have $_{\text{carbamate}}$N-H···N$_{\text{pyr}}$ hydrogen bonds as the primary interaction, usually supported by C23-H23···O2 interactions, as seen in the **CxxM** isomer grid. However, the methoxy moiety often engages in aggregation *via* various interactions. There were no solvates found however, the most remarkable structure among all **CxxR** carbamates is **CmmOMe** (trigonal *R3c*, Z = 18) where three molecules form a unique hydrogen bonded trimer.

7.1.1 **CpxOMe** isomer series

The isomers of the **CpxOMe** triad share many similar crystallographic features: crystallising in the same crystal system and centrosymmetric space group with *Z'* = 1 and have the same primary interaction (N1-H1···N24).

Table 31: Selected crystallographic data for the eight **CxxOMe** isomers†

CxxOMe	*Space group*	*Z'*	*Volume* (Å^3)	$R[F^2 > 2\sigma(F^2)], wR(F^2)$
CppOMe	$P2_1/n$	1	1218.60(5)	0.042, 0.114
CpmOMe	$P2_1/c$	1	1208.45(4)	0.046, 0.129
CpoOMe	$P2_1/c$	1	1144.29(7)	0.048, 0.103
CmpOMe^a	$P2_12_12_1$	1	1201.86(4)	0.028, 0.074
CmmOMe	$R3c$	1	5511.2(2)	0.031, 0.082
CopOMe	$P2_1/c$	1	1166.44(16)	0.043, 0.117
ComOMe	$P\bar{1}$	1	603.40(10)	0.058, 0.114
CooOMe	$P\bar{1}$	1	577.02(13)	0.031, 0.088

† Complete crystallographic, refinement and structural details for the eight **CxxOMe** isomers ($C_{13}H_{12}N_2O_3$) are listed in the ESI II (Section 2.2). ^{a}Obtained with Cu *K*α radiation

Table 32: Relevant structural features (Å, °) in the eight **CxxOMe** isomers^a

CxxOMe	C_6/C_5N	C_6/carbamate	C_5N/carbamate	N···N^b	Packing
CppOMe	56.93(4)	57.31(3)	0.78(8)	2.9183(16)	*C(6)* chains
CpmOMe	73.89(5)	71.49(5)	7.60(8)	2.9361(15)	*C(6)* chains
CpoOMe	86.15(6)	88.90(6)	6.09(8)	2.998(2)	*C(6)* chains
CmpOMe	52.53(5)	62.02(5)	10.28 (10)	2.9130(19)	2-D sheets
CmmOMe	50.61(42)	60.29(11)	10.03(13)	2.970(7)	Trimers
	61.68(38)	58.56(11)	3.14(13)	2.963(7)	
CopOMe	53.28(3)	57.08(4)	4.43(8)	2.9886(16)	$R^2_2(8)$ dimers
ComOMe	82.94(7)	84.74(7)	2.03(17)	2.983(3)	$R^2_2(8)$ dimers
CooOMe	89.05(4)	84.84(5)	4.67(8)	3.0298(18)	$R^2_2(8)$ dimers

^{a} Full structural details are provided in the ESI II (Section 2.2).

^{b} The $_{\text{carbamate}}$N-H···N$_{\text{pyridine}}$ interaction distances.

CppOMe molecular and crystal structure

The **CppOMe** isomer (Fig. **56**) was grown from acetonitrile. The principal interaction is N1-H1···N24^a [N1···N24^a = 2.9183(16) Å, *a* = -1/2+x,1/2-y,1/2+z] hydrogen bonding in an orthogonal manner, forming *zig-zag C(6)* chains along the [101] direction, parallel with the (101) plane. The principal hydrogen bond is aided by a weak N1-H1···C25^a (H1···C25^a = 2.87 Å) contact and augmented with a C25-H25···O2^b [C25···O2^b = 3.2745(17) Å, *b* = 1/2+x,1/2-y,-1/2+z] interaction.

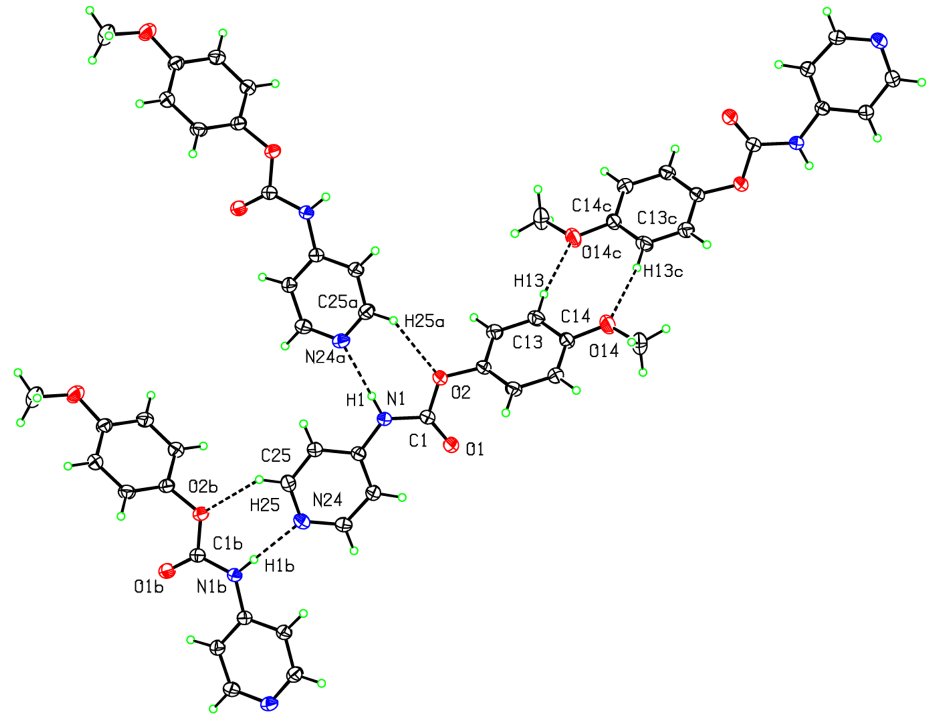

Fig. 56: **CppOMe** (*a* = -1/2+x,1/2-y,1/2+z; *b* = 1/2+x,1/2-y,-1/2+z; *c* = 1-x,-y,2-z).

The secondary interaction involves two adjacent methoxy moieties interacting *via* two remarkable $C13\text{-}H13\cdots O14^{c}$ [$C13\cdots O14^{c}$ = 3.4777(17) Å, *c* = 1-x,-y,2-z] hydrogen bonds that form a $R^{2}_{2}(8)$ cyclic ring. These hydrogen bonds link the *C(6) zig-zag* chains along the *b*-axis direction into an undulating 2-D sheet, parallel with the (101) plane. The 3-D crystal structure formation is achieved by weak $C17\text{-}H17A\cdots O14^{d}$ [$H17A\cdots O14^{d}$ = 2.64 Å, *d* = -1+x,y,z] interactions, stacking the undulating 2-D sheets along the *a*-axis. The 4-pyridinyl ring (**C**-ring, C_5N) and the carbamate plane are nearly perfectly planar. The methoxy group and the *para*-phenyl ring (**O**-ring, C_6) are coplanar and tilted to the carbamate plane by 57.31(3)°. The interplanar angle C_6/C_5N is not significantly different [56.93(4)°] from the C_6/carbamate angle. The conformation of the methoxy group is **Me-*anti***.

CpmOMe molecular and crystal structure

A single crystal was grown from a blend of $CHCl_3$, CH_3CN and toluene. As expected, the main backbone is $N1\text{-}H1\cdots N24^{c}$ [$N1\cdots N24^{c}$ = 2.9360(15) Å, *c* = 1-x, 1/2+y, -1/2-z] hydrogen bonding (Fig. **57**), aided with flanking $C23\text{-}H23\cdots O2^{d}$ [$C23\cdots O2^{d}$ = 3.2826(16) Å, *d* = 1-x, -1/2+y, -1/2-z] interactions.

The hydrogen bonding, as seen in the **CppOMe** isomer, forms *zig-zag C(6)* chains along the *b*-axis direction, parallel with the $(\bar{1}01)$ plane. It is interesting to note that the pyridinyl rings (**C**-rings, C_5N) are parallel with the $(\bar{1}01)$ plane; the angle between the C_5N ring and the carbamate plane is just 7.60(8)° (Table **32**). Therefore, the whole chain is planar and parallel with the $(\bar{1}01)$ plane apart from the rotated [71.49(5)°] *meta*-methoxyphenyl ring (**O**-ring, C_6). The *zig-zag* chains are connected along the [011] direction into a 2-D sheet parallel with the $(\bar{1}01)$ plane *via* bifurcated C14-H14···O1^a [C14···O1^a = 3.2956(17) Å, *a* = 2-x, 1/2+y,1/2-z] and C15-H15···O1^a [C15-H15···O1^a = 3.3014(18) Å] interactions.

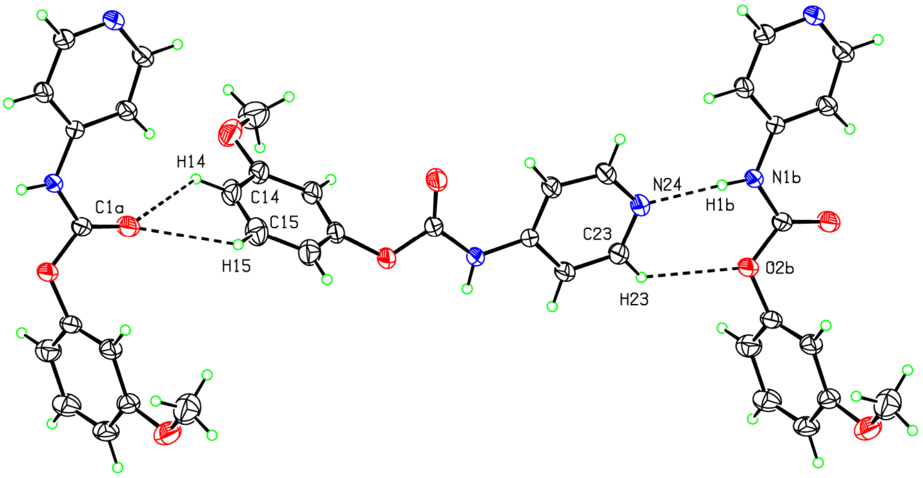

Fig. 57: Hydrogen bonding in the **CpmOMe** isomer (*a* = 2-x,½+y,½-z; *b* = 1-x,-½+y,-½-z)

The sheets are interconnected along the *c*-axis direction into the crystal structure by weak C-H···π(arene) contacts: C16-H16···C21^e [C16···C21^e = 2.83 Å, *e* = x,1/2-y,1/2+z] and C17-H17A···C14^f [C17···C14^f = 3.501(3) Å, *f* = x,1/2-y,-1/2+z].

The interplanar angle C_6/C_5N is 73.89(5)°. The conformation of the *meta*-methoxyphenyl ring (**O**-ring) is ***O-anti*** while the conformation of the CH_3O group is ***Me-syn***.

CpoOMe molecular and crystal structure

Single crystals of the **CpoOMe** isomer (Fig. **58**) were grown from a mixture of $CHCl_3$ and acetone at 4°C. As expected, the primary interaction is the N1-H1···N24^b [N1···N24^b = 2.998(2) Å, *b* = 1-x,1/2+y,5/2-z] hydrogen bonding linking the molecules along the *b*-axis direction into a 1-D chain parallel with the $(\bar{1}01)$ plane. Contrary to the aggregation seen with the other isomers having a similar hydrogen bonding scheme, no augmenting C25-H25···O2 interaction is present. The secondary interaction is C23-H23···O3^c [C23···O3^c = 3.499(2) Å, *c* = x,1/2-y,1/2+z] that connects 1-D chains along the *c*-axis direction into 2-D sheets parallel with the (100) plane.

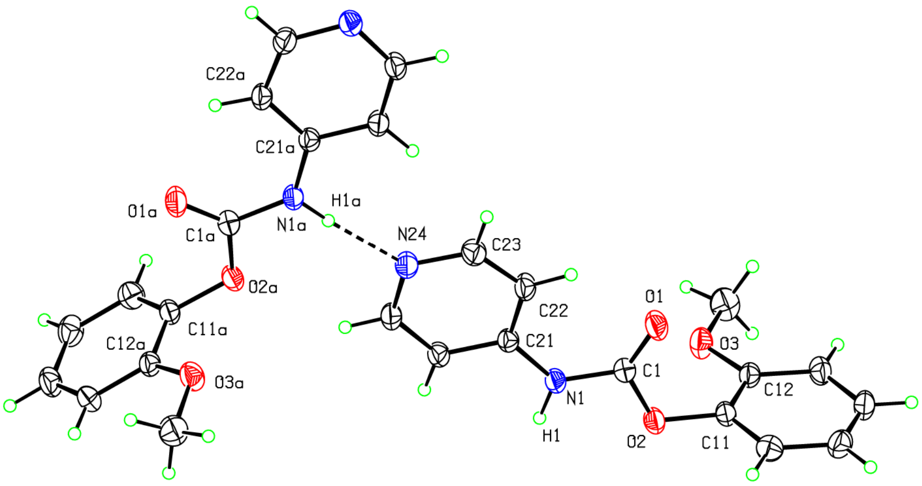

Fig. 58: Hydrogen bonding in the **CpoOMe** isomer (*a* = 1-x,-½+y,$^5/_2$-z)

Formation of the 2-D sheets is supported by the neighbouring alternating C26-H26···O3^d [C26···O3^d = 3.329(2) Å, *d* = 1-x,1-y,2-z] interaction. These 2-D sheets are interconnected *via* double C-H···π(arene) interactions C17-H17B···C15^e [H17B···C15^e = 2.84 Å, *e* = -x,1-y,1-z], as well as by the vicinal π···π stacking C13···C13^e [3.387(3) Å]. The geometry of the **CpoOMe** isomer (Table **32**) is as expected for an *ortho*-substituted phenyl-*N*-pyridinyl-carbamate; the C_6/carbamate angle is near the orthogonal [88.90(6)°] and the C_5N/carbamate angle is close to planarity [6.09(8)°]; the interplanar angle C_6/C_5N is 86.15(6)°.

7.1.2 **CmxOMe** isomer series

The **CmxOMe** triad contains the most remarkable structure of all the **CxxR** series: the disordered trimeric **CmmOMe** isomer. It crystallises in the trigonal *R3c* space group with Z = 18 and forms unique trimers *via* N1-H1···N23 hydrogen bonds. The **CmpOMe** is isostructural with **CmpM**. **CmoOMe** was the only isomer in the **CxxOMe** series that was reluctant to produce single crystals, suitable for SXRD, even after many attempts using a range of solvents and solvent blends; instead of crystal growth, decomposition of the compound occurs.

CmpOMe molecular and crystal structure

Single crystals were grown from $CHCl_3$. The **CmpOMe** isomer is similar to the **CmpM** isomer (Section 6.1.2), in the $P2_12_12_1$ space group (No. 19). The presence of the methoxy group at the *para* position instead of the methyl results in a larger *c*-axis and volume [1201.86(4) Å^3 in **CmpOMe** compared to 1182.66(3) Å^3 in **CmpM**], and different to **CmpM,** the substituent is engaged in a weak C-H···π(arene) interaction.

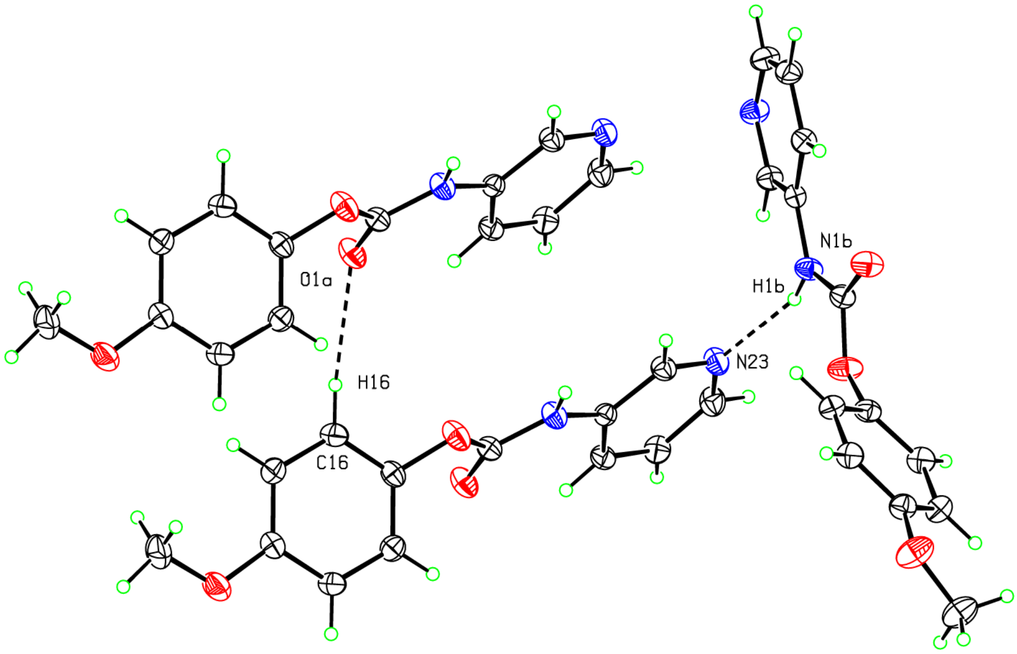

Fig. 59: An ORTEP diagram of **CmpOMe** (*a* = 1+x,y,z; *b* =1-x,-½+y,½-z)

The aggregation in **CmoOMe** is similar as in **CmpM**. The hydrogen bond N1-H1···N23^c [N1···N23^c = 2.9130(19) Å, *c* = 1-x,1/2+y,1/2-z] links molecules along the *b*-axis direction into a spiral *C(5)* chain parallel with the (001) plane (Fig. **59**). The hydrogen bond is less linear [160.6(16)°] than in **CmpM** and is supported by the N1-H1···C22^c side interaction [N1···C22^c = 3.353(2) Å].

The secondary interaction is C16-H16···O1^a [C16···O1^a = 3.463(2) Å, *a* = -1+x,y,z] connecting the chains along the *a*-axis direction into a 2-D sheet, parallel with the (001) plane (Fig. **59**). Weak C-H···π(arene) contacts C24-H24···Cg1^d [C24…Cg1^d = 3.695(2) Å, Cg1 = (C21,…,C26), *d* = 2-x,1/2+y,1/2-z] and C25-H25···Cg2^e [C25···Cg1^e = 3.4291(19) Å, Cg2 = (C11,…,C16), *e* = 2-x,1/2+y,1/2-z] support the sheet formation. As distinct from the **CmpM** isomer, the C-H···π(arene) C17-H17C···Cg2^f [C17···Cg2^f = 3.708(2) Å, *f* = 1/2+x,3/2-y,-z] contact in **CmpOMe** isomer represents the only contact between 2-D sheets.

As expected the geometrical features of the **CmpOMe** isomer are very similar to those in **CmpM** (see Table **32** and **29**). The conformation of the **C**-ring is **C-*syn***.

CmmOMe molecular and crystal structure

The most remarkable structure of all of the **CxxR** compounds is the **CmmOMe** crystal structure. Molecules form unique trimers v*ia* N1-H1···N23 interactions in an unexpected trigonal *R3c* space group (No. 161). Interestingly, no other carbamate, benzamide or pyridinecarboxamide in any series forms a trimeric structure. However, formation of trimers *via* N-H···N hydrogen bonds or by other hydrogen bonds is already observed in many structures,[206-210] as in methyl-4-trifluoromethylpyrazole-3-carboxylate that crystallises as a solvate in *C2/c*.[206] **CmmOMe** was grown with difficulty from MeOH and data were collected with Cu *K*α radiation.

The **CmmOMe** molecules in the crystal structure are conformationally disordered about the C1-O2-C11-C16 torsion angle (*β* angle). 50% of molecules (A, *β* = -56.06°) are **O-*syn***, the remainder (B, *β* = 120.86°) are in an **O-*anti*** conformation (Fig. **60**). The *meta*-methoxyphenyl ring is not disordered. Both the A and B parts of the molecule are involved in the formation of the hydrogen bonded trimer ring *via* N1A-H1A···N23A^{a} [N1A···N23A^{a} = 2.970(7) Å, *a* = 2-y,x-y+1,z] and N1B-H1B···N23B^{c} [N1B···N23B^{c} = 2.963(7) Å, *c* = -x+y+1,2-x,z] hydrogen bonds (Fig. **61**). If viewed when the methoxy moieties are pointed upward (Fig. **61**) it can be noted that the A part forms a trimer ring in a clockwise direction, while the B part does likewise in an *anti*-clockwise direction.

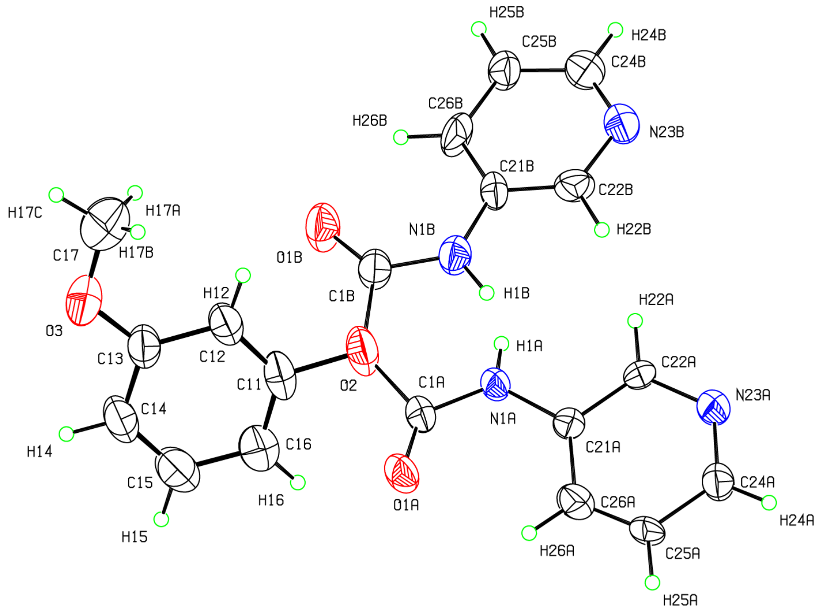

Fig. 60: An ORTEP diagram of the **CmmOMe** disorder showing the A part (**O-*syn*** conformation, 50% occupancy) and B part (**O-*anti*** conformation, 50% occupancy)

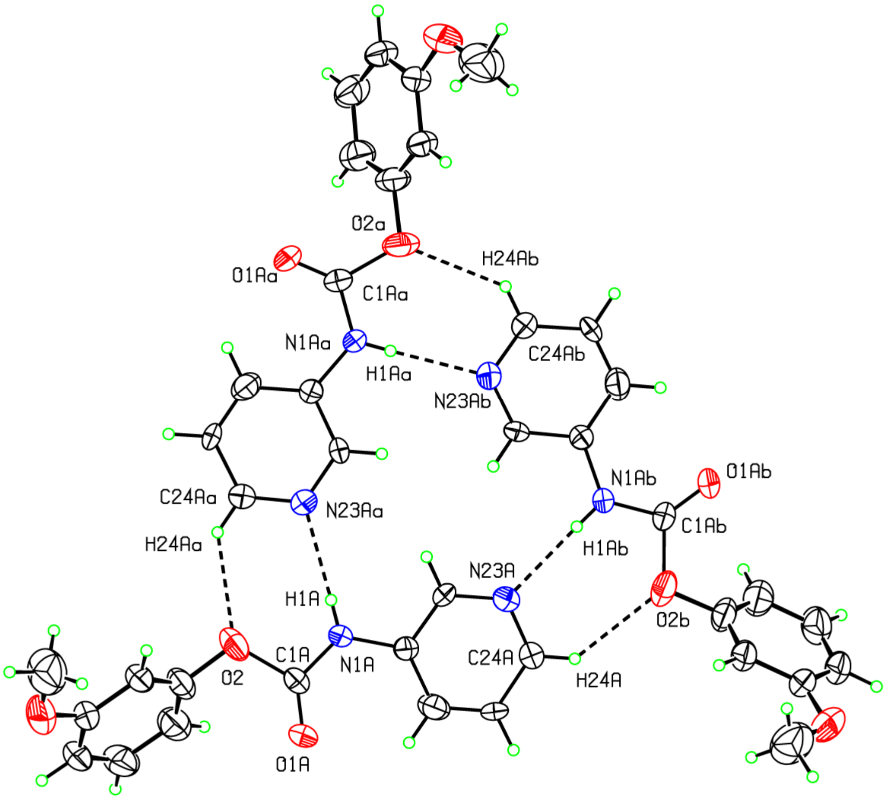

Fig. 61: The **CmmOMe** trimer (only A is shown; *a* = 2-y,1+x-y,z; *b* = 1-x+y,2-x,z).

Trimer rings are interconnected into a 1-D column by stacking along the *c*-axis direction through C12-H12···O1B^d [C12···O1B^d = 3.184(5) Å, *d* = 1-x+y,y,z-1/2] hydrogen bonding, and is additionally stabilised by π–π stacking (C1A···C25A^d and C1A···C26B^d). The columns are linked in the crystal structure by C17-H17C···O1A^e [C17···O1A^e = 3.260(5) Å, *e* = 2/3-x+y,4/3-x,-2/3+z] and C25B-H25B···O3^f [C25B···O3^f = 3.351(19) Å, *f* = 1/3+x,2/3+x-y,1/6+z] interactions. The conformation of the methoxy group is **Me-*syn***.

7.1.3 **CoxOMe** isomer series

As for the **CoxM** compounds, the main interaction in all **CoxOMe** compounds is dimer formation *via* double N1-H1···N22 hydrogen bonds forming cyclic $R^2_2(8)$ hydrogen bonded rings about inversion centres, augmented by flanking C23-H23···O2 interactions. The **ComOMe** and **CooOMe** isomers crystallise in $P\bar{1}$, while the **CopOMe** isomer is in $P2_1/c$. The pyridinyl rings are **C-*syn***.

CopOMe molecular and crystal structure

The **CopOMe** isomer (Fig. **62**) is the most crystalline material among all **CxxR** carbamates, regardless of solvent. Crystals were grown from methanol.

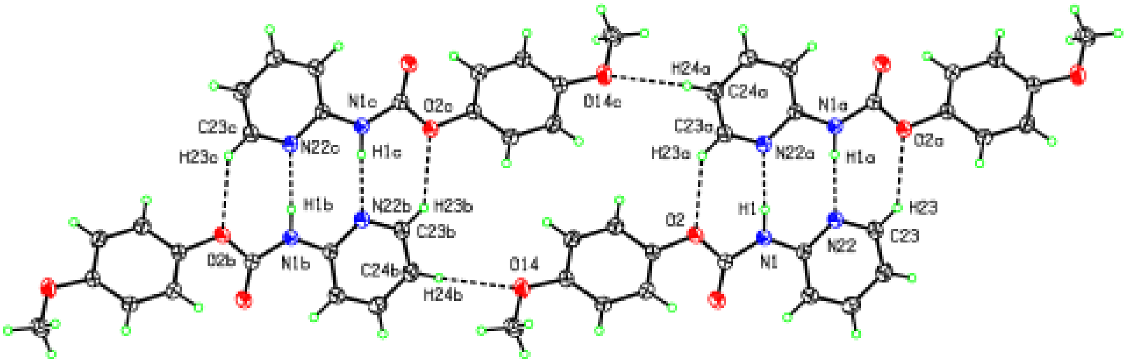

Fig. 62: Hydrogen bonding in **CopOMe** (*a* = 1-x,1-y,1-z; *b* = x,-1+y,z; *c* = 1-x,-y,1-z)

The **CopOMe** isomer crystallises in $P2_1/c$ and is isomorphous with **CopM**. Another similarity with **CopM** is formation of $R^2_2(8)$ hydrogen bonded dimers. Due to the proton accepting abilities of the O2 atom, the methoxy group is involved in crystal structure formation, as distinct from the methyl group in **CopM**.

The primary bonding in the **CopOMe** isomer is dimer formation about inversion centres giving $R^2_2(8)$ rings *via* double N1-H1···N22^a [N1···N22^a = 2.9885(15) Å, *a* = 1-x,1-y,1-z] hydrogen bonds (Fig. **62**). Dimer formation is fortified by C23-H23···O2^a [C23···O2^a = 3.2372(18) Å] interactions.

Compared with the isomorphous **CopM**, the **CopOMe** isomer has different secondary interactions. The methoxy moieties connect dimers along the *b*-axis direction into a 1-D column parallel with the (100) plane through double C24-H24···O14^d [C24···O14^d = 3.3750(18) Å, *d* = x,1+y,z] interactions (Fig. **62**). The columns are interconnected along the *c*-axis direction into a 2-D sheet parallel with the (100) plane *via* C17···O1^e [3.1433(18), *e* = 1-x,-1/2+y,1/2-z] contacts. There are no other interactions in the crystal structure. The geometry of **CopOMe** is similar to that of **CopM**. The C_6/carbamate angle is 57.08(4)°, while the C_5N/carbamate is nearly planar at 4.43(8)°. The interplanar angle C_6/C_5N is 53.28(3)°.

ComOMe molecular and crystal structure

As in all **CoxOMe** compounds, dimerisation is achieved by N1-H1···N22^a [N1···N22^a = 2.983(3) Å, *a* = 2-x,-y,1-z] hydrogen bonding about inversion centres and is augmented by flanking C23-H23$\cdots$O2^a [C23$\cdots$O2^a = 3.236(3) Å] interactions (Fig. **63**). Single crystals were grown from a CHCl$_3$/acetone solvent mixture. Dimers are linked along the *a*-axis direction into a column parallel with the (011) plane, *via* double C12-H12$\cdots$O1^e [C12$\cdots$O1^e = 3.411(3) Å, *e* = 1+x,y,z] interactions and supported by weak C17-H17A$\cdots$Cg2^e [C17$\cdots$Cg2^e = 3.550(3) Å, Cg2 = (C11...C16)] contacts. Furthermore, the columns are linked by C14-H14$\cdots$O3^c (C14$\cdots$O3^c = 2.66 Å, *c* = 2-x,1-y,-z) interactions into a sheet parallel with the (011) plane (Fig. **63**). There are no additional interactions in the crystal structure.

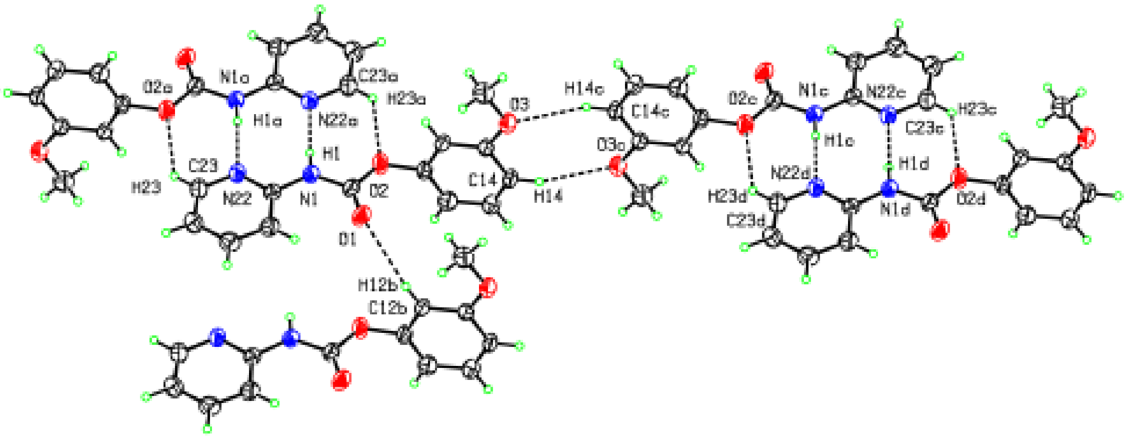

Fig. 63: Hydrogen bonding in **ComOMe** (*a* = 2-x,-y,1-z; *b* = -1+x,y,z; *c* = 2-x,1-y,-z; *d* = x,1+y,-1+z)

The **ComOMe** molecule has an unusual geometry for a *meta*-substituted phenyl-*N*-pyridinyl-carbamate. The *meta*-methoxyphenyl ring is nearly orthogonal to both the carbamate plane and pyridinyl ring (Table **32**) and therefore is barely applicable to ***syn***/***anti*** conformational systematics. However, the *meta*-methoxyphenyl ring is slightly in an **O-*syn*** conformation. The methoxy moiety is **Me-*syn***, whereas the pyridinyl ring is co-planar with the carbamate plane.

CooOMe molecular and crystal structure

The **CooOMe** plate crystals were grown from CDCl$_3$, and the data collection was accomplished using Cu Kα radiation. The **CooOMe** isomer (Fig. **64**) crystallises in the $P\overline{1}$ space group and is isostructural with **ComOMe**.

As with the previous two isomers, the **CooOMe** isomer forms dimers as a primary intramolecular interaction. The dimers are formed about inversion centres *via* N1-H1$\cdots$N22^a [N1$\cdots$N22^a = 3.0298(18) Å, *a* = 1-x,1-y,1-z] hydrogen bonds, giving $R^2_2(8)$ hydrogen bonded rings and aided by flanking C23-H23$\cdots$O2^a [C23$\cdots$O2^a =

3.3572(18) Å] interactions. The longer N1···N22 and C23···O2 interactions suggest a weaker dimer. The crystal aggregation relies on C14-H14···O1^{b} [C14···O1^{b} = 3.3296(18) Å, *b* = 1-x,2-y,-z] interactions, supported by weak C17-H17A···C15^{b} [C17···C15^{b} = 3.677(2) Å] contacts that align dimers into a column along the (011) plane.

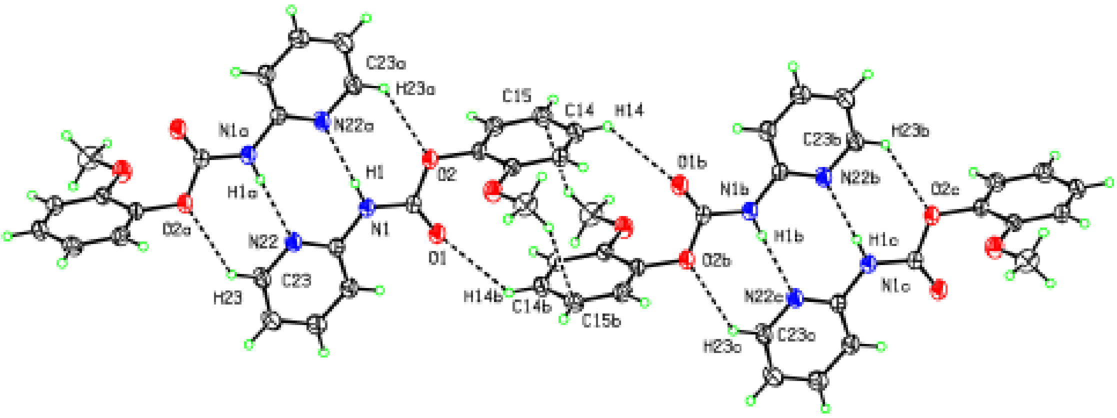

Fig. 64: Hydrogen bonding in **CooOMe** (*a* = 1-x,1-y,1-z; *b* = 1-x,2-y,-z; *c* = x,1+y,-1+z)

The geometry of the **CooOMe** isomer is as expected for an *ortho*-substituted phenyl-*N*-pyridinyl-carbamate. The interplanar angle C_6/C_5N is almost orthogonal [89.05(4)°], while the C_5N/carbamate angle (**C**-ring) is close to planarity [4.67(8)°].

7.2. *Ab initio* calculations and modelling data

7.2.1. Structure optimisation

The five dihedral angles of the optimised **CxxOMe** isomer models are shown in Table **33**. According to the structural characteristics, all **CxxOMe** isomers can be divided into two groups. The first group comprises six **CxpOMe** and **CxmOMe** isomers that share very similar geometries, while another group is the **CxoOMe** triad. In general, all **CxxOMe** isomers show a certain level of planarity, excluding the **O**-ring rotated from planarity. In **CxpOMe** and **CxmOMe** the planarity is more pronounced.

The pyridinyl dihedral angle (**C**-ring, α-angle) is planar (0.10±0.30°) regardless of the isomer, as well as the δ(OCNC) torsion angle (-0.19±0.27° in **CxpOMe** and the **CxmOMe** isomers and 1.11±0.05° in the **CxoOMe** isomers). The γ dihedral angle (COCO) is generally planar (-0.93±0.68° in **CxpOMe** and the **CxmOMe** isomers), but in the **CxoOMe** isomers it is tilted by 9.42±0.39°.

Table 33: Torsion angles (°) of the optimised **CxxOMe** isomers[a]

	α	β	β^*	γ	δ	ω
CppOMe	0.45	67.44	67.44	-0.49	-0.15	-0.97
CpmOMe	-0.29	119.48	64.35	-1.48	-0.26	0.75
CpoOMe	0.32	73.75	73.75	9.49	1.07	5.99
CmpOMe	0.50	66.12	66.12	-0.06	-0.07	-0.89
CmmOMe	-0.30	121.05	62.86	-1.51	-0.34	0.64
CmoOMe	0.03	73.65	73.65	9.77	1.09	5.79
CopOMe	0.07	66.52	66.52	-0.45	0.24	-0.82
ComOMe	0.24	121.09	62.87	-1.61	-0.55	0.60
CooOMe	-0.10	73.92	73.92	9.00	1.16	5.50

[a] The angle C26-C21-C1=O1 (**C**-ring) is designated as α, the C1-O2-C11-C16 angle (**O**-ring) as β, the O1=C1-N1-C21 angle as δ, the O1=C1-O2-C11 as γ and the C-C-O3-C17 (methoxy group, **Me**) as ω. The β^* angle presents the relative deviation from planarity compared to the neighbouring COCO (γ) torsion angle. All geometries are based on B3LYP/6-311++G(d,p) optimisations.

For the methoxyphenyl ring (**O**-ring, β torsion angle) the situation is specific. In the **CxpOMe** isomer triad, the **O**-ring (**pOMe**) is rotated by 66.69±0.68°, while the *meta*-methoxyphenyl ring (**mOMe**) in the **CxmOMe** isomer triad is rotated in the opposite direction by an absolute value of 120.54±0.92°. The corresponding deviation from planarity (relative value) amounts to 63.36±0.86° (β^* in Table **30**), that is very close to the rotation of the **pOMe** ring (**O**-ring) in **CxpOMe**. Therefore, the geometry of both **CxpOMe** and **CxmOMe** triads is very similar but with one important difference: rotation of the **O**-ring is in an opposite direction. The conformation of the *meta*-methoxyphenyl ring (**mOMe**) is ***O-syn***, contrary to the ***M-anti*** in the **CxmM** isomers (Section 6.2.1).

Due to the steric clash between the methoxy and carbonyl moiety in the **CxoOMe** triad, the **O**-ring (**oOMe**) is 73.77±0.14°, close to orthogonality with a minor tilt towards eventual ***O-anti*** conformation. However, as was the case in the analogous **CxoM** isomer triad, the orthogonality of the **O**-ring equalises possible steric or electronic influences of the neighbouring moieties and the ***syn*/*anti*** conformational convention is not applicable.

The **CxxOMe** isomer grid is unique among the **CxxR** carbamates due to the presence of an additional methoxy group that has an additional torsion angle $_{\text{phen}}$C-C-O-CH$_3$ (**Me** dihedral angle, ω). The methoxy group is expected to be planar with its parent phenyl ring; however, it can adopt two conformations (Scheme **36**), proximal (***Me-syn***) or distal (**Me-*anti***) to the carbonyl oxygen or carbamate hydrogen, depending on the conformation of the **O**-ring.

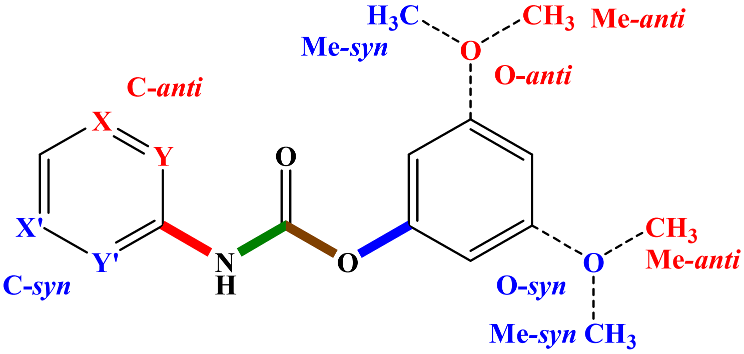

Scheme 36: Possible conformations in the **CxxOMe** compounds

The **Me** (ω) dihedral angle in the **CxpOMe** and **CxmOMe** isomers is planar (-0.12±0.86°) while in the **CxoOMe** triad there is a minor bend of 5.76±0.25° towards the carbonyl group. The conformation in the **CxmOMe** and **CxoOMe** isomers is **Me-*anti***. In **CxpOMe** however, two possible conformations (**Me-*syn***/**Me-*anti***) are practically equivalent, despite the ~67° rotation of the **O**-ring.

7.2.2. Conformational analysis

Fig. **65** depicts the nine PES conformational analysis diagrams of the **CxxOMe** *gas phase* modelled molecular structures. The **C-ring** (pyridinyl ring, α dihedral angle) is drawn as a **full red line**, the **O**-ring (methoxyphenyl ring, β dihedral angle) as a **blue dashed line** and the **Me** dihedral angle (ω) as a **green dashed line**. At $\theta = 0$ and ±180º, the conformation of the asymmetric **C**- or **O**-ring is ***syn*** or ***anti***.

The preferred conformation of the pyridinyl rings (**C**-ring, α dihedral angle) in the **CmxOMe** and **CoxOMe** isomers is, as expected, **C-*syn***. The *meta*-methoxyphenyl ring or **mOMe**-ring (**O**-ring, β dihedral angle) prefers **O-*syn*** conformation, opposite to **M-*anti***, as seen in the **CxxM** isomer grid (Section 6.2.2). As explained in Section 7.2.1 the *ortho*-methoxyphenyl ring or **oOMe**-ring, due to its near orthogonality, cannot be subject of the ***syn***/***anti*** convention.

The PES profile of the pyridinyl rings are generally the same as in the **CxxM** isomers (Section 6.2.2.) with negligible differences in rotational barrier energies. The *para*-pyridinyl ring (**Cp**) shows a PES profile with two global maxima at *ca.* 90° and -90° (TS_{Cp}^{I} = 24.82±0.34 kJ.mol^{-1}) and two global minima at 0° and ±180°. The PES profile of the *meta*-pyridinyl ring (**Cm**) is slightly asymmetric with one global maximum at *ca.* -90° (TS_{Cm}^{II} = 18.35±0.49 kJ.mol^{-1}), one local maximum at *ca.* 90° (TS_{Cm}^{I} = 17.96±0.29 kJ.mol^{-1}), one local minimum at ±180° (LM_{Cm} = 5.63±0.04 kJ.mol^{-1}) and global minimum at 0°. As with the **CmxM** compounds, the opposite **C-*anti*** conformation in *gas phase* is statistically less likely but possible (9%).

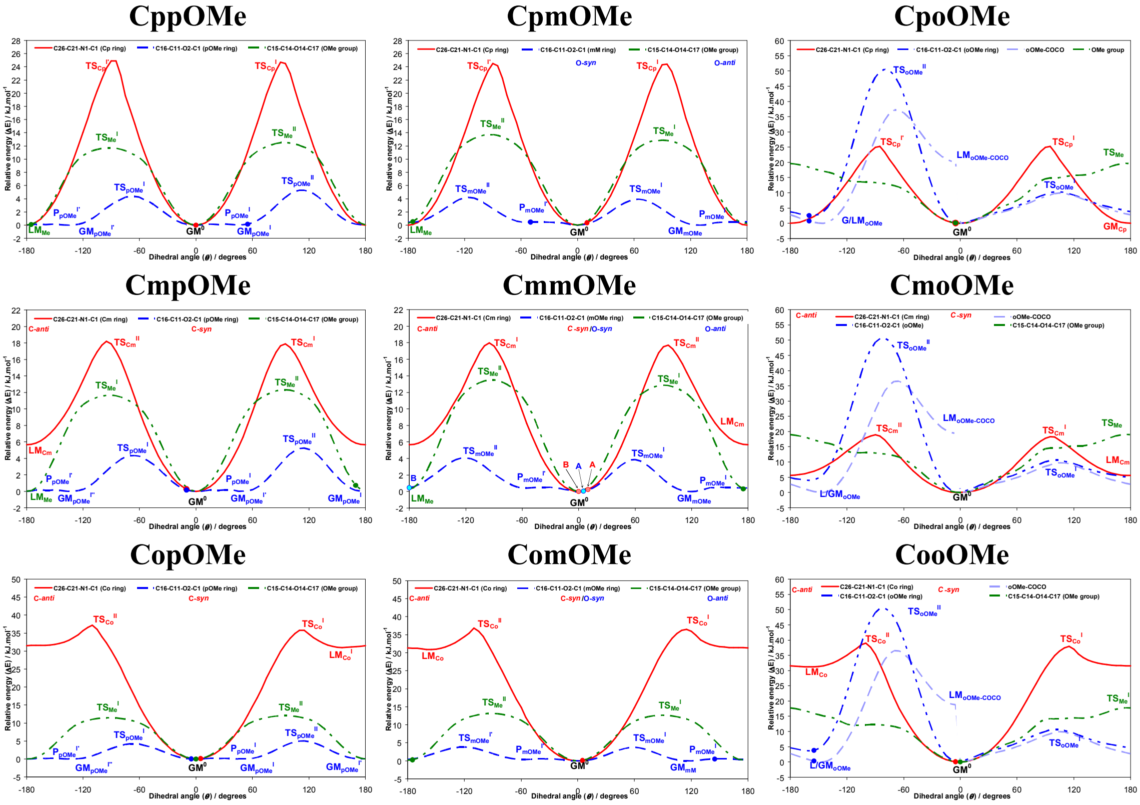

Fig. 65: The PES conformational analysis for the nine **CxxOMe** isomers optimised in the *gas phase*: the equivalent solid state angle is depicted by (●) with, if applicable, an assigned identification letter.

Finally, for the *ortho*-pyridinyl ring (**Co**) the PES profile has one global maximum at *ca.* -110° (TS_{Co}^{II} = 37.70±1.19 kJ.mol^{-1}), one local maximum at *ca.* 115° (TS_{Co}^{I} = 36.73±1.10 kJ.mol^{-1}), one local minimum at *ca.* -160° (*ca.* 160° in **CopOMe**) (LM_{Co} = 31.21±0.20 kJ.mol^{-1}) and one global minimum at 0°.

As for the methoxyphenyl ring, a similar pattern of PES profiles exists, as in the **CxxM** series. The **pOMe** and **mOMe** rings give regular PES profiles, while the **oOMe** ring does not. The *para*-methoxyphenyl ring (**pOMe**), contrary to expectations, has an asymmetric PES profile with one global maximum at *ca.* 115° (TS_{pOMe}^{II} = 5.18±0.14 kJ.mol^{-1}), one local maximum at *ca.* -65° (TS_{pOMe}^{I} = 4.31±0.07 kJ.mol^{-1}), two plateaus from 0° to 60° and from 180° to 120° (P_{pOMe} = 0.14±0.05 kJ.mol^{-1}) and four global minima at 0°, 60°, 120° and ±180°.

A similar PES profile is found in the *meta*-methoxyphenyl ring (**mOMe**): a global maximum at *ca.* 60° ($\mathrm{TS}_{\mathrm{mOMe}}^{\mathrm{II}}$ = 4.05±0.17 kJ.mol^{-1}), local maximum at 120° ($\mathrm{TS}_{\mathrm{mOMe}}^{\mathrm{I}}$ = 3.87±0.07 kJ.mol^{-1}), two plateaus from -60° to -20° and from 140° to 180° ($\mathrm{P}_{\mathrm{mOMe}}^{\mathrm{I}}$ = 0.45±0.04 kJ.mol^{-1}) and two local minima at 0° and 120°.

The plateaus are very low, flat barriers that allow free rotation of the **pOMe** and **mOMe** rings in these regions. Furthermore, low rotational barriers allow full rotation of the **pOMe** and **mOMe** rings and therefore exceptional flexibility. Mild asymmetry of the **pOMe** profile reflects the asymmetric position of the methoxy group. The global minimum of the **mOMe** ring is in an **O-*syn*** conformation, but high flexibility and a very low energy difference (0.45±0.04 kJ.mol^{-1}) into the opposite **O-*anti*** conformation makes both conformations nearly equivalent (55:45).

Conformational analysis of the **oOMe** ring resembles the **oM** ring in the **CxxM** isomer grid. If the COCO ring is not constrained the conformational analysis scan ends up in a *meta*-stable form due to the collision of carbonyl and methoxy moieties and consequent deviation of the COCO dihedral angle. The relaxed PES profile of the **oOMe** ring with COCO angle deviation is shown as a dashed light blue curve (**oOMe-**COCO ring). It has one global maximum at *ca.* -70° ($\mathrm{TS}_{\mathrm{oF}}^{\mathrm{II}}$ = 36.75±0.34 kJ.mol^{-1}), one local maximum at *ca.* 105° ($\mathrm{TS}_{\mathrm{oF}}^{\mathrm{I}}$ = 9.89±0.11 kJ.mol^{-1}) and two global minima at 0 and -145°. Due to the displacement of the COCO dihedral angle into its unlikely local minimum, the PES curve does not end at the starting global minimum, but at an implausible local minimum at 0° ($\mathrm{LM}_{\mathrm{oF\text{-}COCO}}$ = 19.48±0.67 kJ.mol^{-1}).

However, if the COCO ring is kept constrained ("frozen"), only the **oOMe** ring rotates (even forcible), the resulting PES profile is a **deep blue** dashed curve (**oOMe** ring). Similar to the relaxed case, it has one global maximum at *ca.* -80° ($\mathrm{TS}_{\mathrm{oF}}^{\mathrm{II}}$ = 50.58±0.08 kJ.mol^{-1}), one local maximum at *ca.* 100° ($\mathrm{TS}_{\mathrm{oF}}^{\mathrm{I}}$ = 10.56±0.19 kJ.mol^{-1}), one local minimum at *ca.* -160° ($\mathrm{LM}_{\mathrm{oF}}^{\mathrm{II}}$ = 3.38±0.73 kJ.mol^{-1}) and one global minimum at 0°. In contrast to the PES profile, it successfully managed to loop to the starting global minimum. The high rotational barrier upon steric clash of the carbonyl and methoxy groups suggests that in reality (at room temperature) this rotation is not probable; rotation of the COCO dihedral angle into an unlikely local minimum is not probable either. However, in most of the dihedral angle regions two PES profiles overlap, except in the region from 180° to 120° where the constrained PES profile has a local minimum ($\mathrm{LM}_{\mathrm{oF}}^{\mathrm{II}}$ = 3.38±0.73 kJ.mol^{-1}), while the relaxed PES profile has a global minimum. Both curves are approximations since the forcible rotation as seen in the mechanism of conformational analysis is not probable under real conditions.

Instead, a real PES curve would be a combination of both; from 0° to 180° and from -180° to -145° the relaxed would dominate and from -145° to 0° the constrained case would dominate.

The additional dihedral angle in **CxxOMe** compounds is the rotation of the methoxy group about the $_{\text{phen}}$C-C-O-CH_3 angle, or **Me** (ω) dihedral angle. As expected, the PES profile depends on the methoxy group position. If *para*-substituted (**pOMe**) it is nearly symmetric with one global maximum at *ca.* 90° (TS_{Me}^{II} = 12.29±0.23 kJ.mol^{-1}) and one local maximum at *ca.* -90° (TS_{Me}^{I} = 11.62±0.13 kJ.mol^{-1}). The global minimum is at 0°, but the expected second global minimum at ±180° is due to the deviation of the **O**-ring from planarity (66.69±0.68°), a local minimum (LM_{Me} = 0.03 kJ.mol^{-1}). Nevertheless, the energy difference value (0.03 kJ.mol^{-1}) is negligible and in reality both conformations are equivalent. The rotational barriers are relatively high and wide, while the potential well is narrow. This form of PES profile suggests low flexibility and lower interchange rate, but both conformations are equivalent. In *meta*-substituted isomers (**CxmOMe**), the PES profile is very similar as in the **pOMe** rings, but more asymmetric with higher barriers; the global maximum is at *ca.* -90° (TS_{Me}^{I} = 12.81±0.11 kJ.mol^{-1}), the local maximum is at *ca.* 90° (TS_{Me}^{II} = 13.47±0.28 kJ.mol^{-1}) and a global minimum is at 0°. The local minimum is at *ca.* ±180° (LM_{Me} = 0.27±0.03 kJ.mol^{-1}) and both the **Me-*anti*** and the **Me-*syn*** conformations are plausible (53:47). Due to the steric repulsion, the *ortho*-substituted (**oOMe**) rings have differently shaped PES profiles, with only one maximum at *ca.* ±180° (TS_{Me}^{I} = 18.84±0.96 kJ.mol^{-1}) and one global minimum at 0°. The rotational barrier is lower, but the slope is uneven. Therefore, the **oOMe** ring can exist only in the **Me-*anti*** conformation.

The COCO dihedral angle PES profile is symmetric and similar in the **CxpOMe** and **CxmOMe** isomers with two global maxima at *ca.* ±105° (TS_{COCO}^{I} = 27.32±1.54 kJ.mol^{-1}), one local minimum at ±180° (LM_{COCO}^{I} = 18.13±0.42 kJ.mol^{-1}) and a global minimum at 0°.

In the **CxoOMe** isomers the conformational analysis scan ends with neighbouring **oOMe** dihedral angles deviating from their global minima (deep yellow dashed curves). However, if the **oOMe** dihedral angle is kept constrained the result is a different PES profile (brown dashed curves) with global maximum at *ca.* -100° (TS_{COCO}^{II} = 45.64±0.73 kJ.mol^{-1}), local maximum at *ca.* 90° (TS_{COCO}^{I} = 31.70±1.00 kJ.mol^{-1}), local minimum at *ca.* ±180° (LM_{COCO}^{I} = 19.38±0.63 kJ.mol^{-1}) and a plateau at *ca.* 145° (P_{COCO} = 26.88±0.76 kJ.mol^{-1}). Regardless of the actual shape, the high rotational barriers and local minimum do not allow the opposite conformation to be plausible, while the wide potential well suggests a certain level of molecular flexibility.

Finally, the OCNC dihedral angles are approximately the same in all **CxxOMe** compounds with two global maxima at *ca.* -70° and 110° (TS_{OCNC} = 68.96±2.09 kJ.mol^{-1}), one local minimum at ±180° (LM_{OCNC} = 11.62±0.64 kJ.mol^{-1}) and a global minimum at 0°. A very high PES profile suggests the improbability of a conformational change although, as with the COCO ring, a certain level of flexibility is envisaged.

7.3 Comparisons of the solid state and modelling data

Comparison of the **CxxOMe** isomer structures between the eight available crystal structures and calculations is made by marking (as ●) torsion angle differences ($\Delta\theta$) between the available experimental and theoretical structures on the corresponding *gas phase* PES diagrams (Fig. **65**). For the **CmmOMe** isomer the disordered parts of the molecule are labelled as A or B.

In general, the **C**-ring conformations (**C-*syn***) and pyridinyl dihedral angles of the solid state molecular structures match those of modelled structures with deviations of no more than ±10°. Usually, the **C-*syn*** conformation in the **Cm** rings is not favorable for the formation of *C(5)* hydrogen bonded chains, opposite to the **C-*anti*** conformation that exposes pyridinyl N23 atoms to the N1-H1 moieties and allow formation of hydrogen bonded chains. However, aggregation of the **CmpOMe** isomer (and the isomorphous **CmpM**) in the $P2_12_12_1$ space group allows formation of N1-H1···N23 even if the **Cm** rings are in the **C-*syn*** conformation. On the other hand, formation of the **CmmOMe** trimer is another unique example of how aggregation can be accomplished without a conformational change. A similar case is seen in the **NmpF** tetramers and **NmpM** catemers (Chaper I, Section 2.2.5.3) where pyridinyl rings are in the **C-*syn*** conformation too. However, it is quite surprising that trimer formation was not found in any of the benzamide/pyridinecarboxamide isomer grids, where formation of *C(5)* chains with **C-*anti*** conformers are preferred, except for the **NmpF** tetramers and **NmpM** catemers (Chapter I, Section 2.2.5.3).

The **mOMe** dihedral angle has flexibility, allowing free rotation. However, the methoxyphenyl rings in the solid state molecular structures generally correspond with the modelled versions in six out of eight cases with little or no deviations from the global minima. The exception is the **CpmOMe** isomer, where the solid state dihedral angle lies on the $P_{mOMe}{}^{I'}$ plateau, a position that allows formation of five secondary interactions (Section 7.1.1). In the solid state structure of **ComOMe**, the **mOMe** ring is orthogonal to the pyridinyl ring, on the cusp of **C-*syn*** conformation. This position is essential for the formation of secondary C12-H12···O1^{e} (*e* = 1+x,y,z), C17-H17A···Cg2^{i} [Cg2 = (C11…C16)] and C14-H14···O3^{c} (*c* = 2-x,1-y,-z) interactions between dimers, that are crucial for aggregation in the solid state (Fig. **63**).

Finally, for the **CmmOMe** trimer 50% of molecules are in an **O-*syn*** conformation (A part) while the remaining 50% are **O-*anti*** (B part). The B part is on the P_{mOMe}^{I} plateau, however, due to the flexibility of the **O**-ring and very low energy difference (0.45±0.04 kJ.mol^{-1}), the B part (**O-*anti***) is effectively equivalent to A (**O-*syn***). The occurrence of both conformations is justified by the importance of the secondary interactions that are possible only if both conformations are available: the C12-H12···O1B^{d} [*d* = 1-x+y,y,z-1/2] hydrogen bonding as well as the C17-H17C···O1A^{e} [*e* = 2/3-x+y,4/3-x,-2/3+z] and C25B-H25B···O3^{f} [*f* = 1/3+x,2/3+x-y,1/6+z] interactions are essential for the aggregation of trimers into the observed crystal structure.

In five out of eight solid state structures the conformations of the methoxy group (**Me**) do not overlap with the preferred conformation in the optimised structures. However, for the **mOMe** ring, the low energy differences (0.03-0.27 kJ.mol^{-1}) in both **CxpOMe** and **CxmOMe** isomers effectively equalise the plausibility of both conformations. On the other hand, deviations from the minima are rarely higher than 5° (10° in the **CmpOMe** isomer). In each isomer a particular interaction drives the ω dihedral angle conformation into the **Me-*syn*** or **Me-*anti*** conformation.

The COCO and OCNC dihedral angles in the solid state match with the equivalent in optimised structures without or with an offset that does not exceed 15°. The high rotational barriers, especially for the OCNC dihedral angles, as well as high local minima, prevent conformational change.

8. CxxX compounds

8.1. Molecular and crystal structure data

The main challenge with the *halo*-carbamate compounds was their inability to produce quality single crystals. Even after numerous attempts, using various solvents and blends of solvents, only 10 out of 24 synthesised halophenyl-*N*-pyridinyl-carbamates (**CxxF**, **CxxCl** and **CxxBr** isomer grids) gave single crystals suitable for

SXRD. Therefore, structural features of all 10 determined halo-carbamate crystals structures will be described together as **CxxX** (**X** = **F**, **Cl**, **Br**) compounds.

The main structural characteristic of the **CxxX** compounds is the isomorphology of analogous isomers. The **CmpX** compounds are found in the *Pc* space group, **CmmX** in *Cc* and **CopX** (except the **CopBr** isomer) in the $P\bar{1}$ space group. Tables **34** and **35** summarise the basic crystallographic data and structural features.

8.1.1 **CxxF** isomer grid

Three compounds (**CmpF**, **CmmF** and **CopF**) among a total of seven isomers gave single crystals.

CmpF molecular and crystal structure

The **CmpF** crystals were grown from $CHCl_3$. The principal aggregation in the **CmpF** crystal structure is accomplished by two alternating N1-H1···N23 hydrogen bonds (Fig. **66**). The two molecules in the asymmetric unit (A and B) are connected into a pair (A→B) *via* N1A-H1A···N23B [N1A···N23B = 2.996(3) Å] hydrogen bonds, augmented with flanking C22B-H22B···O2A [C22B···O2A = 3.333(3) Å] interactions. The AB pairs are connected along the *c*-axis direction into an undulating *C(5)* chain (···AB→AB···) parallel with the (010) plane by N1B-H1B···N23A^a [N1B···N23A^a = 2.938(3) Å, *a* = x, -y+1, z-1/2] hydrogen bonds (Fig. **66**). In order to allow formation of the *C(5)* chains the pyridinyl rings are in a **C-*anti*** conformation. This conformation is already observed in similar *C(5)* chains in the benzamides (**NmmF**, **Fmm,** Chapter I).

Table 34: Selected crystallographic data for the ten **CxxX** compounds[†]

CxxX	*Space group*	*Z'*	*Volume* (Å^3)	*R[$F^2 > 2\sigma(F^2)$], wR(F^2)*
CmpF	*Pc*	2	1060.50(5)	0.039, 0.097
CmmF	*Cc*	1	1052.85(15)	0.052, 0.122
CopF	$P\bar{1}$	1	526.52(14)	0.046, 0.114
CpmCl	$P2_1$	1	548.85(5)	0.041, 0.076
CmpCl	*Pc*	2	1141.25(18)	0.041, 0.103
CmmCl	*Cc*	1	1108.7(3)	0.094, 0.248
CopCl	$P\bar{1}$	1	559.6(3)	0.092, 0.241
CmpBr	*Pc*	2	1172.65(6)	0.050, 0.091
CmoBr	$P2_1/c$	1	1269.90(7)	0.046, 0.106
CopBr[a]	$P2_1/n$	1	1147.2(9)	0.095, 0.260

† Complete crystallographic, refinement and structural details for the ten **CxxX** isomers are listed in the ESI II (Section 2.3). [a] Obtained with Cu *K*α radiation.

Table 35: Relevant structural features (Å, °) in ten **CxxX** isomers[a]

CxxX	C_6/C_5N	C_6/carbamate	C_5N/carbamate	N…N/O[b]	Packing
CmpF	49.88(7)	60.01(7)	12.89(14)	2.996(3)	*C(5)* chains
	31.61(9)	53.26(8)	45.23(8)	2.938(3)	
CmmF	29.77(12)	51.44(12)	37.18(13)	2.951(4)	*C(5)* chains
CopF	53.34(6)	57.93(6)	4.60(13)	2.997(3)	$R^2_2(8)$ dimers
CpmCl	40.71(9)	54.04(9)	13.68(16)	2.949(4)	*C(6)* chains
CmpCl	31.29(10)	52.94(10)	44.15(11)	2.929(4)	*C(5)* chains
	49.77(7)	60.37(9)	13.09(19)	2.985(4)	
CmmCl	28.26(28)	49.79(26)	37.11(3)	2.937(11)	*C(5)* chains
CopCl	54.32(15)	58.36(14)	4.38(32)	2.994(7)	$R^2_2(8)$ dimers
CmpBr	50.83(14)	58.39(15)	12.43(26)	2.986(7)	*C(5)* chains
	31.86(19)	53.20(18)	43.64(17)	2.925(7)	
CmoBr	65.76(10)	87.10(9)	26.99(15)	2.832(4)[c]	$R^4_4(14)$ dimers
				2.837(4)[d]	
CopBr	55.34(23)	59.73(26)	6.35(55)	2.979(11)	$R^2_2(8)$ dimers

[a] Full structural details are provided in the ESI II (Section 2.3).

[b] The $_{\text{carbamate}}N\cdots N_{\text{pyridine}}$ interaction distances,

[c] The $_{\text{carbamate}}N\cdots O_{\text{water}}$ interaction distances,

[d] The $_{\text{water}}O\cdots N_{\text{pyridine}}$ interaction distances.

The undulating 1-D chains are linked into a 2-D sheet parallel with the (100) plane *via* several bonds and interactions. The strongest among them is the C16A-H16A···O1B^c [C16···O1B^c = 3.203(3) Å, *c* = x, -1+y, z] hydrogen bond, linking A and B molecules from adjacent chains. Other notable interactions that stabilise the 2-D sheet, are C16B-H16B···O1A^d [C16B···O1A^d = 3.314(4) Å, *d* = x, -y+2, z-1/2] and C12A-H12A···O1A^e [C12A···O1A^e = 3.360(3) Å, *e* = x, 1+y, z]. Finally, there are three weak π···π stacking interactions in the sheet: C12A···C16A^e [3.382(4) Å], C13A···C15A^e [3.398(4) Å] and C14B···C13B^e [3.391(5) Å]. The sheets are connected by weak C26B-H26B···F14B^f [C26B···F14B^f = 3.323(3) Å, *f* = -1+x, y, z] contacts linking the 2-D sheets into a 3-D crystal structure.

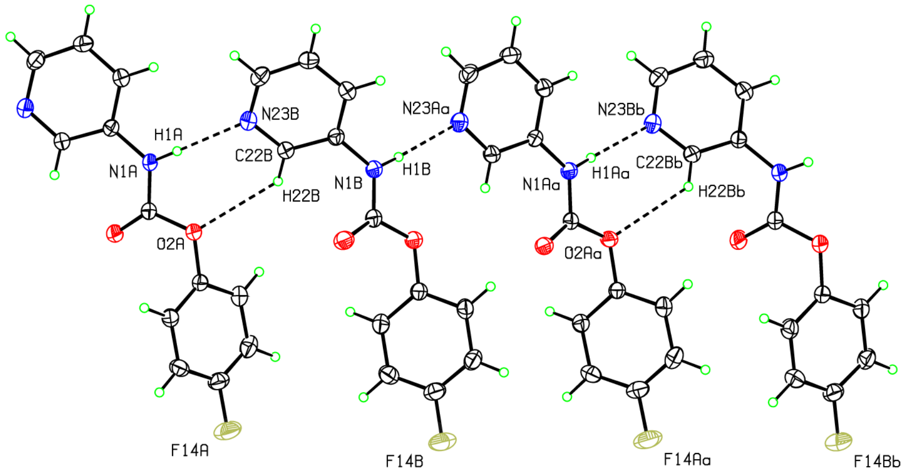

Fig. 66: Hydrogen bonding and aggregation in the **CmpF** isomer, forming AB pairs and ABAB chains (*a*, *b* = x,1-y,-½+z)

As already mentioned, the pyridinyl rings (**C**-ring, C_5N) of both molecules are in a **C-*anti*** conformation. Geometry differences among the A and B molecules are not significant; the most notable is the difference between the interplanar angles (18.27°) and the C_5N/carbamate plane (32.34°).

CmmF molecular and crystal structure

The **CmmF** isomer aggregates in the *Cc* space group (No. 9) with $Z' = 1$. Single crystals were grown from $CHCl_3$.

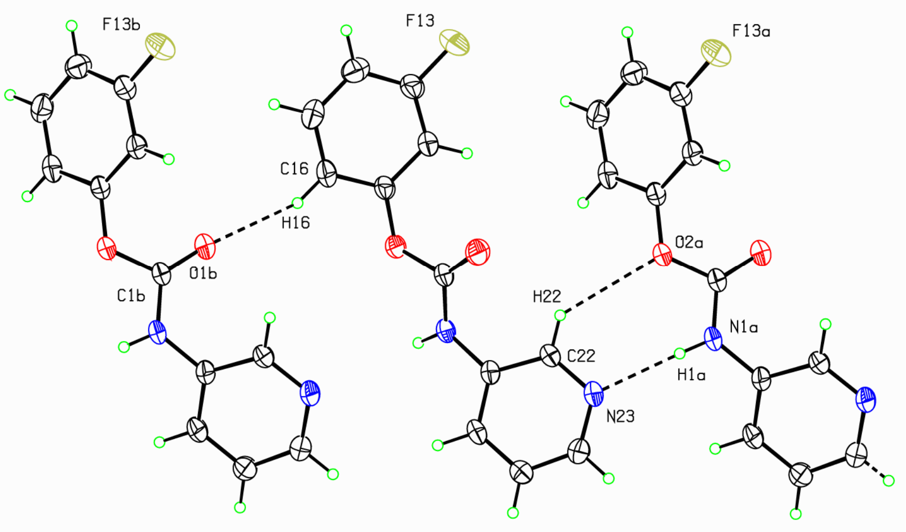

Fig. 67: Hydrogen bonding in the **CmmF** isomer (*a* = x,-y,-½+z; *b* = x,1-y, ½+z)

Despite being in a different space group and having a different *Z'*, there are substantial similarities between **CmpF** and **CmmF** and their intermolecular interactions. The primary interaction in **CmmF** is the N1-H1$\cdots$N23^c [N1$\cdots$N23^c = 2.951(4) Å, *c* = x,-y,1/2+z] hydrogen bond, linking molecules along the *c*-axis direction into a *C(5)* chain parallel with the (010) plane (Fig. **67**). The N1-H1$\cdots$N23 hydrogen bond is aided with flanking C22-H22$\cdots$O2^a [C22-H22$\cdots$O2^a = 3.371(4) Å, *a* = x,-y,-1/2+z] interactions. The *C(5)* chains are interconnected into a 2-D sheet parallel with the (100) plane by C16-H16$\cdots$O1^b [C16$\cdots$O1^b = 3.253(5) Å, *b* = x,1-y,1/2+z] hydrogen bonds. These bonds are aided by weak π-π contacts C14$\cdots$C13^d [3.395(7) Å, *d* = x, 1+y, z]. Finally, the sheets are interconnected through weak C25-H25$\cdots$F13^e [C25$\cdots$F13^e = 3.301(5) Å, *e* = 1/2+x,1/2-y,1/2+z] contacts.

The geometry of the **CmmF** molecule resembles the geometry of the B molecule of the **CmpF** isomer. The interplanar angle of C_6/C_5N is 29.77(12)°, while the C_6/carbamate angle is 51.44(12)° and C_5N/carbamate angle is 37.18(13)°. As expected, the pyridinyl ring (C_5N, **C**-ring) is in the **C-*anti*** conformation, mandatory for the formation of *C(5)* hydrogen bonded chains, and the *meta*-fluorophenyl ring is in the **F-*anti*** conformation.

CopF molecular and crystal structure

CopF forms dimers similar to the **CoxM** and **CoxOMe** isomers, about inversion centres *via* N1-H1···N22^{a} [N1-H1···N22^{a} = 2.997(3) Å, *a* = -x,1-y,2-z] hydrogen bonds producing $R^{2}_{2}(8)$ hydrogen bonded rings. The dimer formation is augmented by flanking C23-H23···O2^{a} [C23···O2^{a} = 3.271(3) Å] interactions (Fig. **68**).

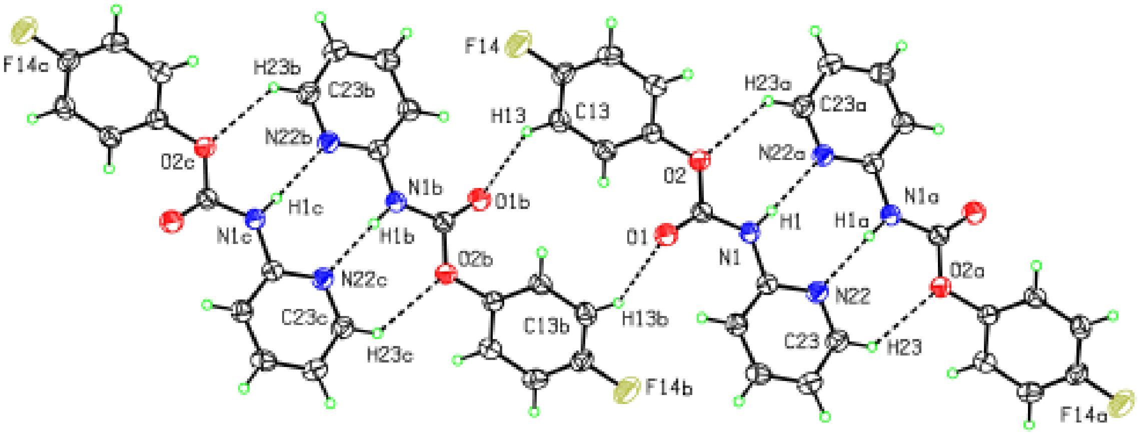

Fig. 68: Hydrogen bonding in **CopF** (*a* = -x,1-y,2-z; *b* = -x,1-y,1-z; *c* = x,y,-1+z)

Apart from the interactions involved in dimerisation, there is only one additional intermolecular interaction. A weak C13-H13···O1^{b} (C13···O1^{b} = 3.444 Å, *b* = -x, 1-y, 1-z) interaction interconnects dimers along the *c*-axis direction into a 1-D chain (Fig. **68**). As a result, **CopF** crystallises as very fine needles (single crystals were grown from CHCl$_3$/acetone mixtures). As a comparison, the **CopOMe** (Section 7.1.3) isomer forms similar dimers, but has additional interactions between a carbonyl moiety, methoxy group and H24 forming a 2-D sheet.

The geometry parameters of the **CopF** molecule are typical for a **CopR** isomer (Table **35**): a pyridinyl ring nearly co-planar with the carbamate plane [4.60(13)°], and a rotated *para*-fluorophenyl ring [57.93(6)°].

8.1.2 **CxxCl** isomer grid

CpmCl molecular and crystal structure

CpmCl is the only **CpxX** compound that gave quality single crystals; the crystallisation solvent was $CHCl_3$. It crystallises in the *$P2_1$* space group *Z'* = 1.

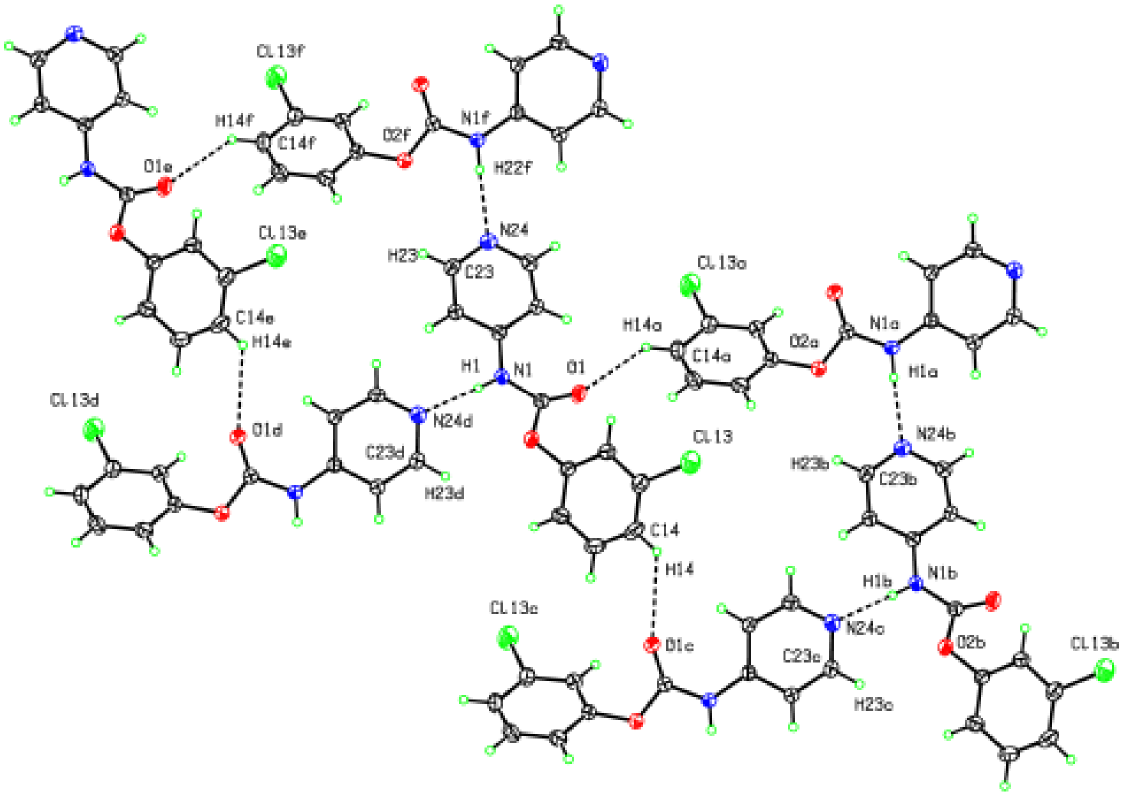

Fig. 69: Hydrogen bonding in the **CpmCl** isomer (*a* = 1-x,-½+y,-z; *b* = 1+x,y,-1+z; *c* = 1-x,½+y,-z; *d* = -x,½+y,1-z; *e* = -1+x,y,1+z; *f* = -x,-½+y,1-z)

The structure of the **CpmCl** isomer is a 2-D sheet (Fig. **69**) and relies on two interactions only. The main interaction is N1-H1···N24^{d} [N1···N24^{d} = 2.949(4) Å, *d* = -x,½+y,1-z] hydrogen bonding, connecting the molecules along the *b*-axis direction into a “fish bone” *C(6)* chain parallel with the (101) plane. Parallel oriented *C(6)* chains are interconnected *via* C14-H14···O1^{a} [C14···O1^{a} = 3.318(4) Å, *a* = 1-x,1/2+y,-z] interactions into a 2-D sheet parallel with the (101) plane. The 2-D sheets stack in the (010) direction. It is interesting to note that chlorine atoms, surrounded by hydrogen atoms and lined up along the (010) direction, do not engage in any interaction.

The conformation of the *meta*-chlorophenyl ring (**Cl**-ring) is **Cl-*anti***. The **CpmCl** molecule has a typical phenyl-*N*-pyridinyl-carbamate geometry (Table **35**); the pyridinyl ring and the carbamate planes are nearly planar [13.68(16)°] while the *meta*-chlorophenyl ring deviates from planarity by [54.04(9)°].

CmpCl molecular and crystal structure

The **CmpCl** isomer (Fig. **70**) is isomorphous with its fluorine analogue **CmpF**. It was grown from $CHCl_3$/toluene solvent mixtures. However, due to the chlorine atom, slight differences in volume and intermolecular interactions exist. The **CmpCl** volume is 1141.25(18) Å^3 and significantly larger than **CmpF** [1060.50(5) Å^3].

The two principal interactions in the **CmpCl** isomer are the N1-H1···N23 and C16-H16···O1 hydrogen bonds. Two molecules in the asymmetric unit, A and B, are linked into a pair (B→A) *via* N1B-H1B···N23A [N1B···N23A = 2.985(4) Å] hydrogen bonds. The interaction is stabilised with flanking C22B-H22B···O2A [C22B···O2A = 3.333(4) Å] interactions.

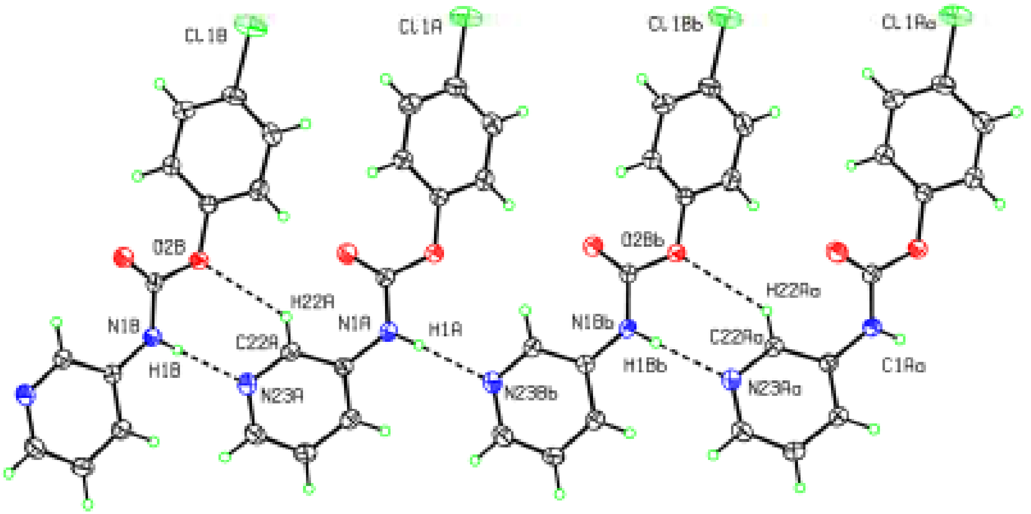

Fig. 70: Hydrogen bonding in **CmpCl**, as BA pairs and BABA chains (*a*, *b* = x,-1-y,½+z)

As similar to the **CmpF** isomer, the BA pairs are linked along the *c*-axis direction into a wavy *C(5)* column (···BA→BA···) parallel with the (010) plane *via* N1A-H1A···N23B^a [N1A···N23B^a = 2.929(4) Å, *a* = x,-1-y,1/2+z] hydrogen bonding. The (···BABA···) columns are interconnected along the *b*-axis direction into a 2-D sheet parallel with the (100) plane *via* secondary C16A-H16A···O1B^c [C16A···O1B^c = 3.306(4) Å, *c* = x,-y,1/2+z] and C16B-H16B···O1A^d [C16B···O1A^d = 3.198(4) Å, *d* = x, -1+y, z] hydrogen bonds, aided by an additional C12B-H12B···O1B^e [C12B···O1B^e = 3.385(4) Å, *e* = x,1+y,z] interaction. As opposite to the **CmpF** isomer, no significant π···π stacking was found in the **CmpCl** crystal structure; the chlorine atom does not engage in any interaction.

As in all **CmxR** carbamates, the pyridinyl rings (**C**-ring, C_5N) have to be in a **C-*anti*** conformation as it is the condition for aggregation *via* N1-H1···N23 hydrogen bonds into *C(5)* chains. Geometries of the A and B molecules in the **CmpCl** isomer are almost identical to those in B and A molecules of the fluorine analogue **CmpF**.

CmmCl molecular and crystal structure

The **CmmCl** isomer in the *Cc* space group with $Z' = 1$ is isomorphous with its fluorine analogue **CmmF**. As for **CmpCl/CmpF**, there are some minor differences between the **CmmCl** and **CmmF** crystal structures. Single crystals were grown from a mixture of $CHCl_3$, acetone and toluene.

The main backbone of the **CmmCl** crystal structure is the N1-H1···N23^a [N1···N23^a = 2.937(10) Å, *a* = x, -y, -1/2+z] hydrogen bonding that connects molecules along the *c*-axis direction into a *C(5)* column parallel with the (100) plane (Fig. **71**). The hydrogen bonds are augmented by C22-H22···O2^b [C22···O2^b = 3.360(11) Å, *b* = x, -y, 1/2+z] interactions. Next, the *C(5)* columns are interconnected along the *b*-axis direction *via* C16-H16···O1^b [C16···O1^b = 3.216(12) Å, *b* = x,1-y,-1/2+z] interactions into 2-D sheets parallel with the (100) plane (Fig. **71**). The sheets are further linked along the $(10\bar{1})$ direction *via* C25-H25···Cl13^c [C25···Cl13^c = 3.620(11) Å, *c* = -1/2+x, 1/2-y, -1/2+z] interactions. No additional π···π stacking was noted in the crystal structure. The geometrical parameters of the **CmmCl** isomer match with those of the analogous **CmmF** isomer (Table **35**). As expected, the pyridinyl ring (C_5N, **C**-ring) is in the **C-*anti*** conformation and the *meta*-chlorophenyl ring (**mCl**) is **Cl-*anti***.

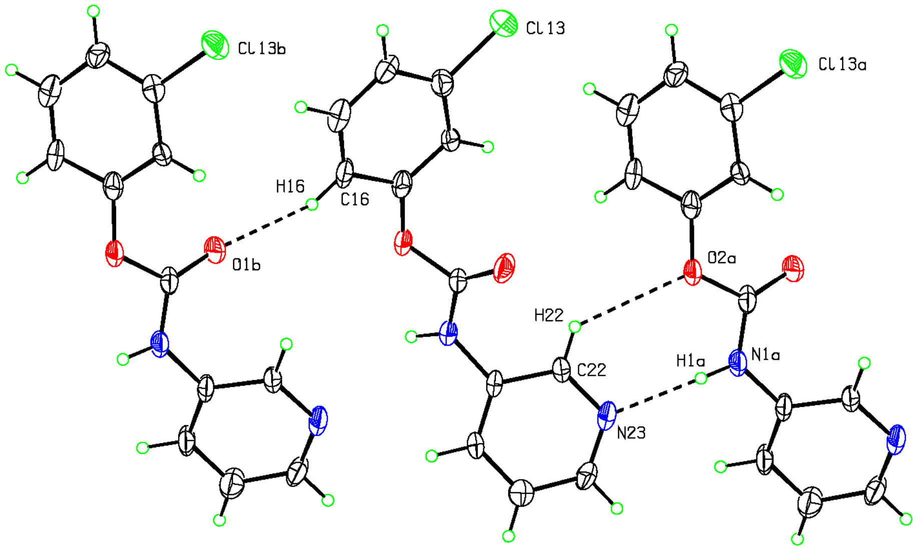

Fig.71: Hydrogen bonding in **CmmCl** (*a* = x,-y,-½+z; *b* = x,1-y,-½+z)

CopCl molecular and crystal structure

The **CopCl** crystal structure is isomorphous with **CopF**. As in other cases, both similarities and differences regarding the intermolecular interactions exist. Needle-like single crystals were grown from a mixture of $CHCl_3$ and acetone.

The main structural feature of all **CoxR** compounds is the formation of dimers through strong N1-H1···N22 hydrogen bonds and **CopCl** is not an exception. The $R^2_2(8)$ hydrogen bonded rings are formed about inversion centres *via* double N1-H1···N22^c [N1-H1···N22^c = 2.994(7) Å, *c* = 1-x,1-y,-z] hydrogen bonds and augmented by C23-H23···O2^c [C23···O2^c = 3.273(8) Å] interactions (Fig. **72**). Furthermore, dimers are linked along the *c*-axis direction into a column parallel with the (010) plane through strong C13-H13···O1^b [C13···O1^b = 3.425(8) Å, *b* = 1-x,1-y,1-z] interactions (Fig. **72**). As opposite to the minimalistic aggregation in **CopF**, there are two additional but weak contacts. The first one is a relatively weak C12-H12···O1^d [C12···O1^d = 3.382(7) Å, *d* = 1+x,y,z] contact that connects columns along the *a*-axis direction into a 2-D sheet parallel with the (010) plane. The second contact is a weak C15···C15^e [C15···C15^e = 3.459(10) Å, *e* = 1-x,2-y,1-z] interaction, and it loosely links 2-D sheets along the $(01\bar{1})$ plane into a 3-D crystal structure. The geometric parameters of the **CopCl** isomer match those of the isomorphous **CopF**.

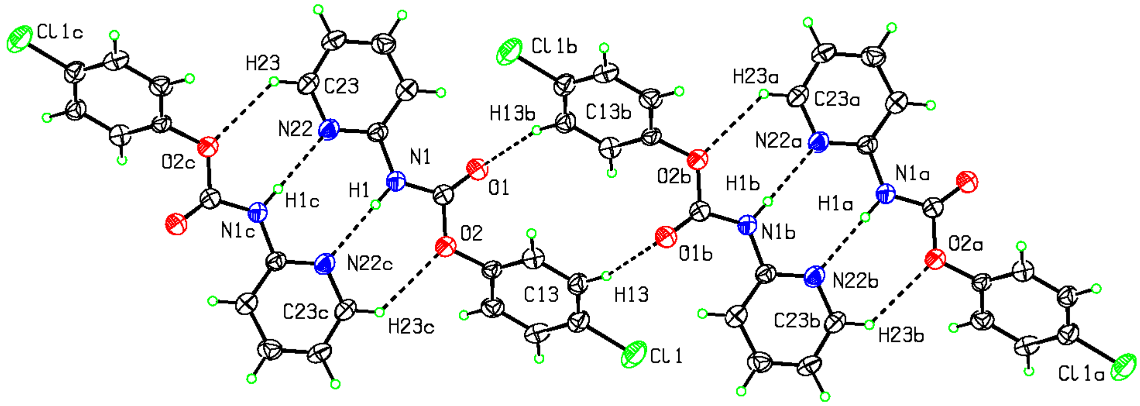

Fig. 72: Hydrogen bonding in the **CopCl** isomer (*a* = x,y,1+z, *b* = 1-x,1-y,1-z; *c* = 1-x,1-y,-z)

8.1.3 **CxxBr** isomer grid

Similar to the **CxxF** isomer grid, only three compounds, **CmpBr**, **CmoBr** and **CopBr** out of the eight **CxxBr** isomers gave suitable single crystals. The rest of the **CxxBr** compounds are less crystalline products; the crystal growth in various solvents gave poor results or decomposition.

CmpBr molecular and crystal structure

The **CmpBr** isomer (Fig. **73**) is isomorphous with **CmpF** and **CmpCl**. The principal interaction in the **CmpBr** crystal structure is, similar to its chloro and fluoro analogues, the N1-H1···N23 interaction. Two molecules of **CmpBr** (A and B) are joined into a pair (A→B) *via* N1A-H1A···N23B [N1A···N23B = 2.986(7) Å] hydrogen bonding. The pairing is augmented by the C22B-H22B···O2A [C22B···O2A = 3.312(7) Å] interaction. The pairs (AB) are connected (···AB→AB···) along the *c*-axis direction into an undulating *C(5)* chain (···ABAB···) through N1B-H1B···N23A^{a} [N1B···N23A^{a} = 2.925(7) Å, *a* = x,1-y,-1/2+z] hydrogen bonds.

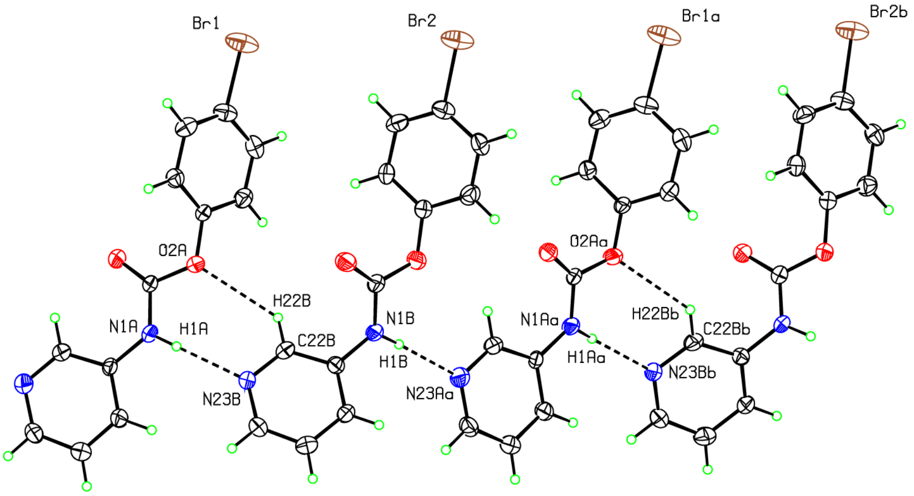

Fig. 73: Hydrogen bonding in **CmpCl**, as AB pairs and ABAB chains (*a*, *b* = x,1-y,-½+z)

As for the chloro- and fluoro- analogues, the chains are interconnected along the *b*-axis direction into 2-D sheets parallel with the (100) plane through C16A-H16A···O1B^{c} [C16A···O1B^{c} = 3.199(8) Å, *c* = x,1+y,z] and C16B-H16B···O1A^{d} [C16B···O1A^{d} = 3.297(8) Å, *d* = x,-y,-1/2+z] hydrogen bonds. The sheet is stabilised by C12A-H12A···O1A^{e} [C12A···O1A^{e} = 3.395(7) Å, *e* = x,-1+y,z] contacts. No interaction involving the bromine atom was found. The geometries of the A and B molecules of the **CmpBr** isomer correspond with those of the analogous **CmpF** isomer.

CmoBr molecular and crystal structure

Along with the **CmoM** isomer, the **CmoBr** compound is an isomer isolated as a monohydrate (**CmoBr**:H_2O) and the crystal structure is isomorphous with the **CmoM**:H_2O crystal structure.

As with the **CmoM**:H_2O complex, two molecules of both water and **CmoBr** aggregate into a hydrogen bonded complex that forms $R^4_4(14)$ hydrogen bonded rings. The molecules of water act as linkers between two **CmoBr** molecules. The key interactions in the formation of the complex are N1-H1···O1W [N1···O1W = 2.832(4) Å] and O1W-H2W···N23^c [O1W···N23^c = 2.837(4) Å, *c* = 1-x,2-y,-z] hydrogen bonds bridging two molecules of **CmoBr** *via* two H_2O molecules (Fig. **74**).

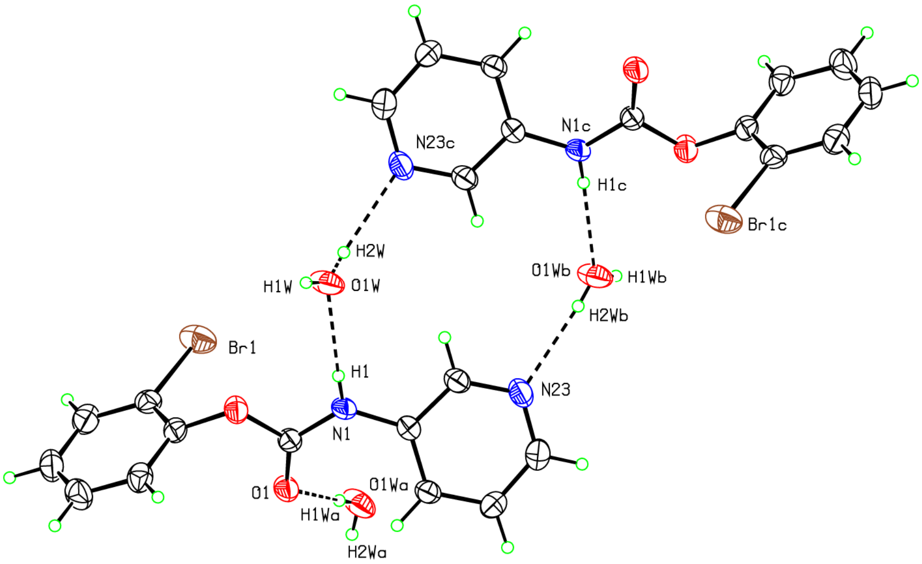

Fig. 74: The hydrogen bonding in the **CmoBr** monohydrate (*a* = x,$^3/_2$-y,-½+z, *b, c* = 1-x,2-y,-z).

Furthermore, the $R^4_4(14)$ hydrogen bonded complexes are directly connected into a 2-D sheet parallel with the (100) plane *via* O1W-H1W···O1^d [O1W···O1^d = 2.925(4) Å, *d* = x,3/2-y,1/2+z] hydrogen bonds. In total, there are three hydrogen bonds interconnecting molecules of **CmoBr** and H_2O into a 2-D sheet. The sheet is stabilised by two interactions. The first is the C26-H26···O1^e [C26···O1^e = 3.384(3) Å, *e* = 1-x,1-y,-z] interaction and second is the C-Br···π(arene) interaction, C12-Br1···C11^a [Br1···C11^a = 3.533(3) Å, *a* = x,3/2-y,-1/2+z]. The geometry of the **CmoBr** molecules agrees with the **CmoM** geometry. The conformation of the **C**-ring is ***C-syn***.

CopBr molecular and crystal structure

Contrary to what would be expected, the **CopBr** crystal structure (Fig. **75**) is not isomorphous with the related fluorine (**CopF**) and chlorine (**CopCl**) isomers. It crystallises in *P2₁/n* with *Z'* = 1 and is therefore more similar to **CopM** and **CopOMe**. Crystals were grown from tetrahydrofuran (THF).

However, as with all **CoxR** compounds, the **CopBr** molecules form dimers about inversion centres *via* double N1-H1···N22^{a} [N1···N22^{a} = 2.979(11) Å, a = 1-x,-y,1-z] hydrogen bonds forming $R^{2}_{2}(8)$ hydrogen bonded rings. The dimer is stabilised by auxiliary C23-H23···O1^{a} [C23···O1^{a} = 3.307(13) Å] interactions. Without forming one-dimensional chains, the dimers are directly interconnected into a 2-D sheet parallel with the $(\bar{1}01)$ plane by C15-H15···O1^{c} [C15…O1^{c} = 3.301(13) Å, c = 1/2-x,-1/2+y,1/2-z] hydrogen bonds. The sheets are interconnected into a crystal structure through weak C-H···π(arene) interaction C13-H13···C13^{d} (H13···C1^{d} = 2.80 Å, d = 3/2-x,1/2+y,1/2-z). Bromine atoms do not engage in intermolecular interactions.

With nearly co-planar pyridinyl ring and carbamate planes [6.35(55)°] and twisted *para*-bromophenyl ring [59.73(26)°], the **CopBr** has the typical "carbamate" molecular geometry.

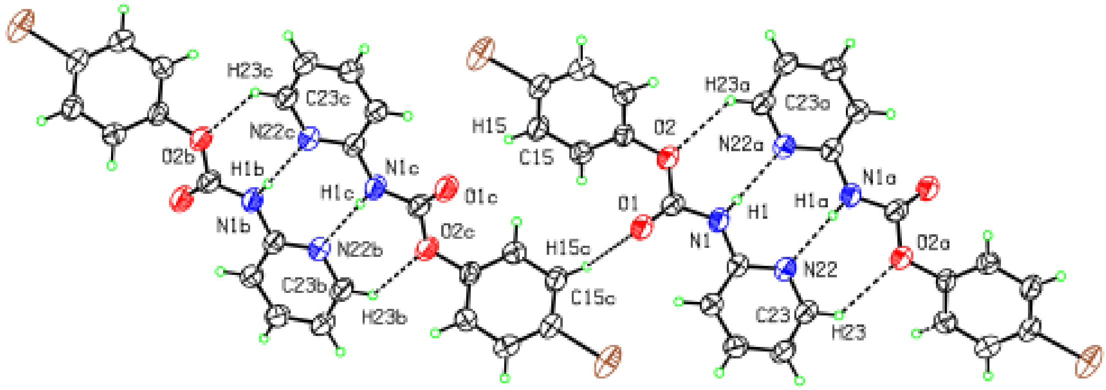

Fig. 75: Hydrogen bonding in **CopBr** (a = 1-x,-y,1-z, b = -½+x,-½-y,-½+z, c = ½-x,- ½+y, ½-z)

8.2. *Ab initio* calculations and modelling data

8.2.1. Structure optimisation

Tables **36a-c** summarise the geometry parameters for the 27 optimised **CxxX** isomers (**CxxF**, **CxxCl** and **CxxBr** isomer grids), including α (**C**-ring), β (**F-**/**Cl-**/**Br-**ring), γ (COCO) and δ (OCNC) dihedral angles, as well as the relative deviation of the **F-**/**Cl-**/**Br**-ring from planarity (β^{*}).

Analysis of the molecular structures uncovers similarities and subtle differences. However, there is no significant difference between the analogous isomers, apart from minor changes in the β and γ dihedral angles. Therefore, aspects of the optimised geometries will be discussed for all of the **CxxX** isomers together. With regards to the geometric parameters, the *halo*-carbamate isomers can be divided into 3 groups; **CxpX** and **CxmX** isomers and **CxoX** isomers, as for the carbamate isomer grids (**CxxM** and **CxxOMe**). The first group has its *para-*/*meta*-halophenyl rings rotated by ~60°, and in the **CxoX** isomers the *ortho*-halophenyl rings are close to orthogonal relative to the pyridinyl rings and the carbamate planes. Nevertheless, all isomers have planar **C**-rings (α) and OCNC (δ) dihedral angles, -0.42±0.52° and 0.17±0.49°, respectively. Conformations of the **Cm** and **Co** rings are always **C-*syn***.

The COCO ring is planar in all of the **CxpX** and **CxmX** isomers (-0.40±0.73°), while in the **CxoX** compounds minor deviations from planarity exist and decrease from **CxoF** (6.05±0.42°) to the **CxoCl** (4.78±0.40°) and **CxoBr** (2.37±0.48°) triads. The opposite trend exists for the β dihedral angle (**X- or F-**/**Cl-**/**Br**-rings) where it increases significantly from **F** to **Br**: in the **CxoF** triad the o**X**-ring is 74.70±0.60°, in **CxoCl** is 90.57±0.15° and in **CxoBr** is 110.88±0.60°.

Therefore, the **oF**-ring is in a slightly **F-*anti*** conformation, the **oBr**-ring is slightly **Br-*syn***, while the **oCl**-ring is almost perfectly orthogonal and the ***syn***/***anti*** convention is not applicable. The obvious reason for the decrease of the COCO angle and the increase of β dihedral angle is the change of substituent: dihedral angles change to accommodate a larger substituent.

Table 36a: Torsion angles (º) of the optimised **CxxF** isomers[a]

	α	β	$\beta*$	γ	δ
CppF	-0.67	62.78	62.78	-0.24	0.21
CpmF	0.10	-58.18	58.18	-0.80	-0.62
CpoF	-0.03	75.37	75.37	6.28	1.00
CmpF	-0.87	62.61	62.61	-0.25	-0.05
CmmF	-0.29	56.8	56.8	0.89	0.72
CmoF	-1.39	74.54	74.54	6.30	1.06
CopF	-0.32	62.24	62.24	-0.29	-0.16
ComF	-0.65	56.02	56.02	0.82	0.75
CooF	-0.98	74.20	74.20	5.56	0.82

Table 36b: Torsion angles (º) of the optimised **CxxCl** isomers[a]

	α	β	β^*	γ	δ
CppCl	-0.76	-58.17	58.17	-0.85	0.13
CpmCl	-0.38	126.03	57.87	-0.82	-0.28
CpoCl	-0.16	90.71	90.71	4.96	0.67
CmpCl	-1.09	-57.99	57.99	-0.88	-0.13
CmmCl	-0.52	126.82	57.10	-0.90	-0.32
CmoCl	-0.97	90.59	90.59	5.06	0.69
CopCl	-0.35	-57.43	57.43	-0.88	-0.29
ComCl	0.18	127.09	56.88	-0.94	-0.58
CooCl	-0.48	90.41	90.41	4.32	0.50

Table 36c: Torsion angles (°) of the optimised **CxxBr** isomers[a]

	α	β	β^*	γ	δ
CppBr	-0.75	-56.89	56.89	-0.92	0.23
CpmBr	-0.43	125.30	58.48	-0.75	-0.35
CpoBr	0.38	111.04	72.71	2.70	0.15
CmpBr	-1.15	-56.63	56.63	-1.03	0.00
CmmBr	0.99	57.98	57.98	0.89	0.47
CmoBr	-0.29	111.38	72.41	2.58	-0.06
CopBr	-0.38	-56.13	56.13	-0.99	-0.20
ComBr	-0.15	57.06	57.06	0.80	0.63
CooBr	0.12	110.21	73.64	1.82	-0.30

[a] The angle C26-C21-C1=O1 (**C**-ring) is designated as α, the C1-O2-C11-C16 angle (**X, F**-/**Cl**-/**Br**-ring) as β, relative deviation of *halo*-phenyl ring from planarity as β^*, the O1=C1-N1-C21 angle as δ and the O1=C1-O2-C11 as γ. All geometries are based on B3LYP/6-311++G(d,p) optimisations.

The remaining isomers, **CpmX** and **CpmX** have their dihedral angles rotated by 58.18±2.13° in one or other equivalent direction. However, the conformations of the **mF**-rings are **F-*anti***, while the conformations of the **mCl**-rings and **mBr**-rings are **Cl-*syn*** and **Br-*syn***, respectively.

8.2.2. Conformational analysis

The PES conformational analysis diagrams of the three isomer grids, **CxxF** (Fig. **76**), **CxxCl** (Fig. **77**) and **CxxBr** (Fig. **78**) are derived from the *gas phase* modelled molecular structures. The **C-ring** (pyridinyl ring, α dihedral angle) is drawn as a **full red line**, and the **X** or **F-**/**Cl-**/**Br**-rings (halo-phenyl ring, β dihedral angle) as a **blue dashed line**. At $\theta = 0$ and ±180°, the conformation of the asymmetric **C**- or **X**-rings (**X** = **F**, **Cl** or **Br**) is noted as ***syn*** or ***anti***.

Generally, the PES profiles of the **CxxX** isomers (**X** = **F**, **Cl** or **Br**) are similar in shape to the **CxxM** isomers but with certain differences, mainly the height of the rotational barriers. Therefore, the characteristics of their PES profiles are presented together. The PES profile of the **Cp** ring has two global maxima at around ±90° and two global minima at 0° and ±180°. In the fluoro and chloro isomers the rotational barrier is 23.51±0.19 kJ.mol^{-1}, while in bromo isomers the barrier is 32.40±0.14 kJ.mol^{-1}. The **Cm** ring PES profile is similar in all **CmxX** isomers, slightly asymmetric and has one global maximum at -90° (TS_{Cm}^{II} = 17.11±0.10 kJ.mol^{-1}), one local maximum at 90° (TS_{Cm}^{I} = 16.85±0.20 kJ.mol^{-1}), one local minimum at ±180° (LM_{Cm} = 5.49±0.07 kJ.mol^{-1}) and a global minimum at 0°.

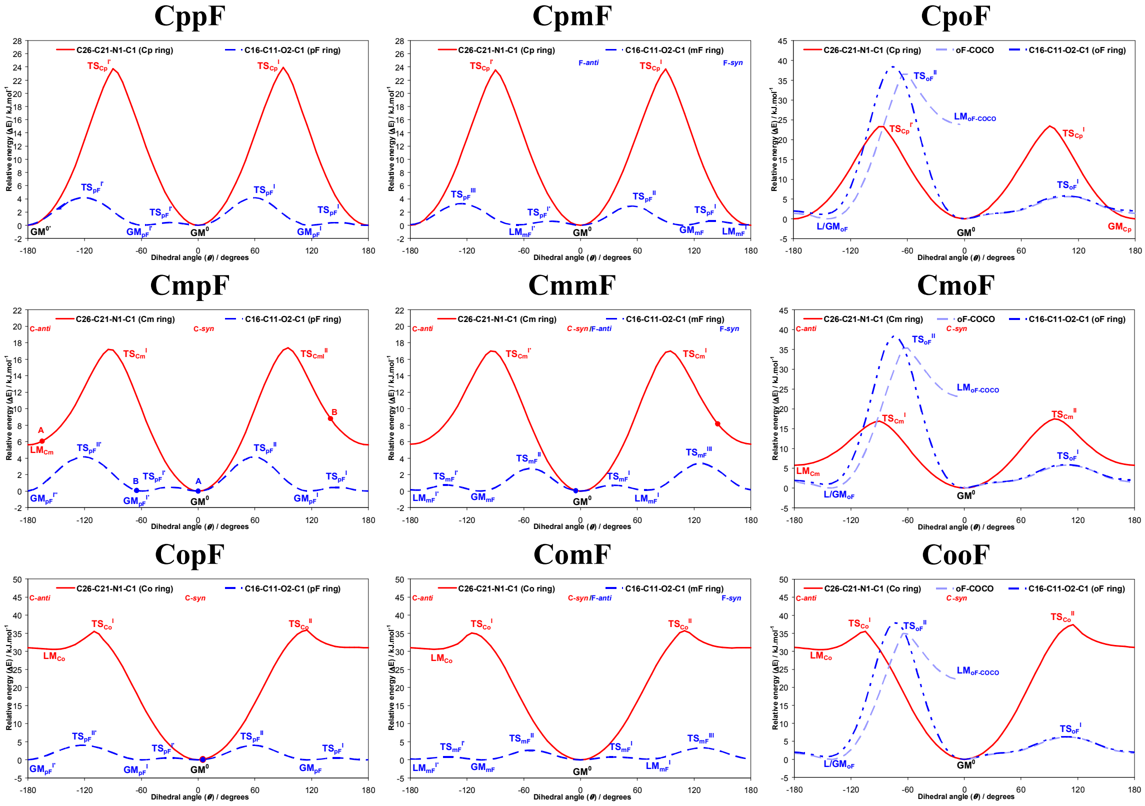

Fig. 76: The PES conformational analysis for the nine **CxxF** isomers optimised in the *gas phase*: the equivalent solid state angle (if available) is depicted by (●) with, if applicable, an assigned identification letter.

The values of the rotational barriers and local minima slightly decrease from fluoro to bromo (0.1-0.2 kJ.mol^{-1}). All **Cm** rings prefer the ***C-syn*** conformation however, as in the previous cases, the difference with the opposite conformation is ~5.5 kJ.mol^{-1} and hence, it is plausible (9.5% according to Boltzmann distribution).

Similarly, the **Co** ring PES profile is approximately the same in all **CoxX** isomers with minor differences. It has one global maximum ($\mathrm{TS_{Co}}^{\mathrm{II}}$ = 35.91±0.62 kJ.mol^{-1}) at *ca.* 115°, one local maximum ($\mathrm{TS_{Co}}^{\mathrm{I}}$ = 34.90±0.44 kJ.mol^{-1}) at *ca.* -110°, one local minimum ($\mathrm{LM_{Co}}$ = 30.00±0.54 kJ.mol^{-1}) at *ca.* -150° (155° in **CopBr** and **ComBr**) and a global minima at 0°. As was the case with the **Cm** ring, rotational barriers in the **Co** ring slightly decrease from fluorine to bromine. The ***C-syn*** conformation is the only one possible. The **pX** and the **mX** rings (**X** = **F**, **Cl** or **Br**) have low rotational barriers (as in **CxxM** and **CxxOMe**) and not exceeding 5 kJ.mol^{-1} suggesting high flexibility and mobility. Therefore, a quick and undemanding interconversion between the ***syn*** and ***anti*** conformers exists, causing a thermodynamic and kinetic balance that allows the possibility of both conformations being isolated. This may cause the formation of highly disordered crystal structures that yield a poor morphology of small, fragile crystals.

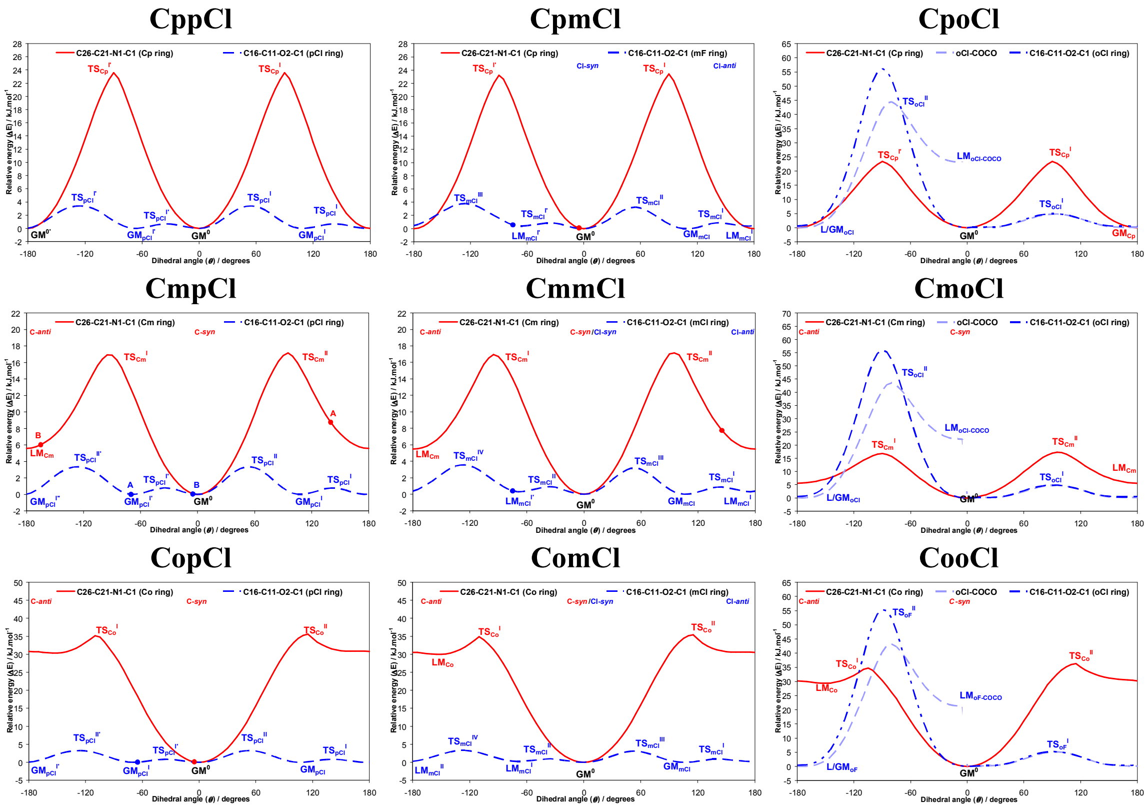

Fig. 77: The PES conformational analysis for the nine **CxxCl** isomers optimised in the *gas phase*: the equivalent solid state angle (if available) is depicted by (●) with, if applicable, an assigned identification letter.

The **pX** ring (**X** = **F**, **Cl** or **Br**) PES profile has two global maxima at *ca.* -120° and 60° (TS_{pF}^{II} = 4.12±0.08 kJ.mol^{-1}, TS_{pCl}^{II} = 3.33±0.07 kJ.mol^{-1}, TS_{pBr}^{II} = 3.25±0.07 kJ.mol^{-1}), two local maxima at *ca.* -30° and 150° (TS_{pF}^{I} = 0.45±0.04 kJ.mol^{-1}, TS_{pCl}^{I} = 0.77±0.07 kJ.mol^{-1}, TS_{pBr}^{I} = 0.88±0.08 kJ.mol^{-1}) and four global minima at -60°, 120°, ±180° and 0°. The **mX** ring (**X** = **F**, **Cl** or **Br**) PES profile is similar in all **CxmX** with minor difference of the rotational barriers. It has one global maximum (TS_{mX}^{III} = 3.53±0.35 kJ.mol^{-1}) at *ca.* -125° or 125°, one major local maximum (TS_{mX}^{II} = 3.09±0.26 kJ.mol^{-1}) at *ca.* 55° or *ca.* -55°, two minor local maxima (TS_{mX}^{I} = 0.81±0.10 kJ.mol^{-1}) at *ca.* -35° (or -145°) and 145 (or 35°), two local minima (LM_{mX}^{I} = 0.28±0.13 kJ.mol^{-1}) at *ca.* -70° (or 70°) and *ca.* ±180° and two global minima at *ca.* -105° (or 105°) and 0°. The height of the rotational barriers insignificantly increases from the fluorine to bromine analogues, while the local minima in fluoro compounds are just 0.14±0.07 kJ.mol^{-1}. The preferred conformation of the **mF** ring is ***F-anti***, whereas in the chloro and bromo analogues it is ***Cl-syn*** (***Br-syn***). However, the low rotational barriers and very low local minima for the opposite conformation equalise the likelihood of each conformation being populated.

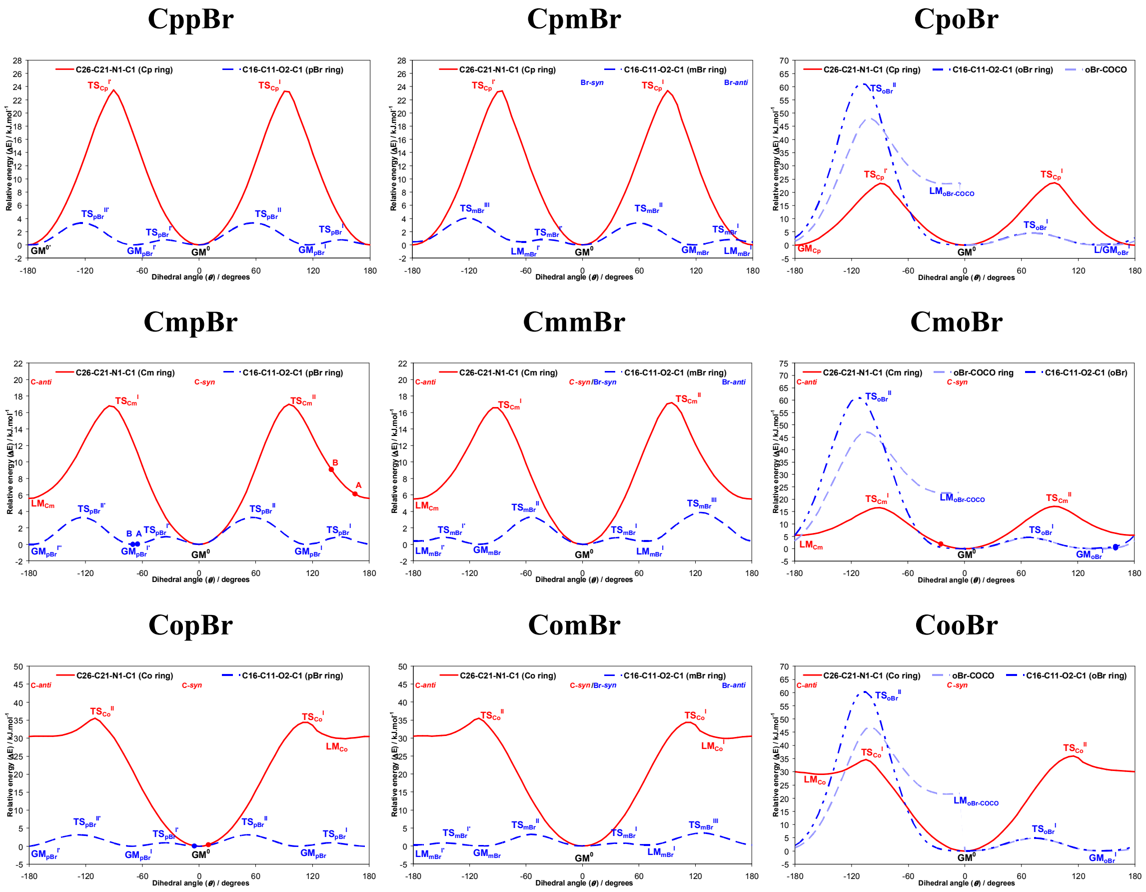

Fig. 78: The PES conformational analysis for the nine **CxxBr** isomers optimised in the *gas phase*: the equivalent solid state angle (if available) is depicted by (●) with, if applicable, an assigned identification letter.

The **oX** rings (**X** = **F**, **Cl** or **Br**) show an effect similar to the **CxxM** and **CxxOMe** isomer grids. The standard procedure of a conformational scan causes a steric collision of the halogen substituent and carbonyl moiety and forces rotation of the COCO dihedral angle upon which the conformational scan finishes with the COCO ring being in its opposite, improbable conformation (high local minimum). Two conformational scanning procedures yielding PES profiles were undertaken; with a constrained COCO dihedral angle (deep blue dashed line) and without it (light blue dashed line). Both PES profiles are models, but the real behaviour of the **oX** ring may be extrapolated as a combination of both PES profiles. Due to the different size of the halogen substituents, both constrained and relaxed profiles are different for each of the **oF**, **oCl**, and **oBr** rings.

The constrained PES profile has one global maximum (TS_{oF}^{II} = 38.26±0.28 kJ.mol^{-1}, TS_{oCl}^{II} = 55.85±0.39 kJ.mol^{-1} and TS_{oBr}^{II} = 60.81±0.47 kJ.mol^{-1}) at *ca.* -75° (**oF**), -90° (**oCl**) and -110° (**oBr**), one local maximum (TS_{oF}^{I} = 5.99±0.26 kJ.mol^{-1}, TS_{oCl}^{I} = 5.02±0.18 kJ.mol^{-1} and TS_{oBr}^{I} = 4.68±0.17 kJ.mol^{-1}) at *ca.* 110° (**oF**), 90° (**oCl**) and -70° (**oBr**), a local minimum (LM_{oF}^{II} = 0.96±0.20 kJ.mol^{-1}, LM_{oCl}^{I} = 0.45±0.09 kJ.mol^{-1}, LM_{oBr}^{I} = 0.14±0.04 kJ.mol^{-1}) at *ca.* -145° (**oF**), 160° (**oCl**) and 145° (**oBr**) and a global minimum at 0°.

The unconstrained PES profile, however, has one global maximum (TS_{oF}^{II} = 35.62±0.81 kJ.mol^{-1}, TS_{oCl}^{II} = 43.71±0.66 kJ.mol^{-1} and TS_{oBr}^{II} = 47.43±0.60 kJ.mol^{-1}) at *ca.* -65° (**oF**), -80° (**oCl**) and -100° (**oBr**), one local maximum (TS_{oF}^{I} = 5.85±0.29 kJ.mol^{-1}, TS_{oCl}^{I} = 4.93±0.19 kJ.mol^{-1} and TS_{oBr}^{I} = 4.66±0.18 kJ.mol^{-1}) at *ca.* 110° (**oF**), 90° (**oCl**) and -70° (**oBr**), one ending local minimum ($LM_{oF\text{-}COCO}$ = 22.64±0.83 kJ.mol^{-1}) at 0° and global minima at -140° (**oF**), -175° (**oCl**), 145° (**oBr**) and 0°.

It is clear that the change from fluorine to bromine dramatically increases the main rotational barrier in the *ortho*-substituted carbamates and effectively blocks full rotation. Furthermore, the rotational barrier becomes wider in the bromo isomers limiting the available rotational space. However, substituent change causes a decrease of the rotational barriers in the ***syn*** conformational area and a flattening of the potential wells. This observation suggests a significant increase of flexibility in the ***syn*** conformational area and a corresponding limited flexibility in the ***anti*** area upon substituent change.

The shape of the PES profiles for the COCO dihedral angles depend on the position or nature of the halogen substituent. If a substutuent is in the *para* position, all PES profiles are similar and symmetrical with two global minima (TS_{COCO}^{I} = 28.55±0.11 kJ.mol^{-1}) at *ca.* ±105°, one local minimum (LM_{COCO}^{I} = 21.23±0.64 kJ.mol^{-1}) at *ca.* ±180° and one global minimum at 0°. If substituents are *meta*, the PES profile is asymmetric and has one global minimum (TS_{COCO}^{II} = 27.37±0.54 kJ.mol^{-1}) at *ca.* -105°, one local minimum (TS_{COCO}^{I} = 26.79±0.43 kJ.mol^{-1}) at *ca.* 105°, one local minimum (LM_{COCO}^{I} = 21.20±0.48 kJ.mol^{-1}) at *ca.* ±180° and one global minimum at 0°.

For the *ortho*-substituted isomers, a difference exists depending on the nature of the substituent, the rotational heights are diffferent. The PES profiles have one global maximum (TS_{COCO}^{II}[**F**] = 35.20±0.35 kJ.mol^{-1}, TS_{COCO}^{II}[**Cl**] = 45.97±1.51 kJ.mol^{-1} and TS_{COCO}^{II}[**Br**] = 45.79±0.98 kJ.mol^{-1}) at *ca.* -110°, one local maximum (TS_{COCO}^{I}[**F**] = 31.65±0.93 kJ.mol^{-1}, TS_{COCO}^{I}[**Cl**] = 34.73±1.31 kJ.mol^{-1} and TS_{COCO}^{I}[**Br**] = 28.34±0.44 kJ.mol^{-1}) at *ca.* 105°, one local minimum (LM_{COCO}^{I} = 22.09±0.31 kJ.mol^{-1}) at *ca.* ±180° and one global minimum at 0°.

The OCNC (δ) dihedral angle is similar for all *halo*-carbamate isomer grids and has two global maxima (TS_{OCNC} = 70.04±2.06 kJ.mol^{-1}) at *ca.* -65° and 120°, one local minima (LM_{OCNC} = 12.16±0.79 kJ.mol^{-1}) at *ca.* ±180° and one global minima at 0°.

As seen in the previous carbamate isomer grids, the COCO and OCNC dihedral angles do not have the ability to flip into opposite conformations, and consequently rotational barriers are extremely high. The local minima are far beyond the thermodynamically acceptable values. Nevertheless, relatively wide potential wells suggest the possibility of a certain flexibility.

8.3 Comparisons of the solid state and modelling data

A comparison of the **CxxX** molecular structure parameters derived from experimental and calculated data are present in the corresponding *gas phase* PES diagrams (Figs. **76-78**).

In four (**CopX** and **CmoBr**) out of ten available solid state structures, the α and β dihedral angles roughly comply with their equivalent modelled versions, having maximal deviation (in **CmoBr**) of 25° from the closest global minimum. In the other six **CxxX** crystal structures (**CmpX**, **CmmX** and **CpmCl**) the α (**C**-ring) or β (**X**-ring) dihedral angles are in opposite conformations as compared to the conformations in the equivalent modelled structures. In contrast, all γ and δ dihedral angles of the solid state structures positively correspond with the modelled equivalents with deviation by no more that 10° from the global minimum (ESI II, Sections 3.3-3.5).

The conformations in the **CopX** analogues and the **CmoBr** monohydrate crystal structures match those in the modelled molecular structures. As seen in the previous isomer grids, primary aggregation in the crystal structures of the **CopX** analogues is dimerisation, and it strictly requires the **Co** rings to be at their global minima. In the **CmoBr** monohydrate, the $R^4_4(14)$ hydrogen bonded ring formation *via* H_2O molecules as well as the O1W-H2W···N23^d (d = 1-x,2-y,-z) hydrogen bond directs a minor distorted (-25°) of the **Cm** ring (β dihedral angle) from the global minima. The flexible **oBr** ring is in its second global minimum, however, that position is suitable not only because of internal stability, but rather because of the formation of C-Br···π(arene) interactions.

In the **CpmCl** crystal structure, the **mCl** ring is ***Cl-anti*** although the conformational analysis (Fig. **77**) suggests that the ***Cl-syn*** conformation is slightly more favourable. The **CpmCl** molecule in the solid state forms a 2-D sheet where the H14 atom engages in a C14-H14···O1^a (a = 1-x,1/2+y,-z) interaction. This interaction is important for aggregation into a 2-D sheet. In contrast, the chlorine atom in the **CpmCl** crystal structure moves away from the carbonyl oxygen (5.426 Å, 1-x,1/2+y,-z). If the

mCl ring was in a **Cl-*syn*** conformation, the chlorine atom would be too close to the carbonyl oxygen, causing a steric clash and eventual disruption of the C14-H14···O1 interaction and crystal structure. The **mCl** ring seems to be rotationally flexible and a conformational change to the opposite conformation is very likely (0.55 $kJ.mol^{-1}$). Hence, the **mCl** ring in the **CpmCl** isomer is in a **Cl-*anti*** conformation, placing the chlorine atom away from the sheet plate and ensuring aggregation.

Finally, in three isomorphous **CmpX** analogues (both A and B molecules) and two isomorphous **CmmX** analogues, the **Cm** ring is in the **C-*anti*** conformation although the **C-*syn*** is more favourable in *gas phase*. This is identical to some benzamides and pyridinecarboxamide isomers with *meta*-pyridine rings. As previously described, the reason for the conformational change is the demand for the formation of $_{carb}N\text{-}H\cdots N_{pyr}$ primary hydrogen bonding that gives *C(5)* chains, therefore, the **Cm** ring has to be in a **C-*anti*** conformation. Furthermore, in accordance with the crystal packing requirements, the **C**-ring dihedral angles deviate by 50° from their LM_{Cm} local minima. In the **CmpF** and **CmpCl** isomers the β dihedral angles of both A and B molecules perfectly match, but not in the **CmpBr** isomer. It is important to stress that aggregation in the **CmpOMe** and **CmpM** isomers is also accomplished by $_{carb}N\text{-}H\cdots N_{pyr}$ hydrogen bonding, but packing in the $P2_12_12_1$ space group, instead of *Pc* or *Cc* excludes the need for the conformational change of the *meta*-pyridinyl rings. Similarly, formation of trimers (**CmmOMe**), tetramers (**NmpF**) or catemers (**NmpM and NmpFM**) does not require conformational change.

The **mCl** ring in the **CmmCl** isomer is found to be in a **Cl-*anti*** conformation although in *gas phase* the **Cl-*syn*** is more stable. However, the **Cl-*anti*** conformation allows formation of secondary C16-H16···O1 and C25-H25···Cl13 interactions, crucial for aggregation. Similar interactions are also found in the **CmmF** isomer, but in *gas phase* the **F-*anti*** conformation is more stable.

An overview of the carbamate results is presented in the "Discussion and Conclusions".

CHAPTER III: TENNIMIDES AND TREZIMIDES

1. Introduction

1.1. Idea

Natural and synthetic macrocycles continue to attract extensive scientific interest, with research developments proceeding in many directions including anion receptors, molecular recognition, drug discovery, therapeutics and nanoscience.[211-215] Macrocyclic systems have evolved from the original crown ethers, spherands, cryptands and porphyrins, through calixarenes, resorcinarenes, rotaxanes, catenanes and beyond, as well as into interdisciplinary fields and biological applications.[211-218] The quest to develop the *perfect* macrocyclic host template or platform with the ability to regulate specific physicochemical properties by simple functionalisation remains the 'holy grail' of macrocyclic scientists. This on-going pursuit has yielded a diverse range of macrocyclic scaffolds over the past five decades,[211-214] but has often been impeded by modest yields from multi-stage syntheses, using high-dilution techniques with complex separations and bearing necessary, but often redundant backbone/side-chain groups.[211-214] The amide (-CONH-) group representing the most important organic functional group in organic chemistry is ubiquitous in biology and chemistry, both in natural and synthetic compounds. Benzamide chemistry (representing a subset) flourishes with a wide range of applications and research interests as scaffolds in a wide range of drugs to key components in both helical assemblies (acycles) and macrocycles. The imide functional group $[CO]_2NR$ (R = H, alkyl/aryl) has featured extensively in 'locked' macrocycles and in polymer chemistry.[219,220] However, macrocycles derived from open chain imides as $(\text{-[O]C-N}R\text{-C[O]-})_{\boldsymbol{n}}$ ($\boldsymbol{n} \geq 2$) are rare with accessible and developed routes practically non-existent.

Our research into benzamide structural systematics (Chapter I, Sections 1.1 and 1.2) yields benzoyl-*N*-(2-pyridyl)benzamides as an additional product when reacting benzoyl chlorides with 2-aminopyridines (**O**).[163,164] These 2:1 systems tend to adopt a distinct open and twisted geometry about the central imide '$(O{=}C)_2NR$' core as shown by their solid-state structures (R = 2-pyridyl). Structural analysis demonstrates that the 2-(dibenzoylamino)pyridines[163,164] constitute ⅜ of the '4+4' macrocyclic scaffold reported by Evans and Gale,[218] (Scheme **37**) as derived from isophthaloyl dichloride (**I**) and both tetrafluoro $\mathbf{F_4}$ and pentafluoroanilines $\mathbf{F_5}$ (with a reasonable geometric fit of the non-hydrogen atoms).

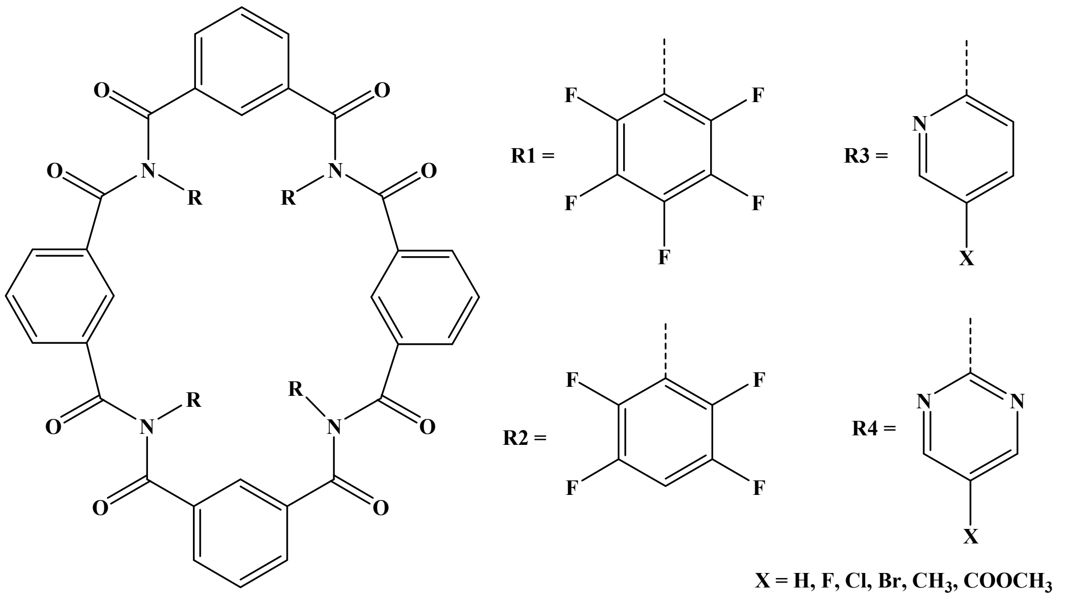

Scheme 37: Scheme of the **IF$_{4/5}$** macrocycles (**R1**, **R2**) and analogous macrocycles (**R3**, **R4**)

Herein the described synthetic strategies to synthesise the analogous 2-pyridyl-derived '4+4' macrocycles directly in one-step using 2-aminopyridines or 2-aminopyrimidines (**O**) and isophthaloyl dichloride (**I**) generates modest-yielding, though, somewhat intractable product mixtures under a range of reaction conditions and reagents, but from which both the previously unreported class of imide-based macrocyclic trimers (**xIO3**, **trezimides**) and tetramers (**xIO4**, **tennimides**) can be isolated and characterised.

The advantages of the reaction derive from (*a*) the ability to vary and fine-tune the isophthaloyl aromatic backbone, (*b*) the wide range of functionalised 2-aminopyridines/pyrimidines that can be employed in the side chain for further derivation and (*c*) the practicality of using just one-step to achieve at least two distinct macrocyclic trimeric and tetrameric systems.

1.2. Historical background and development timeline

The idea of designing imide based macrocycles came as a result of an effort aimed at utilising the dibenzoylation of 2-aminopyridine (2-AP), an unwanted side-reaction in the synthesis of the **Mxo** and **Fxo** triads, for development of new scaffolds, desirably but not necessary with C_4 molecular symmetry that might find a potential use as future external blockers of neural K_v channels.

The 2-aminopyridine reacts with benzoyl chlorides in CH_2Cl_2, and in the presence of Et_3N gives almost exclusively *N*-benzoyl-*N*-pyridin-2-yl-benzamides instead of the expected simple benzamide (Scheme **38**). This reaction has been well known for many years and the first record of dibenzoylation of 2-AP originates in 1894 with a report by Marckwald[221] with occasional appearance during the 20th century,[160,161,163,164,222-225] including the proposed mechanism of the reaction[161] and kinetics.[225]

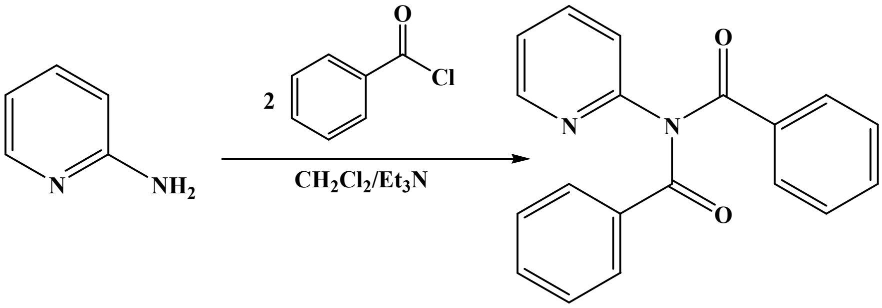

Scheme 38: Dibenzoylation of 2-aminopyridine

However the products have not found any place in any particular synthetic routes nor any specific application. Nevertheless, the Pubchem database[226] reveals 140 substructures based on *N*-benzoyl-*N*-pyridin-2-yl-benzamides, many of them synthesised as members of drug design libraries.

Deady and Stillman proposed a solvent dependant mechanism (Scheme 1),[161] claiming that dibenzoylation of 2-AP in pyridine occurs as a two step reaction where a first step yields a simple benzamide, followed by additional benzoylation of benzamide into a *N*-benzoyl-*N*-pyridin-2-yl-benzamide. Benzoylation in acetone occurs firstly on the pyridine *ortho*-nitrogen, after which the amine moiety, now turned into imine is attacked by benzoyl chloride and finally a rearrangement occurs giving the *N*-benzoyl-*N*-pyridin-2-yl-benzamide. Since the amine moiety in 2-AP is relatively acidic (pK_a = 6.26), and prone to very fast nucleophilic attack this mechanism should be considered as unlikely. The authors do not give any suggestion why mechanisms are different in different solvents (pyridine and acetone). However, studies[225] of dibenzoylation kinetics show a complete, immediate and fast dibenzoylation of 2-AP in $CHCl_3$ at RT.

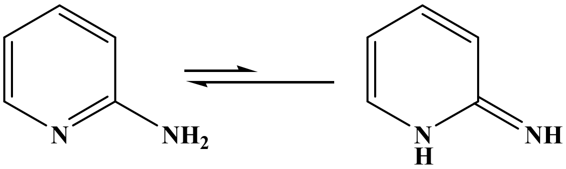

Scheme 39: Tautomeric structures of 2-aminopyridine

The pyridine nitrogen in the *ortho* position causes a delocalisation of electrons. It was found that 2-aminopyridine exists as a mixture of tautomeric amino and imino forms with the predominance of the amino form over the imino form (1000:1) (Scheme **39**).[227]

The presence of a strong base, Et_3N, might cause deprotonation of the imine form of 2-AP. A nucleophilic attack from benzoyl chloride forms a simple benzamide, while the second dibenzoylation immediately follows giving rise to an *N*-benzoyl-*N*-pyridin-2-yl-benzamide (Scheme **40**).

Our experience with the **Fxo**/**Mxo** synthesis in CH_2Cl_2 showed that exclusion of Et_3N gives a ratio of 1:7 in favour of *N*-benzoyl-*N*-pyridin-2-yl-benzamide, while a solventless reaction gives a ratio of 1:1. A possible reason for a decrease of dibenzoylation in pyridine is formation of a hydrogen bonded $N\text{-}H\cdots N_{pyr}$ complex that sterically prevents additional dibenzoylation, while during the solventless synthesis a dimer (as in the **Mxo**/**Fxo** crystal structures) is formed protecting the amide hydrogen atoms from further reaction.

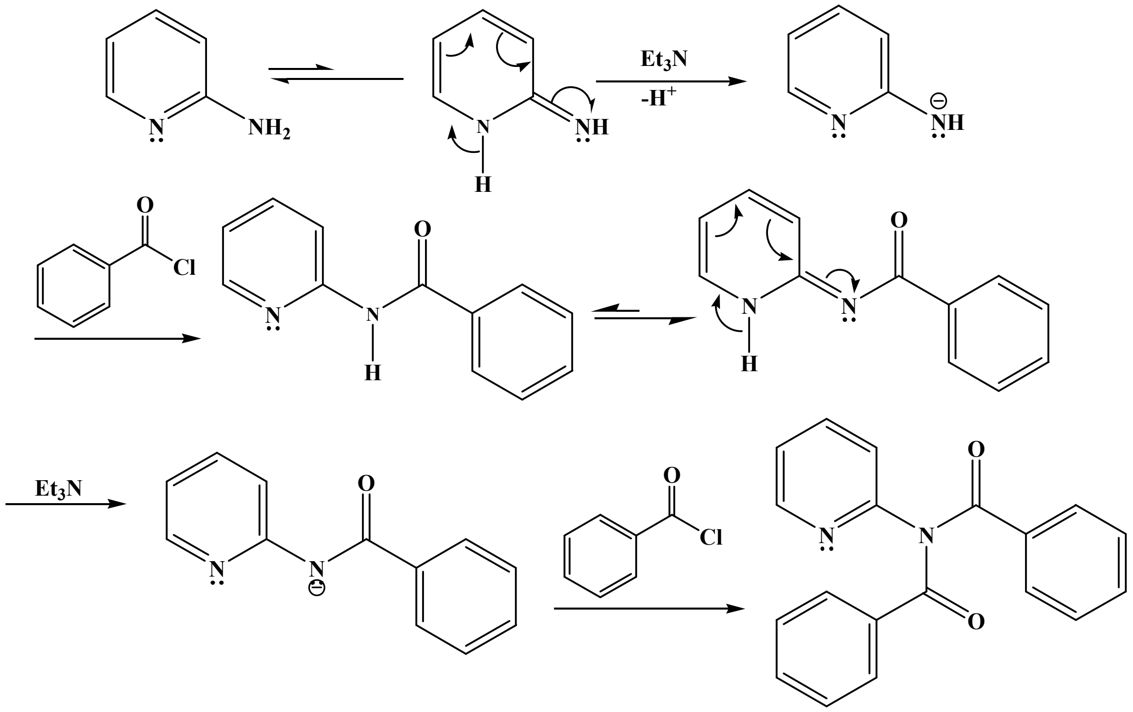

Scheme 40: Possible reaction mechanism of dibenzoylation of 2-aminopyridine

Generally, imides are well known. The important polyimides, based on naphthalene-tetracarboxylic diimides and developed during 1950's, play important roles in technology and various appliances.[228,229] The Pubchem database[226] reveals 309 chemical entities based on basic *N,N*-dibenzoylanilines including many 6-*p*-phenyl-dibenzo[c,e]azepine-5,7-diones.[230] Some macrocyclic analogues of polyimides were developed based on pyromellitic diimides[219,220] and perylene bisimides.[231] However, apart from IYURAV and IYUQUO[218] no imide macrocycles of the type [-(O)C-N*R*-C(O)-]$_n$ (***n*** ≥ 2) have been reported to date.

In the research group of J. F. Gallagher, from 2004 onwards, when condensing acyl chlorides and acids with the *ortho*-aminopyridines, the imide products were always regarded as interesting side-products to a variety of benzamide reactions that were being studied. The first researcher to work on these was Dr. Steven Alley who was working with ferrocene derivatives during 2002-2004. This was later exploited by Katie Donnelly, a final year undergraduate student in early 2007.[162-164] Attempts to synthesise *N*-(4-pyridin-2-yl)-*N*-(pyridinecarbonyl)pyridinecarboxamides (August 2009) ended without success since products proved to be unstable and in contact with silica gel decompose into *N*-(pyridin-2-yl)pyridinecarboxamides.

On December 8th 2009 during a routine, general CSD[8] search through analogues of our simple imides (**Mxod**, **Fxod**) the structures of the tetrameric imide macrocycles IYURAV and IYUQUO[218] were found and analysed. In these macrocycles, formation of the tetrameric imide macrocycle was facilitated by the presence of 4 or 5 fluorine atoms on a fluoroaniline moiety. A large number of fluorine atoms cause withdrawal of electrons and as a consequence the pKa of the amine is lowered. A similar effect was seen in 2-aminopyridine, however it is caused by electron delocalisation with the *ortho*-nitrogen. An overlay of our imides[163,164] with the IYURAV/IYUQUO[218] scaffolds showed a reasonable (yet remarkable) fit of the non-hydrogen atoms. This spurred the idea to develop similar "4+4" tetrameric imide macrocycles, analogues of IYURAV/IYUQUO using 2-aminopyridine instead of tetra- or pentafluoroaniline.[218]

This merging of IYURAV/IYUQUO[218] type scaffolds with dibenzoylation of 2-aminopyridine was planned to be accomplished by reacting 2-aminopyridine with the isophthaloyl dichloride in CH_2Cl_2 as a reaction medium, in the presence of Et_3N as base and DMAP as catalyst. It was expected to obtain the main tetrameric macrocycle, high molecular weight oligomers and polymeric materials.

The first attempt to undertake the "4+4" reaction was performed by Mark Farrell in April 2010 with no apparent success. A second attempt, undertaken by Pavle Mocilac (December 2010) gave a mixture of polymeric resin with dozens of low-molecular compounds that proved to be very difficult to separate.

In order to simplify the mechanism and increase the statistical probability of macrocycle formation we decided to try an alternative synthetic route, the "2+2" reaction of equimolar amounts of *N*^{1},*N*^{3}-di(pyridin-2-yl)isophthalamide (**H-DIP**) (Scheme **41**) with isophthaloyl dichloride in CH_2Cl_2 as solvent and in the presence of

Et_3N and DBU as bases using high dilution techniques. In order to avoid dibenzoylation, N^1,N^3-di(pyridin-2-yl)isophthalamide (**H-DIP**) was synthesised by refluxing (at 110°C) isophthalic acid with double equivalents of 2-AP in presence of triphenyl phosphite (TTP) as a coupling agent and pyridine as solvent. A detailed procedure for the **H-DIP** synthesis is given in the Section 2.1. Reaction of **H-DIP** with isophthaloyl dichloride using the high dilution technique (Scheme **42**) ought to have given a high yield of the desired macrocyclic product with a minimum amount of by-products and polymers. As isophthalic dichloride reacts with water, the solvent used in large quantities as reaction medium, CH_2Cl_2, was supposed to be strictly anhydrous, since even a smallest amount of moisture can deactivate isophthalic dichloride.

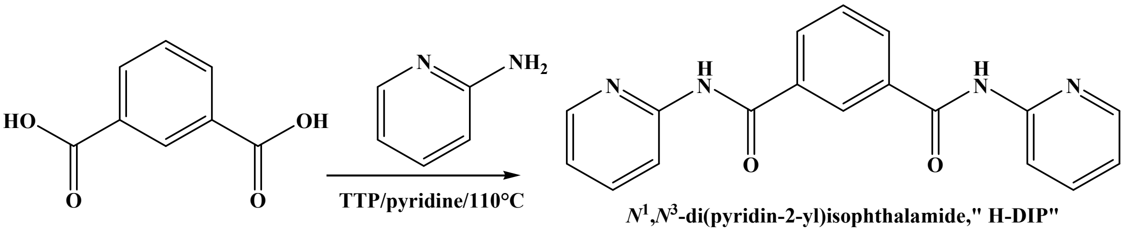

Scheme 41: Synthesis of N^1,N^3-di(pyridin-2-yl)isophthalamide (**H-DIP**)

The first "2+2" reactions were undertaken by Pavle Mocilac on 24th January 2011 yielding a mixture of **H-DIP**, polymer and additional side-products. A detailed procedure of the "2+2" reaction is given in the Section 2.2. The products were separated by column chromatography and subsequently re-crystallised from methanol. Three fractions of small amounts of unknown material were recovered and the ^{1}H-NMR in DMSO at RT was recorded.

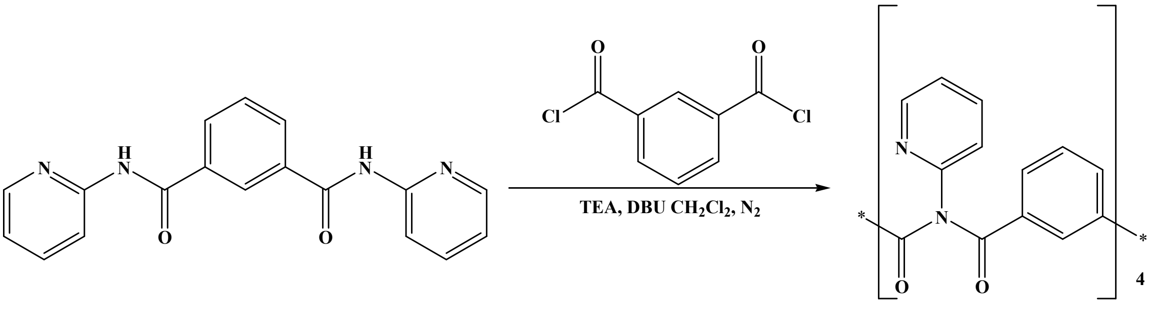

Scheme 42: General scheme for the "2+2" reactions

The first and the third fractions proved to be open chain compounds. However, the second fraction showed a similar pattern of wide and overlapping peaks as in the Gale & Evans publication.[218] This indicated a macrocycle. A potential product was assigned as **IO4** (**I**sophthalic - ***O****rtho*-aminopyridine tetramer). The possible existence of the "**IO2**" dimeric macrocycle was discounted since it is sterically unlikely.

The first real breakthrough came on the February 26th 2011, when a variable temperature ^{1}H-NMR experiment was undertaken raising the temperature from 20°C to 80°C in increments of 10°C. The results including a number of peaks, with shifts and integration were as expected for an imide macrocycle.

An attempt to undertake a mass spectroscopy experiment in order to determine the molecular weight, and consequently decide on the product's final identity failed due to insolubility in water and inability to ionise using electron spray ionisation or MALDI-TOF methods. Nevertheless, in the absence of an appropriate MS result the alternative was to grow a single crystal and solve the molecular and crystal structure.

The first crystal structure determination attempt was on **IO4** grown from $CDCl_3/CH_3CN$ on March 7th and using Mo Kα radiation, (20s/30s to 0.85 Å) on a thin colourless plate (that looked twinned). In fact all of the samples looked twinned and had a soapy surface appearance to the untrained eye. The first structural breakthrough was with a $CDCl_3$ derived sample from an NMR tube and in a glass vial as **[11-032]**. The crystal diffracted very well and to 0.95 Å for Cu and Mo Kα radiations. This was the major breakthrough since the molecular and crystal structure proved that the product was indeed the tetrameric imide macrocycle **IO4**.

Subsequently, DMSO crystals looked very poor and were eventually examined as **[11-041]**. These crystals look twinned, but when viewed from the side though they extinguish plane-polarised light. Crystal samples were then grown from alcoholic solvents and crystals were examined in the following samples: from methanol **[11-040]** data collected with Cu Kα radiation, but was found to be monoacetone solvate, from ethanol as **[11-038]** (Mo Kα) and **[11-039]** (Cu Kα) and from IPA **[11-042]** (Cu Kα). Crystals grown from IPA did not provide good quality data, but yielded a unit cell.

Table 37: List of **IO4** crystals (at RT)

Label	**Emp. form.**	**Kα**	***R1***	**Date**	***SG***	***Θ*$_{max}$, Res.**	**Remark**
[11-032]	$C_{53}H_{33}N_8O_8Cl_3$	Mo	5.59	07/03/2011	$P\bar{1}$	[25°]; 0.85	**IO4**:$CHCl_3$
[11-033]	$C_{53}H_{33}N_8O_8Cl_3$	Cu	4.50	08/03/2011	$P\bar{1}$	[60°]; 0.88	**IO4**:$CHCl_3$
[11-038]	$C_{53}H_{35}N_8O_{8.5}$	Mo	6.11	23/03/2011	*C2/c*	[25°]; 0.85	**IO4**:0.5(EtOH)
[11-039]	$C_{53}H_{35}N_8O_{8.5}$	Cu	3.38	24/03/2011	*C2/c*	[60°]; 0.88	**IO4**:0.5(EtOH)
[11-040]	$C_{53}H_{35}N_8O_{8.5}$	Cu	4.69	25/03/2011	*C2/c*	[60°]; 0.88	**IO4**:0.5(Acet)
[11-041]	$C_{56}H_{46}N_8O_{10}S_2$	Cu	18.0	28/03/2011	*C2*	[60°]; 0.88	**IO4**:2(DMSO)
[11-042]	$C_{58}H_{46}N_8O_{10}$	Cu	N/A	29/03/2011	*C2/c*	[50°]; 1.00	**IO4**:2(IPA)

On March 22nd an ethanol crystalline derivative was mounted which was very small, but later a huge block was mounted which had many faces. This crystal gave a structure with an *R*-factor of 6.1% **[11-038]**. Later, it was tried with Cu Kα radiation (in *C2/c*). These crystals form very well and diffract strongly.

However, new attempts to repeat our synthetic procedure and consequently synthesise more **IO4** failed, yielding only polymer and/or starting **H-DIP**. Adjustments of the reaction conditions were applied, such as additional rigorous drying of CH_2Cl_2, change of solvent, volume of reaction media, *etc*. All subsequent changes proved futile, ending without the **IO4** product. Attempts to perform the “2+2” reaction using preliminary “*in situ*” synthesis of isophthaloyl dichloride in reaction media by converting isophthalic acid into isophthaloyl dichloride using dichlorotriphenylphosphorane[232] and subsequent, direct addition of **H-DIP** and Et_3N also ended without the formation of the desired product (**IO4**).

Although the high dilution technique presents a standard procedure in macrocyclic chemistry and is widely recommended, the procedure described in Gale & Evans publication[218] was **not** a high dilution technique. The relatively inflexible ligands as for **IO4** may actually be suited to higher concentrations of reactants. In addition, **H-DIP** has a very low solubility in CH_2Cl_2, whereas attempts to perform the “2+2” reaction is other solvents, like THF, did not give the desired product. A situation without a positive synthetic outcome lasted from early March to mid-May 2011.

Therefore in June 2011 a decision was made to design a new synthetic procedure (Scheme **43**) and based on Gale & Evans original “4+4” procedure.[218]

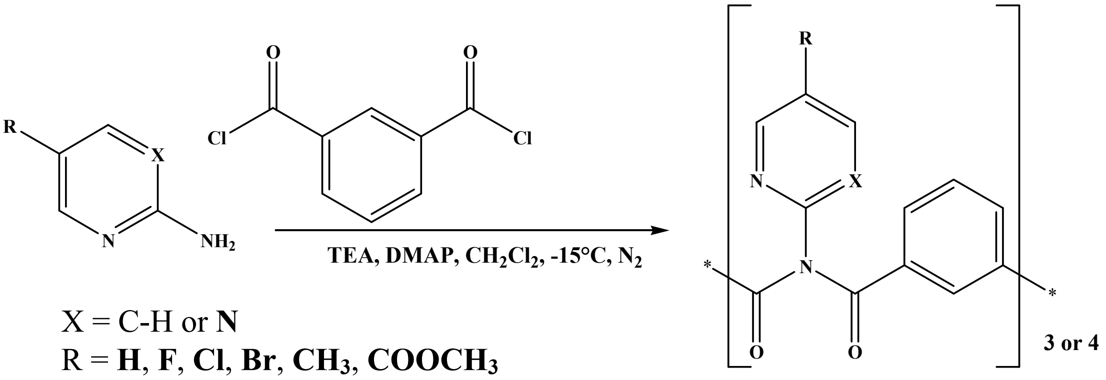

Scheme 43: General synthetic scheme for the “4+4” reactions

As a small sample of **IO4** was available to us, an idea was proposed to check if a modified original procedure could, beside other side-products, yield sufficient amounts of **IO4**. The eventual product ought to be identified by TLC. A hypothesis that slowing down the reaction is useful to suppress formation of polymeric materials lead to the decision to pre-cool the reaction medium (before addition of 2-AP) down to -15°C and leave the reaction to slowly warm to RT over a period of 1-2 hours. This attempt resulted in newly synthesised **IO4**, along with polymeric resin and some other side-products.

However, the induced solidification of the product mixture using Et_2O before chromatographic purification and separation resulted in a very insoluble white powder that was reluctant to be re-dissolved in virtually any organic solvent, even when heated, and effectively preventing chromatographic separation. This was probably the result of the fact that once the polymeric/oligomeric resin chains are solid they form a "molecular ball", tightly wrapped by intermolecular interactions. This molecular "ball" presumably intertwines attached **IO4** molecules.

Hence, a new reaction was undertaken and the crude reaction mixture containing both oligomeric resin and macromolecules was transferred to a chromatographic column and purified immediately after the solvent was removed under reduced pressure. The result was not fully satisfactory since the first separated fraction was a pure unknown fraction and second was a mixture of the first fraction and **IO4**. The unknown fraction was analysed by variable temperature ^{1}H-NMR and the resulting spectrum was similar but not matching with the **IO4** spectrum, except for integration that matched **IO4**. It seemed that the unknown product was a 2-AP imide macrocycle, but not the tetrameric **IO4**. The IR spectra matched almost perfectly suggesting the same moieties.

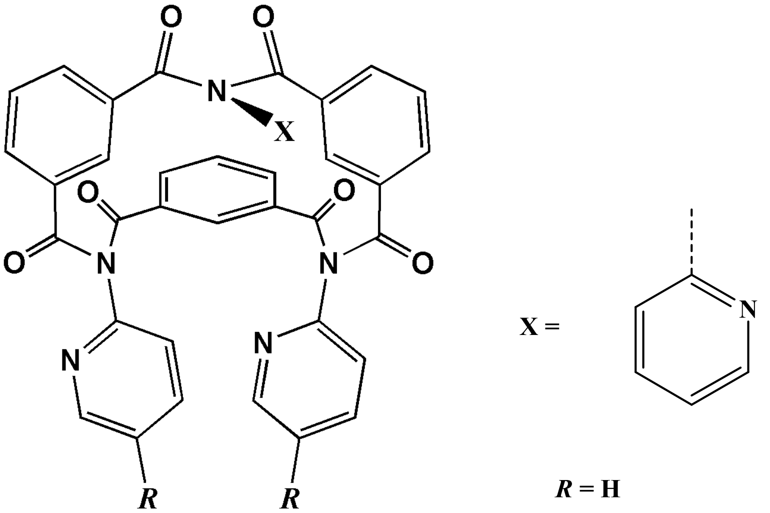

Scheme 44: Structure of the **IO3** trimer

Single crystals of the unknown fraction were grown from DMSO-d_6 and XRD showed that it was a trimer (Scheme **44**). The trimer was named as **IO3**. A standardised, "4+4" synthesis and procedure is described in detail in the Section 2.3.

Shortly afterwards, another reaction, based on a successful "4+4" procedure was performed, but with 2-aminopyridine replaced by 2-aminopyrimidine (2-APM). The result gave a mixture of two imide macrocycles, namely the tetrameric **26IO4** and trimeric **26IO3**. The difference between the **IO4/IO3** and **26IO4/26IO3** chromatographic R_f values was too small and classical column chromatography was unable to separate both macrocycles efficiently. Gel permeation chromatography, as described in Gale's work,[218] was not successful either. Therefore, after many attempts, preparative TLC technique was tried and proved to be successful yielding ~5-10 mg of each compound per plate. Using this method, sufficient amounts of **26IO4** and **26IO3** were isolated for spectroscopic analysis, crystal growth and XRD. Later in 2011 optimal mobile phases for the efficient separation of the two different macrocycles were found and preparative TLC was no longer required.

By the end of 2011 several pairs of imide macrocycles based on 2-AP or 26-APM derivatives bearing different substituents were successfully synthesised, purified, characterised and their structures determined by SXRD: **FIO4/FIO3**, **ClIO4/ClIO3**, **BrIO4/BrIO3**, **26BrIO4/26BrIO3** and finally **EsIO4/EsIO3**. Methyl macrocycle development ended with only the isolated tetramer (**MIO4)**. However, repeated attempts to synthesise the **CNIO** and **25IO** macrocycles, based on 6-amino-3-pyridinecarbonitrile and 2-aminopyrazine, failed and yielded no macrocycles. Nevertheless the synthetic route is quite general and standard, allowing access to a range of macrocycles (trimer/tetramer) based on 2-aminopyridines and 2-aminopyrimidines.

1.3. Polymer formation

A competitive reaction that occurs in parallel with the cyclisation is the formation of an imide polymer (polyimide, Scheme **45**). The polymer probably has medium and longer sized spiral chains with free terminal carboxylic groups that emerge through partial deactivation of isophthaloyl dichloride with moisture from the environment.

The standard strategy in preventing formation of the polymer is the high dilution technique, but in this reaction this approach is not a choice. Instead, cooling of the reaction mixture (-15°C) and reaction slowdown probably helps macrocycle formation. The formation of polymer becomes visible usually after half an hour from the reaction onset, as a clouding of the reaction mixture. When a reaction mixture gradually warms to ambient temperature, the polymer becomes more visible and deposits in the form of a gel on the flask wall.

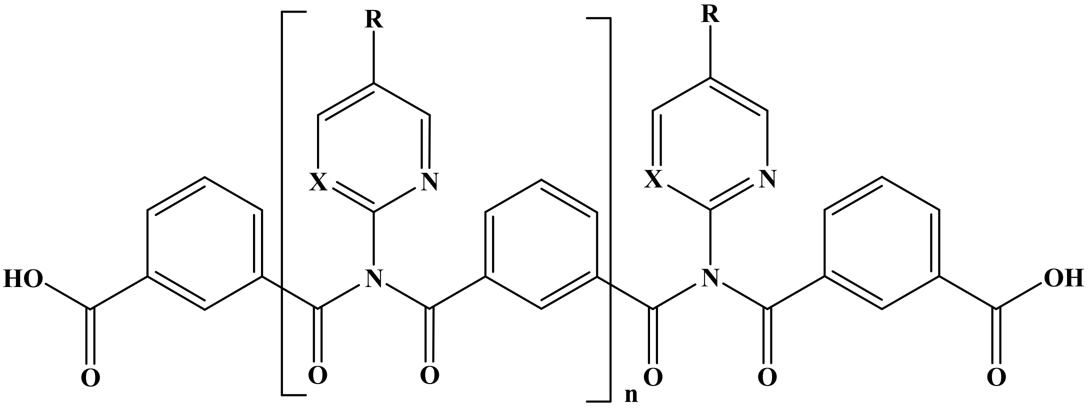

Scheme 45: Possible structure of the imide polymer (**X** = C-H/N, **R** = **H**, **F**, **Cl**, **Br**, **$COOCH_3$**)

During filtration on a sintered funnel the polymer as a gel, shrinks and thickens into a paste as it loses solvent (CH_2Cl_2). Finally, after drying it hardens and solidifies into a hard, brittle solid, insoluble in water and most organic solvents. Once dry and hard it is reluctant to re-absorb solvents; solidification seems to be irreversible. Since it is brittle, it can be easily obtained in a powdered form with a mortar and pestle. When in contact with concentrated and warm acids (*e.g.* H_2SO_4) the polymer undergoes fast degradation.

1.4. The labelling system and nomenclature

Since both the tetramers and trimers consist of the same fragment, 2-aminopyridine or 2-aminopyrimidine and isophthalic acid connected by the imide moiety, the main label "**IO**" is taken from the term "**I**sophthalic" and "***O****rtho*-aminopyridine". The prefix "**26**" is assigned to macrocycles based on 2-aminopyrimidine (26-APM). The suffixes "**3**" or "**4**" mark if the macrocycle is tetramer or trimer. Finally, additional prefix before the **IO** label (**F**, **Cl**, **Br**, **M** [for CH_3], and **Es** [for $COOCH_3$]) denotes substituent at the 2-AP or 26-APM in *para*-position.

All developed imide tetramer or trimer macrocycles share a similar backbone. In the case of the tetramers, it is an irregularly shaped globular molecule with C_4 pseudosymmetry. If the 2-AP moieties, hydrogen atoms and CX4/5/6 atoms are removed the remaining backbone roughly follows a tennis ball seam. Therefore, for all tetrameric imide macrocycles of similar geometry a common name "**tennimides**" is proposed. Similarly, for the trimeric imide macrocycles a common name "**trezimides**" is proposed that originated from the Latin word "tres" meaninig "three". In order to have a unique name the letter "s" is changed into "z".

1.5. Materials, equipment and spectroscopic methods

All vendors, materials, solvents and reagents and equipment for the synthesis, purification and spectroscopic characterisation were as described in Chapter I, Section 1.1.2. Preparative TLC plates were purchase from Analtech Inc., USA. The NMR spectra experiments have been performed in DMSO-*d_6*, except for **EsIO4** and **EsIO3** ($CDCl_3$), at 600 MHz using a Bruker Avance Ultrashield 600 NMR Spectrometer. For most of the compounds variable temperature ^{1}H-NMR, as well as ^{1}H-NMR, ^{13}C-NMR, DEPT, DEPT-Q, HSQC, HMBC, COSY and NOESY experiments were undertaken at higher temperature. For **FIO3** and **FIO4** the ^{19}F-NMR experiments have been performed at 400 MHz on an equivalent Bruker NMR spectrometer. The FTIR experiments were performed as described in Chapter II.

1.6. X-ray crystallographic methods

Single crystal X-ray data collection and data reduction,[176] structure solution and refinement[3,168] was as described for compounds in Chapter I. For some macrocycles, the SQUEEZE program[169] in PLATON was used in order to eliminate the regions of diffuse electron density in solvent accessible voids. Selected crystallographic and structural information are detailed in the ESI III, Section 2. Molecular and hydrogen bonding diagrams (Figs. **79-101**) were generated as described in other isomer grids (with displacement ellipsoids drawn at the 10% probability level).[169]

1.7. Computational methods

The structural geometries of the **IO3** and **26IO3** trezimides and **IO4** and **26IO4** tennimides were investigated by *ab initio* modelling and conformational analysis methods similar to that previously described (Chapter I and II) in order to test structural differences between the experimentally obtained solid state structures (from X-ray diffraction) and the modelled, optimised structures in *gas phase*. The experimental XRD derived conformations were used as a starting point, and all calculations were performed using the DFT method (B3LYP) and 6-31G(d,p) basis set. Calculations were performed with Gaussian 09 software at the Irish Centre for High End Computing (ICHEC).

2. Detailed descriptions of the synthetic procedures

2.1. Synthesis of *N*^{1},*N*^{3}-di(pyridin-2-yl)isophthalamide (H-DIP)

Into a solution of isophthalic acid (2.08 g, 12.5 mmol) in 40-50 ml pyridine, 2-aminopyridine (3.54 g, 37.5 mmol) was added and warmed with stirring for 15 minutes, followed by addition of triphenyl phosphite (9.9 ml, 37.5 mmol). The reaction mixture was refluxed with stirring at 110°C for 5 hours. Next, the pyridine was removed from the reaction mixture by evaporation under reduced pressure on a rotary evaporator. The resulting light brown oil was taken in 150 ml of CH_2Cl_2 and the solution was washed with brine. The product was extracted in 150 ml 1:1 (v/v) aqueous HCl. The acidic aqueous extract was neutralised by NaOH and Na_2CO_3. The resulting white solid was filtered, washed thoroughly with distilled water, air dried and dissolved in 150-200 ml of CH_2Cl_2. The solution was washed twice with aqueous solution of $KHCO_3/Na_2CO_3$ (pH ~9). The organic layer was dried with $MgSO_4$, decolourised with charcoal and double filtered. The product (m = 1.4 g; 35%) was recovered after the solvent evaporation under reduced pressure on a rotary evaporator.

2.2 Method 1: The "2+2" synthesis of the IO4 tennimide

The *N*^{1},*N*^{3}-di(pyridin-2-yl)isophthalamide (H-DIP, 0.1783 g, 0.56 mmol) and Et_3N (0.24 ml, 1.68 mmol) were dissolved in anhydrous CH_2Cl_2 (400 ml) under N_2 and DBU (two drops, 35.2 μl, 0.2360 mmol) was added. Isophthaloyl dichloride (0.1137 g, 0.56 mmol) was added to the vigorously stirred reaction mixture. The reaction mixture was allowed to vigorously stir overnight. The reaction mixture was washed with an aqueous solution of $KHCO_3/Na_2CO_3$ (400 ml, pH ~9) three times, with brine containing NH_4Cl (400 ml, pH ~6) three times, dried over $MgSO_4$ and the solvent reduced on a rotary evaporator affording a yellow resin. The yellow resin was purified by column chromatography using silica as stationary phase and CH_2Cl_2/MeOH (10:1) as a mobile phase. The resulting second fraction was collected, the product was recovered and re-crystallised from MeOH affording 26.6 mg (10.6%) of a white product (**IO4**).

2.3. Method 2: Standardised, “4+4” synthesis of tennimides and trezimides

The reaction medium was prepared by dissolving DMAP (10 mg, 0.08 mmol) and Et_3N (4 ml, 29.8 mmol) in 100 ml of anhydrous CH_2Cl_2. The 2-aminopyridine, 2-aminopyrimidine or its derivative (9.8 mmol) was dissolved or suspended in 5-20 ml of reaction media. Isophthaloyl dichloride (1.98 g, 9.8 mmol) was dissolved with stirring in 80-95 ml of reaction media in a 250 ml round bottom flask, under an inert atmosphere of N_2 and cooled on an ice bath (ice/NaCl/NH_4Cl/EtOH) to -15°C. The solution/suspension of 2-aminopyridine, 2-aminopyrimidine or derivative was quickly and quantitatively added to the cooled flask containing isophthaloyl dichloride. The reaction mixture was stirred overnight.

The reaction mixture was diluted with technical grade CH_2Cl_2 to 200 ml, if necesary filtered over a funnel with a sintered glass frit, to remove the polymeric by-product and washed three times with aqueous solutions of NH_4Cl (pH ~5) (3×200 ml), dried over $MgSO_4$ and filtered. The clear, filtered product solution was left for the next step. Subsequently, the solvent was removed on a rotary-evaporator to afford a resin. This resin was immediately purified by column chromatography on silica gel (Davisil, 70 μm, 82 g, column dimension: $l = 25$ cm, $d = 3$ cm) eluting with a suitable mobile phase to separate and obtain pure macrocyclic products. Isolated yields were from 3 to 13% for both tennimide and trezimide macrocycles.

3. General comments on spectroscopic data

Spectroscopically, the tennimides and trezimides show C_4/C_3 pseudosymmetry, having four/three equivalent segments that consist of 2-aminopyridines (or 2-aminopyridimidines) and the isophthalic moiety. Therefore, all tennimides and trezimides can be considered as tetramers and trimers of a general segment shown in Scheme **46**. Due to conformational rigidity in solution at room temperature, the ^1H NMR experiment at 20°C usually shows very poorly resolved peaks, giving inappropriate integration. However, raising the temperature improves flexibility and peaks were gradually resolved at 80°C.

The variable temperature ^1H-NMR was recorded for all compounds (except for **EsIO3**) showing significant improvements of peak resolution as well as displacement of particular peaks at higher temperatures. This effect is less pronounced in the trezimides than in the tennimides. For **26IO4** and **26BrIO4** a higher temperature (120°C and

140°C) was required due to the low solubility in DMSO-d_6. Elevation of temperature improved the ^{13}C-NMR spectra too. The NOESY experiments did not show any specific proximity of protons in solution.

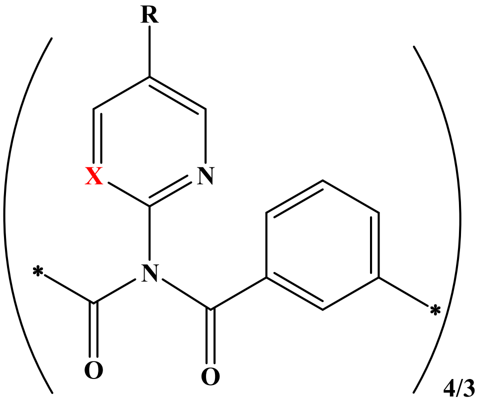

Scheme 46: Tennimides and trezimides (**X** = C-H/N, **R** = **H, F**, **Cl**, **Br**, **CH_3**, **$COOCH_3$**)

4. IO3 and IO4 macrocycles

4.1. Synthesis and purification

The synthesis and purification of the **IO3** trezimide and **IO4** tennimide was as described in previous sections (1 and 2, Scheme **41-43**). The yield were good to modest: the yield of **IO4** obtained with Method 1 (Section 2.1) was 26.6 mg (10.6%) while with Method 2 (Section 2.2) it was 127 mg (6%), for **IO4** and 149 mg (7%) for **IO3**. The chromatographic R*f* values for the $CHCl_3$/ethyl acetate/acetone (4:12:1) mobile phase were 0.57 (**IO4**) and 0.63 (**IO3**).

4.2. General and spectroscopic data

The **IO3** trezimide and **IO4** tennimide are white, odourless powders. Their crystallinity is comparable with those of the benzamides and pyridinecarboxamides, however, better than that of carbamates and **H-DIP**. The **IO3** seems to be more soluble in organic solvents than **IO4**; the solubility difference is especially pronounced in alcohols, **IO3** is readily soluble, while **IO4** is poorly soluble in cold methanol, ethanol or *iso*-propanol. However, both compounds are soluble in chlorinated hydrocarbons, such as $CHCl_3$ or CH_2Cl_2 as well as in ethyl acetate, acetone and DMSO. Solubility in *n*-hexane was modest, poor in diethyl ether. Both **IO4** and **IO3** are insoluble in water.

The basic spectroscopic information for **H-DIP**, **IO4** and **IO3** is given in Appendix I, Sections 4.1 - 4.3, while the comprehensive NMR data and spectra are given in the ESI III, Section 1-3. The ^{1}H-NMR of **IO4** resolves relatively well at 80°C without coupling (Fig. **78a**), whereas for **IO3,** peaks resolve much better and decoupling shows. This suggests that **IO3** is much more flexible than **IO4** where more than one conformation exists. The IR data (Fig. 7**8b**) are almost identical and show a similar distribution of bands with very strong bands around 1720-1690 cm^{-1} corresponding with carbonyl (C=O) stretches The peaks in 1600-1400 cm^{-1} region are associated with C-C and C-N vibrations in the isophthaloyl and pyridinyl rings, while the strong peaks in the 1400-1200 cm^{-1} region belong to C-N and C-C vibrations and

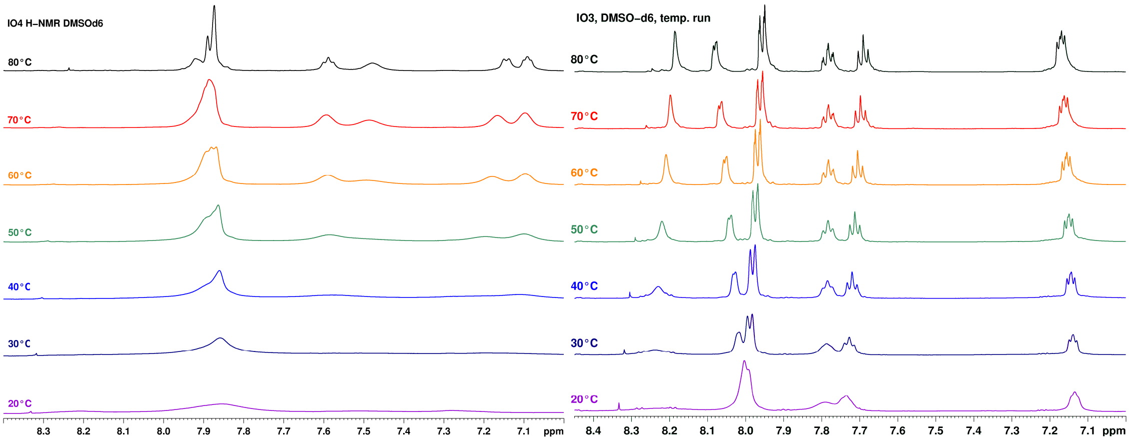

Fig. 78a: Variable temperature ^{1}H-NMR experiment for **IO4** and **IO3**

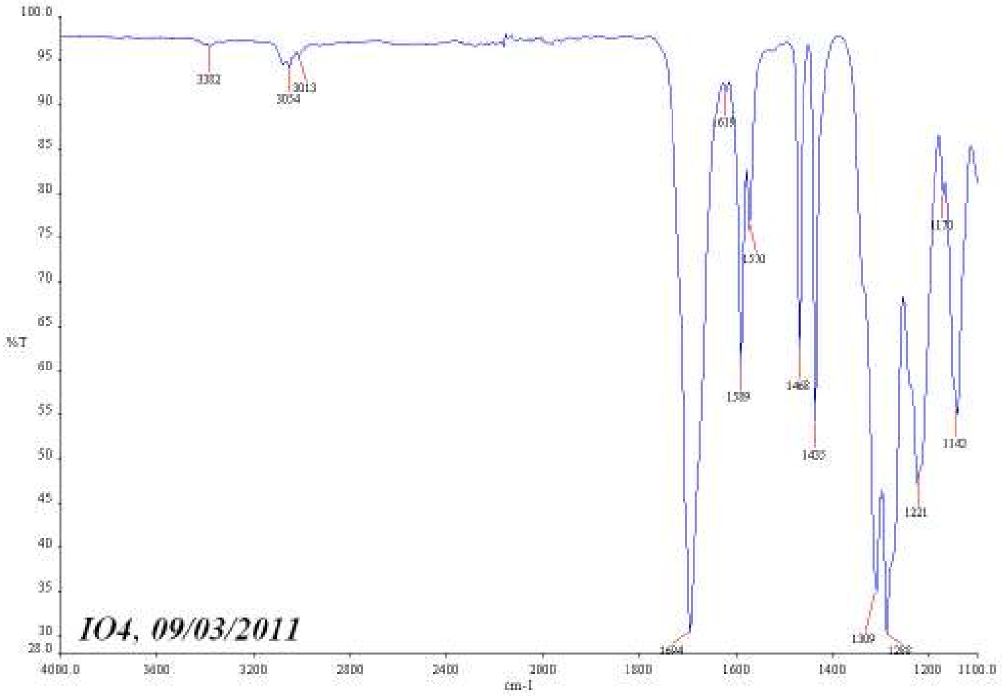

Fig. 78b: IR spectrum of **IO4**

stretches in the imide backbone. Absence of significant peaks *ca.* 3000 cm^{-1} indicates that the bulk **IO3** and **IO4** powders are not in the form of solvate. The stability of **IO4** seems to be very good and better than the stability of **IO3**. Prolonged heating in DMSO-d_6 did not cause disintegration. However, separation using preparative TLC caused partial disintegration of **IO3** suggesting potential stability issues.

4.3. Crystallographic data and discussion

For all crystal structures an initial data collection using Mo radiation provided adequate results with *R* factors from 0.06 to 0.12, however Cu datasets were also obtained providing more data, much lower *R*-factors ($R < 0.06$) and smaller estimated standard deviations on the geometric parameters: the Cu-derived data are discussed herein. Since several single crystals of **IO4** were grown and data was collected, affording various R-factors, the results of the **[11-033]** dataset (**IO4**:CHCl3) will be presented. Table **38** summarises the basic crystallographic data.

Table 38: Selected crystallographic data[a] for the **IO3** and **IO4** macrocycles†

	IO3	**IO4**
Chemical formula	$C_{39}H_{24}N_6O_6{\cdot}(C_2H_6OS)_2$	$C_{52}H_{32}N_8O_8{\cdot}CHCl_3$
Crystal system, space group	Monoclinic, $P2_1/n$, (No. 14)	Triclinic $P\overline{1}$, (No. 2)
a, b, c (Å)	12.5381(1), 11.7299(1), 28.1349(3)	11.9279(9), 12.0291(9), 16.8723(13)
α, β, γ (°)	90, 92.935(1), 90	84.618(6), 86.984(6), 76.201(7)
Z'	1	1
$R[F^2 > 2\sigma(F^2)]$, $wR(F^2)$, S	0.057, 0.163, 1.05	0.045, 0.123, 1.04

† Complete crystallographic, refinement and structural details are listed in the ESI III (Section 2.1). [a] Obtained with Cu $K\alpha$ radiation.

The **IO3** trezimide (Fig. **79**) crystallises as a solvate with two molecules of DMSO-d_6. The solvent molecules are disordered as A/B (0.5:0.5) and C/D (0.5:0:5). The solvent molecules play an important role in aggregation. If viewed along the *c*-axis direction while the *a*-axis is down, the **IO3** molecule roughly resembles to letter “A” with two pyridinyl rings (“1” and “3”) being vertical, pointed down and nearly co-parallel (interplanar angle P1/P3 = 34.67°). The pyridinyl ring “2” is located at the top and is directed backward. The isophthaloyl ring “1” is nearly perpendicular to the two pyridinyl rings “1” and “3” (interplanar angles I1/P1 = 81.22° and I1/P3 = 87.41°).

The internal imide dihedral angles, or so called "**CO**···**CO**" twist angles are -87.03° (O1-C1···C2-O2), 95.45° (O3-C3···C4-O4) and 94.85° (O5-C5···C6-O6). The wide pocket between the carbonyl moieties (O2, O3, and O5) and isophthaloyl hydrogen atoms (H12, H22 and H32) is a macromolecular *niche* and its dimensions are defined by O···O and H···H distances.

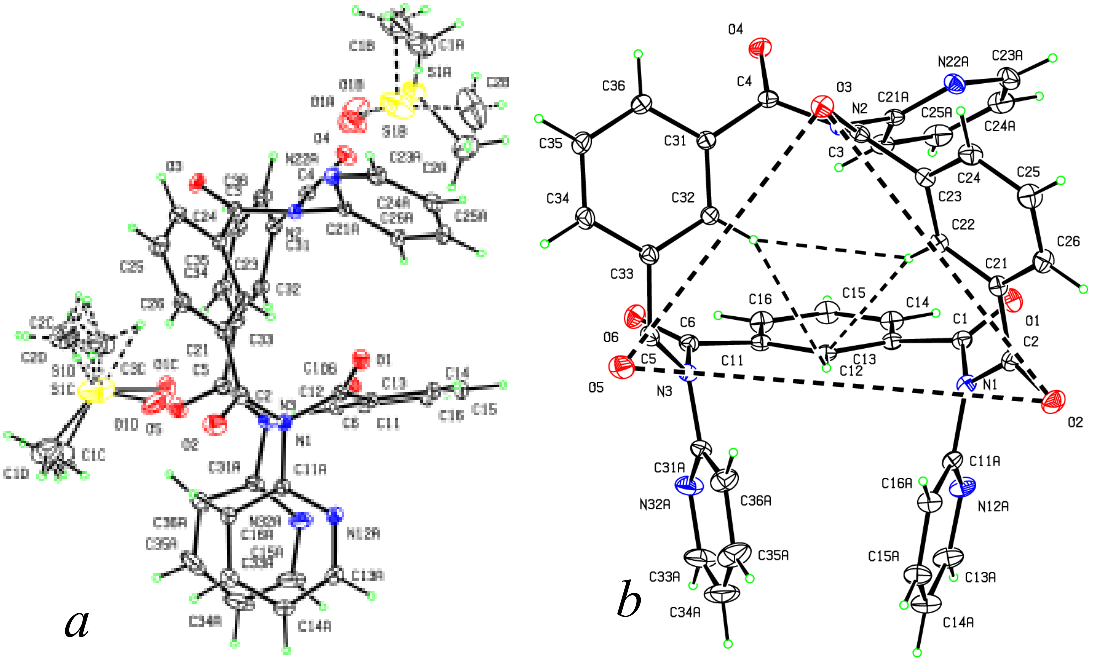

Fig. 79: An ORTEP diagram of **IO3**; *a*) with solvent molecules *b*) with macrocyclic *niche*

For **IO3** the O···O distances range from 6.05 to 7.96 Å, while the H···H distances range from 2.67 to 2.87 Å. The disordered A/B molecule of DMSO-d_6 is anchored to the macromolecular *niche via* strong C16A-H16A···O1D [C16A···O1D = 3.246(12) Å] and C36A-H36A···O1C [C36A···O1C = 3.195(12) Å] hydrogen bonds. The two disordered DMSO-d_6 molecules, A/B and C/D are interconnected *via* C1C/D-H15C/D···O1A/B^{a} [a = 3/2-x,1/2+y,1/2-z] interactions.

The aggregation in **IO3** is mainly accomplished through C-H···O/N contacts with the aid of interactions between the solvent and **IO3** molecules. The main interaction is a C35A-H35A···O2^{b} [C35A···O2^{b} = 3.148(4) Å, b = -x+1/2,y+1/2,-z+1/2] hydrogen bond that alternately links **IO3** molecules into a *zig-zag* 1-D column along the *b*-axis direction. The column is stabilised by weaker C15A-H15A···O5^{c} [C15A···O5^{c} = 3.400(3) Å, c = 1/2-x,-1/2+y,1/2-z] interactions. Secondary interactions are C34A-H34A···O3^{d} [C34A···O3^{d} = 3.306(4) Å, d = x-1,y,z] and C25-H25···O3^{e} [C25···O3^{e} = 3.096(3) Å, e = -x+3/2,y-1/2,-z+1/2] that interconnect the *zig-zag* columns, aided by the C24A-H24A···N12A^{f} [C24A···N12A^{f} = 3.385(3) Å, f = i-x+1,-y+1,-z] interaction. The solvents are supporting the aggregation *via* C36-H36···O1A^g [C36···O1A^g = 3.383(5) Å, *g* = x,y+1,z] interactions.

The **IO4** crystal structure (Figs. **80** and **81**) was found to be in form of a solvate containing one disordered molecule of $CHCl_3$ as A (0.86) and B (0.14). The molecule of $CHCl_3$ is anchored to the **IO4** molecules *via* a strong C1A-H1A···N12A [C1A···N12A = 3.306(4) Å] hydrogen bond.

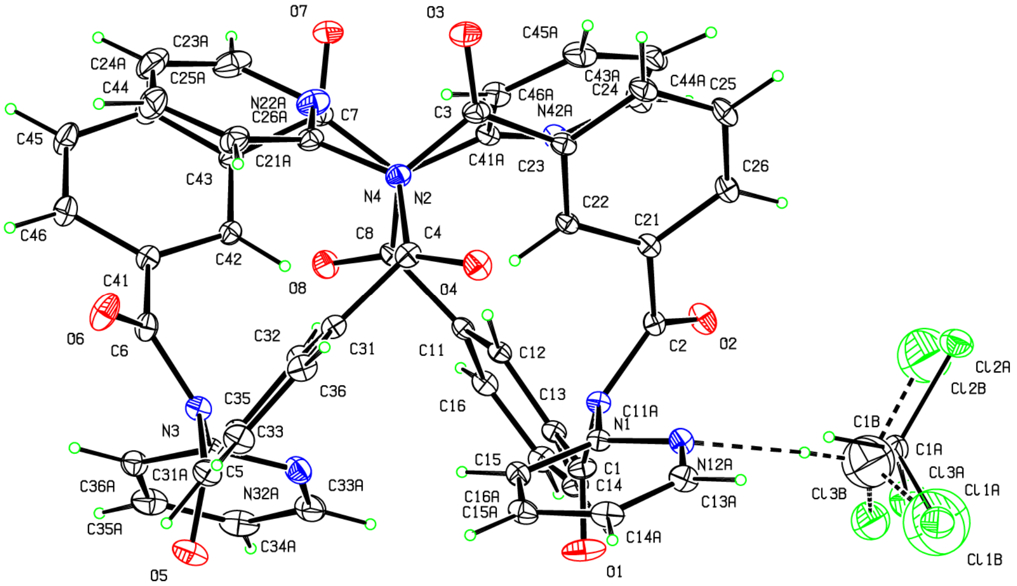

Fig. 80: A view of the **IO4** molecule with disordered $CHCl_3$

The geometry of **IO4** is essentially similar to **IF$_{4/5}$**[218] with four 2-AP/isophthalic segments twisted in a circle around the central cavity. The molecule has C_4 pseudosymmetry. The internal imide dihedral angles, "**CO**···**CO**" twists are 106.02° (O1-C1···C2-O2), -92.50° (O3-C3···C4-O4), 106.69° (O5-C5···C6-O6) and -98.86° (O5-C5···C6-O6). The H···H distances of the intraannular cavity are 4.13 Å (H12···H32) and 4.33 Å (H22···H42). Similarly as in benzamides, pyridinecarboxamides (Chapter I) and carbamates (Chapter II), in tennimides derived from 2-amnopyridines the 2-pyridine rings can adopt a conformation close (**P-*anti***) or distant (**P-*syn***) to the carbonyl oxygen, *e.g.* having their nitrogen atoms pointed toward medial line of the central pore (medially, **P-*anti***) or opposite (laterally, **P-*syn***). If the both pyridine rings are **P-*anti*** the pore of the central cavity is in an open state, while if **P-*syn*** the pore is closed. If one ring is **P-*anti*** and another is **P-*syn*** than the pyridine nitrogen and pyridine hydrogen are pointed towards one another and the pore might be in either state (*opened* or *closed*) depending on other geometrical factors. In total, since a tennimide molecule has two pores; they can be in *closed-closed* ("**cc**"), *open-open* ("**oo**") or *open-closed* ("**oc**") state.

For the **IO4** molecular structure from **[11-033]**, the pyridinyl rings are in both **P-*anti*** (medial, rings “2” and “3”) and **P-*syn*** (lateral, rings “1” and “4”) conformations. Therefore, both sides are similar, with pyridine hydrogen being pointed towards the neighbouring pyridine nitrogen. However, the N···H distances are 3.90 Å (N32···H16A) and 2.85 Å (N22···H46A) which means that the pores are in the “**oc**” state.

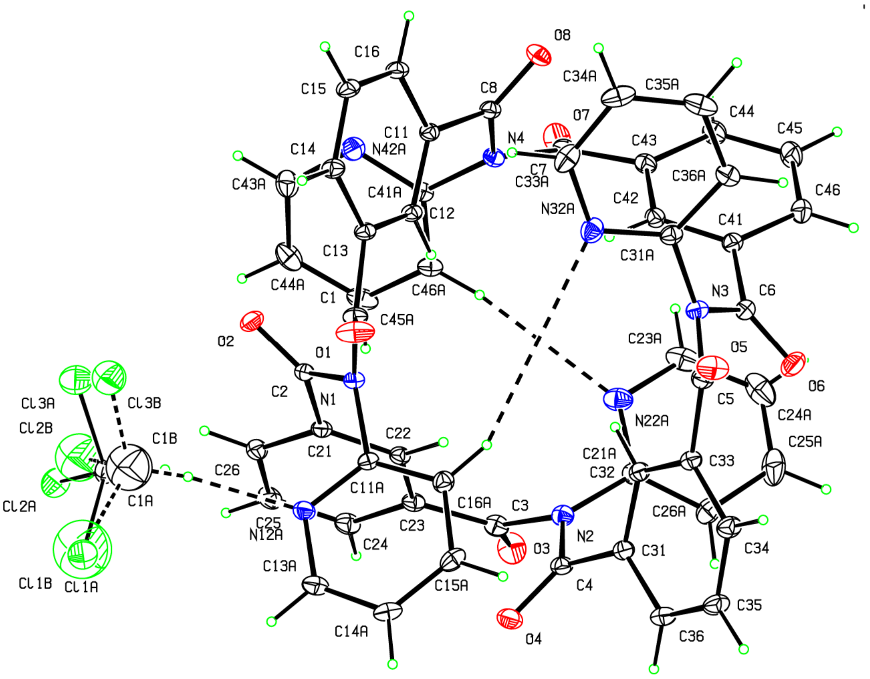

Fig. 81: A view of the **IO4** molecule with disordered $CHCl_3$

The aggregation (Figs. **80** and **81**), as in **IO3**, relies on C-H···O interactions while the $CHCl_3$ molecule supports the aggregation. The main interaction is the C25-H25···O8^{a} [C25 ···O8^{a} = 3.238(3) Å, *a* = x+1,y,z] hydrogen bond that aggregates the **IO4** molecules into a column along the *a*-axis direction. The secondary interaction is C15-H15···O2^{b} [C15···O2^{b} = 3.297(3) Å, *b* = -x,-y+1,-z+1] that links two columns into a pair, aided by π···π [C15···C15 = 3.390(3) Å] contacts. Next, the column pairs are further linked into a 2-D sheet parallel with the $(0\bar{1}1)$ plane *via* C46-H46···O6^{c} [C46···O6^{c} = 3.358(3) Å, c = -x,-y,-z]. Two sheets are combined into a pair by C15A-H15A···O5^{d} [C15A···O5^{d} = 3.087(3) Å, *d* = -x,1-y,-z] interactions. Final aggregation is accomplished through weak C-H…O interactions as well as by solvent molecules and C-Cl···O supporting contacts.

5. 26IO3 and 26IO4 macrocycles

5.1. Synthesis and purification

The synthesis and purification of the **26IO3** tennimide and **26IO4** tennimide was undertaken as described in the standardised "4+4" procedure (Section 2.3) using 2-aminopyrimidine (26-APM, 0.932 g, 9.8 mmol) instead of 2-aminopyridine (2-AP). The chromatographic separation was accomplished with a $CHCl_3$/MeOH blend (10:1) as a mobile phase, yielding the **26IO3** trezimide (89 mg, 4%, R*f*= 0.579) and the **26IO4** tennimide (134 mg, 6%, R*f* = 0.699). However, a further purification in order to obtain highly pure samples for characterisation and crystal growth was undertaken using re-crystallisation from $CHCl_3$ and preparative TLC.

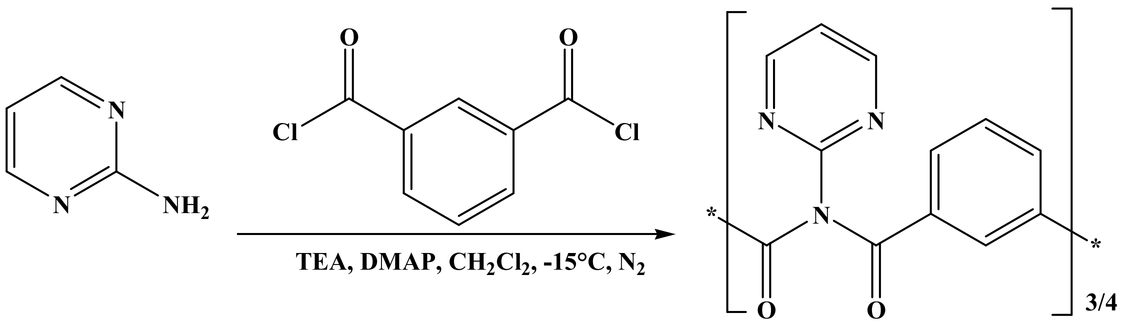

Scheme 47: General diagram of the **26IO3/4** synthesis

5.2. General and spectroscopic data

In general, the **26IO3** and **26IO4** macrocycles show similar physical properties as their 2-AP analogues, however, they are less soluble and more crystalline. Compared to **IO4**, the **26IO4** tennimide is less soluble in most organic solvents even in DMSO. Therefore, the NMR data for **26IO4** was obtained in DMSO-d_6 at 120°C. The **26IO4** is significantly less soluble in $CHCl_3$ than **26IO3** and therefore can be separated from **26IO3** using a standard re-crystallisation procedure. Paradoxically, the **26IO4** shows higher solubility in cold $CHCl_3$ than in warm: if a cold solution with a few crystals is heated new **26IO4** crystals are formed, but re-dissolve upon cooling. This unexpected paradox occurs presumably due to easier aggregation of **26IO4** and $CHCl_3$ into a solvate after the structure of **26IO4** is conformationaly equalised in warmer conditions. The **26IO4** tennimide shows higher crystallinity compared to **IO4**.

The NMR and IR data are listed in Appendix I, Sections 4.3 and 4.4, while the spectra are given in the ESI III, Sections 1.3 and 1.4. The variable temperature ^{1}H-NMR was undertaken from 120°C down to 20°C. Peaks resolve at 80°C, while the coupling fully emerges at 120°. The **26IO4/3** macrocycles show two protons less than the **IO3/4** macrocycles. In **26IO3** peaks are fully resolved even at 20°C suggesting a high rate of conformational interchange and flexibility.

5.3. Crystallographic data and discussion

Single crystals of **26IO3** ($CH_2Cl_2/CHCl_3$ with MeOH) and **26IO4** ($CH_2Cl_2/CHCl_3$) were obtained using standard crystallization conditions in a range of common solvents. Table **39** summarises the key crystallographic data for the **26IO3** trezimide and for two datasets of the **26IO4** tennimide.

For **26IO4** a second crystal **[11-104]** was grown and the lattice voids contained partial occupancy and disordered solvent molecules of $CHCl_3$, acetone, methanol and water (crystallisation arose after several successive attempts using more polar solvents). In this case only, the SQUEEZE program was used to improve the overall results with the *R*-factor dropping from 13.2 to 4.2%.

The **26IO3** trezimide (Fig. **82**) crystallises as a solvate with a disordered molecule of $CHCl_3$ (partial occupancy of 0.25), CH_2Cl_2 (partial occupancy of 0.3) and CH_3OH (partial occupancy of 0.25). As seen previously, the disordered solvents are creating additional networks of interactions supporting aggregation. The **26IO3** crystal structure aggregates with $Z' = 2$, although molecules seem to be very similar.

Table 39: Selected crystallographic data[a] for the **26IO3** and **26IO4** macrocycles†

	26IO3	**26IO4-[11-103]**	**26IO4-[11-104]**
Chemical formula	$C_{36.80}H_{22.85}Cl_{1.35}N_9O_{6.25}$	$(C_{48}H_{28}N_{12}O_8)_2 \cdot C_3H_5Cl_7$	$C_{48}H_{28}N_{12}O_8$
Crystal system, space group	Triclinic, $P\bar{1}$	Tetragonal, $P\bar{4}2_1c$	Tetragonal, $P\bar{4}2_1c$
a, b, c (Å)	13.3884(4), 13.5458(4), 20.0062(7)	22.7814(1), 22.7814(1), 19.0308(1)	15.9127 (3), 15.9127 (3), 19.3896 (5)
α, β, γ (°)	76.205 (3), 89.176 (2), 89.633 (2)	90, 90, 90	90, 90, 90
Z'	2	3	1
$R[F^2 > 2\sigma(F^2)]$, $wR(F^2)$, S	0.060, 0.176, 1.03	0.046, 0.136, 1.03	0.042, 0.116, 1.02

† Complete crystallographic, refinement and structural details are listed in the ESI III (Section 2.2). [a] Obtained with Cu *K*α radiation.

The most striking characteristic of both **26IO3** molecular structures (Fig. **82**) is that they have very different conformations as compared to **IO3**. The two molecules (A and B) are different and almost mirror images of each other. The molecular *niches* (Fig. **82**) are located between the carbonyl oxygen atoms O1A, O3A and O6A (molecule A) and O1B, O4B and O5B (molecule B); the O···O distances range from 6.71 to 6.92 Å (molecule A) and from 6.61 to 7.25 Å (molecule B). The isophthalic H···H (H12, H22 and H32) distances range from 2.76 to 3.59 Å (molecule A) and from 2.71 to 3.67 Å (molecule B). However, the internal imide "**CO**···**CO**" twist dihedral angles are 97.6° (O1-C1···C2-O2), 66.1° (O3-C3···C4-O4) and -113.6° (O5-C5···C6-O6) in molecule A, while in the molecule B are 116.3° (O1-C1···C2-O2), -70.44° (O3-C3···C4-O4) and -79.5° (O5-C5···C6-O6). The interplanar angles between the isophthalic angles are close to orthogonality; the 1A/3A interplanar angle is 80.8° and the 1B/3B is 85.1°. This conformation was assigned as the **R** conformation, opposite to typical **P** conformation of **IO3**.

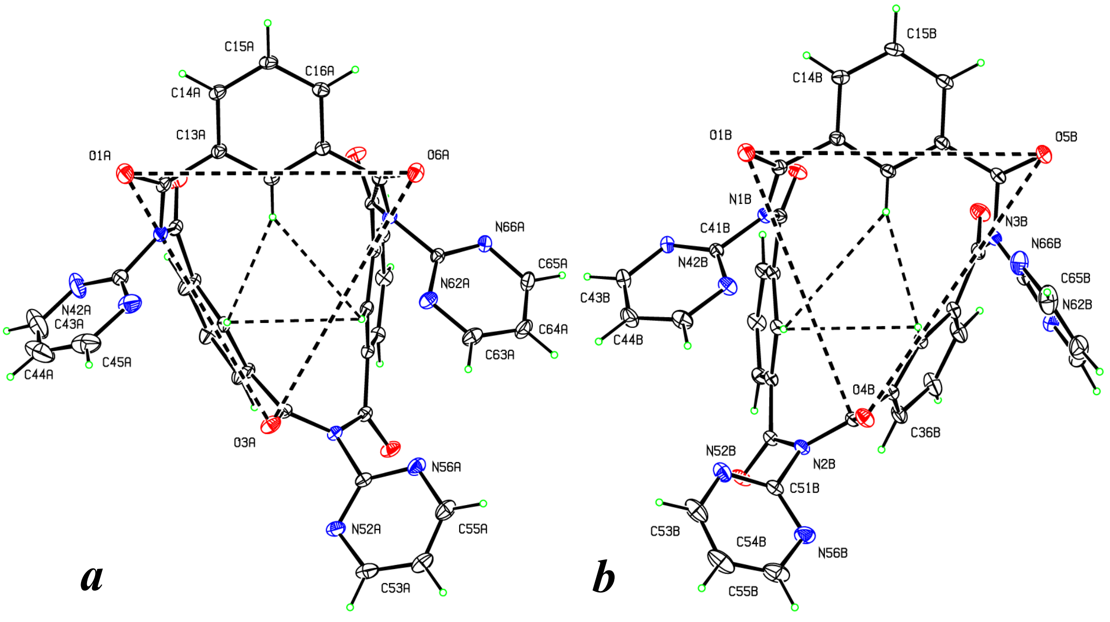

Fig. 82: An ORTEP diagram of **26IO3** with macrocyclic *niches* shown: *a*) molecule A, *b*) molecule B

The aggregation in **26IO3** is enhanced by solvent molecules that form a myriad of intermolecular interactions. The main backbone of the crystal structure is a double 1-D chain formed along the *a*-axis direction by molecules B *via* C16B-H16B···O3B^a [C16B-H16B···O3B^a = 3.333(3) Å, *a* = -1+x,y,z] and C15B-H15B···N42B^b [C15B-H15B···N42B^b = 3.415(4) Å, *b* = -x,1-y,1-z] interactions. Molecules A do not engage in strong interconnections internally itself, but rather serve as a joints between the chains of molecule B *via* several interactions such as C24A-H24A···O6B [C24A···O6B =

3.194(4) Å], C53B-H53B···N62A^{c} [C53B···N62A^{c} = 3.418(5) Å, *c* = 1+x,1+y,z], C43A-H43A···O4B^{d} [C43A···O4B^{d} = 3.286(6) Å, *d* = -x,1-y,-z] and C35B-H35B···O2A^{e} [C35B···O2A^{e} = 3.212(5) Å, *e* = 1+x,y,z].

The **26IO4** structures are shown to be the most symmetric among the tennimides. Both datasets crystallise in the $P\overline{4}2_1c$ space group with similar aggregation patterns, but differ in *Z′* and geometry. In the **[11-103]** crystal **26IO4** crystallises with a disordered molecule of $CHCl_3$ with *Z'* = 3: molecule A consists of two equivalent halves (C_2 symmetry) that stand in relation *via* symmetry code -x,1-y,z while the molecules C and O have C_4 symmetry with four identical segments (26-APM/isophthalic) standing in relation by symmetry codes 1-y,x,-z, 1-x,1-y,z and y,1-x,-z (Molecule C) and 1-x,1-y,z, 1-y,x,1-z and y,1-x,1-z (Molecule O). The molecules differ by their geometry. In molecule A internal imide "**CO**···**CO**" twist angles are -88.6° (O1-C1···C2-O2) and 96.5° (O3-C3···C4-O4), while in the molecule C and O only one value exists due to the C_4 symmetry, ±87.2° (molecule C) and ±91.9° (molecule O). The H···H distances of the intraannular cavity in molecule A are 4.224 Å (H12···H12A^{a}, *a* = -x,1-y,z) and 5.282 Å (H22···H22A^{a}), in the molecule C are 4.539 Å (H12C···H12C^{b}, *b* = 1-x,1-y,z) and in the molecule O are 3.943 Å (H12O···H12O^{b}).

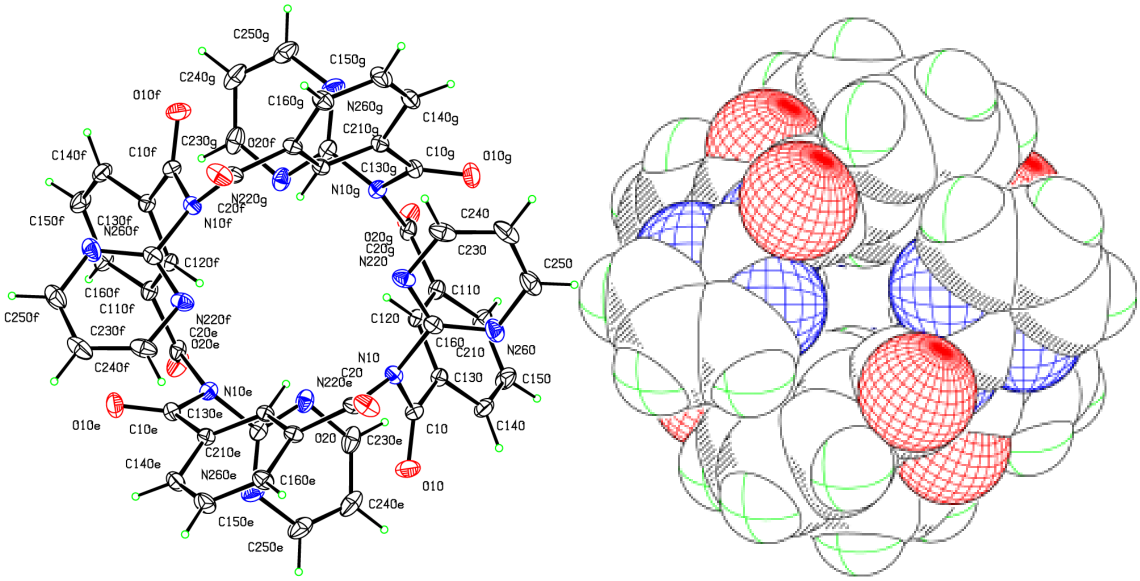

Fig. 83: An ORTEP and CPK view of **26IO4** (**[11-103]** dataset, molecule O)

The N22…N22 distances are 3.259 Å (N12···N12A^{a}), and 4.098 Å (N22···N22A^{a}) in the molecule A, 3.520 Å (N22C···N22C^{b}) in the molecule C and 4.679 Å (N22O···N22O^{b}) in the molecule O. Therefore, it seems that the cavity pores in the molecule A are in the *open-closed* state ("**oc**"), while the *closed-closed* ("**cc**") in the molecule C and the *open-open* ("**oo**") in molecule O. In the same time intraannular cavity in molecule A is distorted, in molecule C is expanded, while in molecule O is constricted.

The aggregation in the **11-103** crystal structure relies on C-H···O interactions. The molecules are connected into columns along the *c*-axis direction *via* C13A-H13A···O4^{c} [C13A···O4^{c} = 3.121(4) Å, *c* = -1/2+y,1/2+x,1/2+z], C23C-H23C···O2O^{d} [C23C···O2O^{d} = 3.310(6) Å, *d* = 1-x,1-y,z-1], C16O-C16H···O2C^{e} [C16O···O2C^{e} = 3.264(4) Å, *e* = y,1-x,-z] and C23A-H23A···O2^{f} [C23A-H23A···O2^{f} = 3.448 Å, *f* = -1/2+y,1/2+x,-1/2+z] interactions.

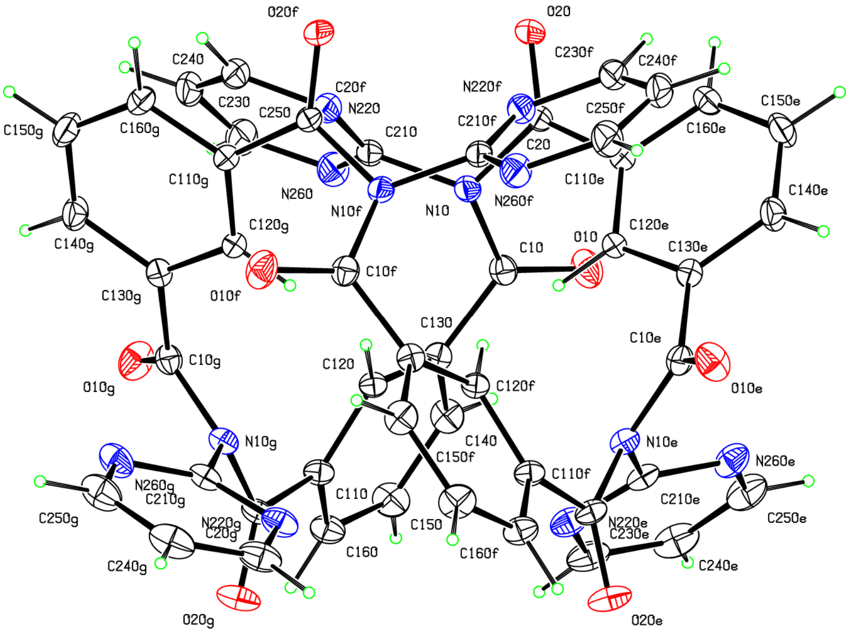

Fig. 84: A side-view of **26IO4** (**[11-103]** dataset, molecule O)

The columns are linked along the *a*- and *b*-axes by C25O-H25O···O3^{g} [C25O···O3^{g} = 3.258(4) Å, *g* = 1/2-x,-1/2+y,1/2-z], C15C-H15C···O1^{h} [C15C···O1^{h} = 3.159(3) Å, *h* = 1-y,1+x,-z] and C15A-H15A···O1O^{f} [C15A···O1O^{f} = 3.124(4) Å] interactions.

The **11-104** crystal structure of the **26IO4** tennimide is very similar, but with *Z′* = 1. The geometry of the **26IO4** molecule resembles molecule A from the **11-104** dataset, having C_2 symmetry with symmetry code *a* = 1-x,-y,z. The internal imide "**CO**···**CO**" dihedral twists are -81.05° (O1-C1···C2-O2) and 95.94° (O1-C1···C2-O2). The H···H distances of the intraannular cavity are 4.355Å (H12···H12^{a}) and 4.181 Å (H22···H22^{a}), while the pyrimidine N···N distances are 3.253 Å (N12···N12^{a}) and 4.077 Å (N22···N22^{a}). Therefore, cavity pores are in the *open-closed* "**oc**" state. Aggregation in the **11-104** crystal structure is similar to **[11-103]**. The principal interaction is a strong C13A-H13A···O3^{b} [C13A···O3^{b} = 3.166(3) Å, *b* = 1/2-y,1/2-x,-1/2+z] hydrogen bond that aggregates molecules along the *c*-axis direction into a 1-D column. The columns are interconnected into the 3-D structure along the *a*- and *b*-axes *via* C25-H25···O4^d [C25···O4^d = 3.361(3) Å, *d* = 1-y,-1+x,-z], C26-H26···O3^e [C26···O3^e = 3.489 Å, e = 1-y,-1+x,-z] and C15-H15···N16A^f [C15···N16A^f = 3.476 Å, *f* = 3/2-x,1/2+y,1/2-z] contacts.

5.4. *Ab initio* geometry optimisation, energies and conformational analysis

The geometry of the tennimides and trezimides structures was optimised by *ab initio* modelling methods in order to investigate structural differences between the experimentally obtained solid state structures and modelled optimised structure in *gas phase*. The experimental XRD derived structures were taken as a starting point and all calculations were performed using the DFT method (B3LYP) and 6-31G(d,p) basis set. All optimisations were successful and did not produce vibrations with negative values.

To examine flexibility of the imide backbone, a structural fragment containing two isophthalic and one 2-pyridinyl (2-pyrimidinyl) moieties was isolated from the non-optimised **IO4** and **26IO4** structures based on experimental solid state structures. The main torsion angles of the fragments, 2-AP-ring angle, 26-APM-ring angle, two imide torsion angles (O-C8-N-C, O-C9-N-C), two isophthalic angles (O-C8-C-C, O-C9-C-C), (ESI III, Section 3, Fig. **1**) were subjected to conformational analysis by performing PES scans of each torsion angle while the rest of the torsion angles were kept static. By this model, the rigidity of the tennimides was nullified and the PES scans were enabled. However, as this model presents only an approximate model, the resulting PES diagrams can be taken only as providing a generalised, approximate insight into the flexibility of the imide backbone moiety. Furthermore, the structural fragments of both **IO4** and **26IO4** were optimised to inspect the extent of structural change after rigidity was removed and relaxation achieved.

Since the **IO3** and **26IO3** trezimides were found in two distinct conformations, **IO3-P** and **23IO3-R**, the hypothetical counter-conformations **IO3-R** and **26IO3-P** were built, based on the existing **IO3-P** and **23IO3-R** conformations, by simple swapping of the aromatic C-H atoms with aromatic N atom and the reverse. Both experimental and hypothetical conformer geometries were optimised and the resulting geometries were compared by simple structure overlays.

Optimisation of both **IO4** and **26IO4** significantly equalises structural parameters across the macrocycle making the structures more symmetrical (Fig. **85**).

Most of the **IO4** torsion angles in the main backbone rotate no more than 12° except for the C31A-N3-C5-C33 (+16°) and O4-C4-C31-C32 (+13°) torsion angles (ESI III, Section 3.1).

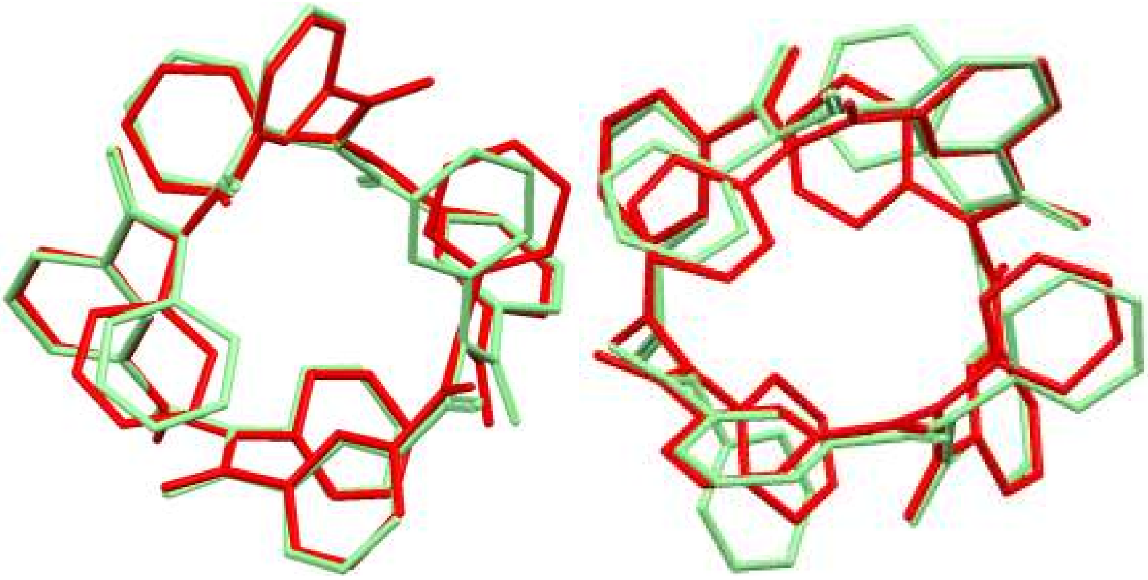

Fig. 85: *left*) overlay of solid state (**in red**) and optimised (**in light green**) **IO4** structure; *right*) overlay of solid state (**in red**) and optimised (**in light green**) **26IO4** structure

Since a solvent molecule of $CHCl_3$ was excluded from the modelling, pyridinyl rings 2 and 3 significantly rotate closing the pore. Generally, the **IO4** tennimide closes the pores upon optimisation (H12···H32), height (O7···O6) increases, while diameter (N2···N2^{a}, *a* = 1-x,-y,z) slightly contracts (ESI III, Section 3.1).

For **26IO4** tennimide, the 2-aminopyrimidine rings significantly move apart upon optimisation (~1-2 Å), opening the central cavity (Fig. **85**). At the same time, the isophthalic rings move slightly medially (~0.2-0.3 Å). In summation, the **26IO4** diameter (C3···C3^{a}) slightly expands, its height (O3···O1) increases, while the central pore (H12···H12^{a}, N22A···N22A^{a}) was found to open. This is mainly due to the changes in isophthalic torsion angles, less in imide torsion angles and 2-aminopyrimidine (26-APM) ring, since the isolated molecule without intermolecular interactions adopts a more stable and symmetric geometry.

The PES diagrams (ESI III, Section 3.2) show that the torsion angles of both **26IO4** and **IO4** are approximately in their global minimum, except the 2-AP ring and imide 8 torsion angles whose global minimum is in the negative value area. Apart from slight tensions of the imide torsion angles caused by movement restriction in the macrocycle, the result indicates no significant tensions in the **IO4**/**26IO4** macrocycles. Furthermore, optimisations of the **IO4** and **26IO4** fragments (ESI, Section 3.3) show larger changes of imide 8 torsion angles compared to other torsion angles, supporting the indications drawn from PES diagrams. High rotational barriers of the imide and 26-APM/2-AP torsion angles suggest relative inflexibility and opposite to the more flexible isophthalic angles. In agreement with this, optimisation of **26IO4** causes more significant changes in the isophthalic angles compensating for tension in imide torsion angle.

All *ab initio* modelling information of the tennimides suggests that the solid state structures of **IO4** and **26IO4** are rigid and not particularly different from their optimised model structures. Crystallisation with or without a solvent will not significantly change the overall structural parameters, while the solid state geometries are not expected to dramatically change upon dissolving in a solvent. Furthermore, modelling information suggests that steric stability of the tennimides contributes to the probability of tennimide formation.

Comparisons of the **IO3-P** and **26IO3-R** solid state structures as well as their hypothetical solid state counter-conformations (ESI III, Section 3.4) with their optimised structures show no significant change in geometries apart from slight rotations of the 2-AP and 26-APM rings. There were no negative values of the calculated vibrations observed, which suggests that the optimised structures reached their minima. The optimisation results suggest that the existence of both conformations is likely and that conformational polymorphism is plausible.

6. FIO3 and FIO4 macrocycles

6.1. Synthesis and purification

The synthesis was as described for Method 2 (standard “4+4” reaction, Section 2.3) using 2-amino-5-fluoropyridine (1.0986 g, 9.8 mmol) as a functionalised 2-aminopyridine (Scheme **48**). The polymer was not precipitated – the reaction mixture stayed clear overnight, suggesting better solubility of the polymer. Chromatographic purification and separation was undertaken using a mobile phase containing $CHCl_3$ and ethyl acetate (4:1), yielding **FIO4** (140 mg, 5.9%, R*f* = 0.302) and **FIO3** (150 mg, 6.3%, R*f* = 0.202). The isolated **FIO3** contained minor amounts of **FIO4**; therefore a final re-purification was accomplished using preparative TLC.

6.2. General and spectroscopic data

The general characteristics of **FIO3** and **FIO4** macrocycles, such as colour and crystallinity are broadly similar to the basic **IO4** and **IO3** macrocycles, however, its solubility in organic solvents, especially in chlorinated hydrocarbons is better.

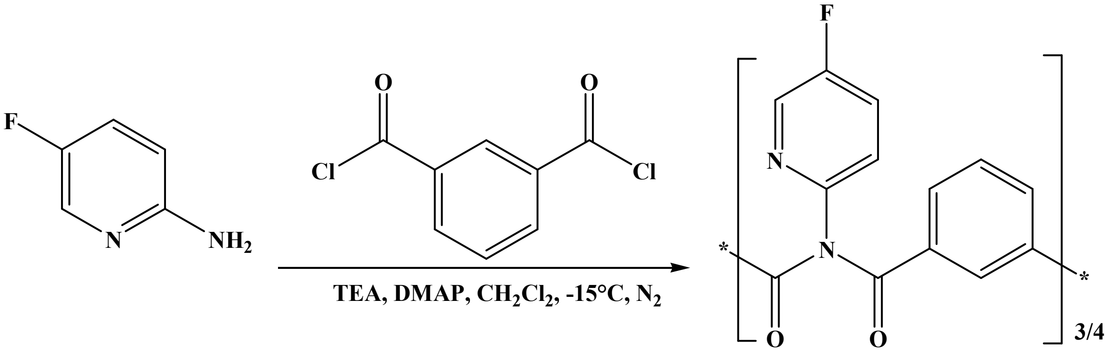

Scheme 48: General diagram of the **FIO3/4** synthesis

Results of the NMR experiments at RT and 80°C (^{1}H-, ^{13}C- and ^{19}F-NMR data are listed in Appendix I, Sections 4.5 and 4.6, spectra are provided in the ESI III, Sections 1.6 and 1.7) are comparable with those of the **IO4** and **IO3** macrocycles. Since fluorine atoms were present, ^{19}F-NMR experiments were undertaken including variable temperature studies. In **FIO3** two weak signals were noticed at RT at -129.8 and -128.7 ppm. At 40°C the signals merge into a one signal that intensifies and sharpens at -129.2 ppm as the temperature increases. In **FIO4** at RT two broad and weak signals are located at -127.5 and -128.5 ppm, while they merge at 40°C and the peak intensifies at -128.1 ppm (80°C). These results suggest the existence of two major conformers at room temperature in both of the **FIO3** and **FIO4** macrocycles, with relatively low energy difference. The IR of **FIO3** reveals additional peaks in the region between 2800 and 3100 cm^{-1} suggesting that bulk **FIO3** crystalline material is in form of solvate.

6.3. Crystallographic data and discussion

Table **40** summarises the basic crystallographic data for the **FIO3** and **FIO4** macrocycles. The **FIO3** trezimide (Fig. **86**) crystallises as a solvate with one molecule of CH_2Cl_2 (single crystals were grown from CH_2Cl_2 and MeOH). The molecule of CH_2Cl_2 is located near pyridinyl rings 1 and 3, and is not critical for aggregation in the **FIO3** crystal structure.

The **FIO3** macrocycle molecular structure resembles the **IO3** analogue**;** the conformation is P.

Table 40: Selected crystallographic data for the **FIO4** and **FIO3** macrocycles†

	FIO3^a	**FIO4**^{a}
Chemical formula	$C_{39}H_{21}F_3N_6O_6 \cdot CH_2Cl_2$	$C_{52}H_{28}F_4N_8O_8 \cdot CHCl_3$
Crystal system, space group	Monoclinic $P2_1/c$, (No. 14)	Triclinic $P\overline{1}$, (No. 2)
a, *b*, *c* (Å)	11.6181(1), 12.7879(1) 24.7200(2)	12.007(1) 12.0935(9), 17.6041(14)
α, β, γ (°)	90, 91.4752(6), 90	100.016(7), 103.607(7), 90.467(7)
Z'	1	1
$R[F^2 > 2\sigma(F^2)]$, $wR(F^2)$, S	0.036, 0.098, 1.03	0.058, 0.184, 1.02

† Complete crystallographic, refinement and structural details are listed in the ESI III (Section 2.3). ^{a} Obtained with Cu *K*α radiation.

The macromolecular *niche* is also similar: the three isophthalic H atoms H12, H22, H32 are oriented towards the base, with H···H distances from 2.55 to 2.98 Å, while the carbonyl atoms O2A, O3A and O5A are separated by distances of 6.34 to 8.28 Å (Fig. **86**). The pyridinyl rings 1 and 3 are not parallel, but the interplanar angle is 51.69(8)°. The imide "**CO**···**CO**" twist dihedral angles are -97.63° (O1-C1···C2-O2), 88.91° (O3-C3···C4-O4) and 100.06° (O5-C5···C6-O6).

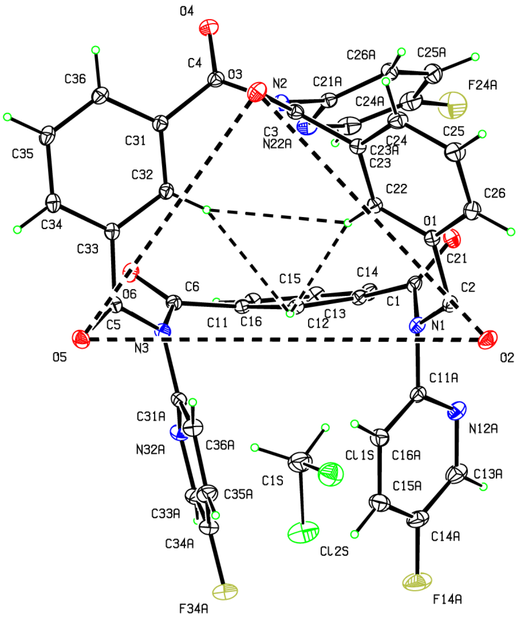

Fig. 86: An ORTEP diagram of **FIO3** with macrocyclic *niche* shown.

Aggregation in the crystal structure relies on several interactions. The strongest is C35-H35···O1^a [C35···O1^a = 3.136(2) Å, *a* = -1+*x*,*y*,*z*] that connects **FIO3** macrocycles into a 1-D chain along the *a*-axis direction. This aggregation is aided by weaker C13A-H13A···O5^{b} [C13A···O5^{b} = 3.388(3) Å, *b* = 1+x,y,z] contacts. The second important interaction is C34-H34···O2^{c} [C34···O2^{c} = 2.976(2) Å, *c* = -x,1/2+y,1/2-z] contact that links 1-D chains along the *b*-axis direction into a 2-D sheet parallel with the (001) plane. The remainder are weak C-H···O contacts. It is interesting to note the existence of F24A···F14A^{d} [2.821(3) Å, *d* = 1-x,1/2+y,1/2-z] and F24A···C14A^{d} [3.079(3) Å] contact.

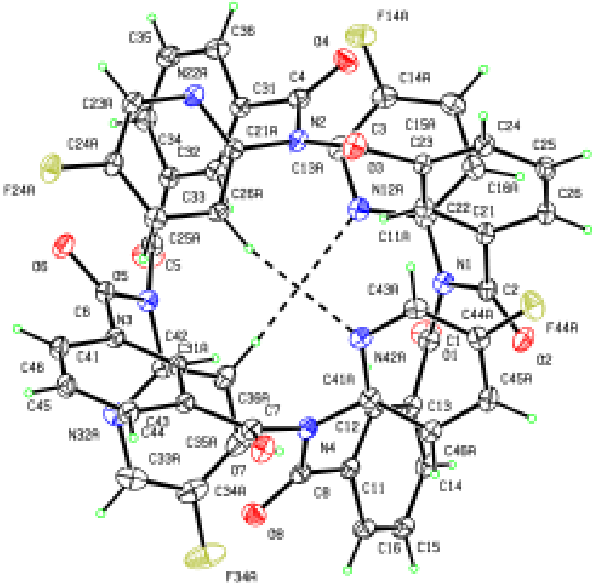

Fig. 87: A view of the **FIO4** molecule

The **FIO4** crystal (Figs. **87** and **88**) was grown from $CHCl_3$ and aggregates in $P\overline{1}$ with one disordered molecule of $CHCl_3$ as seen in **IO4**. The symmetry of the molecule is similar to **IO4**, less symmetric than **26IO4**. The internal imide '**CO**···**CO**' twist dihedral angles are different for all four segments: -107.51° (O1-C1···C2-O2), 107.15° (O3-C3···C4-O4), -98.35° (O5-C5···C6-O6) and 87.54° (O7-C7···C8-O8). The H···H distances of the intraannular cavity are 4.110 Å (H12···H32) and 4.306 Å (H22···H42).

The pyridinyl rings 1 and 4 have their nitrogen atoms oriented medially (**P-*anti***), towards the intraannular cavity entrance, while the pyridine nitrogen atoms of the 2 and 3 rings are oriented opposite (laterally, **P-*syn***), as seen in **IO4**. The H···N distances are 3.300 Å (H36A···N12A) and 2.809 Å (H26A···N42A) with no established interaction. Therefore, the **FIO4** tennimide is in *open-closed* ("**oc**") state.

The aggregation in **FIO4** is aided by a disordered molecule of $CHCl_3$ having occupancy of 50%. It is interesting to note the existence of a weak C44A-F44A···Cl1A^{a} [F44A···Cl1A^{a} = 3.173(4) Å, 1-x,1-y,1-z] and a strong C34A-F34A···Cl1B^{b}

[F34A···Cl1B^b = 2.84(2) Å, b = x,-1+y,z] contacts. The crystal structure of **FIO4** relies mostly on C-H···F interactions such as C1A-H1A···F34A^c [C1A···F34A^c = 3.193(8) Å, c = x,1+y,z], and C-H···O interactions, the most prominent being C15-H15···O6^d [C15···O6^d = 3.456(4) Å, d = x,y-1,z], C45-H45···O4^e [C45···O4^e = 3.273(4) Å, e = x-1,y,z] and C45A-H45A···O7^f [C45A···O7^f = 3.270(5) Å, f = 1-x,-y,1-z] interactions. Another interaction is O1···Cl2A^g [3.058(5) Å, g = 1+x,-1+y,z]. The rest of interactions are weaker C-H/F/O···π contacts.

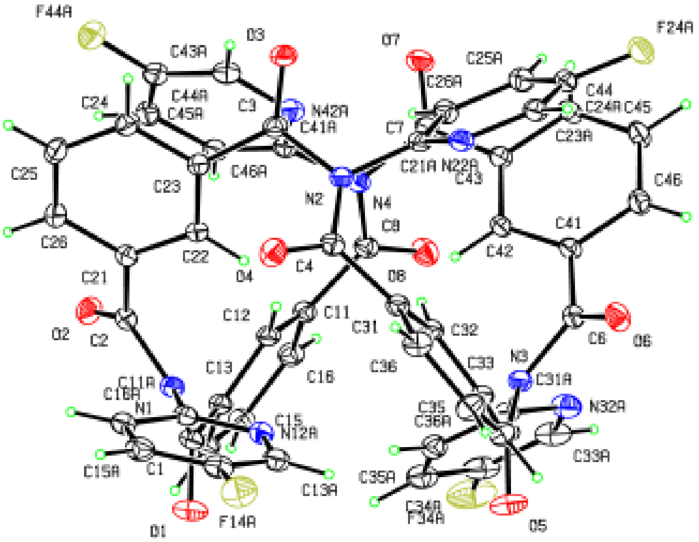

Fig. 88: A view of the **FIO4** molecule

7. ClIO3 and ClIO4 macrocycles

7.1. Synthesis and purification

Synthesis of the **ClIO3/4** was as described for **FIO3/4** (Section 6) using 2-amino-5-chloropyridine (1.2599 g, 9.8 mmol) as a functionalised 2-aminopyridine. The only difference is that a polymer precipitated and was removed by filtration, as in the **IO3/4** and **26IO3/4** macrocycles. The column chromatography was as for the **FIO3/4** purification (Section 6) yielding the **ClIO4** tennimide (197 mg, 7.7%, Rf = 0.595) and the **ClIO3** trezimide (120 mg, 4.73%, Rf = 0.393).

7.2. General and spectroscopic data

The **ClIO3** and **ClIO4** macrocycles have similar properties as the analogous fluoro macrocycles (Section 6); white, odourless crystalline solids with a shade of yellow colour. As compared to the fluoro analogues, the **ClIO3** and **ClIO4** macrocycles appear to be slightly less soluble in organic solvents.

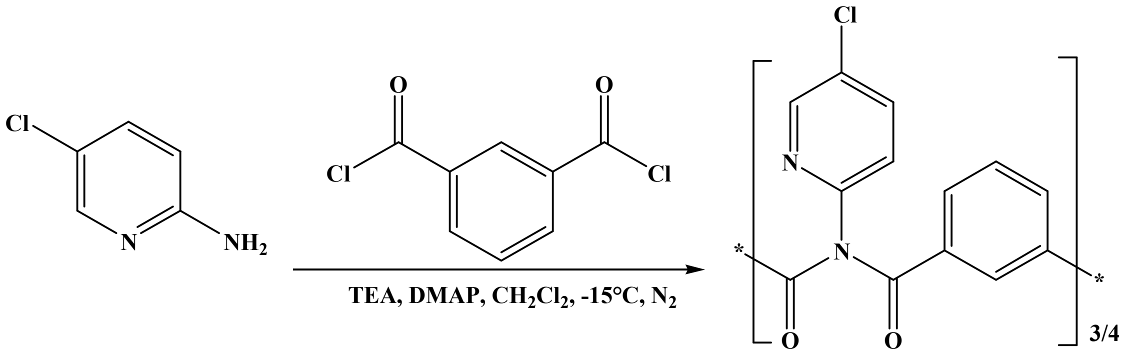

Scheme 49: Diagram of the **ClIO3/4** synthesis

The NMR and IR data (^{1}H- and ^{13}C-NMR data at 80°C are listed in Appendix I, Sections 4.7 and 4.8, whereas the spectra are provided in the ESI III, Sections 1.8 and 1.9) confirm the identity of the compounds and are very similar to the **FIO4/3** results .

As seen in **FIO3** the IR spectrum of **ClIO3** has weak to moderate bands between 2800 and 3100 cm^{-1} suggesting that the bulk **ClIO3** is a solvate.

7.3. Crystallographic data and discussion

Table **41** shows the basic crystallographic information for **ClIO3** and **ClIO4**. The **ClIO3** trezimide crystallises in orthorhombic crystal system, *Fdd2*. Since the crystal growth was not successful in common organic solvents, single crystals were grown from DMSO-*d*$_6$. Hence, the **ClIO3** was found to be a solvate with 1.9 equivalents of highly disordered DMSO-*d*$_6$ molecules and 1.2 equivalents of disordered waters (Fig. **89**).

Table 41: Selected crystallographic data^a for the **ClIO3** and **ClIO4** macrocycles†

	ClIO3	**ClIO4**
Chemical formula	$C_{42.8}H_{32.4}Cl_3N_6O_{9.3}S_{1.9}$	$C_{53}H_{32}Cl_4N_8O_9$
Crystal system, space group	Orthorhombic, *Fdd2*, (No. 43)	Orthorhombic, *Pccn*, (No. 56)
a, *b*, *c* (Å)	55.0537(10) 36.3597(5) 10.6018(2)	13.8337(1) 19.0181(1) 19.0737(1)
α, β, γ (°)	90, 90, 90	90, 90, 90
Z'	1	1
$R[F^2 > 2\sigma(F^2)]$, $wR(F^2)$, S	0.050, 0.143, 1.05	0.053, 0.186, 1.63

† Complete crystallographic, refinement and structural details are listed in the ESI III (Section 2.3). ^{a} Obtained with Cu *K*α radiation

In order to model the solvents the SQUEEZE software (part of PLATON) was successfully employed giving a solution with *R*-factor of 5%. The molecules of DMSO-d_6 (A, B, C and D) and water are found around the **ClIO3** molecule in three distinctive positions. One disordered molecule is in the macrocyclic *niche*, (partial occupancies of 0.75 [A] and 0.25 [B]). Another disordered molecule (C) is in proximity of the Cl1 atom with partial occupancy of 0.4, having an additional oxygen atom (O1C) with partial occupancy of 0.2. The third molecule of DMSO-d_6 (D) is in the proximity of the Cl3 atom (molecule D, partial occupancy of 0.5) together with two disordered molecules of water (partial occupancies of 0.8 [W1] and 0.4 [W2]).

The **ClIO3** molecule (Fig. **90**) has the P conformation with similar geometric parameters as seen in **IO3** and **FIO3**. The macromolecular *niche* hosts a disordered molecule of DMSO-d_6: the three isophthalic H···H distances (H12, H22, and H32) range from 2.56 to 2.81 Å. The carbonyl atoms O2, O3 and O4 form a triangle with O···O distances of 6.11 to 7.64 Å (Fig. **89**). The oxygen (O1A) of DMSO-d_6 (molecule A) forms a C12-H12···O1A [3.417(11) Å] hydrogen bond, anchoring the molecule of DMSO-d_6 in the macromolecular *niche*. The interplanar angle between the pyridine rings 1 and 3 (P1/P3) is 42.04°. The imide "**CO**···**CO**" twist dihedral angles are -100.34° (O1-C1···C2-O2), -95.92° (O3-C3···C4-O4) and 99.21° (O5-C5···C6-O6).

The molecules of DMSO-d_6 are important for the aggregation, forming a myriad of C-H···O/S interactions. However, the primary bonding is a very strong Cl2···O4^b [3.018(3) Å, *b* = x,y,1+z] halogen bond that connects **ClIO3** molecules into a 1-D column along the *c*-axis direction.

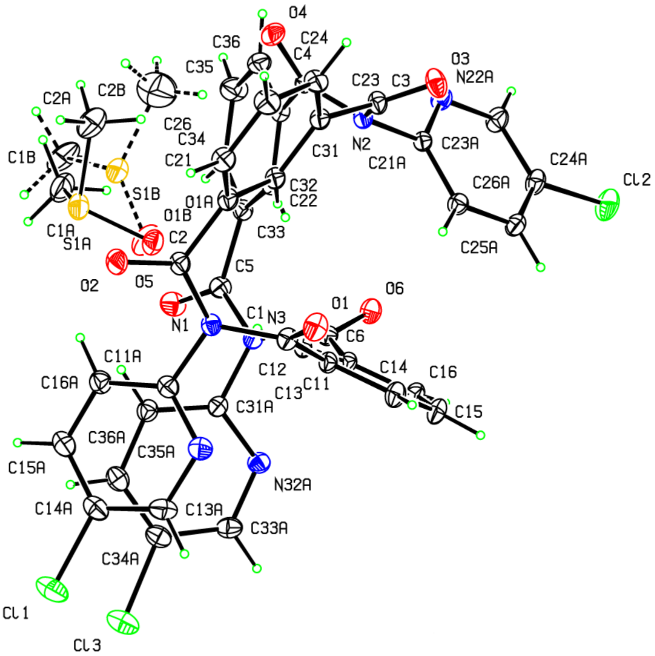

Fig. 89: A view of **ClIO3** with molecules of DMSO-d_6

The column is aided by the C2A-H2A3···O6^c [C2A···O6^c = 3.419(11) Å, *c* = -x,y,-1+z] interaction by which the disordered molecule of DMSO-d_6, placed in the macromolecular *niche,* links adjacent **ClIO3** molecules. Four 1-D columns are interconnected *via* Cl3···Cl3^a [3.165(3) Å, *a* = -x,-y,z], C25-H25···N32A^d [C25-H25···N32A^d = 3.334(7) Å, *d* = 1/4-x,1/4+y,-3/4+z], Cl1···N22A^e [3.277(4) Å, *e* = -1/4+x,1/4-y,-1/4+z] interactions and by disordered DMSO-d_6 (C and D) molecules *via* C33A-H33A···O1C^b [H33A···O1C^b = 2.56 Å] and C15A-H15A···O1C [H15A···O1C = 2.68 Å] contacts as well as by many other less important contacts.

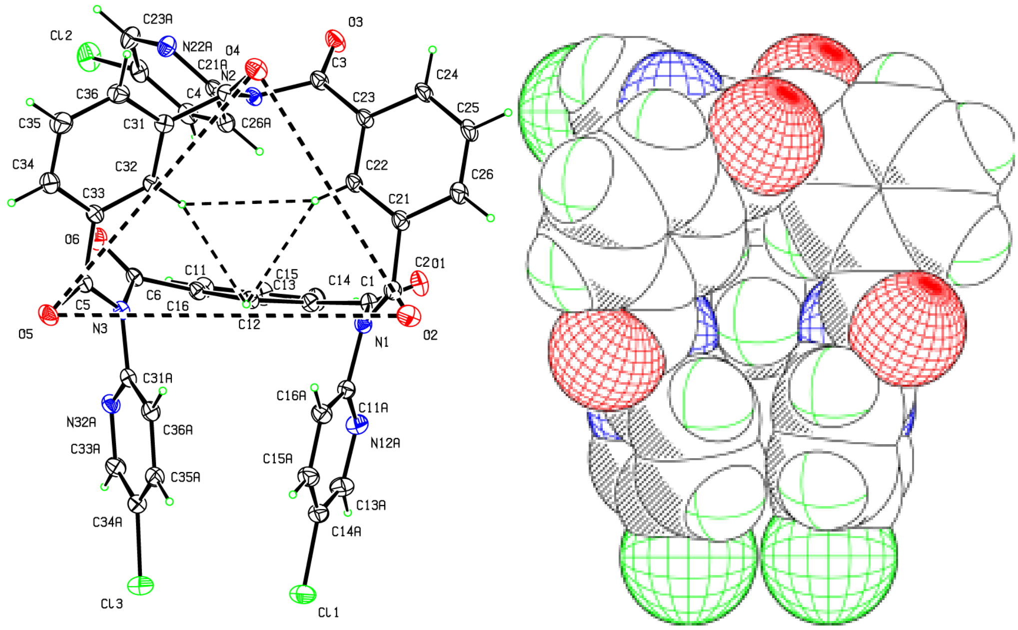

Fig. 90: ORTEP and CPK diagram of **ClIO3** the showing macromolecular *niche*

The **ClIO4** tennimide (Fig. **91**) was grown from a mixture of $CHCl_3$, MeOH and CH_2Cl_2. Hence, the **ClIO4** aggregates with a disordered molecule of either $CHCl_3$ or CH_2Cl_2. The **ClIO4** molecular structure is more symmetrical than the **FIO4**, similar to the **26IO4** structure (Section 5); it consists of two symmetrical halves related by symmetry code 3/2-x,1/2-y,z. The internal "**CO**···**CO**" twist dihedral angles are 102.22° (O1-C1···C2-O2) and -92.48° (O3-C3···C4-O4). The H···H distances of the intraannular cavity are 4.365 Å (H12···H12^a, *a* = 3/2-x,1/2-y,z) and 4.091 Å (H22···H22^a). The pyridinyl nitrogen atoms on both sides are in the ***anti*** (medial) conformation with a distance of 3.85 Å (N12A···N12A^a) and 4.3 Å (N12A···N12A^a). Therefore, both sides ("1" and "2") of the **ClIO4** molecules are in the *opened* ("**oo**") state exposing the intraannular cavity.

The primary aggregation in **ClIO4** crystal structure is formation of "pore-to-pore" columns along the *c*-axis direction *via* C13A-H13A···O3^b [C13A-H13A···O3^b =

3.375(4) Å, *b* = 3/2-x,y,-1/2+z] hydrogen bonds, aided by weaker C23A-H23A···O1^c [C23A···O1^c = 3.487(4) Å, *c* = 3/2-*x*,*y*,1/2+*z*.] interactions.

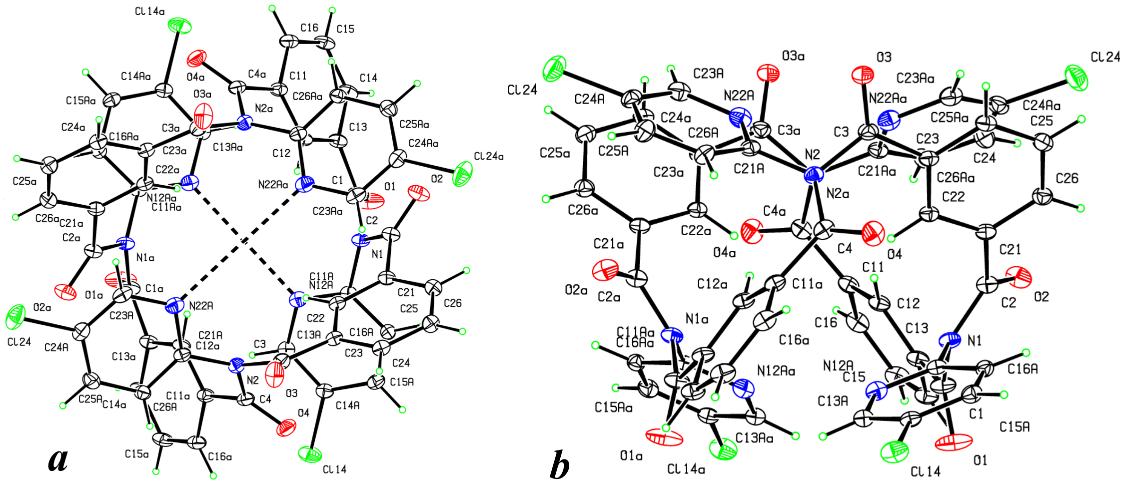

Fig. 91: A top-view (*a*) and a side-view (*b*) of **ClIO4**

Each column is surrounded by six other columns, interconnected *via* C15A-H15A···O4^d [C15A···O4^d = 3.209(3) Å, *d* = 2-x,1-y,-z] and C15-H15···O2^e [C15···O2^e = 3.461(3) Å, *e* = 2-*x*,1-*y*,-*z*] hydrogen bonds. The disordered molecule of solvent is placed between the columns and additionally interconnects them through several interactions such as O2···Cl2S^f [2.981(5) Å, *f* = 1+x,1/2-y,-1/2+z] and O1···Cl1S^f [2.992(6) Å] as well as C16A-H16A···Cl2S^b [C16A···Cl2S^b = 3.541(5) Å] interactions.

8. BrIO3 and BrIO4 macrocycles

8.1. Synthesis and purification

The synthesis and purification of **BrIO3/4** was as described for the **ClIO3/4** macrocycles (Section 7) with 2-amino-5-bromopyridine (1.6964 g). Chromatographic separation was accomplished as for the previous *halo*-substituted macrocycles, yielding **BrIO4** (177.37 mg, 6.0%, R*f* = 0.668) and **BrIO3** (212.12 mg, 7.14%, R*f* = 0. 455). The resulting material was reasonably pure and no additional preparative TLC was required.

8.2. General and spectroscopic data

Compared with the analogous fluoro and chloro derivatives, the solubility of the **BrIO3** and **BrIO4** analogues is generally similar (soluble in CH_2Cl_2, $CHCl_3$, alcohols, acetone, THF, ethyl acetate, poorly soluble in diethyl ether and *n*-hexane, insoluble in water) but lower; especially the **BrIO4** tennimide appeared to be significantly less soluble.

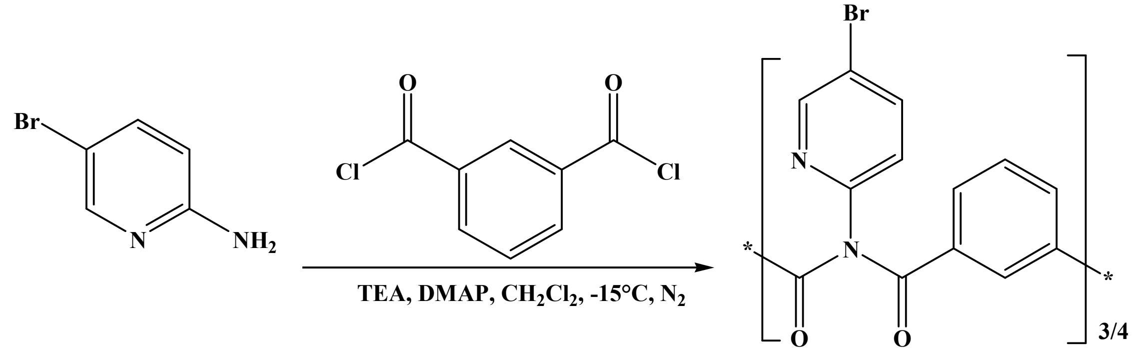

Scheme 50: General diagram of the **BrIO3/4** synthesis

However, this is as expected, since the starting material (2-amino-5-bromopyridine) was much less soluble in CH_2Cl_2 than the chloro and fluoro analogues. The NMR and IR results (^{1}H- and ^{13}C-NMR data at 80°C are listed in Appendix I, Sections 4.9 and 4.10, spectra are provided in the ESI III, Sections 1.10 and 1.11) have confirmed the identity of the compounds and are similar with those of **ClIO4** and **ClIO3**. The IR data show additional peaks around 3000 cm^{-1} suggesting that the bulk **BrIO4** is a solvate, but not **BrIO3**.

8.3. Crystallographic data and discussion

Table **42** presents the basic crystallographic data for the **BrIO3** and **BrIO4** macrocycles. The **BrIO3** trezimide (Fig. **92**) crystallises as a solvate in *P2₁/n*, with two **BrIO3** molecules in the asymmetric unit and one molecule of ethyl acetate. The ethyl acetate molecule is not disordered and engages in aggregation.

Table 42: Selected crystallographic data[a] for **BrIO3** and **BrIO4** †

	BrIO3	**BrIO4**
Chemical formula	$(C_{39}H_{21}Br_3N_6O_6)_2{\cdot}C_4H_8O_2$	$C_{52}H_{28}Br_4N_8O_8{\cdot}(CHCl_3)_{0.41}$
Crystal system,	Monoclinic	Orthorhombic
space group	$P2_1/n$, (No. 14)	*Pccn*, (No. 56)
a, *b*, *c* (Å)	10.9531(2) 65.7107(9) 11.2388(2)	14.0441(4) 19.1432(3) 19.1482(4)
α, β, γ (°)	90, 110.454(2), 90	90, 90, 90
Z'	2	1
$R[F^2 > 2\sigma(F^2)]$, $wR(F^2)$, *S*	0.0598, 0.1406, 1.14	0.0466, 0.1272, 1.04

† Complete crystallographic, refinement and structural details are listed in the ESI III (Section 2.4). [a] Obtained with Cu *K*α radiation.

However, the most interesting feature of **BrIO3** is presence of C-Br···O=C halogen bonds that contribute to crystal structure formation. The two **BrIO3** molecules (A and B) (Fig. **92**) are found to be in the **P** conformation as in most trezimides (except **26IO3**) and are geometrically similar. Since the Br2 atoms in both molecules are disordered, in the molecule A it was assigned as Br2A (0.5) and Br2C (0.5), while in the molecule B the Br2 atom exists as Br2B [0.61(2)] and Br2D [0.39(2)].

Similarly as with the molecules of DMSO-d_6 in the **ClIO3** structure, the molecule of ethyl acetate is located within the macromolecular *niche* of the **BrIO3** molecule A, anchored *via* C1S-H1S2···O4A [C1S···O4A = 3.302(10) Å] and C16A-H16A···O1S [C16A···O1S =3.332(10) Å] hydrogen bonds. The macromolecular *niches* of the A and B molecules are similar, but slightly different. The three H···H distances (H12, H22 and H32) in molecule A range from 2.58 to 2.93 Å, and from 2.53 to 2.96 Å in molecule B. The carbonyl atom (O2, O3 and O4) distances are 6.43 to 7.91 Å in molecule A and 6.26 to 8.10 Å in molecule B. The interplanar angles between the pyridine rings (1 and 3, molecule A) are 56.47(18)° and 43.31(22)° (4 and 6, molecule B). The imide "**CO**···**CO**" twist dihedral angles in molecule A are 110.00°, 87.69° and -99.83°, while in molecule B are -98.39°, -99.31° and 101.81°.

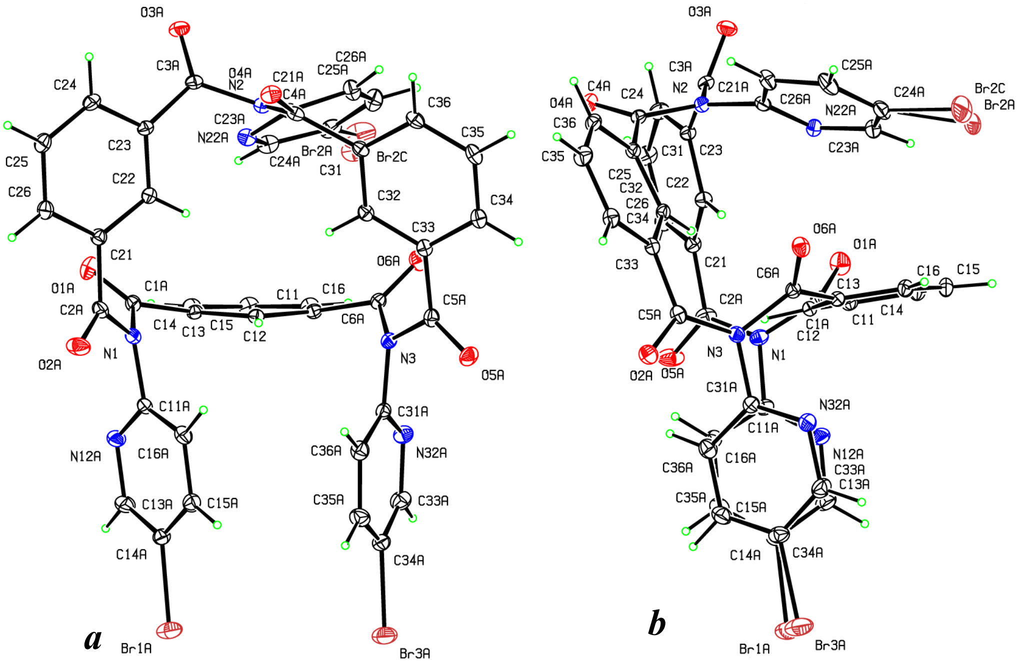

Fig. 92: ORTEP diagrams of **BrIO3** (view [*a*], and side-view [*b*], only molecule A is shown)

The aggregation in the **BrIO3** crystal structure mostly relies on strong C-H···O=C interactions, however the most interesting are C-Br···O=C halogen bonds such as C64A-Br3B···O6B^{a} [Br3B···O6B^{a} = 3.169(4) Å, *a* = 1/2+x,1/2-y,-1/2+z] and C56A-Br2B···O1B^{b} [Br2B···O1B^{b} = 3.312(6) Å, *b* = -1+x,y,z]. The first is especially strong since it is directional [C64A-Br3B···O6B^{a} angle is 160.20(18)°]. The C-Br···O=C halogen bonds have been explained in both experimental and theoretical studies.[233-236]

The strength of this bond comes from contact of a bromine σ-hole[233] having positive electrostatic potential with the electronegative carbonyl oxygen. However, the main interactions in the **BrIO3** crystal structure are numerous C-H···O=C interaction, such as C54-H54···O1A^{c} [C54···O1A^{c} = 3.144(7) Å, *c* = x,y,1+z], C35A-H35A···O5A^{d} [C35A···O5A^{d} = 3.219(8) Å, *d* = 1-x,-y,2-z], C15A-H15A···O5A^{d} [C15A···O5A^{d} = 3.423(8) Å] and C65A-H65A···O3B^{e} [C65A-H65A···O3B^{e} = 3.202(7) Å, *e* = x,y,-1+z] interactions. The solvent, ethyl acetate, does not engage significantly in the aggregation, in contrast to DMSO-d_6 or chlorinated solvent molecules in other macrocycles, apart from a C4S-H4S3···Br1A^{f} [C4S···Br1A^{f} = 3.654(10) Å, *f* = 1-*x*,-*y*,1-*z*] interaction. Other interactions are C-H···π contacts such as C24-H24···C5B [C24···C5B = 3.577(7) Å], C=O…π contacts such as C2B-O2B···C23A [O2B···C23A = 3.118(7) Å] and a myriad of C-Br…π contacts, the strongest being the C54A-Br2D···C63A^{g} [Br2D···C63A^{g} = 3.195(18) Å, *g* = -1/2+x,1/2-y,1/2+z] interaction.

The **BrIO4** tennimide (Fig. **93**) is essentially isomorphous with **ClIO4**, although the cell dimensions are slightly longer. It crystallises with a molecule of CHCl$_3$ that has a partial occupancy of 0.82 and is disordered about a rotation axis (1/2-*x*,1/2-*y*,*z*). As seen in **ClIO4** and **26IO4** the molecular structure of **BrIO4** is symmetric and consists of two equivalent halves about the rotation axis (1/2-*x*,1/2-*y*,*z*). However, and differently to **ClIO4,** the molecule of **BrIO4** has the “2” bromo-pyridinyl rings disordered about the Br24···N2 axis, with 63% of the ring being in ***syn*** (lateral, part A) and 37% being in ***anti*** (medial, part B) conformation. The cause of disorder is a partial hydrogen bond between the N22A atom and the solvent hydrogen atom, C1S-H1S···N22A^{a} [C1S-H1S···N22A^{a} = 3.43(2) Å, *a* = 1/2-x,1/2-y,z]. If this hydrogen bond is fully established, a very repulsive and unfavourable H26A···H26A^{a} (1.90 Å) contact emerges. Therefore, the disorder of the “2” bromo-pyridinyl rings is caused by a balance between the stabilising, favourable C1S-H1S···N22A^{a} hydrogen bond and destabilising steric clash H26A···H26A^{a}.

In general, the **BrIO4** molecule is symmetrical; the intraannular cavity distances (H···H) are 4.128 Å (H12···H12^{a}) and 4.352 Å (H22···H22^{a}). The internal “**CO**···**CO**” twist dihedral angles are 94.33° (O1-C1···C2-O2) and -103.78° (O3-C3···C4-O4). The bromo-pyridinyl ring “1” is in the ***syn*** conformation (lateral) with a H16···H16^{a} distance of 2.65 Å; hence the pore is closed. In total, the pores are 63% in “**cc**” state and 37% in the “**oc**” state.

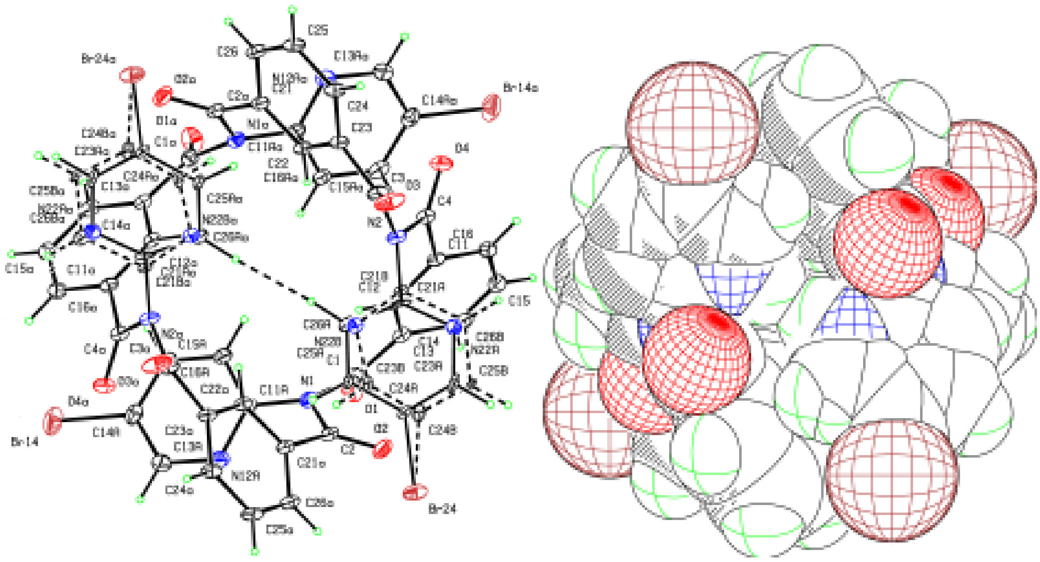

Fig. 93: ORTEP and CPK diagrams of the **BrIO4** tennimide

The aggregation in **BrIO4** is similar to the aggregation in **ClIO4**. The molecules are “pore-to-pore” lined up along the *c*-axis direction into a 1-D column *via* strong C25A-H25A···O1^{b} [C25A···O1^{b} = 3.329(9) Å, b = 1/2-x,y,1/2+z] hydrogen bonds. The columns are interconnected by a C25B-H25B···O2^{c} [C25B···O2^{c} = 3.09(2) Å, c = -x,1-y,-z] hydrogen bond and weaker C25-H25···O4^{d} [C25···O4^{d} = 3.514(5) Å, d = -x,-y,-z] and C23A-H23A···O2^{c} [C23A···O2^{c} = 3.373(16) Å] interactions. The aggregation is aided by the disordered $CHCl_3$ molecule through the partial C1S-H1S···N22A^{a} hydrogen bond, as well as by Cl3S···O4^{e} [3.077(5) Å, e = 1+x,y,z] and Cl2S···O3^{a} [3.126(8) Å] halogen bonds. In contrast with the **BrIO3** crystal structure, no C-Br···O=C halogen bond is present, although a weak C14A-Br14···Cl2S^{f} [Br14···Cl2S = 3.516(6) Å, f = 3/2-x,y,-1/2+z] halogen contact exists.

9. 26BrIO3 and 26BrIO4 macrocycles

9.1. Synthesis and purification

The **26BrIO3/4** macrocycles were synthesised (Scheme **51**) and purified using identical procedures as described for the **BrIO3/4** macrocycles (Section 8) with 2-amino-5-bromopyrimidine (1.7053 g, 9.8 mmol) instead of 2-amino-5-bromopyridine. The 2-amino-5-bromopyrimidine was quite insoluble in dry CH_2Cl_2, even upon heating, and was added into the reaction mixture in the form of a suspension. The result was **26BrIO3** (164.4 mg, 5.5%, R*f* = 0.472) and **26BrIO4** (110.0 mg, 3.67%, R*f* = 0.607).

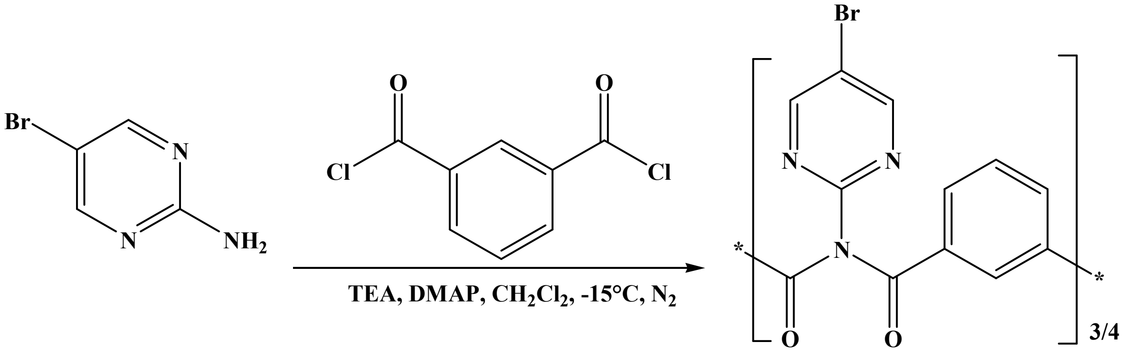

Scheme 51: General diagram of the **26BrIO3/4** synthesis

9.2. General and spectroscopic data

The **26BrIO3/4** macrocycles proved to be the most insoluble. However, **26BrIO3** was significantly more soluble than **26BrIO4** that proved to be very insoluble in most organic solvents, even in warm DMSO. Hence, the NMR characterisation of **26BrIO4** was accomplished in DMSO-d_6 at 140°C. Unfortunately, such a high temperature caused partial disintegration of the compound. The ^{1}H-NMR with variable temperature procedure was undertaken from the highest towards the lowest temperature. All the spectroscopic information including NMR and IR is listed in Appendix I (Sections 1.12 and 1.13) and the spectra are given in the ESI III (Sections 1.12 and 1.13).

9.3. Crystallographic data and discussion

Table **43** summarises the basic crystallographic data of the **26BrIO3/4** macrocycles. The **26BrIO3** trezimide (Fig. **94**) crystallises as a solvate with two molecules of CH_2Cl_2, one (molecule "1") and another disordered as molecule "2" (0.75) and "3" (0.25). The CH_2Cl_2 molecule plays important an role in the aggregation of the **26BrIO3** trezimide, in contrast with the disordered molecule.

The **26BrIO3** molecule (Fig. **94**) is in the typical P conformation, in contrast with the parent **26IO3** trezimide that was found in the R conformation (Section 5). The geometric parameters are as expected: the three H···H distances (H12, H22 and H32) range from 2.48 to 3.02 Å, the carbonyl atoms O···O distances (O2, O4 and O4) range from 6.44 to 8.12 Å, while the interplanar angle between the pyridine rings 1 and 3

(P1/P3) is 41.88(15)°.The imide "**CO**···**CO**" twists are -94.73° (O1-C1···C2-O2), -86.58° (O3-C3···C4-O4) and 95.55° (O5-C5···C6-O6).

Table 43: Selected crystallographic data for the **26BrIO3** and **26BrIO4** macrocycles†

	26BrIO3	**26BrIO4**
Chemical formula	$C_{36}H_{18}Br_3N_9O_6 \cdot (CH_2Cl_2)_2$	$(C_{48}H_{24}Br_4N_{12}O_8)_2 \cdot (CHCl_3)_{3.8} \cdot H_2O$
Crystal system, space group	Triclinic, $P\bar{1}$, (No. 2)	Monoclinic $P2_1/n$, (No. 14)
a, b, c (Å)	12.2390(5), 13.6149(5), 13.6447(5)	10.5779(3), 13.2805(3), 40.7855(13)
α, β, γ (°)	100.749(3), 99.990(3), 95.463(3)	90, 95.936(2), 90
Z'	1	1
$R[F^2 > 2\sigma(F^2)]$, $wR(F^2)$, S	0.0667, 0.1877, 1.02	0.0763, 0.2053, 1.03

† Complete crystallographic, refinement and structural details are listed in the ESI III (Section 2.4).

The most important and strongest interaction in the **26BrIO3** structure is a strong C14A-Br14···O4^a [Br14···O4^a = 2.982(3) Å, a = x,y,z-1] halogen bond.[237] As mentioned in the previous section, the strength comes from a direct contact [168.2(2)°] of a positive σ-hole with the electronegative carbonyl oxygen. This halogen bond links the **26BrIO3** molecules along the c-axis direction into a 1-D column.

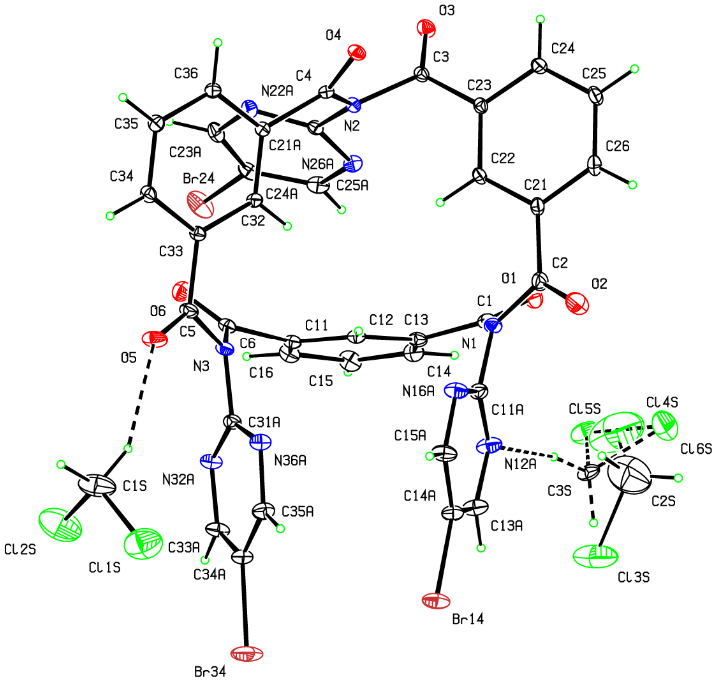

Fig. 94: An ORTEP diagram of **26BrIO3** and solvent molecules

Two columns are interconnected *via* the non-disordered CH_2Cl_2 molecule (“1”) by C1S-H1S1···N16A^b [C1S···N16A^b = 3.262(9) Å, *b* = -x,-y,1-z] and C1S-H1S2···O5 [C1S···O5 = 3.435(10) Å] interactions, aided by the C35-H35···O4^c [C35···O4^c = 3.427(5) Å, *c* = -x,-y,2-z] interaction. The C15-H15···O3^d [C15···O3^d = 3.235(7) Å, *d* = 1-x,1-y,2-z] and C14-H14···O3^d [C15···O3^d = 3.248(6) Å] interactions connect the column pairs into a 2-D sheet. Finally, a strong C25-H25···O4^e [C35···O4^e = 3.271(6) Å, *e* = 1-x,-y,2-z] interaction, with support of the C-Br···π interactions such as C24A-Br24···C34^f [Br24···C34^f = 3.395(5) Å, *f* = -x,1-y,2-z] and C24A-Br24···C35^f [Br24···C35^f= 3.362(5) Å] contacts aggregates 2-D sheets into a crystal structure.

The **26BrIO4** molecule (Fig. **95**) was grown from $CHCl_3$ and crystallised with two molecules of $CHCl_3$ and a molecule of H_2O. The first $CHCl_3$ molecule (“S”) is located in proximity of the O1 atom, shows no disorder but has partial occupancy of 0.9, while the second $CHCl_3$ molecule (“T”) is in proximity of the O6 carbonyl atom, shows disorder (1T = 0.7, 2T = 0.3), but has total occupancy of 1. The H_2O molecule is located beside the pore entrance close to the “B” bromo-pyrimidine ring and has partial occupancy of 0.5. The solvent molecules form many strong interactions with the **26BrIO4** molecules that largely contribute to crystal aggregation and stability, but are not crucial. However, the high quality of **26BrIO4** single crystals is due to the presence of solvent molecules in its crystal structure.

The **26BrIO4** molecule is less symmetrical, as in the **IO4** and **FIO4** crystal structures and the structural parameters are different for each segment. The imide **'CO···CO'** twist torsion angles are 86.66° (O1-C1···C2-O2), -101.25° (O3-C3···C4-O4), 101.95° (O5-C5···C6-O6) and -97.22° (O7-C7···C8-O8). The intraannular cavity (H···H) distances are 4.061 Å (H12···H32) and 4.199 Å (H22…H42^a). The distances between the medial pyrimidine nitrogen atoms are 4.467 Å (N12B···H12D) and 4.564 Å (H12A···H12C). Therefore, the pores are in the “**oo**” state.

Intermolecular interactions in the **26BrIO4** crystal structure, due to the presence of both $CHCl_3$ and H_2O molecules are numerous and include a myriad of C-H…O interactions, hydrogen and halogen bonds. The interactions formed by the solvent molecules are stabilising, but are not crucial for the aggregation, since the **26BrIO4** crystal structure mainly relies on interactions formed by the **26BrIO4** molecules themselves.

The major interactions are C13D-H13D···O5^a [C13D···O5^a = 3.197(8) Å, *a* = -1+x,y,z] and C34-H34···O3^b [C34···O3^b = 3.288(7) Å, *b* = 1+x,y,z] hydrogen bonds that aggregate the **26BrIO4** molecules along the *a*-axis direction in a “pore-to-pore” manner into a 1-D column. The columns are interconnected along the *b*-axis direction into a 2-D sheet parallel with (001) plane *via* a strong C14B-Br1B···N16A^c [Br1B···N16A^c = 3.028(4) Å, *c* = x,1+y,z] halogen bond.

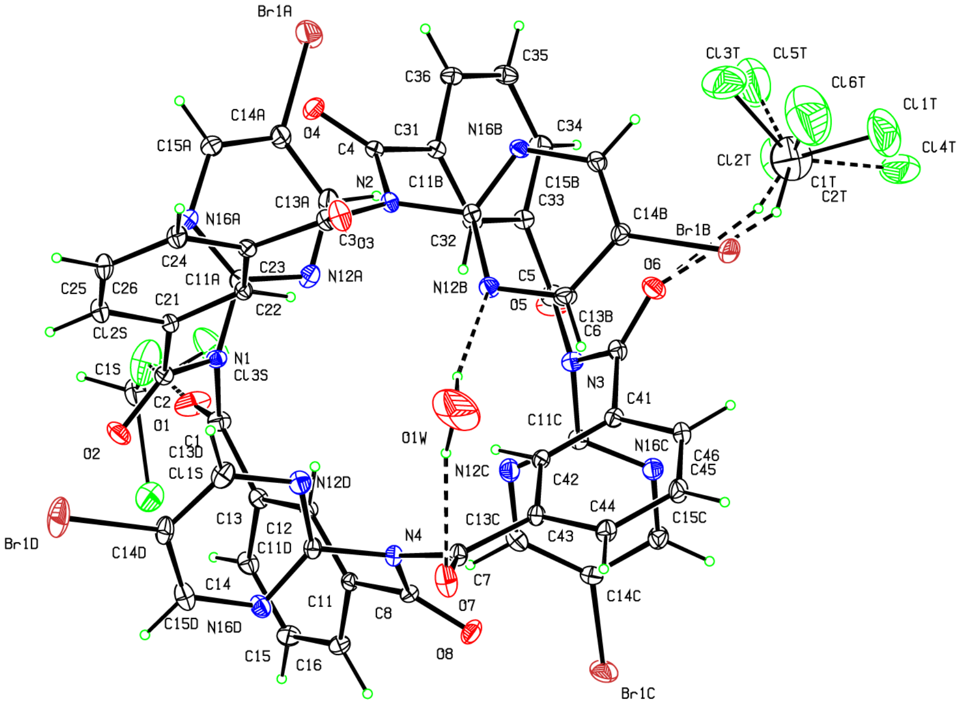

Fig. 95: A view of the **26BrIO4** tennimide

This halogen bond is similar to the C-Br···O=C bond found in the **BrIO3** and **26BrIO3** crystal structures. Two adjacent sheets are interconnected by C15A-H15A···O4^d [C15A···O4^d = 3.356(7) Å, *d* = -x,1-y,-z] hydrogen bonds, supported by weak C-Br···π contacts C14A-Br1A···C24^d [Br1A···C24^d = 3.482(6) Å]. Finally, the pairs of sheets aggregate into a 3-D crystal structure *via* lateral multiple interactions of the O8 carbonyl oxygen with the isophthalic ring "1" such as C14-H14···O8^e [C14···O8^e = 3.114(6) Å, *e* = 1/2-x,-1/2+y,1/2-z] and C15-H15···O8^e [C15···O8^e = 3.174(7) Å] interactions. The $CHCl_3$ and H_2O solvent molecules form an additional supporting network of interactions.

10. MIO4 macrocycle

10.1. Synthesis and purification

The **MIO4** tennimide (Figs. **97** and **97**) was synthesised using the standardised "4+4" method (Section 2.3), with 2-amino-5-methylpyridine (6-amino-3-picolinate, 1.0600 g, 9.8 mmol), (Scheme **52**). The crude product was purified by column chromatography eluting with a solvent blend of $CHCl_3$ and ethyl acetate (2:1). Although an additional compound was detected by TLC (possible trezimide, **MIO3**) only separation of the first fraction was successful (**MIO4**, 110 mg, 5%, R*f* = 0.270).

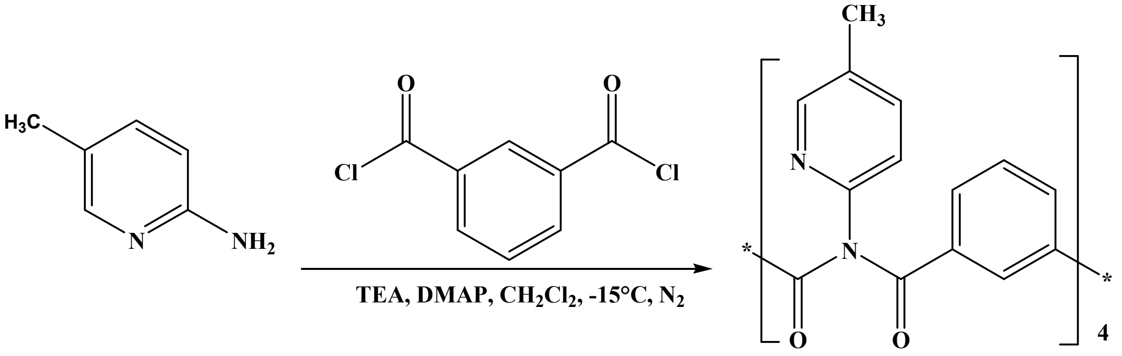

Scheme 52: General diagram of the **MIO4** synthesis

10.2. General and spectroscopic data

The **MIO4** tennimide is a white, moderately crystalline solid, readily soluble in chlorinated hydrocarbons ($CHCl_3$, CH_2Cl_2), ethyl acetate and MeOH, less soluble in diethyl ether and insoluble in water and *n*-hexane.

The ^{1}H-NMR experiments in DMSO-d_6 at 80°C (Appendix I, Section 4.13 and the ESI III, section 1.14) shows good resolving of the core tennimide proton peaks. The methyl peak is at 2 ppm, while the ^{13}C-NMR (same conditions) shows the methyl carbon at 17.25 ppm. No evidence of instability was detected by the NMR experiments, suggesting overall stability of the **MIO4** tennimide being comparable with the parent **IO4** tennimide.

10.3. Crystallographic data and discussion

The **MIO4** tennimide (Table **44**, Figs. **97** and **97**) crystallises as a solvate with one disordered molecule of CH_2Cl_2.

Table 44: Selected crystallographic data for the **MIO4**^{a} macrocycle†

Chemical formula	$C_{56}H_{40}N_8O_8.CH_2Cl_2$
Crystal system, space group	Orthorhombic, Pccn, (No. 56)
a, b, c (Å)	13.9556(3) 19.0850(4) 19.1230(3)
α, β, γ (°)	90, 90, 90
Z'	1
$R[F^2 > 2\sigma(F^2)], wR(F^2), S$	0.0666, 0.1628, 1.0

† Complete crystallographic, refinement and structural details are listed in the ESI III (Section 2.5). ^{a}Obtained with Cu $K\alpha$ radiation.

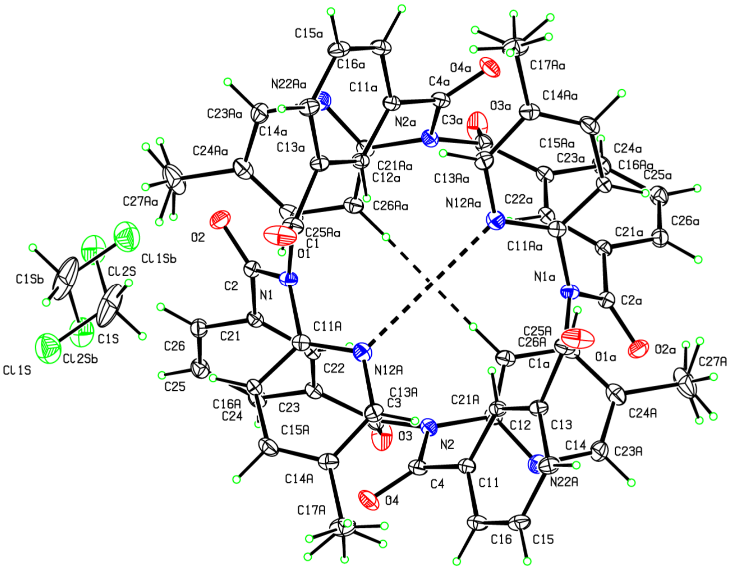

Fig. 96: An ORTEP diagram of the **MIO4** structure

Similar to the **26IO4**, **ClIO4** and **BrIO4** tennimides, the **MIO4** tennimide molecule is symmetrical and consists of two halves related by symmetry code 1/2-x,1/2-y,z. Dihedral angles of the internal imide '**CO···CO**' twist are 101.12° (O1-C1···C2-O2) and -92.15° (O3-C3···C4-O4). The intraannular cavity H···H distances are 4.361 Å (H12···H12^a, *a* = 1/2-x,1/2-y,z) and 4.152Å (H22···H22^a). Two pyridinyl rings (N12A, N12A^a) are in the medial conformation (**P-*anti***) with distance of 3.84 Å, while the two pyridinyl nitrogen on the opposite side (N22A) are in (**P-*syn***) lateral conformation, exposing the two H26A hydrogen atoms medially (H26A···H26A^a = 2.564 Å). Therefore, it seems that side 2 has wider pore than side 1 ("**oc**" state). The methyl moieties are disordered about the C-C axis by 60°.

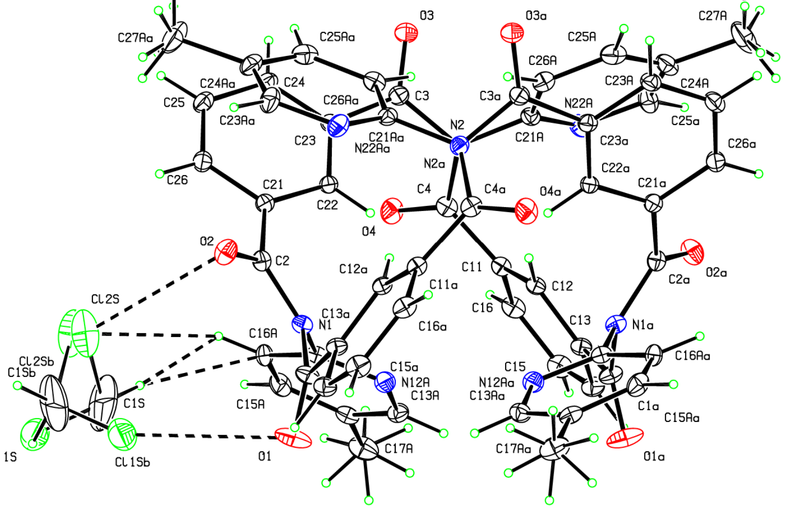

Fig. 97: An ORTEP diagram of **MIO4** viewed down *b*-axis

Aggregation in **MIO4** involves a disordered molecule of solvent (CH_2Cl_2). The **MIO4** and solvent molecule are connected by multiple contacts such as Cl2S···O2 [3.038(7) Å] and C16A-H16A···C1S [C16A···C1S = 3.51(2) Å], and arranged into a 1-D column along the *a*-axis *via* Cl1S···O1^b [3.135(6) Å, *b* = 3/2-x,1/2-y,z] and C16A-H16A···Cl2S^b [C16A···Cl2S^b = Å] interactions. Another interaction is C15A-H15A···O4^d [C15A···O4^d = 3.249(5) Å, *d* = 1-x,1-y,1-z] hydrogen bond that links the 1-D columns along the $(\bar{1}10)$ plane direction into a wavy 2-D sheet, parallel with the (101) plane.

11. EsIO3 and EsIO4 macrocycles

11.1. Synthesis and purification

The **EsIO3** and **EsIO4** molecules were synthesised using the standard "4+4" synthetic procedure described in Section 2.3 (Scheme **53**). The methyl-6-aminopyridine-3-carboxylate (1 g, 6.57 mmol), having a $COOCH_3$ moiety in the *para* position of the 2-AP ring, was used. Chromatographic purification and separation of the macrocycles was accomplished using $CHCl_3$/ethyl acetate (1:1) as an appropriate mobile phase system. The result was pure **EsIO3** (300 mg, 16%, R*f* = 0.60) and **EsIO4** (156.5 mg, 9%, R*f* = 0.33) macrocycles.

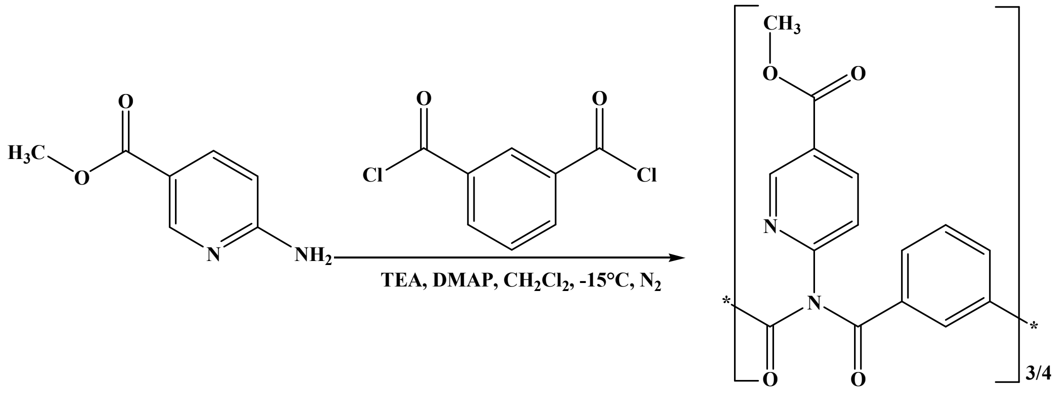

Scheme 53: Synthesis of the **EsIO3** and **EsIO4** macrocycles

11.2. General and spectroscopic data

The **EsIO3** and **EsIO4** macrocycles are white odourless substances, insoluble in water and readily soluble in most organic solvents apart from *n*-hexane and diethyl ether.

The NMR and IR spectral data are listed in Appendix I, sections 4.14 and 4.15, while the spectra are provided in the ESI III, Sections 1.15 and 1.16. Due to conformational rigidity in solution at the room temperature, the ^{1}H-NMR experiment of **EsIO4** at 20°C in $CDCl_3$ failed to show sufficiently resolved peaks and appropriate integration. The ^{13}C-NMR and HSQC experiments failed to show the C14 peak clearly as well as C1 in DEPT and DEPT-Q. The variable temperature ^{1}H-NMR in DMSO-d_6 raising the temperature from 20°C to 80°C improved the conformational interconversion rate and peaks were gradually resolved. Problems seen in $CDCl_3$ at 20°C were overcome with the corresponding experiments in DMSO-d_6 at 80°C. However, heating of **EsIO3** in DMSO-d_6 caused disintegration suggesting its relative instability. Therefore, variable temperature ^{1}H-NMR and the corresponding experiments in DMSO-d_6 at 80°C didn't prove useful. However, NMR experiments in $CDCl_3$ at 20°C gave good peak separation as well as coupling, suggesting conformational mobility in solvent.

The IR spectra show very strong bands around 1720-1690 cm^{-1} corresponding with both imide and ester carbonyl (C=O) stretches. The peaks at 1600-1400 cm^{-1} are associated with C-C and C-N vibrations in isophthalic and pyridinyl rings while the strong peaks in 1400-1200 cm^{-1} region belong to C-N and C-C vibrations and stretches in imide backbone.

11.3. Crystallographic data and discussion

Table **45** summarises the key crystallographic data for **EsIO3** and **EsIO4**. Crystals of **EsIO3** were obtained as poor-quality lathes from diethyl ether/*n*-hexane mixtures (though suitable for study by single crystal X-ray diffraction) whereas crystals of **EsIO4** were grown as long needles from $CHCl_3$/MeOH solutions.

Table **45**: Selected crystallographic data for **EsIO3** and **EsIO4** †

	EsIO3[a]	**EsIO4**
Chemical formula	$C_{45}H_{30}N_6O_{12}$	$C_{60}H_{40}N_8O_{16}$
Crystal system, space group	Triclinic, $P\bar{1}$ (No. 2)	Monoclinic, $P2_1/n$ (No.14)
a, *b*, *c* (Å)	16.3411(13), 16.5747(4), 17.4806(16)	10.6870(1), 22.4852(2), 22.6756(2)
α, β, γ (°)	87.273(5), 83.350(7), 89.825(4)	90, 101.721(1), 90
Z′	2	1
$R[F^2 > 2\sigma(F^2)]$, $wR(F^2)$, S	0.121, 0.352, 0.91	0.041, 0.120, 1.02

† Complete crystallographic, refinement and structural details are listed in the ESI III (Section 2.5). [a] Obtained with Cu Kα radiation.

The crystal structures of **EsIO3** (Fig. **98**) and **EsIO4** (Fig. **99**) show several unique features. The **EsIO3** structure ($Z' = 2$) crystallises in the triclinic system ($P\overline{1}$) with small but significant differences between the two molecules (molecule A is depicted) both in the *P* conformation. The three isophthalic H···H distances (H12, H22 and H32) range from 2.64 to 2.80 Å, whereas the carbonyl O…O distances (O2A, O3A and O5A) are from 5.76 to 7.92 Å (in molecule A, Fig. **98**).

Two pyridine groups at N1 and N3 adopt parallel orientations with their *ortho*-N ring atoms N12A, N32A positioned *syn* at a distance of 4.89 Å, and with their methyl carboxylates at contact distances. The imide "**CO**···**CO**" twists in molecule A are 95.45° (O1-C1···C2-O2), -111.30° (O3-C3···C4-O4) and -91.92° (O5-C5···C6-O6).

The **EsIO3** trezimide, as an acceptor rich system comprising nine 9 C=O, three pyridine and methoxy acceptor groups (neglecting the three tertiary N1-N3 atoms that are oriented towards the macrocycle *niche*); molecular aggregation is dominated by the cumulative effect of several weak C-H···O interactions such as C35A-H35A···O31A^a [C35A···O31A^a = 3.204(13) Å, *a* = 1-x,1-y,2-z] and C65A-H65A···O61A^b [C65A···O61A^b = 3.227(14) Å, *b* = 2-x,-y,-z] and C55-H55···O3A [C55···O3A = 3.377(14) Å].

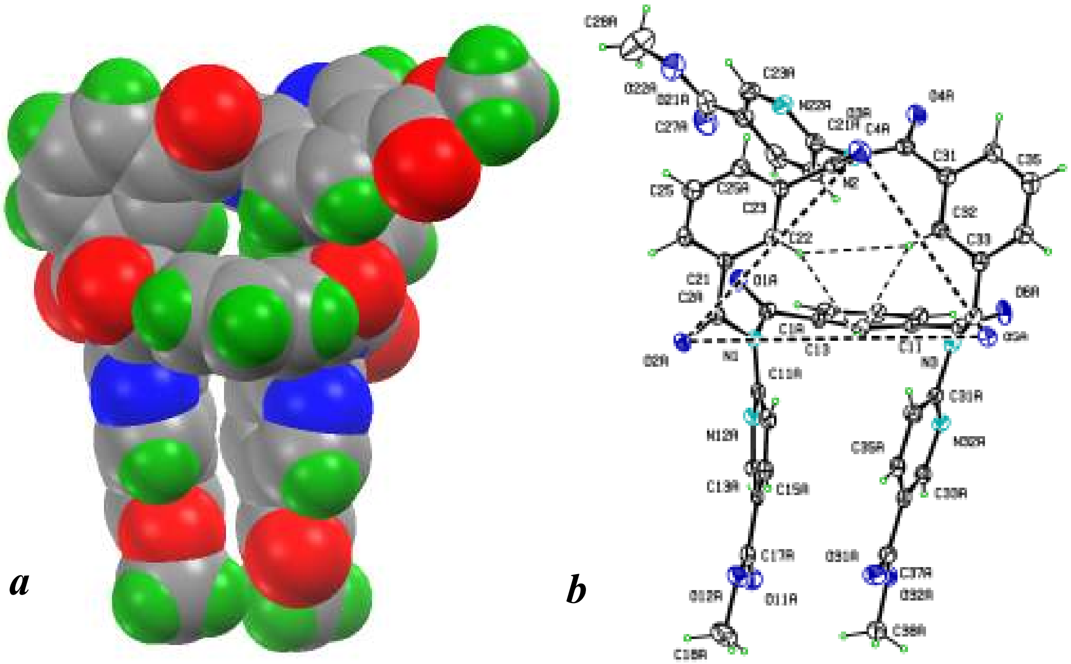

Fig. 98: *a*) space-filling and *b*) ORTEP diagrams of **EsIO3** (molecule A)

Crystals of **EsIO3** grow as very fragile thin lathes that diffracted very weakly.

The first attempt (Mo radiation) gave a unit cell and diffraction data only to 2.5 Å resolution, whereas a second data collection gave reflection data to a 1.5 Å resolution limit [data were collected to 0.94 Å with Cu Kα radiation, 1° ω-scans, the detector at 60mm and with three shells collected for 16s/48s/48s per frame]. This dataset was not sufficient to produce a structural solution (data redundancy were 1.7, F^2 = 2.1 and R_{int} = 0.16). Finally, on a third attempt, using Cu radiation at 40 kV/40 mA over 72 hours, reflection data were collected to a diffraction limit of 1.35 Å, with frames to 1.00 Å with 0.5° scans, shells collected for 24s/48s per frame and the detector at 60 mm (data redundancy = 1.8, F^2 = 4.3 and R_{int} = 0.083). This enabled a structural solution from a moderate direct methods attempt. It was apparent at an intermediate stage of refinement that there were considerable voids in the lattice amounting to 21% of the unit cell and containing solvent molecules of unknown composition and occupancy. The program SQUEEZE[169] was used and the *R*-factor dropped from 18% to 12% after using this program. The refinement proceeded without any problems or use of restraints to give a satisfactory **EsIO3** structure (with Z' = 2). There are small but significant differences between the two molecules A and B in the asymmetric unit. Crystals of **EsIO3** can be grown from acetonitrile (CH_3CN) solutions to produce colourless plates; however these decompose rapidly when handled (using several inert handling conditions) and we were able to observe diffraction and obtain a unit cell of one of these crystals: a =11.89(2) Å, b = 12.24(2) Å, c = 18.77(2) Å, α = 86.38(13)°, β = 78.71(14)°, γ = 65.49(16)°, Volume = 2439(7) Å ^{3} which is consistent with triclinic (Z' = 2) and an indeterminate solvent composition in the lattice voids.

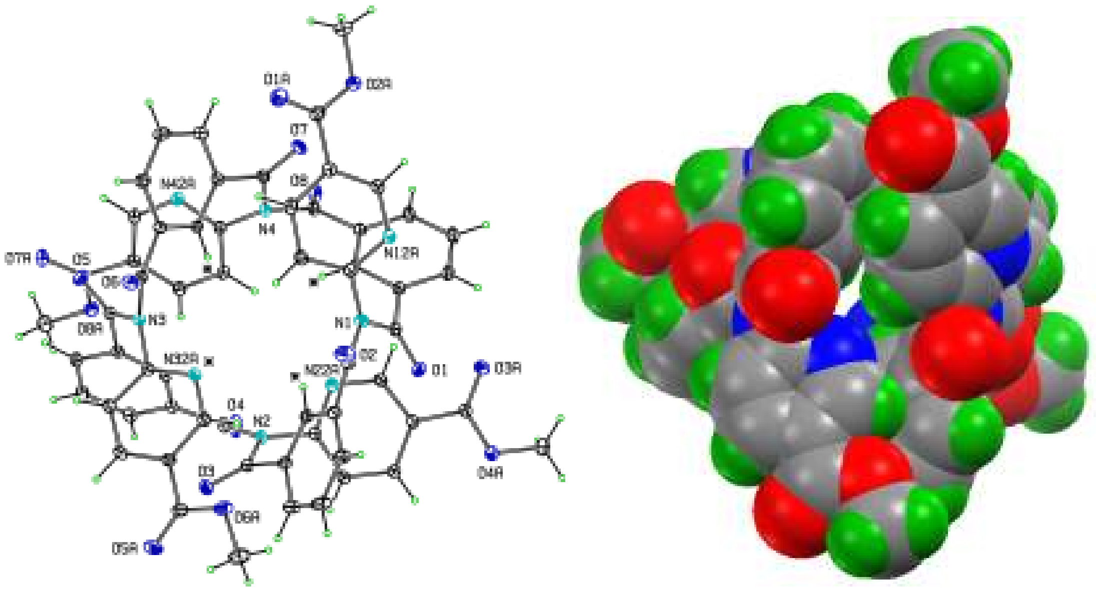

Fig. 99: *a*) ORTEP and *b*) space-filling diagrams of **EsIO4**

The **EsIO4** structure (Fig. **99**), contrary to most of the tennimides and trezimides was not isolated as solvate. The **EsIO4** macrocyclic cavity is compact with H···H intra-annular distances across the cavity of 4.13 and 4.18 Å. The internal amide "**CO**···**CO**" twist angles are 113.01° (O1-C1···C2-O2), -112.52° (O3-C3···C4-O4), 94.33° (O5-C5···C6-O6) and -88.90° (O7-C7···C8-O8). The pyridine rings are in the **P-*syn*** (lateral, rings "1" and "4") and **P-*anti*** (medial, rings "2" and "3") conformations as in **IO4**, with distances between the medial pyridine nitrogen and hydrogen atoms of 3.191 Å (N12A···H16A) and 3.308 Å (N22A···H46A), Hence, the pores are in "**cc**" state. The methyl ester $COOCH_3$ moieties are co-planar with the pyridine rings. Due to the presence of many carbonyl and methyl moieties the aggregation in the **EsIO4** crystal structure relies on a myriad of C-H···O interactions.

An overview of the tennimides and trezimides results is presented in the "Discussion and Conclusions".

DISCUSSION AND CONCLUSIONS

1. Benzamides and pyridinecarboxamides

The design of new materials continues unabated with a preoccupancy to maximise distinct physicochemical properties *e.g.* fluorescence, with thermal stability and melting point behaviour regarded as a relatively unimportant physical characteristic. Even though an enormous quantity of melting point data is available in the chemical literature and from databases, the prediction of melting points of organic compounds remains difficult though correlations of classes of organic compound have provided some distinct trends.[238]

The melting point results (Table **46**) for 4 × [3 × 3] series of **Mxx**, **NxxM**, **NxxF** and **Fxx** isomers demonstrate that trends previously noted in di-substituted benzenes[11, 239] for *meta*- < *ortho*- < *para*-substitution show similar patterns, but with distinct combinations producing both the highest and lowest melting point ranges. Melting point differences between 62 and 112°C are observed between the highest and lowest mp's in the four benzamide and pyridinecarboxamide isomer grids (depicted with ♦ and *). The results suggest that proper consideration has to be given to the thermal stability and behaviour of closely related aromatic isomers and especially if they are combinations of di-substituted aromatics (as found in many materials). While melting point behaviour depends on many factors the following trends are clear.

There is a decrease in average melting point from the symmetrical **pp** (*para-para*) compounds to the **F**/**Mmo** compounds of the **F**/**Mxx** series and two **NomF**/**M** derivatives in the **NxxM**/**F** series.

Table 46: Melting points[a] for **Mxx**, **NxxM**, **NxxF** and **Fxx** isomer grids.[c]

Mxx	**Mp**	**Mm**	**Mo**	**No**	**Nm**	**Np**	**NxxM**
p	181♦	106	129	105	148	*162*♦	**pM**
m	*128*	91	108	*50**	115	142	**mM**
o	105	79*	116	65	*107*	*125*	**oM**
o	120	77*	85	107	117	140♦	**oF**
m	*150*, 148	151	*89*	78*	122	132	**mF**
p	187♦	186	135	94	133	*135*	**pF**
Fxx[b]	**Fp**	**Fm**	**Fo**	**No**	**Nm**	**Np**	**NxxF**

[a] Average melting point range for all 36 compounds with highest denoted by ♦ and lowest by *.

These four **F**/**Mmo** and **NomF**/**M** compounds possess an *ortho*-pyridine C_5N ring N atom in combination with a C_6 aromatic ring *meta*-F/CH_3 substituent. The trend follows Carnelly's rule.[239] Of note is that the four compounds with **oo** substituents have higher melting points by *ca*. 20°C with a range of 65 to 116°C, (average of 93°C) as compared to the four **mo**/**om** derivatives 60 to 79°C (average of 71°C).

Comparisons between the **Fxx** (131°C mp average) and **Mxx** (116°C) series with **NxxF** (117°C) and **NxxM** (113°C) series demonstrates that the average melting points are remarkably similar (except for **Fxx**) although the ranges and order of melting point trends are unique within each of the four series.

The average *para*-isomer has a melting point of 137°C, the average *meta*-isomer 115°C and the average *ortho*-isomer 102°C and averaged over the 20 of 36 isomers which contain each *p*-/*m*-/*o*-substituent. This helps explain why the overall melting point trend is $p > m > o$ but not the observed substitution pattern whereby the **mo**/**om** combination have the lowest melting points.

Table **47** summarises the salient features of all thirty six **Mxx**, **Fxx**, **NxxM** and **NxxF** benzamide/pyridinecarboxamide isomer grids and the two additional polymorphs. The table contains crystallographic and solid state results (space group, *Z*/*Z'*, primary interaction, solid-state conformation), modelling data (*gas phase* conformation) and ^{1}H-NMR (amide N-H shift, CDCl$_3$).

Although benzamides and pyridinecarboxamides are not, strictly speaking, congeners, they have, sharing similar moieties, a high level of similarity (apart from the reversed amide bridge) that facilitates comparisons. The most common crystal system is monoclinic with 23 (61%) of all crystal structures (38) with most frequent space group $P2_1/c$ or $P2_1/n$ (10). The space group *Cc* is represented by (**NpoM**, **NpmF**, **NpoF**), $P2_1$ (**Fom_O** and **NomM**), *P*2/c (**NppM**) and *P*c (**Mop**). The triclinic system is also prevalent (10), with $P\bar{1}$ as the most frequent (9) and **Mpm** in *P1*. The triclinic system is more prevalent in **F**/**Mxx** benzamides than the **NxxF**/**M** pyridinecarboxamides and especially for **Mxx**. The orthorhombic crystal system is less abundant, with five structures in four space groups, $Pca2_1$ (**Mom**, **Fmm**) $P2_12_12_1$ (**NmoF**), *Pbca* (**NmoM**) and *Pbcn* (**Fpo**).

The primary hydrogen bonding in the crystal structures of all 38 isomers can be analysed in four groups. The most common interaction is the $_{\text{amide}}$N-H···N$_{\text{pyridine}}$ as *zig-zag* chains in 18 structures. This usually arises in molecules where the pyridine N atom is positioned as *para*- or *meta*- and while having N as *para*- makes the N-H···N convenient, isomers with *meta*-N usually have to have their **P** or **N** rings in a *meta*-stable ***anti*** conformation.

Table 47: Summary list of four isomer grids with selected structural features

Isomer	Space group	*Z*/*Z'*	Hydrogen bonding in solid state	Conformation (solid state)	Conformation (*gas phase*)	Match	Amide H shift (CDCl$_3$) /ppm
Mpp	$P2_1/n$	4/1	N-H···N	—	—	—[1]	8.30
Mmp	$P\bar{1}$	4/2	N-H···N	**M-*syn***	**M-*anti***	✗	8.25
Mop	Pc	4/2	N-H···N	**M-*syn*|M-*anti***	**M-*anti***	✗/✓[2]	8.23
Mpm	$P1$	4/4	N-H···O=C	**P-*syn***	**P-*syn***	✓	8.11
Mmm	$P\bar{1}$	4/2	N-H···N	**M-*anti*/P-*anti***	**M-*anti*/P-*syn***	✗	8.16
Mom	$Pca2_1$	4/1	N-H···N	**M-*anti*/P-*anti***	**M-*anti*/P-*syn***	✗	7.98
Mpo	$P\bar{1}$	2/1	(N-H···N)$_2$	**P-*syn***	**P-*syn***	✓	8.70
Mmo	$P2_1/c$	4/1	(N-H···N)$_2$	**M-*anti*/P-*syn***	**M-*anti*/P-*syn***	✓	8.78
Moo	$P\bar{1}$	2/1	(N-H···N)$_2$	**M-*syn*/P-*syn***	**M-*anti*/P-*syn***	✗	8.99
Fpp	$P2_1/c$	4/1	N-H···N	—	—	—[1]	8.01
Fmp	$P2_1/c$	4/1	N-H···N	**F-*anti***	**F-*anti***	✓	8.01
Fop	$P2_1/c$	4/1	N-H···N	**F-*syn***	**F-*syn***	✓	8.68
Fpm_O	$P2_1/n$	4/1	N-H···O=C	**P-*syn***	**P-*syn***	✓	8.56
Fpm_N	$P2_1/n$	4/1	N-H···N	**P-*anti***	**P-*syn***	✗	8.56
Fmm	$Pca2_1$	4/1	N-H···N	**F-*anti*/P-*anti***	**F-*anti*/P-*syn***	✗	8.45
Fom_O	$P2_1$	12/6	N-H···O=C	**F-*syn*/P-*syn*|*anti***	**F-*syn*/P-*syn***	✗/✓[3]	8.53
Fom_F	$P2_1/n$	4/1	N-H···O=C	**F-*syn*/P-*anti***	**F-*syn*/P-*syn***	✗	8.53
Fpo	$Pbcn$	8/1	(N-H···N)$_2$	**P-*syn***	**P-*syn***	✓	9.04
Fmo	$P\bar{1}$	4/2	(N-H···N)$_2$	**F-*anti*/P-*syn***	**F-*anti*/P-*syn***	✓	8.75
Foo	$P\bar{1}$	4/2	(N-H···N)$_2$	**F-*syn*/P-*syn***	**F-*syn*/P-*syn***	✓	9.03
NppM	$P2/c$	4/1	N-H···O=C	—	—	—[1]	8.00
NpmM	$P2_1/n$	4/1	N-H···N	**M-*anti***	**M-*anti***	✓	7.96
NpoM	Cc	4/1	N-H···O=C	**M-*syn***	**M-*syn***	✓	7.90
NmpM	$P2_1/c$	4/1	(N-H···N)cat[4]	**N-*syn***	**N-*syn***	✓	8.22
NmmM	$P\bar{1}$	4/2	N-H···N	**N-*anti*/M-*anti***	**N-*syn*/M-*anti***	✗	8.26
NmoM	$Pbca$	8/1	N-H···O=C	**N-*anti*/M-*anti***	**N-*syn*/M-*syn***	✗	7.81
NopM	$P2_1/c$	4/1	(N-H···N)$_i$	**N-*syn***	**N-*syn***	✓	9.90
NomM	$P2_1$	4/2	N-H···O=C	**N-*syn*/M-*anti***	**N-*syn*/M-*anti***	✓	9.94
NooM	$P2_1/c$	4/1	(N-H···N)$_i$	**N-*syn*/M-*syn***	**N-*syn*/M-*syn***	✓	10.03
NppF	$P\bar{1}$	4/2	N-H···O=C	—	—	—[1]	7.91
NpmF	Cc	4/1	N-H···N	**F-*syn***	**F-*anti***	✗	8.03
NpoF	Cc	4/1	N-H···N	**F-*anti*** [5]	**F-*syn***	✗	8.15
NmpF	$P\bar{1}$	8/4	(N-H···N)$_4$[6]	**N-*syn***	**N-*syn***	✓	8.44
NmmF	$P2_1/n$	4/1	N-H···N	**N-*anti*/ F-*anti***	**N-*syn*/F-*anti***	✗	8.75
NmoF	$P2_12_12_1$	4/1	N-H···N	**N-*syn*/F-syn**	**N-*syn*/F-syn**	✓	8.23
NopF	$P2_1/c$	4/1	(N-H···N)$_i$	**N-*syn***	**N-*syn***	✓	10.04
NomF	$P2_1/n$	8/2	(N-H···N)$_i$	**N-*syn*/F-*anti*** [7]	**N-*syn*/F-*anti***	✓	10.13
NooF	$P2_1/n$	4/1	(N-H···N)$_i$	**N-*syn*/F-syn**	**N-*syn*/F-syn**	✓	10.36

Notes: [1] — non-applicable (N/A); [2] **Mop** crystallises with two molecules in asymmetric unit, each with different **M**-ring conformation; [3] **Fom_O** polymorph has one of six molecules in the **F-*syn*/P-*anti*** conformation; [4] **NmpM** forms catemers; [5] minor component only in **F-*syn*** conformation; [6] **NmpF** forms tetramers; [7] with only 3% as **F-*syn*.**

This is the case with all **'XmmX'** compounds as well as the **Fpm_N** polymorph. Exceptions include the tetrameric **NmpF**, catemeric **NmpM**, mixed methyl/fluoro system **NmpFM**) and **NmoF**. A second group comprising 9 structures has the less common N-H···O=C hydrogen bonding with *C(4)* chains and is present in some **NxxF/M** isomers such as **NppF**, **NppM**, **NpoM**, and **NmoM**. The **Mpm** isomer and **Fpm_O** aggregate by N-H···O=C interactions having similar structures, as well as **Fom_O** (**P-*syn***) and **Fom_F** (**P-*anti***). The **NomM** structure forms N-H···O=C hydrogen bonds unexpectedly, however, the presence of an intramolecular $(N\text{-}H\cdots N)_i$ interaction hampers the stability of the N-H···O=C hydrogen bond. **NomM** has a low melting point (50°C) with difficulty in getting diffraction quality crystals. The third group comprises the six **Mxo** and **Fxo** isomers where the pyridine N atom is located *ortho* so that it has a unique role in dimer formation. Two N-H···N interactions form a $R^2_2(8)$ ring by the perfect match of **Mxo** molecular pairs, less so for **Fxo**. This is labelled in **Table 29** as $(N\text{-}H\cdots N)_2$ and is similar to the hydrogen bonded $(RCOOH)_2$ carboxylic acid dimers observed in centrosymmetric carboxylic acids. The **Mxo** and **Fxo** solid state and modelled conformations almost always match except for **Moo** where the **Mo** ring rotates in order to accomplish the important and short C-H···π(arene) interaction. The *ortho* nitrogen also causes an additional acidity of the amide hydrogen as can be observed in the ^{1}H-NMR as a small additional deshielding effect (higher values of chemical shifts). The fourth group comprises the **NoxM** and **NoxF** isomers. Here the pyridine nitrogen is positioned *ortho*-, however, due to the amide linkage reversal, the amide hydrogen is now directed towards the pyridine N atom, facilitating the formation of intramolecular N-H···N hydrogen bonding designated by $(N\text{-}H\cdots N)_i$. The weakening of the amide hydrogen is noted in additional deshielding in the ^{1}H-NMR ($CDCl_3$). In **NooF** the additional N-H···F interaction additionally deshields the amide hydrogen ensuring its chemical shift is the lowest for all isomers (at 10.36 ppm).

The type of hydrogen bonding can also be detected using IR spectroscopy. The presence of N-H···N interactions gives a diffuse pattern of weak peaks ranging from 3400 to 2800 cm^{-1} whereas N-H···O=C hydrogen bonding is noted by a sharp peak *ca.* 3300 cm^{-1}. The cyclic $(N\text{-}H\cdots N)_2$ hydrogen bonding has a typical complex of elevated and merged medium peaks ranging from 3100 to 2900 cm^{-1}. Finally, isomers with $(N\text{-}H\cdots N)_i$ hydrogen bonding have a very strong and sharp peak *ca.* 3330 cm^{-1}. It is interesting that in the unusual **NomM** isomer where both N-H···O=C and $(N\text{-}H\cdots N)_i$ hydrogen bonding occurs the relevant N-H (at 3286 cm^{-1}) and C=O (at 1700 cm^{-1}) stretching vibrations are positioned at lower wavenumbers.

2. Carbamates

The melting point results for the five carbamate isomer grids are presented in Table **48**. The most striking difference when comparing melting points of the benzamides and pyridinecarboxamides is the general increase of the carbamate melting points and the decrease of variability range. On average, the carbamate melting points are ~40° higher than the previous grids. The variability span is narrower and m.p. values are distributed more evenly. Nevertheless all **CmoR** compounds are found to have the lowest melting point in each isomer grid, especially **CmoM** and **CmoBr**, as found as monohydrates.

In the benzamides and pyridinecarboxamides, the melting point distribution approximately follows Carnelly's rule[239] while in the carbamate isomers the pattern seems to be less regular. The trends in melting points are different and the grids can be divided into the **CxxM/OMe** and **CxxX** grids.

Table 48: Melting points[a] for the **CxxR** isomer grids

CxxF	**pF**	**mF**	**oF**
Cp	185.3♦	162.9	169.0
Cm	167.4	152.3	136.5*
Co	179.9	-	-

CxxM	**pM**	**mM**	**oM**
Cp	165.7	134.6	131.0
Cm	170.6	113.0	84.0*
Co	191.8♦	143.8	162.3

CxxCl	**pCl**	**mCl**	**oCl**
Cp	199.6	197.5	170.3
Cm	175.4	171.2	125.6*
Co	199.8♦	175.4	146.1

CxxOMe	**pOMe**	**mOMe**	**oOMe**
Cp	156.7	134.7	191.8♦
Cm	162.5	142.5	109.6*
Co	184.7	145.4	159.8

CxxBr	**pBr**	**mBr**	**oBr**
Cp	206.4♦	193.4	168.5
Cm	170.4	154.7	86.9*
Co	196.6	175.5	-

[a] Average melting point range for all 42 carbamates with highest in a grid denoted by ♦ and lowest by *.

In the **CxxX** isomer grids the **Cm** compounds undoubtedly have lower melting points, while a decrease of melting points can be roughly estimated along the **pX** > **mX** > **oX** triad. The influence of the substituent can be roughly estimated as **Cl** > **Br** > **F**. It is interesting to note that the **CppX** and **CopX** isomers, both in the forms of *micro*-needles have very high melting points. Nevertheless, it seems that the **CxxX** isomers irregularly follow the Carnelly's rule,[239] while the **CmoX** compounds have the lowest melting points.

The melting points in the **CxxM/OMe** grids are lower that in the *halo*-carbamates, with **CxxM** being lowest among all carbamates, but there is a certain lack of regularity as seen in the benzamides or the *halo*-carbamates. It seems that in the **CxxM/OMe** grids (especially in **CxxOMe**) other factors different from symmetry are important. In **CmmOMe** it is clear that intramolecular forces involving methoxy moieties strongly influence the melting points, for the **CpoOMe** and **CooOMe** isomers melting points are unusually high.

Table **49** summarises the salient features of the **CxxR** isomer grids. The table, as in the previous section, contains crystallographic and solid state results (space group, *Z/Z'*, primary interaction, solid-state conformation), modelling data (*gas phase* conformation) and ^{1}H-NMR (amide N-H shift, $CDCl_3$). The **ComF**, **CooF** and **CooBr** data are excluded form the list.

Considering the fact that there are no *N*-(pyridyl)phenyl carbamates and only 29 basic phenylcarbamates structures available in CSD[8], the 25 carbamate structures from this study presents an important contribution to structural science.

The majority of the determined structures (*18*) were found to be in the monoclinic crystal system, while two structures (**CmpM** and **CmpOMe**) are orthorhombic ($P2_12_12_1$), one (**CmmOMe**) trigonal (*R3c*) and four are triclinic ($P\overline{1}$). The most prevalent space group is $P2_1/c$.

All crystal structures, except for the **CmoBr** and **CmoM** isomers, have some form of $_{\text{carbamate}}$N-H···N$_{\text{pyr}}$ hydrogen bonding as their strongest and primary aggregation interaction. In contrast to the benzamides and pyridinecarboxamides no primary interactions involving the carbamate N-H with carbonyl or O2 moiety were found. Most of these structures have chains forming N-H···N interactions (14) while the **CoxR** compounds (8) form cyclic (N-H···N)$_2$ hydrogen bonding dimers as seen in the **Fxo** and **Mxo** benzamides. Finally, the most remarkable carbamate structure is certainly the **CmmOMe** isomer with the disordered **mOMe** dihedral angle being in both plausible conformations. Apart from the (N-H···N)$_2$ dimerisation that is mandatory in *ortho*-pyridinyls, formation of trimers, tetramers and catemers rather than chains and columns is relatively rare but a peculiar phenomenon in the isomer grids.

Apart from the **CmmOMe** trimer, no disordered structures were found among the 25 carbamate structures. If the fact that conformational analysis showed **xR** (**R**-phenyl) moieties to be very flexible and the conformations readily interchangeable is taken into account, the absence of disorder, relatively widespread in benzamides and pyridinecarboxamides is indeed remarkable.

Table 49: Summary of the five carbamate isomer grids with selected structural features

Isomer	**Space group**	***Z/Z'***	**Hydrogen bonding in solid state**	**Conformation (solid state)**	**Conformation (*gas phase*)**	**Match**	**Amide H shift /ppm**[a]
CppM	$P2_1/c$	1	N-H···N	-	-	-	8.12
CpmM	$P2_1/n$	1	N-H···N	**M-*anti***	**M-*anti***	✓	8.17
CpoM	$P2_1/n$	2	N-H···N	-	-	-	8.02
CmpM	$P2_12_12_1$	1	N-H···N	**C-*syn***	**C-*syn***	✓	8.07
CmmM	-	-	-	-	**C-*syn*/ M-*anti***	-	8.27
CmoM	$P2_1/c$	1	(N-H···O-H)$_2$*	**C-*syn***	**C-*syn***	✓	8.19
CopM	$P2_1/c$	1	(N-H···N)$_2$	**C-*syn***	**C-*syn***	✓	10.47
ComM	-	-	-	-	**C-*syn***	-	10.52
CooM	$P2_1/n$	1	(N-H···N)$_2$	**C-*syn***	**C-*syn***	✓	10.42
CppOMe	$P2_1/n$	1	N-H···N	-	-	-	7.87
CpmOMe	$P2_1/c$	1	N-H···N	**O-*anti***	**O-*syn***	✗	8.20
CpoOMe	$P2_1/c$	1	N-H···N	-	-	-	8.14
CmpOMe	$P2_12_12_1$	1	N-H···N	**C-*syn***	**C-*syn***	✓	7.88
CmmOMe	$R3c$	1	(N-H···N)$_3$	**C-*syn*/O-*syn*|*anti***	**C-*syn*/O-*syn***	✓/✗	8.09
CmoOMe	-	-	-	-	**C-*syn***	-	7.81
CopOMe	$P2_1/c$	1	(N-H···N)$_2$	**C-*syn***	**C-*syn***	✓	9.57
ComOMe	$P\bar{1}$	1	(N-H···N)$_2$	**C-*syn*/ O-*syn***	**C-*syn*/O-*syn***	✓	10.40
CooOMe	$P\bar{1}$	1	(N-H···N)$_2$	**C-*syn***	**C-*syn***	✓	10.40
CppF	-	-	-	-	-	-	7.30
CpmF	-	-	-	-	**F-*anti***	-	8.10
CpoF	-	-	-	-	-	-	7.71
CmpF	Pc	2	N-H···N	**C-*anti***	**C-*syn***	✗	7.82
CmmF	Cc	1	N-H···N	**C-*anti*/ F-*anti***	**C-*syn*/F-*anti***	✗	8.10
CmoF	-	-	-	-	**C-*syn***	-	8.26
CopF	$P\bar{1}$	1	(N-H···N)$_2$*	**C-*syn***	**C-*syn***	✓	9.47
CppCl	-	-	-	-	-	-	7.98
CpmCl	$P2_1$	1	N-H···N	**Cl-*anti***	**Cl-*syn***	✗	7.14
CpoCl	-	-	-	-	-	-	8.04
CmpCl	Pc	2	N-H···N	**C-*anti***	**C-*syn***	✗	7.49
CmmCl	Cc	1	N-H···N	**C-*anti*/ Cl-*anti***	**C-*syn*/Cl-*syn***	✗	7.70
CmoCl	-	-	-	-	**C-*syn***	-	8.40
CopCl	$P\bar{1}$	1	(N-H···N)$_2$	**C-*syn***	**C-*syn***	✓	9.43
ComCl	-	-	-	-	**C-*syn*/Cl-*syn***	-	9.58
CooCl	-	-	-	-	**C-*syn***	-	10.5
CppBr	-	-	-	-	-	-	7.09
CpmBr	-	-	-	-	**Br-*syn***	-	7.27
CpoBr	-	-	-	-	-	-	8.22
CmpBr	Pc	2	N-H···N	**C-*anti***	**C-*syn***	✗	7.83
CmmBr	-	-	-	-	**C-*syn*/Br-*syn***	-	8.08
CmoBr	$P2_1/c$	1	(N-H···O-H)$_2$	**C-*syn***	**C-*syn***	✓	8.06
CopBr	$P2_1/n$	1	(N-H···N)$_2$	**C-*syn***	**C-*syn***	✓	9.36
ComBr	-	-	-	-	**C-*syn*/Br-*syn***	-	10.00

[a] in CDCl$_3$, * monohydrates

Alternatively, the flexibility of the **R**-phenyl rings along with steric blockage in the *ortho* isomers and relative instability may be the cause of low crystallinity and poor morphology for most of the *N*-(pyridyl)phenyl carbamates that prevented better growth of single crystals and completion of crystal structure determination. Secondly, most of the **CxxOMe** and **CxxM** isomer crystal structures have been solved, in contrast to the **CxxX** crystal structures. Therefore, there is a relative negative influence of halogen substituents on carbamate crystal growth; while the methyl and methoxy moieties readily engage into secondary interactions; the halogen substituents do not have that desirable feature especially if in the *ortho* and *meta* positions. Instead, the main N-H···N interactions are formed, contributing to one dimensional crystal growth, typically resulting in microscopic fragile needles.

The conformational analysis shows that conformations in 13 solid state molecular structures (52%) comply with corresponding calculated structures. The conformational match is perfect in the **CxxM** isomer grid, frequent in the **CxxOMe** isomer grid, but significantly less frequent in the **CxxX** isomer grids, mostly due to the ***syn***/***anti*** swops in the **CmxX** isomers. The occurrence of mismatch is approximately equally frequent in carbamates as for the benzamides and pyridinecarboxamides.

The relationship between the crystal structure of the carbamates and their IR spectra is well represented in so-called "N-H" region. This region spans from 3300 cm^{-1} to 2700 cm^{-1} where the N-H vibration bands usually appear. Generally, as shown for the benzamides and pyridinecarboxamides, isomers with similar bonding schemes usually have similar band patterns in the N-H region, and it might be considered as a useful predictor of primary bonding similarity. Moreover, if band patterns of two or more analogous isomers are almost identical, it might indicate the presence of isomorphism. It is best seen in the analogous isomers, such as the **CmpX** and **CopX** (except **CopBr**) isomers as well as between the **CmpM** and **CmpOMe** isomers where the band patterns in N-H region are almost identical, and structure determination by SXRD reveals isomorphism.

Next, the N-H regions of the analogous **CmmF** and **CmmCl** isomers are shown to be identical, while XRD revealed isostructurality. However, crystal structure determination of the bromine analogue **CmmBr** failed due to the poor single crystal quality. Nevertheless, the **CmmBr** isomer has a band pattern in N-H region identical to **CmmCl**, which clearly indicates that the **CmmBr** isomer is probably isostructural with the analogous **CmmCl** and **CmmF** isomers.

For the **CppR** compounds, the N-H region of **CppM** is similar to the **CppCl** and **CppBr** but different to **CxxOMe**, which is similar to **CppF**. Next, the similarity of the N-H region can be noticed between other analogous isomers, like the **CpoX** isomers as well as the **CpmX** isomers, suggesting the same or similar intermolecular bonding schemes.

The N-H regions of the trimeric **CmmOMe** (*R3c*) isomer and its methyl analogue **CmmM** are very similar, indicating possible trimeric hydrogen bonding in **CmmM**. Unfortunately, low quality of the **CmmM** single crystals hampered its structural determination. A similar situation is in the case of the analogous **ComOMe** and **ComM** isomers. Correlation of band patterns in the N-H region may result in predictions opposite to the expected ones, and/or lead to a surprising conclusion.

The N-H region band pattern of the **CmoOMe** isomer is similar to the **CmoCl** and **CmoF** isomers, but different from the **CmoM** isomer suggesting that hydrogen bonding in **CmoOMe** is, perhaps, not as seen in **CmoM** (hydrate complex in $P2_1/c$), but is more similar to the hydrogen bonding in the **ComX** isomers. However, in **CmoBr** a strong band is present at 3524 cm^{-1}, corresponding with presence of a water molecule as solvate. Surprisingly, this band is absent in **CmoM**, the only other carbamate that was found in the monohydrate form. This clearly suggests that bulk **ComBr** is monohydrate, while the **CmoM** is probably not**,** although the melting point assessment suggests the opposite. The **CmoM** monohydrate single crystal was perhaps formed only during the crystal growth process, possibly due to the moisture in solvent or environment. Hence, the crystal structure of the dry, bulk **CmoM** should be considered as it is still unknown.

All these cases, together with similar trends in benzamides and pyridinecarboxamides emphasise the importance of IR spectroscopy and its ability to predict primary hydrogen bonding in analogous isomers with acceptable confidence.

3. Tennimides and trezimide

The development of tennimides and trezimides presents an important entry point into a new class of compounds. Despite preliminary difficulties and the low yields, the “4+4” synthesis of tennimides and trezimides as described in standardized procedure 2 (Chapter III, section 2.3) proved to be reliable and reproducible, yielding satisfactory amounts of both tennimides and trezimides. However, it is evident that the synthesis of tennimides and trezimides bearing the **CN** functional group at the *para*-position (using 6-amino-3-pyridinecarbonitrile) or **25IO** macrocycles (using aminopyrazine) failed, even after several attempts. Possible explanations might be found in the relationship between electron-withdrawing/donating properties of a substituent or heteroatom and stability of the imide backbone. It was noticed (Chapter

III, Section 11.2) that the **EsIO3** trezimide is labile in a strong polar solvent such as DMSO, while most other macrocycles are stable, including the **EsIO4** tennimide. Table **50** shows common organic functional groups and their electron-withdrawing/donating properties relative to hydrogen as a reference. All the functional groups that were substituents in the attempted 2-aminopyridines are shown in red. It is indicative that stability of tennimides and trezimides *e.g.* imide backbone declines with a substituent having stronger electron-withdrawing property; **MIO4**, **IO3/4**, **26IO3/4**, **FIO3/4**, **ClIO3/4**, and **BrIO3/4** were stable, **EsIO3/4** less stable, while the synthesis of the supposed **CNIO3/4** macrocycles failed. One possible explanation is that a strong withdrawal of electrons as expected with **CN**, **NO_2** and **COOH/CH_3** moieties destabilises the imide "$(O{=}C)_2NR$" linker. Nevertheless, additional synthesis with other functional groups such as hydroxy, amino, methoxy, ethyl, nitro and trifluoromethyl are required in order to examine this hypothesis and establish a rule.

In general, both tennimides and trezimides are white, odourless crystalline compounds. The stability of tennimides seems to be better than the stability of trezimides as shown by the ^{1}H-NMR of **EsIO3/4** and by the experience with preparative TLC. Moreover, the variable temperature ^{1}H-NMR (ESI III, Section 1) indicates differences in stability and rigidity/flexibility between tennimides and trezimides, suggesting much better flexibility for trezimides since the trezimide peaks resolve at lower temperatures.

The stability of tennimides arises from the fact that a natural conformation of the imide linker $[(O{=}C)_2NR]$ is almost perfectly appropriate for the cyclisation into a tetramer, without need for significant conformational change. The imide linker naturally has a conformational twist of ≈ 90±15° that can be observed in all tennimides as successive '**CO···CO**' dihedral angle twist along the condensed macrocycles as +/–/+/–90±15°. Fig. **102** shows successful overlap of the **IO4** molecular structure with **DOXKOR**[163] with no significant deviation.

Table 50: Common organic functional groups (carbonyl oxygen as [O])

Electron donating groups (EDG)			Reference	Electron withdrawing groups (EDG)		
Strong	Moderate	Weak		Weak	Moderate	Strong
-O^-, -NR_2, -NH_2, -OH, -OR	-HN-C[O]-R -O-C[O]-R	-**R**, -Ph, -CH=CR_2	**H-**	-**F**, -**Cl**, -**Br**, -**I**	-C[O]H, -C[O]R, -**COOR**, -COOH	-CF_3, -**CN**, -SO_3H, -NH_3^+ -NO_2, -NR_3^+

Tennimide and trezimide stability

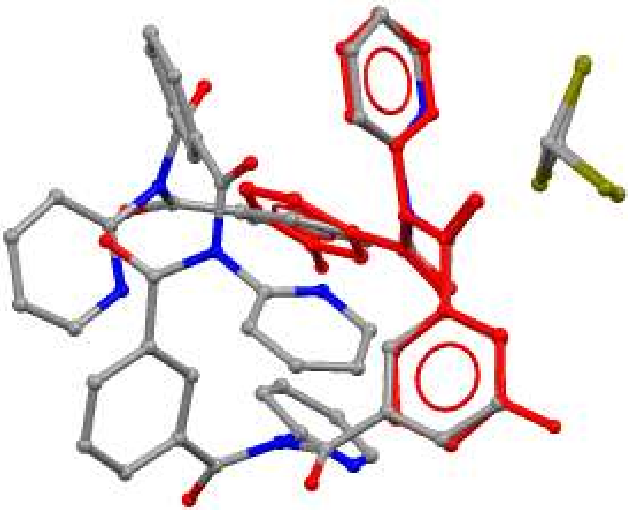

Fig. 100: Overlap of (**IO4**:$CDCl_3$) with **DOXKOR**[163] frame (**red**) highlights their close fit of 0.24 Å per non-H atom.

Finally, the *ab initio* modelling (Chapter III, Section 5.4) suggests that the imide linker geometry found in tennimides is almost equal to its expected *gas phase* global minimum. Therefore, tennimides can be formed and be stable since a natural conformation of the imide linker moiety matches a conformation required for the tetrameric cyclisation.

The same '**CO**···**CO**' twists dihedral angle of ≈90° can be observed in the P conformation of most of the trezimides, usually accompanied by considerable distortion about the isophthaloyl residue to accommodate cyclisation (in a wider range of 'CO···CO' torsion angles). As a result, trezimides are more flexible, although less stable. In general, trezimides tend to adopt the P conformation, as seen in all trezimides apart from **26IO3** where another, the R conformation was discovered. In the **R** conformation two 'CO···CO' twist dihedral angles are ≈90°, while the third is ≈60°. However, conformational change involves deviations of more than one torsion angle. Even though the rigorous high accuracy energy calculations (CBS-QB3)[171] for the P and R conformations were not undertaken (due to exceptional computational costs and limitations), the *ab initio* molecular modelling and overlays of experimental and hypothetical conformers (Chapter III, Section 5.4) suggest the plausibility of both conformations and possible existence of conformational polymorphs.

It is interesting to note that Evans and Gale[218] managed to isolate the **IF$_{4/5}$** tetramer, but not a hypothetical **IF$_{4/5}$** trimer that would be analogous to the **xIO3** trezimides. Apart from possible technical reasons, the inability of tetra- and pentafluoroaniline to form a trimer might be explained by possible unfavourable steric conditions due to the presence of fluorine atoms in positions 2 and 6 (*ortho*). Compared with the **xIO3** trezimides, such an **$IF_{4/5}$** trimer might not be sufficiently stable to be isolated using standard methods.

There is no significant difference between molecular structures of the tennimides, since they all have similar geometries. The observed differences of the solid state structure parameters, such as the imide "**CO**···**CO**" twist angles, intraannular H···H distances, *open* or *closed* cavity pores, **P-*syn***/**P-*anti*** conformational isomerism depend mostly on crystallisation conditions and solvent. Since both tennimides and trezimides are abundant in acceptors incorporation of a solvent during crystal growth is almost a rule, especially in the trezimides. However, IR data reveals that even some macrocycles (**BrIO3**) were found to be solvates, their bulk material is not in the form of a solvate. This indicates that incorporation of solvent is a result of a slow crystal growth, significantly improving quality of single crystals.

Tennimides derived from 2-AP show existence of **P-*syn***/**P-*anti*** conformational isomerism, while those derived from 26-APM don't. This fact can also be observed in variable temperature ^{1}H-NMR experiments (ESI III) where peaks of the **26IO4/3** macrocycles resolve at lower temperature compared to the **IO4/3** macrocycles. In general, ^{1}H-NMR experiments show that **P-*syn***/**P-*anti*** conformational isomerism contributes to their conformational variability. The solid state molecular and crystal structures reveal that different tennimides are found to have different **P-*syn***/**P-*anti*** conformational states; particular conformations are often the result of intermolecular interactions and influence of crystal solvent. However, no definitive conclusion can be drawn and additional conformational studies, both theoretical and experimental should be undertaken in order to examine which conformation (under which conditions) is more plausible. The main limitation for theoretical studies is the actual size of the tennimide molecules, since rigorous conformational study on a whole molecule would be computationally very costly. Therefore, experimental conformational studies might be more appropriate for these systems in order to answer the questions on both **P-*syn***/**P-*anti*** conformational isomerism and "*open-closed*" dynamics of the tennimide pore.

4. Conclusions

The study of isomer grids has facilitated an in-depth analysis of the solid-state and computational models for 61 compounds in nine isomer grids as well as being able to broaden the correlations when examining physicochemical trends *e.g.* melting points.

Of particular note is that *ca*. 35% of the molecules studied in benzamide/pyridinecarboxamide and *ca*. 50% in carbamate isomer grids have different conformations in the solid state and *ab initio* calculations in a three/four torsion angle system that can be reduced to two with the linker torsion angles (δ and γ) considered invariant due to multiple bonding character. This is of relevance especially in the modelling of more complex molecules in guest:host systems where the models and diffraction derived data may differ due to local minima (LM)/saddle points being mistaken for global minima (GM). This disparity varies little with basis set and incorporation of additional diffuse/polarisation functions. Analysis using solvation models typically drops the rotational barriers with increasing polarity which can facilitate interconversion between different conformations/rotamers. While solid state computational calculations will enable more comparisons and provide more answers in the future, the important message is that the use of solid state results for *ab initio* calculations and optimisations (from experiments) may only provide (optimise to) a local minimum (LM) and not the global minimum (GM) for the molecule in question. The calculation of theoretical data at local minima would only be valid for that particular local minimum and not a true representation of the molecule. It is critically important to analyse (scan) all relevant torsion angles (±180°) where possible and rank in order of importance so as to get a 'true' picture of the conformational preferences of the molecule under study. In the present isomer grids the **“XmmX”** compounds are examples where the solid-state and calculated results do not match. The combined analysis has proven extremely useful in rationalising the structural results and difficulty in obtaining quality crystals for particular isomers. Furthermore, the current study shows the potential of *ab initio* conformational analysis in *gas phase* in understanding polymorphism and disorder in the solid state. The most remarkable structures of the benzamides and pyridinecarboxamide, **Moo**, **NmpF**, **NmpM**, present a valuable addition to the area of crystallography and structural science.

Next, despite the difficulties, the study has faced the challenge of structurally unexplored and demanding carbamates *i.e.* phenyl-*N*-pyridinyl-carbamates crystal structures, adding 25 new structures to CSD, and upgrading structural knowledge on carbamates. The most remarkable structure, **CmmOMe** presents an important and rare example of small drug-like molecule aggregation as a hydrogen bonded trimer.[206-210] Correlation of physical-chemical properties showed the importance of position of a substituent, rather than its nature. IR spectroscopy proved useful due to its ability to predict primary hydrogen bonding in analogous isomers with acceptable confidence, and to challenge the generalisation of structural data.

The development of tennimides and trezimides as new macrocycles based on an imide backbone, presents an important entry point into a potentially fruitful area of rich chemistry. A series of new macrocycles including **IO3/4** and **26IO3/4** and their derivatives (**F**, **Cl**, **Br**, **CH_3**, and **COOCH3**) has been synthesised, thoroughly characterised by IR and NMR spectroscopy and their molecular and crystal structures have been fully determined and analysed. Although based on a previously reported prototype,[218] development of tennimides as stable and rigid molecules presents an important breakthrough. Furthermore, discovery of trezimides is especially important since no analogous trimeric imide macrocycle has been reported.

Synthesis of tennimides and trezimides has been accomplished using a one-step synthetic strategy, while the purification relies on simple organic and chromatographic methods. The described standardised “4+4” synthetic and purification procedure proved to be reproducible over a range of derivatives and presents a firm basis for synthesis of analogous macrocycles using a range of 2-AP/26-APM derivatives or other acyl dichlorides such as pyridine-2,6-dicarbonyl dichloride. Future studies on stability over a range of conditions, as well as synthesis of additional derivatives ($-NH_2$, -OH, -OR, -COOH, $-CH=CR_2$), theoretical and spectroscopic studies have yet to answer opened questions.

Tennimides and trezimides proved to be rigid and stable compounds with similar macrocyclic geometry. Their stability, especially stability of bromo derivatives, will allow further derivatisation and utilisation *via* simple substitution reactions expanding the area. Addition of hydrophilic moieties such as amino or carboxyl will increase solubility in water and open possibilities for future biological and pharmacological studies, especially targeting K_v channels or other biological targets with new molecules based on tennimide or trezimide scaffolds. In particular, geometry and symmetry of these macrocycles, as well as stability and rigidity of tennimides suggest possible roles in medicinal chemistry. Another direction of investigations might be organometallic derivatisation and utilisation in the area of supramolecular chemistry and molecular machines.

REFERENCES

1 A. G. Orpen, *Chem. Soc. Rev.*, 1993, **22**, 191-197.

2 F. H. Allen and W. D. S. Motherwell, *Acta Crystallogr. Sect. B-Struct. Sci.*, 2002, **B58**, 407-422.

3 G. M. Sheldrick, *Acta Crystallogr. Sect. A*, 2008, **A64**, 112-122.

4 G. G. Hall, *Chem. Soc. Rev.*, 1973, **2**, 21-28.

5 J. Gerratt, D. L. Cooper, P. B. Karadakov and M. Raimondi, *Chem. Soc. Rev.*, 1997, **26**, 87-100.

6 W. Thiel, *Adv. Chem. Phys.*, 1996, **93**, 703-757.

7 M. Zimmer, *Chem. Rev.*, 1995, **95**, 2629-2649.

8 F. H. Allen, *Acta Crystallogr. Sect. B-Struct. Sci.*, 2002, **B58**, 380-388.

9 T. Gelbrich, M. B. Hursthouse and T. L. Threlfall, *Acta Crystallogr. Sect. B-Struct. Sci.*, 2007, **B63**, 621-632.

10 R. Boese, M. T. Kirchner, J. D. Dunitz, G. Filippini and A. Gavezzotti, *Helv. Chim. Acta*, 2001, **84**, 1561-1577.

11 Y. L. Slovokhotov, I. S. Neretin and J. A. K. Howard, *New J. Chem.*, 2004, **28**, 967-979.

12 T. Gelbrich and M. B. Hursthouse, *CrystEngComm*, 2006, **8**, 448-460.

13 D. Chopra and T. N. G. Row, *CrystEngComm*, 2008, **10**, 54-67.

14 C. Capacci-Daniel, S. Dehghan, V. M. Wurster, J. A. Basile, R. Hiremath, A. A. Sarjeant and J. A. Swift, *CrystEngComm*, 2008, **10**, 1875-1880.

15 A. Abad, C. Agullo, A. C. Cunat, C. Vilanova and M. C. R. de Arellano, *Cryst. Growth Des.*, 2006, **6**, 46-57.

16 G. Tuchalski, F. Emmerling, K. Groeger, A. Haensicke, T. Nagel and G. Reck, *J. Mol. Struct.*, 2006, **800**, 28-44.

17 C. M. Coleman, J. M. D. MacElroy, J. F. Gallagher and D. F. O'Shea, *J. Comb. Chem.*, 2002, **4**, 87-93.

18 E. A. Collier, R. J. Davey, S. N. Black and R. J. Roberts, *Acta Crystallogr. Sect. B-Struct. Sci.*, 2006, **B62**, 498-505.

19 K. Kato, M. Sugahara, N. Tohnai, K. Sada and M. Miyata, *Cryst. Growth Des.*, 2004, **4**, 263-272.

20 V. R. Thalladi, M. Nusse and R. Boese, *J. Am. Chem. Soc.*, 2000, **122**, 9227-9236.

21 S. M. S. V. Wardell, M. V. N. de Souza, J. L. Wardell, J. N. Low and C. Glidewell, *Acta Crystallogr. Sect. B-Struct. Sci.*, 2007, **B63**, 879-895.

22 F. H. Allen, S. E. Harris and R. Taylor, *J. Comput. Aided Mol. Des.*, 1996, **10**, 247-254.

23 A. D. McNaught and A. Wilkinson, *IUPAC. Compendium of Chemical Terminology*, Blackwell Scientific Publications, Oxford, 1997.

24 K. A. Brameld, B. Kuhn, D. C. Reuter and M. Stahl, *J. Chem. Inf. Model.*, 2008, **48**, 1-24.

25 M. J. Frisch, G. W. Trucks, H. B. Schlegel, G. E. Scuseria, M. A. Robb, J. R. Cheeseman, G. Scalmani, V. Barone, B. Mennucci, G. A. Petersson, H. Nakatsuji, M. Caricato, X. Li, H. P. Hratchian, A. F. Izmaylov, J. Bloino, G. Zheng, J. L. Sonnenberg, M. Hada, M. Ehara, K. Toyota, R. Fukuda, J. Hasegawa, M. Ishida, T. Nakajima, Y. Honda, O. Kitao, H. Nakai, T. Vreven, J. A. Montgomery Jr., J. E. Peralta, F. Ogliaro, M. Bearpark, J. J. Heyd, E. Brothers, K. N. Kudin, V. N. Staroverov, T. Keith, R. Kobayashi, J. Normand, K. Raghavachari, A. Rendell, J. C. Burant, S. S. Iyengar, J. Tomasi, M. Cossi, N. Rega, J. M. Millam, M. Klene, J. E. Knox, J. B. Cross, V. Bakken, C. Adamo, J. Jaramillo, R. Gomperts, R. E. Stratmann, O. Yazyev, A. J. Austin, R. Cammi, C. Pomelli, J. W. Ochterski, R. L. Martin, K. Morokuma, V. G. Zakrzewski, G. A. Voth, P. Salvador, J. J. Dannenberg, S. Dapprich, A. D. Daniels, O. Farkas, J. B. Foresman, J. V. Ortiz, J. Cioslowski and D. J. Fox, *Gaussian 09*, *Revision B. 01,* Gaussian, Inc., Wallingford CT, 2010.

26 W. H. Moos, C. R. Hurt and G. A. Morales, *Mol. Divers.*, 2009, **13**, 241-245.

27 J. Elemans, E. J. A. Bijsterveld, A. E. Rowan and R. J. M. Nolte, *Eur. J. Org. Chem.*, 2007, **5**, 751-757.

28 R. B. Moffett, A. Robert and L. L. Skaletzky, *J. Med. Chem.*, 1971, **14**, 963-968.

29 S. W. Miao, J. M. Bao, M. L. Garcia, J. L. Goulet, X. F. Hong, G. J. Kaczorowski, F. Kayser, G. C. Koo, A. Kotliar, W. A. Schmalhofer, K. Shah, P. J. Sinclair, R. S. Slaughter, M. S. Springer, M. J. Staruch, N. N. Tsou, F. Wong, W. H. Parsons and K. M. Rupprecht, *Bioorg. Med. Chem. Lett.*, 2003, **13**, 1161-1164.

30 J. M. McBride, D. T. Smith, S. R. Byrn, R. B. Borgens and R. Shi, *Neuroscience*, 2007, **148**, 44-52.

31 M. C. Jetter, J. J. McNally, M. A. Youngman, M. E. McDonnell, A. E. Dubin, N. Nasser, S. P. Zhang, E. E. Codd, R. W. Colburn, D. R. Stone, M. R. Brandt, C. M. Flores and S. L. Dax, *Bioorg. Med. Chem. Lett.*, 2008, **18**, 2730-2734.

32 Z. Gao, T. Zhang, M. Wu, Q. Xiong, H. Sun, Y. Zhang, L. Zu, W. Wang and M. Li, *J. Biol. Chem.*, 2010, **285**, 28322-28332.

33 R. Berger, G. Resnati, P. Metrangolo, E. Weber and J. Hulliger, *Chem. Soc. Rev.*, 2011, **40**, 3496-3508.

34 Dalfampridine, US Food and Drug Administration, **2011**.

35 M. Yoshikawa, K. Motoshima, K. Fujimoto, A. Tai, H. Kakuta and K. Sasaki, *Bioorg. Med. Chem.*, 2008, **16**, 6027-6033.

36 P. M. Harrington, *Heterocycles*, 1993, **35**, 683-687.

37 R. U. Kadam, J. Tavares, V. M. Kiran, A. Cordeiro, A. Ouaissi and N. Roy, *Chem. Biol. Drug Des.*, 2008, **71**, 501-506.

38 J. Y. Qi, Q. Y. Yang, S. S. Chan, Z. Y. Zhou and A. S. C. Chan, *Acta Crystallogr. Sect C-Cryst. Struct. Commun.*, 2004, **C60**, M210-M211.

39 C. R. Wilson and O. Q. Munro, *Acta Crystallogr. Sect. C-Cryst. Struct. Commun.*, 2010, **C66**, 513-516.

40 S. H. van Rijt, A. J. Hebden, T. Amaresekera, R. J. Deeth, G. J. Clarkson, S. Parsons, P. C. McGowan and P. J. Sadler, *J. Med. Chem.*, 2009, **52**, 7753-7764.

41 C. Ge, X. Zhang, W. Guan and Q. Liu, *J. Chem. Crystallogr.*, 2006, **36**, 459-464.

42 C. Ge, H. Kou, Z. Ni, Y. Jiang and A. Cui, *Inorg. Chim. Acta*, 2006, **359**, 541-547.

43 W. Jacob and R. Mukherjee, *Inorg. Chim. Acta*, 2006, **359**, 4565-4573.

44 J. Y. Qi, H. X. Ma, X. J. Li, Z. Y. Zhou, M. C. K. Choi, A. S. C. Chan and Q. Y. Yang, *Chem. Commun.*, 2003, **11**, 1294-1295.

45 A. Das, S. M. Peng, G. H. Lee and S. Bhattacharya, *New J. Chem.*, 2004, **28**, 712-717.

46 S. Nag, R. J. Butcher and S. Bhattacharya, *Eur. J. Inorg. Chem.*, 2007, **9**, 1251-1260.

47 M. Dasgupta, H. Tadesse, A. J. Blake and S. Bhattacharya, *J. Organomet. Chem.*, 2008, **693**, 3281-3288.

48 T. Yang, J. Y. Zhang, C. Tu, J. Lin, Q. Liu and Z. J. Guo, *Chin. J. Inorg. Chem.*, 2003, **19**, 45-48.

49 J. Y. Qi, Y. M. Li, Z. Y. Zhou, C. M. Che, C. H. Yeung and A. S. C. Chan, *Adv. Synth. Catal.*, 2005, **347**, 45-49.

50 W. Jacob and R. Mukherjee, *J. Chem. Sci.*, 2008, **120**, 447-453.

51 J. Y. Zhang, Q. Liu, C. Y. Duan, Y. Shao, J. Ding, Z. H. Miao, X. Z. You and Z. J. Guo, *J. Chem. Soc.*, *Dalton Trans.*, 2002, **4**, 591-597.

52 T. W. Greene and P. G. M. Wuts, *Protective Groups in Organic Synthesis*, John Wiley & Sons Inc., New York, 1999.

53 D. T. Smith, R. Shi, R. B. Borgens, J. M. McBride, K. Jackson and S. R. Byrn, *Eur. J. Med. Chem.*, 2005, **40**, 908-917.

54 J. M. McBride, D. T. Smith, S. R. Byrn, R. B. Borgens and R. Y. Shi, *Eur. J. Pharm. Sci.*, 2006, **27**, 237-242.

55 F. Norberto, S. Santos, D. Silva, P. Herves, A. S. Miguel and F. Vilela, *J. Chem. Soc. -Perkin Trans. 2*, 2002, **6**, 1162-1165.

56 I. Lalezari, H. Golgolab, A. Shafiee and M. Wossoughi, *J. Pharm. Sci.*, 1973, **62**, 332-333.

57 H. Matondo, N. Benevides, M. Tissut, M. Bergon, A. Desavignac, J. P. Calmon and A. Lattes, *J. Agric. Food Chem.*, 1989, **37**, 169-172.

58 D. Kopecny, P. Briozzo, H. Popelkova, M. Sebela, R. Koncitikova, L. Spichal, J. Nisler, C. Madzak, I. Frebort, M. Laloue and N. Houba-Herin, *Biochimie*, 2010, **92**, 1052-1062.

59 V. Kapchina-Toteva and D. Stoyanova, *Biol. Plant.*, 2003, **46**, 337-341.

60 M. Somleva, V. Kapchina-Toteva, V. Alexieva, I. Sergiev and E. Karanov, *J. Plant Physiol.*, 2000, **156**, 623-627.

61 M. M. Somleva, V. Kapchina, V. Alexieva and E. Golovinsky, *Plant Growth Regul.*, 1995, **16**, 109-112.

62 R. Shimizu, H. Iwamura and T. Fujita, *Z. Naturforsch. (C)*, 1990, **45**, 89-95.

63 A. D. Wickenden, J. L. Krajewski, B. London, P. K. Wagoner, W. A. Wilson, S. Clark, R. Roeloffs, G. McNaughton-Smith and G. C. Rigdon, *Mol. Pharmacol.*, 2008, **73**, 977-986.

64 L. Guidoni and P. Carloni, *Biochim. Biophys. Acta*, 2002, **1563**, 1-6.

65 L. Guidoni, V. Torre and P. Carloni, *Biochemistry-US*, 1999, **38**, 8599-8604.

66 S. Berneche and B. Roux, *Nature*, 2001, **414**, 73-77.

67 R. J. Mashl, Y. Z. Tang, J. Schnitzer and E. Jakobsson, *Biophys. J.*, 2001, **81**, 2473-2483.

68 J. Aqvist and V. Luzhkov, *Nature*, 2000, **404**, 881-884.

69 S. Garofoli, G. Miloshevsky, V. L. Dorman and P. C. Jordan, in *Ion Channels: from Atomic Resolution Physiology to Functional Genomics*, Novartis Foundation Symposium, 2002, pp. 109-126.

70 C. Biervert, B. C. Schroeder, C. Kubisch, S. F. Berkovic, P. Propping, T. J. Jentsch and O. K. Steinlein, *Science*, 1998, **279**, 403-406.

71 J. Vohra, *Heart Lung Circ.*, 2007, **16**, S5-S12.

72 S. Y. Chiu and J. M. Ritchie, *Nature*, 1980, **284**, 170-171.

73 S. I. V. Judge and C. T. Bever, *Pharmacol. Therapeut.*, 2006, **111**, 224-259.

74 R. MacKinnon, *Nature*, 1991, **350**, 232-235.

75 E. V. Orlova, M. Papakosta, F. P. Booy, M. van Heel and J. O. Dolly, *J. Mol. Biol.*, 2003, **326**, 1005-1012.

76 M. S. P. Sansom, I. H. Shrivastava, J. N. Bright, J. Tate, C. E. Capener and P. C. Biggin, *Biochim. Biophys. Acta*, 2002, **1565**, 294-307.

77 C. D. Sansom and S. P. Mark, *Biophys. J.*, 2003, **85**, 2787-2800.

78 D. A. Doyle, J. M. Cabral, R. A. Pfuetzner, A. Kuo, J. M. Gulbis, S. L. Cohen, B. T. Chait and R. MacKinnon, *Science*, 1998, **280**, 69-77.

79 Y. Zhou, J. H. Morais-Cabral, A. Kaufman and R. MacKinnon, *Nature*, 2001, **414**, 43-48.

80 A. Kuo, J. M. Gulbis, J. F. Antcliff, T. Rahman, E. D. Lowe, J. Zimmer, J. Cuthbertson, F. M. Ashcroft, T. Ezaki and D. A. Doyle, *Science*, 2003, **300**, 1922-1926.

81 Y. Jiang, A. Lee, J. Chen, V. Ruta, M. Cadene, B. T. Chait and R. MacKinnon, *Nature*, 2003, **423**, 42-48.

82 S. B. Long, E. B. Campbell and R. MacKinnon, *Science*, 2005, **309**, 897-903.

83 C. E. Capener, H. J. Kim, Y. Arinaminpathy and M. S. Sansom, *Hum. Mol. Genet.*, 2002, **11**, 2425-2433.

84 V. B. Luzhkov, J. Nilsson, P. Arhem and J. Aqvist, *Biochim. Biophys. Acta*, 2003, **652**, 35-51.

85 S. Mondal, R. M. Babu, R. Bhavna and S. Ramakumar, *In Silico Biol.*, 2007, **7**, 175-186.

86 M. Recanatini, A. Cavalli and M. Masetti, in *The hERG Cardiac Potassium Channel: Structure, Function and Long QT Syndrome: Novartis Foundation Symposium 266*, ed. D. J. Chadwick and J. Goode, John Wiley & Sons, Ltd, Chichester, UK, 2008, pp. 171-185.

87 E. Y. Isacoff, Y. N. Jan and L. Y. Jan, in *Comparative Molecular Neurobiology*, ed. Y. Pinchon, Birchauser Verlag, Basel, Switzerland, 1993, pp. 338-351.

88 S. Grissmer and M. Cahalan, *Biophys. J.*, 1989, **55**, 203-206.

89 K. L. Choi, R. W. Aldrich and G. Yellen, *Proc. Natl. Acad. Sci. USA*, 1991, **88**, 5092-5095.

90 G. Yellen, D. Sodickson, T. Y. Chen and M. E. Jurman, *Biophys. J.*, 1994, **66**, 1068-1075.

91 Y. Liu, M. E. Jurman and G. Yellen, *Neuron*, 1996, **16**, 859-867.

92 L. Kiss and S. J. Korn, *Biophys. J.*, 1998, **74**, 1840-1849.

93 H. R. Guy and P. Seetharamulu, *Proc. Natl. Acad. Sci. USA*, 1986, **83**, 508-512.

94 I. H. Shrivastava, S. R. Durell and H. R. Guy, *Biophys. J.*, 2004, **87**, 2255-2270.

95 S. R. Durell, I. H. Shrivastava and H. R. Guy, *Biophys. J.*, 2004, **87**, 2116-2130.

96 N. Yang, A. L. George and R. Horn, *Neuron*, 1996, **16**, 113-122.

97 D. M. Starace and F. Bezanilla, *Nature*, 2004, **427**, 548-553.

98 Y. Jiang, V. Ruta, J. Chen, A. Lee and R. MacKinnon, *Nature*, 2003, **423**, 33-41.

99 H. Meves and Y. Pichon, *J. Physiol-London*, 1975, **251**, P60-P62.

100 G. E. Kirsch and T. Narahashi, *Biophys. J.*, 1978, **22**, 507-512.

101 A. R. Blight, *Neuroscience*, 1983, **10**, 1471-1486.

102 A. R. Blight, *Brain Res. Bull.*, 1989, **22**, 47-52.

103 A. R. Blight and J. A. Gruner, *J. Neurol. Sci.*, 1987, **82**, 145-159.

104 A. R. Blight, J. P. Toombs, M. S. Bauer and W. R. Widmer, *J. Neurotraum.*, 1991, **8**, 103-119.

105 F. A. Davis, D. Stefoski and J. Rush, *Ann. Neurol.*, 1990, **27**, 186-192.

106 R. R. Hansebout, A. R. Blight, S. Fawcett and K. Reddy, *J. Neurotraum.*, 1993, **10**, 1-18.

107 K. C. Hayes, P. J. Potter, D. L. Wolfe, J. T. C. Hsieh, G. A. Delaney and A. R. Blight, *J. Neurotraum.*, 1994, **11**, 433-446.

108 R. E. Jones, J. R. Heron, D. H. Foster, R. S. Snelgar and R. J. Mason, *J. Neurol. Sci.*, 1983, **60**, 353-362.

109 C. H. Polman, F. W. Bertelsmann, A. C. Vanloenen and J. C. Koetsier, *Arch. Neurol-Chicago*, 1994, **51**, 292-296.

110 D. Stefoski, F. A. Davis, M. Faut and C. L. Schauf, *Ann. Neurol.*, 1987, **21**, 71-77.

111 H. A. M. Vandiemen, C. H. Polman, M. Vandongen, J. J. P. Nauta, R. L. M. Strijers, A. C. Vanloenen, F. W. Bertelsmann and J. C. Koetsier, *J. Neurol. Sci.*, 1993, **116**, 220-226.

112 P. J. Potter, K. C. Hayes, J. T. C. Hsieh, G. A. Delaney and J. L. Segal, *Spinal Cord*, 1998, **36**, 147-155.

113 P. J. Potter, K. C. Hayes, J. L. Segal, J. T. C. Hsieh, S. R. Brunnemann, G. A. Delaney, D. S. Tierney and D. Mason, *J. Neurotraum.*, 1998, **15**, 837-849.

114 J. L. Segal and S. R. Brunnemann, *Pharmacotherapy*, 1997, **17**, 415-423.

115 J. L. Segal, M. S. Pathak, J. P. Hernandez, P. L. Himber, S. R. Brunnemann and R. S. Charter, *Pharmacotherapy*, 1999, **19**, 713-723.

116 C. T. Bever, P. A. Anderson, J. Leslie, H. S. Panitch, S. DhibJalbut, O. A. Khan, R. Milo, J. R. Hebel, K. L. Conway, E. Katz and K. P. Johnson, *Neurology*, 1996, **47**, 1457-1462.

117 R. Shi and A. R. Blight, *Neuroscience*, 1997, **77**, 553-562.

118 C. M. Stork and R. S. Hoffman, *Clin. Toxicol.*, 1994, **32**, 583-587.

119 F. Pena and R. Tapia, *Neuroscience*, 2000, **101**, 547-561.

120 F. Pena and R. Tapia, *J. Neurochem.*, 1999, **72**, 2006-2014.

121 N. A. Castle, S. Fadous, D. E. Logothetis and G. K. Wang, *Mol. Pharmacol.*, 1994, **45**, 1242-1252.

122 A. Loboda and C. M. Armstrong, *Biophys. J.*, 2001, **81**, 905-916.

123 A. Nino and C. Muñoz-Caro, *Biophys. Chem.*, 2001, **91**, 49-60.

124 C. Muñoz-Caro and A. Nino, *Biophys. Chem.*, 2002, **96**, 1-14.

125 A. Nino, C. Muñoz-Caro, R. Carbo-Dorca and X. Girones, *Biophys. Chem.*, 2003, **104**, 417-427.

126 N. A. Caballero, F. J. Melendez, A. Nino and C. Muñoz-Caro, *J. Mol. Model.*, 2007, **13**, 579-586.

127 W. A. Schmalhofer, J. M. Bao, O. B. McManus, B. Green, M. Matyskiela, D. Wunderler, R. M. Bugianesi, J. P. Felix, M. Hanner, A. R. Linde-Arias, C. G. Ponte, L. Velasco, G. Koo, M. J. Staruch, S. W. Miao, W. H. Parsons, K. Rupprecht, R. S. Slaughter, G. J. Kaczorowski and M. L. Garcia, *Biochemistry-US,* 2002, **41**, 7781-7794.

128 S. N. Gradl, J. P. Felix, E. Y. Isacoff, M. L. Garcia and D. Trauner, *J. Am. Chem. Soc.,* 2003, **125**, 12668-12669.

129 C. Ader, R. Schneider, S. Hornig, P. Velisetty, E. M. Wilson, A. Lange, K. Giller, I. Ohmert, M. F. Martin-Eauclaire, D. Trauner, S. Becker, O. Pongs and M. Baldus, *Nat. Struct. Mol. Biol.*, 2008, **15**, 605-612.

130 V. Martos, S. C. Bell, E. Santos, E. Y. Isacoff, D. Trauner and J. de Mendoza, *Proc. Natl. Acad. Sci. U. S. A.*, 2009, **106**, 10482-10486.

131 J. B. Baell, R. W. Gable, A. J. Harvey, N. Toovey, T. Herzog, W. Hansel and H. Wulff, *J. Med. Chem.*, 2004, **47**, 2326-2336.

132 S. Peukert, J. Brendel, B. Pirard, A. Bruggemann, P. Below, H. W. Kleemann, H. Hemmerle and W. Schmidt, *J. Med. Chem.*, 2003, **46**, 486-498.

133 S. Peukert, J. Brendel, B. Pirard, C. Strubing, H. W. Kleemann, T. Bohme and H. Hemmerle, *Bioorg. Med. Chem. Lett.*, 2004, **14**, 2823-2827.

134 M. A. Goetz, O. D. Hensens, D. L. Zink, R. P. Borris, F. Morales, G. Tamayo-Castillo, R. S. Slaughter, J. Felix and R. G. Ball, *Tetrahedron Lett.*, 1998, **39**, 2895-2898.

135 J. P. Felix, R. M. Bugianesi, W. A. Schmalhofer, R. Borris, M. A. Goetz, O. D. Hensens, J. M. Bao, F. Kayser, W. H. Parsons, K. Rupprecht, M. L. Garcia, G. J. Kaczorowski and R. S. Slaughter, *Biochemistry-US*, 1999, **38**, 4922-4930.

136 R. Vianna-Jorge, C. F. Oliveira, M. L. Garcia, G. J. Kaczorowski and G. Suarez-Kurtz, *Br. J. Pharmacol.*, 2000, **131**, 772-778.

137 Potiga, US Food and Drug Administration, 2011.

138 C. A. Seaman, P. H. Sheridan, J. Engel, M. Molliere, P. K. Narang and F. J. Nice, in *New anticonvulsant drugs: Current Problems in Epilepsy 4*, ed. B. S. Meldrum and R. J. Porter, Libbey, London, 1986, pp.135-146.

139 C. Rundfeldt, *Epilepsy Res.*, 1999, **35**, 99-107.

140 C. Rundfeldt, *Eur. J. Pharmol.*, 1997, **336**, 243-249.

141 C. Rundfeldt and R. Netzer, *Neurosci. Lett.*, 2000, **282**, 73-76.

142 A. D. Wickenden, W. F. Yu, A. Zou, T. Jegla and P. K. Wagoner, *Mol. Pharmacol.*, 2000, **58**, 591-600.

143 L. Tatulian, P. Delmas, F. C. Abogadie and D. A. Brown, *J. Neurosci.*, 2001, **21**, 5535-5545.

144 A. D. Wickenden, A. R. Zou, P. K. Wagoner and T. Jegla, *Br. J. Pharmacol.*, 2001, **132**, 381-384.

145 T. V. Wuttke, G. Seebohm, S. Bail, S. Maljević and H. Lerche, *Mol. Pharmacol.*, 2005, **67**, 1009-1017.

146 G. Biagi, I. Giorgi, O. Livi, A. Nardi, V. Calderone, A. Martelli, E. Martinotti and O. L. Salerni, *Eur. J. Med. Chem.*, 2004, **39**, 491-498.

147 V. Calderone, A. Coi, F. L. Fiamingo, I. Giorgi, M. Leonardi, O. Livi, A. Martelli and E. Martinotti, *Eur. J. Med. Chem.*, 2006, **41**, 1421-1429.

148 V. Calderone, F. L. Fiamingo, I. Giorgi, M. Leonardi, O. Livi, A. Martelli and E. Martinotti, *Eur. J. Med. Chem.*, 2006, **41**, 761-767.

149 Y. J. Wu, C. G. Boissard, C. Greco, V. K. Gribkoff, D. G. Harden, H. He, A. L'Heureux, S. H. Kang, G. G. Kinney, R. J. Knox, J. Natale, A. E. Newton, S. Lehtinen-Oboma, M. W. Sinz, D. V. Sivarao, J. E. Starrett, L. Q. Sun, S. Tertyshnikova, M. W. Thompson, D. Weaver, H. S. Wong, L. Zhang and S. L. Dworetzky, *J. Med. Chem.*, 2003, **46**, 3197-3200.

150 B. H. Bentzen, N. Schmitt, K. Calloe, W. D. Brown, M. Grunnet and S. P. Olesen, *Neuropharmacology*, 2006, **51**, 1068-1077.

151 Y. J. Wu, L. Q. Sun, H. He, J. Chen, J. E. Starrett, P. Dextraze, J. P. Daris, C. G. Boissard, R. L. Pieschl, V. K. Gribkoff, J. Natale, R. J. Knox, D. G. Harden, M. W. Thompson, W. Fitzpatrick, D. Weaver, D. D. Wu, Q. Gao and S. I. Dworetzky, *Bioorg. Med. Chem. Lett.*, 2004, **14**, 4533-4537.

152 R. S. Hansen, T. G. Diness, T. Christ, J. Demnitz, U. Ravens, S. P. Olesen and M. Grunnet, *Mol. Pharmacol.*, 2006, **69**, 266-277.

153 R. S. Hansen, T. G. Diness, T. Christ, E. Wettwer, U. Ravens, S. P. Olesen and M. Grunnet, *Mol. Pharmacol.*, 2006, **70**, 1319-1329.

154 R. S. Hansen, S. P. Olesen and M. Grunnet, *J. Pharm. Exp. Ther.*, 2007, **321**, 996-1002.

155 O. Casis, S. P. Olesen and M. C. Sanguinetti, *Mol. Pharmacol.*, 2006, **69**, 658-665.

156 P. Elmedyb, S. P. Olesen and M. Grunnet, *Neuropharmacology*, 2007, **53**, 283-294.

157 J. Zhou, C. E. Augelli-Szafran, J. A. Bradley, X. Chen, B. J. Koci, W. A. Volberg, Z. Q. Sun and J. S. Cordes, *Mol. Pharmacol.*, 2005, **68**, 876-884.

158 E. Gordon, I. M. Lozinskaya, Z. Lin, S. F. Semus, F. E. Blaney, R. N. Willette and X. Xu, *Mol. Pharmacol.*, 2008, **73**, 639-651.

159 Q. Lu, J. Peevey, F. Jow, M. M. Monaghan, G. Mendoza, H. Zhang, J. Wu, C. Y. Kim, J. Bicksler, L. Greenblatt, S. S. Lin, W. Childers and M. R. Bowlby, *Bioorg. Med. Chem.*, 2008, **16**, 3067-3075.

160 P. A. Lyon and C. B. Reese, *J. Chem. Soc. Perk. Trans. 1*, 1974, **23**, 2645-2649.

161 L. W. Deady and D. C. Stillman, *Aust. J. Chem.*, 1979, **32**, 381-386.

162 K. Donnelly, J. F. Gallagher and A. J. Lough, *Acta Crystallogr. Sect C-Cryst. Struct. Commun.*, 2008, **C64**, O335-O340.

163 J. F. Gallagher, K. Donnelly and A. J. Lough, *Acta Crystallogr. Sect. E-Struct Rep. Online*, 2009, **E65**, O102-O103.

164 J. F. Gallagher, K. Donnelly and A. J. Lough, *Acta Crystallogr. Sect. E-Struct Rep. Online*, 2009, **E65**, O486-O487.

165 Enraf Nonius BV, 1997, *Windows 3.11 Version*.

166 Bruker APEXII, *(Version 2. 0-1)*, 2005, Bruker AXS Inc., Madison, Wisconsin, USA.

167 Z. Otwinowski and W. Minor, in *Macromolecular Crystallography*, *Part A,* ed. J. N. Abelson, M. I. Simon, C. W. Carter and R. M. Sweet, Academic Press Inc., New York, 1997, pp. 307-326.

168 P. McArdle, *J. Appl. Cryst.*, 1995, **28**, 65-65.

169 A. L. Spek, *J. Appl. Cryst.*, 2003, **36**, 7-13.

170 A. V. Marenich, C. J. Cramer and D. G. Truhlar, *J. Phys. Chem. B*, 2009, **113**, 6378-6396.

171 J. A. Montgomery, J. W. Ochterski and G. A. Petersson, *J. Chem. Phys.*, 1994, **101**, 5900-5909.

172 J. McMahon, F. P. Anderson, J. F. Gallagher and A. J. Lough, *Acta Crystallogr. Sect. C-Cryst. Struct. Commun.*, 2008, **C64**, O493-O497.

173 G. R. Desiraju and T. Steiner, *The Weak hydrogen Bond in Structural Chemistry and Biology*, Oxford University Press, Oxford, UK, 1999.

174 E. A. Meyer, R. K. Castellano and F. Diederich, *Angew. Chem. Int. Edit.*, 2003, **42**, 1210-1250.

175 M. Nishio, M. Hirota and Y. Umezawa, *The CH/π interaction*, Wiley, New York, 1998.

176 Crysalis, Oxford Diffraction, 2010, *Version 1.171.33.55.*

177 R. G. N. Manjunatha, K. Vasantha M.V., T. N. G. Row and N. Suryaprakash, *Phys. Chem. Chem. Phys.*, 2010, **12**, 13232-13237.

178 J. C. Noveron, M. S. Lah, R. E. Del Sesto, A. M. Arif, J. S. Miller and P. J. Stang, *J. Am. Chem. Soc.*, 2002, **124**, 6613-6625.

179 H. G. Brittain, *J. Pharm. Sci.*, 2011, **100**, 1260-1279.

180 J. Bernstein, *Cryst. Growth Des.*, 2011, **11**, 632-650.

181 H. G. Gebreslasie, Ø. Jacobsen and C. H. Görbitz, *Acta Crystallogr. Sect. C-Cryst. Struct. Commun.*, 2011, **C67**, O283-O287.

182 G. J. Gainsford, M. D. H. Bhuiyan and A. J. Kay, *Acta Crystallogr. Sect. E. -Struct Rep. Online*, 2008, **E64**, O874-O875.

183 G. Ferguson, J. F. Gallagher, C. Glidewell, J. N. Low and S. N. Scrimgeour, *Acta Crystallogr. Sect. C-Cryst. Struct. Commun.*, 1992, **C48**, 1272-1275.

184 G. Ferguson, J. F. Gallagher, D. Murphy, T. R. Spalding, C. Glidewell and H. D. Holden, *Acta Crystallogr. Sect C-Cryst. Struct. Commun.*, 1992, **C48**, 1228-1231.

185 H. V. R. Dias and Goh, T. K. H. H., *Polyhedron*, 2004, **23**, 273-282.

186 G. J. S. Venter, A. Roodt and R. Meijboom, *Inorg. Chim. Acta*, 2009, **362**, 2475-2479.

187 Q. Zhang, S. P. Zhang and S. C. Shao, *Acta Crystallogr. Sect. E: Struct. Rep. Online*, 2006, **E62**, O4695-O4696.

188 J. Y. Qi, Q. Y. Yang, K. H. Lam, Z. Y. Zhou and A. S. C. Chan, *Acta Crystallogr. Sect. E: Struct. Rep. Online*, 2003, **E59**, O374-O375.

189 A. S. Gilbert, *Thermochim. Acta*, 2007, **452**, 135-139.

190 S. A. Barnett, A. T. Hulme and D. A. Tocher, *Acta Crystallogr. Sect. C-Cryst. Struct. Commun.*, 2006, **C62**, O412-O415.

191 F. G. Vogt, J. A. Vena, M. Chavda, J. S. Clawson, M. Strohmeier and M. E. Barnett, *J. Mol. Struct.*, 2009, **932**, 16-30.

192 W. H. Ojala, K. M. Lystad, T. L. Deal, J. E. Engebretson, J. M. Spude, B. Balidemaj and C. R. Ojala, *Crystal Growth & Des.*, 2009, **9**, 964-970.

193 J. McMahon, J. F. Gallagher, F. P. Anderson and A. J. Lough, *Acta Crystallogr. Sect. C-Cryst. Struct. Commun.*, 2009, **C65**, O345-O351.

194 B. T. Gowda, B. P. Sowmya, J. Kozisek, M. Tokarcik and H. Fuess, *Acta Crystallogr. Sect. C-Cryst. Struct. Commun.*, 2007, **C63**, O2906.

195 D. Percival, J. M. D. Storey and W. T. A. Harrison, *Acta Crystallogr. Sect. E-Structural Reports Online.*, 2007, **E63**, O1851-O1852.

196 G. V. De Lucca, U. T. Kim, B. J. Vargo, J. V. Duncia, J. B. Santella, D. S. Gardner, C. S. Zheng, A. Liauw, Z. Wang, G. Emmett, D. A. Wacker, P. K. Welch, M. Covington, N. C. Stowell, E. A. Wadman, A. M. Das, P. Davies, S. Yeleswaram, D. M. Graden, K. A. Solomon, R. C. Newton, G. L. Trainor, C. P. Decicco and S. S. Ko, *J. Med. Chem.*, 2005, **48**, 2194-2211.

197 C. H. Mack, H. H. McGregor and S. R. Hobart, *J. Chem. Eng. Data*, 1969, **14**, 258-261.

198 D. M. Swanson, A. E. Dubin, C. Shah, N. Nasser, L. Chang, S. L. Dax, M. Jetter, J. G. Breitenbucher, C. L. Liu, C. Mazur, B. Lord, L. Gonzales, K. Hoey, M. Rizzolio, M. Bogenstaetter, E. E. Codd, D. H. Lee, S. P. Zhang, S. R. Chaplan and N. I. Carruthers, *J. Med. Chem.*, 2005, **48**, 1857-1872.

199 E. F. V. Scriven and K. Turnbull, *Chem. Rev.*, 1988, **88**, 297-368.

200 T. Curtius, *J. Praktische Chem.*, 1894, **50**, 275-294.

201 T. Shioiri, K. Ninomiya and S. Yamada, *J. Am. Chem. Soc.*, 1972, **94**, 6203-6205.

202 A. Sasse, X. Ligneau, A. Rouleau, S. Elz, C. R. Ganellin, J. M. Arrang, J. C. Schwartz, W. Schunack and H. Stark, *J. Med. Chem.*, 2002, **45**, 4000-4010.

203 A. Sasse, H. Stark, X. Ligneau, S. Elz, S. Reidemeister, C. R. Ganellin, J. C. Schwartz and W. Schunack, *Bioorg. Med. Chem.*, 2000, **8**, 1139-1149.

204 A. Rutar, U. Zbontar, D. Kikelj and I. Leban, *Chirality*, 1998, **10**, 791-799.

205 M. Takadoi, T. Katoh, A. Ishiwata and S. Terashima, *Tetrahedron*, 2002, **58**, 9903-9923.

206 B. Beagley, K. J. Farnworth, E. T. Moss, R. G. Pritchard, S. Tajammal and A. E. Tipping, *Acta Crystallogr. Sect. C-Cryst. Struct. Commun.*, 1994, **C50**, 1130-1132.

207 C. N. Foces-Foces, I. Alkorta and J. Elguero, *Acta Crystallogr. Sect. B-Struct. Sci.*, 2000, **B56**, 1018-1028.

208 E. F. Maverick, P. L. Wash and D. A. Lightner, *Acta Crystallogr. Sect. C-Cryst. Struct. Commun.*, 2001, **C57**, 284-285.

209 R. E. Gerkin, *Acta Crystallogr. Sect. C-Cryst. Struct. Commun.*, 1998, **C54**, 1887-1889.

210 I. Alkorta, J. Elguero, C. Foces-Foces and L. Infantes, *Arkivoc*, 2006, 15-30.

211 S. Higson and F. Davis, *Macrocycles: Construction, Chemistry and Nanotechnology applications*, John Wiley & Sons Ltd, U.K., 2011.

212 J. W. Steed and J. L. Atwood, *Supramolecular Chemistry*, John Wiley & Sons, West Sussex, U.K., 2009.

213 J. Vicens and J. Harrowfield, *Calixarenes in the Nanoworld*, Springer, Dordrecht, The Netherlands, 2007.

214 K. Gloe, *Macrocyclic Chemistry, Current trends and Future Perspectives*, Springer, Dordrecht, The Netherlands, 2005.

215 E. M. Driggers, S. P. Hale, J. Lee and N. K. Terrett, *Nat. Rev. Drug Discov.*, 2008, **7**, 608-624.

216 D. Parker and J. A. G. Williams, *J. Chem. Soc.-Perkin Trans. 2*, 1995, **7**, 1305-1314.

217 D. Parker, I. Helps and R. Morphy, *Br. J. Cancer*, 1986, **54**, 531-531.

218 L. S. Evans and P. A. Gale, *Chem. Commun.*, 2004, 1286-1287.

219 H. M. Colquhoun, Z. Zhu, D. J. Williams, C. J. Cardin, Y. Gan, A. G. Crawford and T. B. Marder, *Chem. Eur. J.*, 2010, **16**, 907-918.

220 J. Gawroński, M. Brzostowska, K. Gawrońska, J. Koput, U. Rychlewska, P. Skowronek and B. Nordén, *Chem.-Eur. J.*, 2002, **8**, 2484-2494.

221 W. Marckwald, *Chem. Ber.*, 1894, **27**, 1317-1339.

222 A. E. Tschitschibabin and J. G. Bylinkin, *Chem. Ber.*, 1922, **55**, 1000-1002.

223 J. P. Wibaut and E. Dingemanse, *Recl. Trav. Chim. Pay-B.*, 1923, **42**, 240-250.

224 E. H. Huntress and H. C. Walter, *J. Org. Chem.*, 1948, **13**, 735-737.

225 T. Suzuki, N. Kenbou and K. Mitsuhashi, *J. Heterocycl. Chem.*, 1979, **16**, 645-648.

226 E. E. Bolton, J. Chen, S. Kim, L. Han, S. He, W. Shi, V. Simonyan, Y. Sun, P. A. Thiessen, J. Wang, B. Yu, J. Zhang and S. H. Bryant, *J. Cheminf.*, 2011, **3**, 32.

227 S. Shimizu, N. Watanabe, T. Kataoka, T. Shoji, N. Abe, S. Morishita and H. Ichimura, in *Ullmann's Encyclopedia of Industrial Chemistry, 5th ed.*, *Vol. A22.*, ed. B. Elvers, S. Hawkins, M. Ravenscroft and G. Schulz, VCH Publishers, Würzburg, Germany, 1993, pp. 399-418.

228 R. B. Seymour and G. S. Kirshenbaum, *High Performance Polymers: Their Origin and Development*, Elsevier, New York, 1986.

229 D. Wilson, H. D. Stenzenberger and P. M. Hergenrother, *Polyimides*, Blackie & Son Ltd., Glasgow and London, 1990.

230 A. R. Murthy, S. D. Wyrick, P. J. Voorstad and I. H. Hall, *Eur. J. Med. Chem.*, 1985, **20**, 547-550.

231 F. Wurthner, Z. J. Chen, F. J. M. Hoeben, P. Osswald, C. C. You, P. Jonkheijm, J. von Herrikhuyzen, A. P. H. J. Schenning, P. P. A. M. van der Schoot, E. W. Meijer, E. H. A. Beckers, S. C. J. Meskers and R. A. J. Janssen, *J. Am. Chem. Soc.*, 2004, **126**, 10611-10618.

232 M. Tominaga, T. Hatano, M. Uchiyama, H. Masu, H. Kagechikac and I. Azumaya, *Tetrahedron Lett.*, 2006, **47**, 9369-9371.

233 K. E. Riley, J. S. Murray, J. Fanfrlik, J. Rezac, R. J. Sola, M. C. Concha, F. M. Ramos and P. Politzer, *J. Mol. Model.*, 2011, **17**, 3309-3318.

234 J. V. Coelho and M. P. Freitas, *J. Mol. Struc. -TheoChem*, 2010, **941**, 53-55.

235 K. E. Riley, J. S. Murray, P. Politzer, M. C. Concha and P. Hobza, *J. Chem. Theory. Comput.*, 2009, **5**, 155-163.

236 P. Auffinger, F. A. Hays, E. Westhof and P. S. Ho, *Proc. Natl. Acad. Sci. U. S. A.*, 2004, **101**, 16789-16794.

237 A. De Santis, A. Forni, R. Liantonio, P. Metrangolo, T. Pilati and G. Resnati, *Chem. -Eur. J.*, 2003, **9**, 3974-3983.

238 A. R. Katritzky, M. Kuanar, S. Slavov, C. D. Hall, M. Karelson, I. Kahn and D. A. Dobchev, *Chem. Rev.*, 2010, **110**, 5714-5789.

239 R. J. C. Brown and R. F. C. Brown, *J. Chem. Educ.*, 2000, **77**, 724-731.